

Advances in CFD Prediction of Shock Wave Turbulent Boundary Layer Interactions

Doyle Knight and Hong Yan
Department of Mechanical and Aerospace Engineering
Rutgers - The State University of New Jersey
Piscataway, NJ 08854
Argyris G. Panaras Consulting Engineer
P.O. Box 64053
Athens 15710, Greece
Alexander Zheltovodov
Institute of Theoretical and Applied Mechanics
Siberian Branch of the Russian Academy of Sciences
Novosibirsk 630090, Russia

Submitted to:
Dr. K. J. Orlik-Rückemann
749 Chapman Boulevard
Ottawa, Ontario K1G 1T8
Canada

Revision 2 November 2002

Address all correspondence to:
Prof. Doyle Knight
Department of Mechanical and Aerospace Engineering
Rutgers - The State University of New Jersey
98 Brett Road
Piscataway, NJ 08854-8058
Telephone: 732 445 4464
Faxsimile: 732 445 3124
Email: ddknight@rci.rutgers.edu

Report Documentation Page				Form Approved OMB No. 0704-0188	
Public reporting burden for the collection of information is estimated to average 1 hour per response, including the time for reviewing instructions, searching existing data sources, gathering and maintaining the data needed, and completing and reviewing the collection of information. Send comments regarding this burden estimate or any other aspect of this collection of information, including suggestions for reducing this burden, to Washington Headquarters Services, Directorate for Information Operations and Reports, 1215 Jefferson Davis Highway, Suite 1204, Arlington VA 22202-4302. Respondents should be aware that notwithstanding any other provision of law, no person shall be subject to a penalty for failing to comply with a collection of information if it does not display a currently valid OMB control number.					
1. REPORT DATE 01 JAN 2006		2. REPORT TYPE N/A		3. DATES COVERED -	
4. TITLE AND SUBTITLE Advances in CFD Prediction of Shock Wave Turbulent Boundary Layer Interactions				5a. CONTRACT NUMBER	
				5b. GRANT NUMBER	
				5c. PROGRAM ELEMENT NUMBER	
6. AUTHOR(S)				5d. PROJECT NUMBER	
				5e. TASK NUMBER	
				5f. WORK UNIT NUMBER	
7. PERFORMING ORGANIZATION NAME(S) AND ADDRESS(ES) Department of Mechanical and Aerospace Engineering Rutgers - The State University of New Jersey Piscataway, NJ 08854				8. PERFORMING ORGANIZATION REPORT NUMBER	
9. SPONSORING/MONITORING AGENCY NAME(S) AND ADDRESS(ES)				10. SPONSOR/MONITOR'S ACRONYM(S)	
				11. SPONSOR/MONITOR'S REPORT NUMBER(S)	
12. DISTRIBUTION/AVAILABILITY STATEMENT Approved for public release, distribution unlimited					
13. SUPPLEMENTARY NOTES See also ADM001860, Technologies for Propelled Hypersonic Flight (Technologies des vols hypersoniques propulsés). , The original document contains color images.					
14. ABSTRACT					
15. SUBJECT TERMS					
16. SECURITY CLASSIFICATION OF:			17. LIMITATION OF ABSTRACT UU	18. NUMBER OF PAGES 212	19a. NAME OF RESPONSIBLE PERSON
a. REPORT unclassified	b. ABSTRACT unclassified	c. THIS PAGE unclassified			

Abstract

The paper presents a summary of recent Computational Fluid Dynamics (CFD) simulations of shock wave turbulent boundary layer interactions. This survey was prepared as part of the activity of NATO RTO Working Group 10 which was established in December 1998, and considers results obtained subsequent to the previous survey paper on the same topic by Knight and Degrez (“Shock Wave Boundary Layer Interactions in High Mach Number Flows – A Critical Survey of Current CFD Prediction Capabilities”, AGARD Advisory Report AR-319, Volume II, December 1998). Five configurations are considered: 2-D compression corner, 2-D shock impingement, 2-D expansion-compression corner, 3-D single fin and 3-D double fin. Recent Direct Numerical Simulations (DNS), Large Eddy Simulations (LES) and Reynolds-averaged Navier-Stokes (RANS) simulations are compared with experiment. The capabilities and limitations are described, and future research needs identified.

Keywords

boundary layers compressible flow, Computational Fluid Dynamics (CFD) Direct Numerical Simulation (DNS), gas dynamics, Large Eddy Simulation (LES), shock waves, turbulence

Contents List

1	Introduction
2	2-D Compression Corner and Shock Impingement
2.1	Case 1: Mach 3, $\alpha = 8^\circ$
2.2	Case 2: Mach 3, $\alpha = 18^\circ$
2.3	Case 3: Mach 3, $\alpha = 24^\circ$
2.4	Case 4: Mach 3, $\alpha = 25^\circ$
2.5	Case 5: Mach 2.3, $\alpha = 8^\circ$
3	2-D Expansion-Compression Corner
3.1	Case 1: Mach 3, $\alpha = 25^\circ$
4	3-D Single Fin
4.1	Cases 1-3: Mach 3, $\alpha = 15^\circ$ and Mach 4, $\alpha = 20^\circ$ and 30.6°
5	3-D Double Fin
5.1	Case 1: Mach 4, $\alpha_1 = 15^\circ, \alpha_2 = 15^\circ$
5.2	Case 2: Mach 4, $\alpha_1 = 7^\circ, \alpha_2 = 11^\circ$
5.3	Case 3: Mach 5, $\alpha_1 = 18^\circ, \alpha_2 = 18^\circ$
5.4	Case 4: Mach 5, $\alpha_1 = 23^\circ, \alpha_2 = 23^\circ$
6	Conclusions
7	Future Needs
8	Acknowledgments

Nomenclature

c_f	Skin friction coefficient
c_h	Heat transfer coefficient
c_p	Pressure coefficient
H_i	Incompressible shape factor, $H_i = \delta_i/\theta_i$
k	Turbulence kinetic energy
L	Length
ℓ	Turbulence length scale
M	Mach number
p	Pressure
Re	Reynolds number
T	Static temperature
u, v, w	Cartesian velocity components
x, y, z	Cartesian coordinates
u_τ	Wall friction velocity
α	Corner angle
δ	Boundary layer thickness
δ_i	Incompressible displacement thickness
κ	Von Karman's constant
ρ	Density
τ	Shear stress
θ_i	Incompressible momentum thickness
μ	Dynamic molecular viscosity ($= \nu\rho$)
aw	Adiabatic wall
c	Characteristic length
DNS	Direct Numerical Simulation
E	Experiment
LES	Large Eddy Simulation
LES-D	Dynamic Smagorinsky model LES
LES-M	Monotone Integrated Large Eddy Simulation
LES-X	Mixed scale model LES
LES-S	Static Smagorinsky model LES
m	Mean value
RANS	Reynolds-averaged Navier-Stokes
SA	Spatial accuracy
sep	Separation length
SS	Computation is converged to steady state

SWTBLI	Shock wave turbulent boundary layer interaction
TA	Temporal accuracy
TML	Throat middle line
VD	Van-Driest transformation
w	Wall
∞	Upstream
"	Favre-fluctuating component
+	Normalized by ν_w/u_τ

1 Introduction

Effective design of supersonic and hypersonic air vehicles requires accurate simulation methods for predicting aerothermodynamic loads (*i.e.*, mean and fluctuating surface pressure, skin friction and heat transfer). Shock wave turbulent boundary layer interaction (SWTBLI) is common in high speed flight, and can significantly affect the aerothermodynamic loads. The recent AGARD Working Group 18 (WG 18) study edited by Knight and Degrez [1] examined the capability of general¹ Reynolds-averaged Navier-Stokes (RANS) methods for prediction of 2-D and 3-D shock wave turbulent boundary layer interactions. The study comprised 13 configurations and 37 computations contributed by 18 participants. The recent review by Zheltovodov [3] also examined the capability of RANS models for prediction of SWTBLI. Both studies concluded that general RANS methods accurately predicted mean surface pressure and heat transfer, and primary separation location for weak to moderate² 2-D and 3-D shock wave turbulent boundary layer interactions. For strong interactions, computed surface pressure and heat transfer distributions, and location of primary separation, show significant disagreement with experiment. In addition, the RANS calculations failed to capture the high level of unsteadiness in the shock system observed in the experiment and the appearance of secondary separation, and no RANS calculation provided a prediction of rms fluctuating surface pressure and heat transfer.

RTO Working Group 10 (WG 10) was established in December 1998 to examine three specific technologies for propelled hypersonic flight: plug nozzles (Subgroup 1), scramjet propulsion (Subgroup 2) and Computational Fluid Dynamics (Subgroup 3). Six specific topics were selected for evaluation by Subgroup 3, namely, boundary layer instability and transition, real gas flows, laminar hypersonic viscous-inviscid interactions, shock-shock interactions, shock wave turbulent boundary layer interactions, and base flows with and without plume interactions. In each topic, specific experiments were identified for CFD validation. A description of test cases was published [4]. The test cases are also described in [5].

This paper presents an expanded version of the summary report of the study of shock wave turbulent boundary layer interactions [6]. Five separate configurations are considered. The 2-D compression corner (Fig. 1) and expansion-compression corner (Fig. 3) represent, for example, deflected aerodynamic control surfaces. The 2-D shock impingement (Fig. 2) typifies a shock boundary layer interaction within an inlet, for example. The 3-D single fin (Fig. 4) is typical of a fin-fuselage juncture. The 3-D double fin (Fig. 5) represents a sidewall compression inlet. All five configurations have been extensively studied and a substantial

¹By *general* RANS method we mean a RANS model which has not been modified to take into account specific details of the flowfield structure. Significant progress has been made in development of *engineering* RANS methods which incorporate configuration-dependent flow physics. An example is Panaras [2].

²In this context, “weak” and “moderate” refer to the overall static pressure rise.

set of experimental data is available for each configuration.

Contributions of recent³ numerical simulations for the five cases were solicited through the RTO WG 10 membership and the RTO WG 10 website [7]. The studies include Direct Numerical Simulation (DNS), Large Eddy Simulation (LES) and Reynolds-averaged Navier Stokes (RANS). The computed results are compared herein with the experimental data, and the overall capabilities of the CFD methods are assessed. Readers interested in additional test cases for SWTBLI may consult Settles and Dodson [8] and Haase *et al* [9].

2 2-D Compression Corner and Shock Impingement

The 2-D supersonic compression corner (Fig. 1) and 2-D shock impingement (Fig. 2) are standard CFD validation cases for shock wave turbulent boundary layer interactions. In the former, an equilibrium supersonic turbulent boundary layer of height δ approaches a compression corner defined by an angle α_{cc} . The deflection of the flow by the corner generates a shock system. For sufficiently large pressure rise, the boundary layer separates and a λ -shock forms. In the latter, a incident shock generated by a wedge of angle α_{si} compresses the boundary layer leading to a complex system of compression and expansion waves which interact with a reflected shock.

The flowfield structures in the compression corner and shock impingement configurations were investigated in the pioneering experimental study by Petrov *et al* [10]. On the basis of extensive experiments for laminar and turbulent flows they concluded that the 2-D compression corner and 2-D shock impingement have several similar features, and were the first to formulate the free interaction concept. In accordance with this concept, the interaction in the vicinity of the separation line is local for developed separation zones and the critical shock wave strength (the static pressure ratio across the separation shock wave) is the same for these cases as well as for the 2-D shock wave turbulent boundary layer interaction in the vicinity of the shock wave which appears at the exit in an overexpanded nozzle. It does not depend of the strength of the initial ("inviscid") shock wave which initiates the interaction process and depends only on the freestream Mach number and the incoming boundary layer parameters. Petrov *et al* proposed the first empirical correlation for the critical shock wave strength (which is close to the specific plateau pressure ratio in the separated zone) and concluded that it is approximately proportional to the freestream Mach number at high Reynolds numbers. They also proposed the first empirical correlations for the ratio of the detachment distance of the separation shock wave relative the surface trace of the initial

³Simulations were selected from 1997 through 2002, since the review of Knight and Degrez [1] for AGARD WG 18 was completed in early 1997.

"inviscid" shock wave to the thickness of subsonic part of undisturbed boundary layer for the 2-D compression corner and the 2-D shock impingement configurations. On the basis of these correlations they concluded that this "subsonic region thickness" is the specific parameter which to a first approximation scales the data (by a single curve for every case) for some range of Mach and Reynolds numbers as well as the boundary layer thickness as a function of the flow inclination angle in the initial "inviscid" shock wave.

Chapman *et al* [11] also developed the free interaction concept through an extensive set of experiments. Gogish and Stepanov [12] developed a local theory of the turbulent boundary layer to predict the critical shock wave strength and used it to analyze the influence of wall temperature. They successfully applied this theory to different cases of turbulent separation including the 2-D compression corner and 2-D shock impingement. Their prediction for the adiabatic wall case is in good agreement with the empirical correlation by Petrov *et al* [10] and the free interaction theory of Chapman *et al* [11].

The similarity between the flow properties for the 2-D compression ramp and 2-D shock impingement (as well as for some additional cases), in accordance with the free interaction concepts, were discussed and analyzed in the reviews by Green [13], Charwat [14], Stanewsky [15], Delery and Marvin [16].

Similarity of the data downstream has also been noted. Experiments performed by Holden [17] and Law [18], as well as computations by Shang [19] (Fig. 6) have shown that, to a first approximation, the surface pressure distribution along the entire length of interaction region for a compression corner of angle α_{cc} is similar to a shock impingement generated by a wedge of angle $\alpha_{si} = \alpha_{cc}/2$.

Despite such similarity in the surface pressure, differences in the flowfield structure and curvature of the separated shear layer streamlines in these flows are obvious (Figs. 1 and 2). As described in the monograph by Smits and Dussuge [20] and in the recent review by Andreopoulos *et al* [21], such differences are important and can cause different turbulence transformation and relaxation processes in the disturbed boundary layer through the interaction region. These difference are manifest in the surface skin friction and heat transfer distributions downstream of such interactions.

2-D Compression Corner

In his review, Delery [22] detailed the effect of the incoming boundary layer profile (especially, the incompressible shape factor H_i and relative height y_s/δ of the sonic line) on the size of the separation region, and noted the opposite trends of separation length (normalized by δ) with Reynolds number Re_δ based on the incoming boundary layer thickness δ . In particular, for Re_δ less than approximately 10^5 , the separation length (normalized by δ) increases with Re_δ (for fixed M_∞ , corner angle α and wall temperature T_w), while the opposite trend occurs for $Re_\delta > 10^5$. Delery also summarized the effects of wall cooling and

surface transpiration on the separation region.

Zhel'tovodov and Schülein [23, 24] correlated the separation length L_s for a large set of experimental data of 2-D compression corners according to

$$\frac{L_{sep}}{L_c} = f(Re_\delta) \quad (1)$$

where

$$L_c = \frac{\delta}{M_\infty^3} \left(\frac{p_2}{p_{pl}} \right)^{3.1} \quad (2)$$

where p_2 is the downstream inviscid pressure, and p_{pl} is the plateau pressure computed according to the empirical formula by Zukoski [25]

$$p_{pl} = p_\infty \left(\frac{1}{2} M_\infty + 1 \right) \quad (3)$$

Their correlation, shown by Band 1 in Fig. 7 from [24], encompasses the range $3 \times 10^4 \leq Re_\delta \leq 3 \times 10^6$ and shows the change in trend of separation length with Reynolds number at $Re_\delta \approx 10^5$. The change in behavior at $Re_\delta \approx 10^5$ correlates with the change [26] in the exponent n of the incoming velocity profile

$$\frac{u}{U_\infty} = \left(\frac{y}{\delta} \right)^n \quad (4)$$

The variation of the exponent n with Reynolds number is discussed in Johnson and Bushnell [27]. They showed that the exponent n and velocity “fullness” initially decrease with increasing Reynolds number, but that the opposite behavior occurs at higher Reynolds number. Increased values of n implies a higher resistance to separation (see also Delery and Marvin [16]).

Settles [28, 29] developed an expression for the variation of the upstream influence length L_i , defined as the distance between the initial pressure rise and the corner, with Reynolds number Re_δ and α at $M_\infty \approx 3$,

$$\frac{L_i}{\delta} = 0.9 e^{0.23\alpha} \quad (5)$$

The correlation was verified for $10^5 \leq Re_\delta \leq 10^7$ and $10^\circ \leq \alpha \leq 26^\circ$.

Adamson and Messiter [30] described the application of Triple Deck Theory, originally developed for separation of a laminar compressible boundary layer by Stewartson and Williams [31] and Neiland [32], to turbulent boundary layer separation associated with shock impingement. Agrawal and Messiter [33] analyzed an unseparated 2-D compression corner using asymptotic methods.

Zhelтоводов [34] described the principal elements of the flowfield structure and turbulence transformation in the compression corner (Fig. 8) on the basis of a series of experimental studies [35, 36, 37, 38, 39, 40, 41] which included optical (spark shadowgraph and Schlieren) flowfield visualization and surface flow pattern visualization, surface pressure, skin friction and heat transfer measurements as well as pitot and static pressure survey, velocity profiles, hot wire measurements of the mass flow, velocity, density and total temperature fluctuations. These elements include the amplification of the turbulence by shock waves in the boundary layer (1) and external flow (2), suppression of turbulence by the expansion fan (3), formation of a new layer in the near wall part of the attaching flow (4), formation of Taylor-Görtler vortices (5), and reverse transition (6) in the separation region due to the favorable pressure gradient and decreasing of the local Reynolds number in the reverse flow caused by the decrease in the velocity in the direction of the separation point.

The unsteadiness of the shock system and separation flow in the compression corner is an additional important aspect. Detailed reviews have been prepared by Dolling [42, 43], Smits and Dussauge [20] and Adams [44]. This phenomena have been analyzed by several investigators. For example, the shock wave deformations caused by the unsteadiness have been observed using the optical (spark Schlieren) visualization by Zheltovodov *et al* [36, 45] and using hot wires by Zheltovodov and Yakovlev [35, 46]. It was shown that the appearance of separation and accompanying large scale eddies in the separated shear layer for $\alpha = 25^\circ$ and 45° at Mach 2.9 stimulates a very high level of fluctuations of mass flow, velocity and total temperature (compared to the unseparated interaction at $\alpha = 8^\circ$) in both the separated and attached boundary layers and in the external flow. For example, the mass flow fluctuations in the external flow above the boundary layer edge at $\alpha = 25^\circ$ and 45° were amplified by a factor of 11 to 12, while the corresponding amplification factor was approximately 2 for $\alpha = 8^\circ$.

Zhelтоводов *et al* [34, 39, 40, 47] and Borisov *et al* [48] concluded on the basis of experimental studies and theoretical analysis that the amplification of turbulence is the important factor which stimulates the increase in the surface heat transfer level in the interaction region as well as downstream in the attached flow. The DNS of Adams [44] at Mach 3 and $\alpha = 18^\circ$ revealed compression waves emanating from the separated boundary layer edge which are in qualitative agreement with the Schlieren visualization of Zheltovodov *et al* at Mach 2.9 and $\alpha = 25^\circ$. Both computations and experiments therefore indicate that moving compression waves are formed at the upstream edges of the large-scale eddies which appear in the process of oscillations of the separation shock.

The unsteadiness of the shock system in the compression corner has been studied in detail by Dolling and Murphy [49] and Dolling and Or [50] who observed separation shock motion on the scale of δ at frequencies more than an order of magnitude below the frequency U_∞/δ of the energy containing eddies of the incoming boundary layer. Andreopoulos and Muck

[51] observed that the frequency of the separation shock unsteadiness is approximately the same as the bursting frequency of the upstream boundary layer. Erenkil and Dolling [52, 53] identified both small- and large-scale fluctuations of the separation shock motion. Dolling [54] reviewed the literature on shock unsteadiness through the early 1990s; see also Dolling [42, 43].

Bibko *et al* [55, 56] performed detailed experimental studies of surface pressure fluctuation distributions as well as their spectra upstream of compression corners for different inclination angles $\alpha = 10^\circ$ to 90° in the Mach number range from 2 to 4. They concluded that the influence of the incoming turbulent boundary layer fluctuations on the fluctuations of the shock wave induced by separation (the "separation shock") is very small. According to their investigations, the main reason for the shock wave fluctuations is the disturbances which appear in the developed (large scale) separation zone as well as in the attachment regions. On a basis of analysis of the experiments by Bibko *et al*, Zheltovodov [3] concluded that the stabilization of the surface pressure fluctuation spectra in the separation zone as well as in the vicinity of the separation shock with increasing α is attributable to the inviscid shock detachment when the maximum separation zone is formed.

Glotov [57] proposed a physical interpretation of the shock wave unsteadiness variation in the vicinity of axisymmetric compression corners at different stages of the separation development in the process of its interaction with the large eddies. Using simultaneous high speed shadowgraphy and surface pressure fluctuation measurements in the vicinity of the corner apex, he concluded that for small scale separation the large eddies in the external part of the boundary layer periodically supplant the separation (reverse flow) zone and prevent the penetration of disturbances from downstream to upstream. He concluded that this process stimulates large deformations of the shock wave similar to the interaction of a shock wave with a vortex ring. For large scale separation, such eddies are displaced downstream of the separation shock wave above the surface together with the separated shear layer, and the disturbances penetrating upstream from the attachment region play the main role in stimulating low frequency shock wave fluctuations, with high frequency fluctuations stimulated by the former mechanism superimposed upon these. This interpretation is in agreement with conclusions by Bibko *et al*.

Wu and Miles [58] visualized the interaction of the large eddies in the incoming boundary layer with the separation shock using a high speed (MHz) pulse-burst laser with a charge-coupled-device framing camera. They observed shock motion on the scale of δ at the frequency of the incoming eddies U_∞/δ and compression of the eddies in the streamwise direction by the shock.

Zheltovodov [3, 47] and Dolling [42] summarized the status of RANS simulations of the compression corner flow. They observed that no RANS model was capable of accurate prediction of all aspects of the flowfield. In particular, the RANS calculations did not

display the unsteadiness of the separation shock which was concluded to be a major defect in the simulation and the cause of the lack of agreement with the experimental mean surface pressure.

Yan *et al* [59] compiled a summary of RANS predictions of separation length for various 2-D compression corner configurations [60, 61, 62, 63, 64, 65]. In general the simulations (Fig. 9, see also Table 1) do not accurately predict the separation length in comparison with the experimental correlation (1).

Ad hoc modifications to RANS models have achieved improved prediction of the 2-D compression corner; however, such modifications are not general in nature and therefore cannot be readily extended to other SWTBLI configurations. Examples are Borisov *et al* [65] and Bedarev *et al* [66] who demonstrated the capability for the $k - \omega$ model to predict relaminarization in the reversed flow region through an *ad hoc* modification of ω . These computations indicate the necessity to model this phenomenon in order to achieve better prediction of the surface skin friction and heat transfer in the separation zone.

2-D Shock Impingement

The studies of 2-D shock impingement are not as numerous as the 2-D compression corner. Several of these studies have been reviewed by Green [13], Charwat [14], Stanewsky [15], Delery and Marvin [16].

Kuehn [67] performed a series of experiments for 2-D shock impingement at Mach 2.6 to 2.85 and proposed criteria for incipient separation based on the appearance of an inflection point in the mean surface pressure distribution. He also observed unsteadiness in the shock structure for separated interactions.

Reda and Murphy [68] measured surface pressure and pitot/static pressure profiles for a 2-D shock impingement at Mach 2.9 for $\alpha = 5^\circ$ to 13° . Significant 3-D effects were observed in both surface pressure and oil film visualization due to test section side wall and corner boundary layer effects. Reda and Murphy [69] examined the effect of the sidewall boundary layers on incipient separation and interaction size.

Law [70] measured surface pressure and flowfield density (using a holographic interferometer technique) at Mach 2.96 for $\alpha = 8^\circ$ to 11° . The holographic images, however, incorporated significant 3-D effects within and downstream of the interaction region due to corner effects.

Kussoy and Horstman [71] performed experiments for an axisymmetric shock impingement at Mach 7 for $\alpha = 7.5^\circ$ and 15° . Measurements include surface pressure, temperature and skin friction, and profiles of pitot pressure, static pressure and total temperature at several locations. Kussoy and Horstman [72] measured surface pressure and heat transfer for a 2-D shock impingement interaction at Mach 8.2 for $\alpha = 5^\circ$ to 10° .

Zakharov and Kutuzova [73] developed approximate (semi-empirical) methods to predict

the upstream influence line position (the line where the surface pressure starts to increase) regarding the trace of "inviscid" shock for its interaction with laminar, transitional and turbulent boundary layers.

Brazhko [74] performed optical visualization of Göertler-type vortices using the laser sheet technique and showed that they resulted in periodical variation of the heat transfer at Mach 5 and 6 for both laminar and turbulent regimes of separated flows.

The studies by Rose and Johnson [75], Mikulla and Horstman [76], Modarress and Johnson [77], and Meyer *et al* [78] provide detailed information regarding the mean flowfield and turbulence measurements. They demonstrate the increase in fluctuations of mass flow and velocity, turbulence intensity, Reynolds shear stress and turbulent kinetic energy downstream of the interaction. The strength of the impingement shock has a significant effect on the downstream properties. Most of the turbulence properties also increased with shock strength near the interaction in unseparated cases with the exception of the cross-stream velocity fluctuations. It was also noted that the mean flow and turbulent properties as well as relaxation of the disturbed flow aft of the separation region were noticeably different than observed for unseparated cases. A strong influence of the separation flow unsteadiness on the turbulence energy was revealed. The increase of turbulence intensity and Reynolds shear stress downstream of the interaction in such situations was small compared to the unseparated case.

The complex influence of the flowfield unsteadiness may explain the differences between RANS computations and experimental data when separation occurs. For example, recent computations by Fedorova *et al* [79] using the $k-\omega$ turbulence model clearly demonstrate increasing differences between computed and experimental velocity profiles, surface skin friction and heat transfer with stronger impinging shock waves. Linbland *et al* [80] and Rizzetta [81] showed significant differences in the prediction of flow properties using different turbulence models. These conclusions are supported by the measurements of fluctuating heat transfer performed by Hayashi *et al* [82] for both unseparated and separated flows, as well as the subsequent analysis of this data by Brusniak and Dolling [83]. Their analysis shows that the fluctuating heat transfer signals from a region of shock motion bear a close resemblance to the character of fluctuating pressure signals taken from the same region. Analysis of the data for different cases including the 2-D compression corner and the 2-D shock impingement demonstrates the important role of shock unsteadiness and indicates directions for development of adequate engineering and CFD methods for prediction.

Holden and Chadwick [84] conducted an experimental study of the effects of tangential film and transpiration cooling on surface heat transfer in a 2-D shock impingement at Mach 6 and 8. They concluded that film cooling was ineffective for all but weak shock interactions due to the dispersal of the film by the shock boundary layer interaction. Transpiration cooling was found to be effective.

In the following sections, DNS and LES results are presented for several configurations of the 2-D compression corner and one configuration of the 2-D shock impingement. Mean quantities represent combined time and spanwise averages.

2.1 Case 1: Mach 3, $\alpha = 8^\circ$

Urbin *et al* [85] and Kannepalli *et al* [86] simulated a Mach 3, $\alpha = 8^\circ$ compression corner at $Re_\delta = 2 \times 10^4$ and adiabatic wall conditions. Experimental data of Zheltovodov *et al* [35, 36, 37] is available for $\alpha = 8^\circ$ at Reynolds numbers $Re_\delta = 7.5 \times 10^4$ and 1.1×10^5 . The flow conditions are summarized in Table 2. The inviscid pressure ratio across the shock $p_2/p_1 = 1.8$. In accordance with the boundaries of the different stages of separation development in compression ramps as defined by Zheltovodov [3], this configuration corresponds to an incipient intermittent separation. Although the mean flowfield is not separated, instantaneous reversed flow can exist for a short time in the vicinity of the shock wave and near the wall due to the unsteadiness of the interaction process.

Details of the computations are presented in Table 3 where SA and TA indicate the spatial and temporal accuracy. Urbin *et al* used an unstructured grid LES algorithm with a static Smagorinsky model. The inflow conditions were obtained from a separate computation of a flat plate adiabatic boundary layer at Mach 3. The inflow velocity profile satisfied the compressible Law of the Wall [87]. The inflow skin friction coefficient agreed with the empirical value obtained from the compressible Law of the Wall and Wake to within 6%, and the inflow adiabatic wall temperature was within 3% of the theoretical value obtained from the empirical formula

$$T_{aw} = T_\infty \left[1 + \frac{(\gamma-1)}{2} Pr_{tm} M_\infty^2 \right] \quad (6)$$

where $Pr_{tm} = 0.89$ is the mean turbulent Prandtl number. Kannepalli *et al* used the MILES [88] (Monotone Integrated Large Eddy Simulation) approach wherein the inherent dissipation in the numerical algorithm constitutes the SGS model.

An instantaneous image of the shock wave (as visualized by the isosurface $p/p_\infty = 1.25$) and the streamwise velocity at $y^+ = 10$ is shown in Fig. 10 from Urbin *et al*. Regions of negative velocity (instantaneous separation) are visible in agreement with the conclusion of Zheltovodov [3] regarding an incipient intermittent separation regime at such conditions.

The mean wall pressure distribution is shown in Fig. 11 for Urbin *et al*. The experimental profiles for the two different Reynolds numbers are essentially identical. The computed profile shows close agreement with experiment.

Additional results by Urbin *et al* are presented in Figs. 12 to 15. The mean velocity profiles upstream and downstream of the corner are displayed in Fig. 12. The experimental

data is for $Re_\delta = 1.1 \times 10^5$. The upstream profile is 3.3δ ahead of the corner and in the undisturbed flat plate boundary layer. The downstream profile is 3.5δ from the corner and located close to the position where the wall pressure reaches its asymptotic value. The computed results are in close agreement with experiment. The mean static temperature profiles at the same locations are shown in Fig. 13. Upstream of the interaction the computed and experimental profiles are in close agreement. Downstream of the interaction, the profiles agree except within the region $0.05 \leq y/\delta \leq 0.25$ where the experimental value exceeds the prediction.

The Reynolds streamwise and shear stresses are displayed in Figs. 14 and 15, respectively, where the stresses have been normalized by the upstream wall shear stress τ_w . The experimental data of Muck *et al* [89] is shown. The experimental Reynolds number $Re_\delta = 1.6 \times 10^6$ is a factor of eighty greater than the LES. However, scaling of the Reynolds shear stress in a flat plate boundary layer by the wall shear stress τ_w has been shown to collapse the experimental data for a range of Mach and Reynolds numbers [20]. Thus, the comparison of the LES and experiment is justified if only for qualitative comparison. The effect of the shock boundary layer interaction is to increase the level of Reynolds normal $\bar{\rho}u''u''$ and shear $\bar{\rho}u''v''$ stresses. The predicted values are in good agreement with experiment except for $y/\delta \leq 0.1$.

In summary, the following conclusions can be made:

- LES of the Mach 3, $\alpha = 8^\circ$ compression corner shows good agreement with the experimental mean surface pressure distribution and qualitatively correct modification of the mean velocity and turbulence profiles by the shock wave
- The mean flowfield is unseparated (and consequently, this case does not represent a particularly difficult case for LES), but the instantaneous flowfield indicates an incipient intermittent separation regime in accordance with the generalization of experimental data and analysis by Zheltovodov [3]

2.2 Case 2: Mach 3, $\alpha = 18^\circ$

Adams [44, 90, 91], Rizzetta *et al* [92] and Stolz *et al* [93] simulated a Mach 3, $\alpha = 18^\circ$ compression corner at $Re_\delta = 2.1 \times 10^4$ and adiabatic wall conditions. The flow conditions are summarized in Table 4. No experimental data is available for this configuration. However, in accordance with the generalizations by Zheltovodov [3] for the boundaries of the different stages of separation development, mean separation occurs for this configuration. The inviscid pressure ratio across the shock is $p_2/p_1 = 3.37$.

Details of the computations are presented in Table 5. Adams performed a DNS. Rizzetta *et al* used three different approaches, namely, a DNS, an LES using a static Smagorinsky model for the SGS stresses (LES-S), and an LES using a dynamic (Germano *et al*

[94]) Smagorinsky model (LES-D). Stolz *et al* used an Approximate Deconvolution Method (ADM). The inflow conditions were obtained in each instance from a separate computation of a flat plate adiabatic boundary layer at Mach 3 (Fig. 16).

A comparison of the simulations of Adams and Rizzetta *et al* are presented in Figs. 17 to 24. Although the Mach number and Reynolds number were nominally identical, the inflow profiles differ significantly. Figs. 17 and 18 display the mean and rms fluctuating streamwise velocity at the inflow boundary. Major differences are evident, and have a significant effect on the computed shock boundary layer interaction as discussed below.

The computed mean surface pressure coefficient $c_p = (p - p_\infty) / \frac{1}{2} \rho_\infty U_\infty^2$ is shown in Fig. 19. The size of the interaction region, defined by the location of the initial rise in c_p and intersection of c_p with the downstream inviscid value ($c_p = 0.376$), is substantially larger in the simulation of Adams compared to Rizzetta. This is attributable to the differences in the inflow velocity profile (Fig. 17), as the momentum flux ρu is lower near the wall in Adams' profile (see also Fig. 22). The DNS and LES profiles of Rizzetta are virtually identical, implying the SGS model has negligible effect.

The computed mean skin friction coefficient $c_f = \tau_w / \frac{1}{2} \rho_\infty U_\infty^2$ is shown in Fig. 20. The upstream skin friction level is virtually identical for both Adams and Rizzetta (see Fig. 17 which indicates the velocity profiles are essentially the same within the viscous sublayer). The separation length predicted by Adams is approximately 130% larger than Rizzetta. This is attributable to the lower momentum flux in the incoming boundary layer (Fig. 17). The DNS and LES profiles of Rizzetta are virtually identical, again indicating the SGS model has negligible effect.

The mean velocity and static temperature are displayed in Figs. 21 and 22, respectively. Station Nos. 1, 2 and 3 are located upstream of the interaction region, at the corner, and downstream of the corner, respectively. The mean velocity profiles are displayed using the Van Driest [95] transformation. All profiles exhibit agreement with the Law of the Wall logarithmic profile in the region $20 \leq y^+ \leq 100$ (Station No. 1). Downstream of the corner, the simulations by Rizzetta show recovery of the near wall region to the equilibrium Law of the Wall, while the simulation by Adams does not. Significant differences in the mean temperature between Adams and Rizzetta are evident both upstream, at and downstream of the corner. These are associated with differences in the mean velocity, since the total temperature is approximately constant across the boundary layer. For both the velocity and temperature profiles, the DNS and LES results of Rizzetta are virtually identical.

Spanwise turbulent kinetic energy spectra at two separate positions within the boundary layer and three streamwise locations are shown in Figs. 23 and 24 where the location is defined in terms of the inflow boundary layer condition. All curves have been normalized to unity at $k_3 = 1$. The results of Rizzetta are consistently higher than Adams, implying a higher level of turbulent kinetic energy. This result is confirmed by comparison of profiles for

the streamwise, normal vertical and spanwise rms fluctuating velocities [92]. The profiles of Rizzetta display the emergence of an inertial subrange ($E(k) \propto k^{-5/3}$). The inertial subrange properly occurs at wavenumbers above the peak in the energy spectrum [96]. Adams' results do not display an inertial subrange. The spectra of Rizzetta at high wavenumber show higher energy for the LES than DNS calculations. This is an unexplained result, since it would be expected that the SGS model would dissipate more energy at higher wavenumber than the DNS.

A comparison of the results of Adams and Stolz *et al* show close agreement. An example is presented in Fig. 25 which displays the rms of the Reynolds fluctuations of the streamwise momentum, density, streamwise velocity and static temperature. The maximum difference between the DNS and LES is less than 5% everywhere. The LES, however, required substantially less computer resources.

The computed separation length, normalized using (2), is shown in Fig. 26. The computed separation lengths of Rizzetta are below the linear extrapolation of the lower bound of the experimental band, while the computed separation length of Adams and Stolz *et al* lies above the upper bound.

In summary, the following conclusions may be made:

- DNS of shock wave turbulent boundary layer interactions is sensitive to the inflow profiles
- The DNS and LES of Rizzetta are virtually identical for all profiles. This implies that the SGS model has a negligible effect.
- The computed mean separation lengths are outside the linear extrapolation of the experimental data
- The DNS of Adams and LES (ADM) of Stolz *et al* are in close agreement

2.3 Case 3: Mach 3, $\alpha = 24^\circ$

Rizzetta and Visbal [97] and Kannepalli *et al* [86] simulated a Mach 3, $\alpha = 24^\circ$ compression corner at $Re_\delta = 2 \times 10^4$ and adiabatic wall conditions⁴. Experimental data is available from Settles *et al* [98], Dolling and Murphy [49] and Smits and Muck [99] at $\alpha = 24^\circ$ and from Zheltovodov *et al* [3, 35, 36, 37, 100] at $\alpha = 25^\circ$ as indicated in Table 6. The experimental data of Zheltovodov *et al* at $\alpha = 25^\circ$ are referenced here since Kannepalli *et al* compared their results at $\alpha = 24^\circ$ with this experimental dataset. The Reynolds numbers for the experiments at $\alpha = 24^\circ$ are significantly higher than the simulation of Rizzetta and Visbal

⁴Rizzetta and Visbal [97] also simulated $\alpha = 8^\circ, 16^\circ$ and 20° at $Re_\delta = 2 \times 10^4$.

by a factor of 40 to 77, and therefore the comparison between this simulation and experiment is qualitative. The Reynolds number for the experiments at $\alpha = 25^\circ$ are a factor of 3.1 larger than the simulation of Kannepalli *et al.* The inviscid pressure ratio across the shock for the $\alpha = 24^\circ$ corner is $p_2/p_1 = 4.68$.

Details of the computations⁵ are presented in Table 7. A structured grid LES algorithm using a dynamic Smagorinsky model was utilized by Rizzetta and Visbal, while the MILES methodology was utilized by Kannepalli *et al.*

The results of Rizzetta and Visbal are presented in Figs. 26 to 35. The effect of the difference in Reynolds number is evident in the inflow profiles of streamwise velocity (Fig. 27), streamwise Reynolds stress (Fig. 28) and Reynolds shear stress (Fig. 29). The computed inflow mean velocity is lower than the experiment near the wall as expected.

The mean wall pressure is shown in Fig. 30. The upstream influence, plateau and recovery regions are accurately predicted, notwithstanding the difference in Reynolds number between the simulation and experiment. The standard deviation σ_p of the surface pressure fluctuations, normalized by the local mean wall pressure p_w , is displayed in Fig. 31. The experimental [49] peak value is associated with the fluctuating motion of the separation shock. The simulation significantly underestimates the peak value, and overestimates the level of fluctuations downstream of the corner. Similarly, Fig. 32 indicates that the simulation underestimates the peak value of skewness $S = \overline{p'^3}/\sigma_p^3$ near separation. These discrepancies can be understood by considering the time history of the surface pressure fluctuations in the experiment and simulation. Fig. 33 shows a time history of the surface pressure at midspan and $x/\delta = -2.1$ which is near the location of the peak values of the standard deviation (Fig. 31) and skewness (Fig. 32). The experiment displays a high intermittency of the pressure signal associated with low frequency motion of the separation shock. The simulation displays no low frequency component.

The mean skin friction coefficient is shown in Fig. 34. The position of separation and reattachment (as measured from the corner at $x = 0$) are significantly overestimated, and the recovery of the skin friction downstream of attachment substantially underpredicts the experiment. The computed separation length, normalized using (2), is shown in Fig. 26. The computed separation length is at the lower limit of a linear extrapolation of the experimental band. Velocity profiles at two locations downstream of the corner at $x/\delta = 1.33$ and 2.65 are displayed in Fig. 35. The underestimate in the velocity in the near wall region is consistent with the comparison of computed and experimental upstream profiles (Fig. 27).

The results of Kannepalli *et al* are presented in Figs. 36 and 37. The mean surface pressure (Fig. 36) shows good agreement with the experimental data of Zheltovodov *et al*

⁵A coarse grid simulation ($211 \times 76 \times 81$) was also performed by Rizzetta and Visbal which demonstrated that the fine grid solution for the surface pressure was grid converged.

including the presence of the plateau region. The computed results of Yan *et al* [59] at $\alpha = 25^\circ$, discussed in the next section, are shown for comparison. The mean skin friction (Fig. 37) also shows good agreement with experiment, and in particular is in good agreement with the mean separation and reattachment locations. The computed separation length, normalized using (2), is shown in Fig. 26 and is within the limits of a linear extrapolation of the experimental band.

In summary, the following conclusions can be made:

- The mean surface pressure predicted by Rizzetta and Visbal shows good agreement with experiment. This may be fortuitous, however, in view of the significant difference in Reynolds number between the simulation and experiment, and the substantial differences in surface pressure fluctuation statistics in the vicinity of separation. The computed separation length is at the lower limit of the experimental data correlation. The near wall velocity profiles downstream of the corner are significantly underpredicted, likely due to the difference in inflow profiles associated with the disparity in Reynolds numbers.
- The mean surface pressure and skin friction predicted by Kannepalli *et al* show good agreement with the experiment. The Reynolds numbers of the simulation and experiment are much closer than for Rizzetta and Visbal.

2.4 Case 4: Mach 3, $\alpha = 25^\circ$

Yan *et al* [59] simulated a Mach 2.88, $\alpha = 25^\circ$ compression corner at $Re_\delta = 2 \times 10^4$ and adiabatic wall conditions. Experimental data of Zheltovodov *et al* [3, 35, 36, 37, 100] is available for $\alpha = 25^\circ$ at Reynolds number $Re_\delta = 6.4 \times 10^4$. The flow conditions are summarized in Table 8. The inviscid pressure ratio across the shock $p_2/p_1 = 4.7$. The mean flowfield is separated at the corner.

Details of the computation are presented in Table 9. An unstructured grid LES algorithm using the MILES model [88] was utilized. The inflow velocity profile satisfied the Law of the Wall. The inflow skin friction coefficient agreed with the empirical value obtained from the compressible Law of the Wall and Wake to within 6%. The inflow adiabatic wall temperature was within 3% of the theoretical value obtained from (6).

The mean wall pressure is shown in Fig. 38. The upstream influence (*i.e.*, the location of the initial pressure rise) is accurately predicted; however, the computed pressure distribution does not show the distinct plateau evident in the experiment, and recovers to the downstream inviscid pressure more rapidly than the experiment.

The mean skin friction coefficient is shown in Fig. 39. The initial drop in skin friction associated with the adverse pressure gradient is reasonably predicted. The predicted recovery

of the skin friction downstream of reattachment is more rapid than in the experiment, similar to the results for the surface pressure. The computed mean separation length is shown in Fig. 26. The value lies within a linear extrapolation of the band of experimental data.

Fig. 40 displays the instantaneous shock wave structure defined by isosurfaces of static pressure at $p/p_\infty = 1.4$ and 2.0, together with the contours of the streamwise velocity at $y^+ = 7$. The λ shock is consistent with the experimental Schlieren image (Fig. 41).

In summary, the following conclusions can be made:

- The LES does not accurately reproduce the mean surface pressure. This may be attributable to the difference in Reynolds numbers between the LES and experiment; however, the results of Kannepalli *et al* [86] (Case 3) at nearly the same conditions as the present case show good agreement with the experimental surface pressure at a comparably larger Reynolds number, so the difference in this case is yet unresolved.
- The LES predicts a mean separation length consistent with a linear extrapolation of the experimental data.

2.5 Case 5: Mach 2.3, $\alpha = 8^\circ$

Garnier *et al* [101, 102] simulated a Mach 2.3 impinging shock at $Re_\delta = 6.0 \times 10^4$. The incident shock angle is 32.4° corresponding to a wedge angle $\alpha = 8^\circ$. The wall is adiabatic. Experimental data of Deleuze [103] and Laurent [104] is available. The flow conditions are summarized in Table 10. The overall inviscid pressure ratio across the shocks $p_2/p_1 = 2.47$.

Details of the computation are presented in Table 11. A structured grid LES algorithm was utilized. Three computations (denoted by LES-X (a) to LES-X (c)) were performed using the Mixed Scale Model [105, 106, 107], and one computation using MILES (denoted by LES-M (d)). The inflow conditions were obtained from a separate computation of a flat plate adiabatic boundary layer. The inflow velocity satisfies the compressible Law of the Wall as indicated in Fig. 42 where HWA indicates the experimental data obtained using Hot Wire Anemometry.

The mean skin friction coefficient is shown in Fig. 43. The computations using the Mixed Scale Model are in close agreement with experiment and each other. The MILES computation (Case D) also displays close agreement with experiment, and exhibits a smaller separation region consistent with higher inflow turbulence level near the wall [101, 102].

The evolution of the compressible displacement thickness δ_1 is displayed in Fig. 44. All computations show good agreement with experiment within the interaction region, although overestimating δ_1 in the recovery region downstream by approximately 10%.

The mean streamwise velocity profiles at $x = 351$ mm (computations) and $x = 345$ mm (experiment) are shown in Fig. 45 where LDA indicates the experimental measurements

using Laser Doppler Anemometer. An additional profile for Case A is shown at $x = 345$ mm. The x location is immediately downstream of reattachment (Fig. 43). Note the velocity is the ordinate and the distance from the wall (normalized by the incoming boundary layer thickness) is the abscissa. The offset between the x locations for the computations and experiment accounts for the apparent displacement of the incident shock in the computations. The overall agreement between computation and experiment is good.

The rms streamwise fluctuating velocity profiles at $x = 326$ mm (computations) and $x = 320$ mm (experiment) are shown in Fig. 46, and at $x = 351$ mm (computations) and $x = 345$ mm (experiment) in Fig. 47. An additional profile for Case A is shown at $x = 320$ mm and $x = 345$ mm in Figs. 46 and 47, respectively. The profiles in Fig. 46 correspond to the separated region, and the profiles in Fig. 47 are located downstream of the reattachment of the boundary layer (Fig. 43). In Fig. 46, the computed profiles display general agreement with experiment (LDA). In Fig. 47, there is a significant difference between the HWA and LDA measurements especially in the middle of the boundary layer. The computations show good agreement with the LDA data.

In summary, the following conclusions can be made:

- The LES accurately predicts the displacement thickness, skin friction coefficient, and velocity profiles
- The LES shows reasonable agreement with the LDA measurements of rms streamwise turbulent fluctuations
- The differences between the Mixed Model and MILES results are small

3 2-D Expansion-Compression Corner

The expansion-compression corner (Fig. 3) is a typical configuration to study the response of a compressible turbulent boundary layer to the effects of a favorable pressure gradient, convex streamline curvature and bulk dilatation. As a supersonic flow passes through an expansion corner, the flow is accelerated through an expansion fan formed around the corner and the boundary layer becomes thicker due to the decrease in density. The inviscid flowfield immediately behind the expansion fan can be obtained from Prandtl-Meyer theory. The boundary layer experiences a relaxation process after the expansion fan and exhibits different turbulence features from the incoming equilibrium flow. Several critical features of this flow configuration will be addressed.

The primary experimental observation is the increase of the boundary layer thickness. In the measurements of Dawson *et al* [108] and Arnette *et al* [109] for a Mach 3 turbulent boundary layer through centered or gradual expansions of 7° and 14° , the time-average Schlieren

images indicate that the boundary layer thickness increases approximately 150% across the 7° expansion and 200% across the 14° expansion (Fig. 48). It has been demonstrated by Morkovin [110] that the induced bulk dilatation serves to increase the boundary layer thickness. The instantaneous Filtered Rayleigh Scattering (FRS) visualization (Fig. 49) shows that the structures undergo an increase in both scale and angular orientation behind the expansion. Arnette *et al* [109] suspected that the increase in structure angle is a kinematic effect associated with the acceleration of the bottom of the structure through the inclined expansion region before the top of the structure.

The reduction of turbulence is another significant feature of this flow configuration. This flow configuration experiences the suppression of turbulence due to the combined effects of the favorable pressure gradient, the convex streamline curvature and the bulk dilatation. The reduction in the turbulence may be strong enough to relaminarize the flow. Early work by Morkovin [110] found that longitudinal turbulence intensities and wall shear stress decreased significantly due to a favorable pressure gradient and a bulk dilatation.

Thomann [111] isolated the effect of streamline curvature on the heat transfer rate at the wall for a Mach 2.5 and 20° of convex curvature turbulent boundary layer by placing appropriately shaped bodies in the free stream above convex and concave surfaces to eliminate pressure gradients. The heat transfer rate at the wall decreased approximately 20%, indicating decreased turbulent mixing between the boundary layer and the freestream.

Lewis *et al* [112] studied a Mach 4 turbulent boundary layer subject to isolated adverse and favorable pressure gradients. The experiments showed that under a favorable pressure gradient the ability of the turbulence to transport momentum to the wall was markedly decreased, which was largely due to the effect of the strong expansion on intermittency. In the analytical analysis, a compressible pressure gradient parameter $\beta_K = \delta_K^* / \tau_w (dp/dx)$ (where δ_K^* is the kinematic displacement thickness) suggested by Alber and Coats [113] was used as the dominant parameter. The boundary layer, when subjected to a large negative β_K , was shown to be poorly characterized by the Law of the Wake and was found to relax to an equilibrium-like profile after fifty initial boundary layer thickness. A similar parameter suggested by Narasimha and Sreenivasan [114] will be discussed later on as an important criterion for the flow relaminarization.

So and Mellor [115, 116] performed a series of experiments providing detailed turbulence measurements in boundary layers perturbed by convex curvature. The parameter δ/R was kept constant at approximately 0.08 and 0.12, respectively, over a distance of approximately $50\delta_0$ where δ and δ_0 are local and incoming boundary layer thickness, respectively, and R is the radius of the curvature. These experiments showed that the shear stress for $y/\delta \geq 0.5$ collapsed to virtually zero within a few boundary-layer thicknesses. The absence of shear stress in the outer layer means there is no turbulence production mechanism and consequently the turbulence there decays as it moves downstream. The most interesting aspect was a

change of scale. After a sustained region of convex curvature, $-\overline{u'v'}/u_\tau^2$ scaled with y/R rather than y/δ .

Gillis *et al* [117, 118] studied the effect of a convex curvature on turbulent boundary layers. Two experiments were performed, with δ_0/R approximately 0.1 and 0.05, respectively. The curvature persisted for about $20\delta_0$ and $40\delta_0$, respectively and the total turning angle in both cases was 90° . Thereafter, the curvature was suddenly removed and the boundary layer was allowed to relax on a flat plate with zero pressure gradient. The experiment found that the flow showed a very slow recovery; the skin friction coefficient showed no sign of recovery for about $40\delta_0$ downstream, although this recovery behavior appears to scale with x/R rather than x/δ_0 . This slow response is a direct result of the almost total absence of shear stress in the outer layer, similar to the observations by So and Mellor [115, 116]. Those observations led Gillis and Johnston to propose a two-layer model for the perturbed boundary layer, consisting of an inner active layer where the turbulence is still in production and an outer layer containing nearly isotropic “debris” from the thick, turbulent boundary layer upstream of curvature. The recovery is dominated by the slow growth of the inner active layer and the newly created turbulence in the inner layer retains little memory of the upstream history [119].

Dussauge and Gaviglio [120] studied the behavior of a boundary layer as it passes through an expansion produced by a sudden deflection of the wall at a sharp edge. The flow experienced a short region of favorable pressure gradient, as well as the stabilizing effects of convex curvature and bulk dilatation. Dussauge and Gaviglio measured the longitudinal turbulence intensity and the static temperature fluctuation intensity and they found that $\overline{u'^2}$ was reduced to half its upstream value. However, Morkovin’s “strong Reynolds analogy” [121] is still valid supported by the fact that the temperature-velocity correlation coefficient remained constant at a value of -0.8. The dilatation appeared to be responsible for about two-thirds of the observed reduction in $\overline{u'^2}$, with the pressure-strain term contributing to the remaining third. The choice for the pressure-strain term model was not crucial; three different models all gave about the same result.

Dussauge and Gaviglio [122] investigated a 12° centered expansion of a Mach 1.76 equilibrium turbulent boundary layer at $Re_\theta = 5000$ and $\delta_0 = 10$ mm where δ_0 is incoming boundary layer thickness. Experiments showed that the mean velocity profiles downstream of the expansion initially displayed a thick sublayer region possessing a larger normal gradient of mean streamwise velocity than the equilibrium profiles, with no apparent logarithmic region until approximately $10\delta_0$ downstream of the corner. The reduction of longitudinal turbulent intensities across the entire boundary layer was observed in the experiments. The reductions were substantial closer to the wall while they became smaller for $y/\delta > 0.7$ (where δ is the local boundary layer thickness). Downstream measurements showed the near-wall region to re-establish turbulence intensities well below the incoming levels more quickly ($10\delta_0$

downstream of the corner) than the outer part of the boundary layer, where the evolution was slow. This rapid recovery of the region near the wall led Dussauge and Gaviglio to propose that a new internal layer formed downstream of the expansion and that the incoming boundary layer had been relaminarized.

Rapid Distortion Theory was used to isolate the effects of bulk dilatation by neglecting all the triple-product terms and the dissipation terms. The calculation reproduced the reduction in longitudinal turbulence intensity very well in the outer portions of the boundary layer, but provided a poor prediction near the wall. This indicated that the bulk dilatation played a relatively less important role near the wall. It also indicated that while Rapid Distortion Theory may be capable of describing the initial response to a sudden perturbation, it cannot in principle describe the whole relaxation process.

Smith and Smits [123] studied a 20° centered expansion of a Mach 2.84 boundary layer at $Re_\theta = 77600$ and $\delta_0 = 26$ mm. Measurements at $3.5\delta_0$ downstream of the expansion corner compared favorably with those of Dussauge and Gaviglio [122] in which no evident logarithmic region in the mean velocity profile and both the reduced longitudinal turbulence intensity and Reynolds stress were observed. A prominent observation was that the mass flux fluctuation profile remained unchanged through the expansion. This raised some doubts about the relaminarization.

The relaminarization of a turbulent flow when it passes an expansion corner has been reported by many investigators [110, 122, 123, 124, 125, 126, 127, 128]. In particular, Narasimha and Sreenivasan [114] proposed that relaminarization occurs when the ratio of the pressure gradient to a characteristic Reynolds stress gradient ($\delta dp/dx/\tau_w$) is larger than 75, where δ is the local boundary layer thickness and τ_w is the wall shear stress in the boundary layer just upstream of the expansion corner. Taking $dp/dx \sim \Delta p/\delta$, this correlation is simplified to $\Delta p/\tau_0 > 75$ [129], where Δp is the pressure drop across the expansion fan. In the study by Smith and Smits [123], although this published criterion for relaminarization had been met, caution was urged in using the term.

Arnette *et al* [109, 125, 130] used Filtered Rayleigh Scattering to investigate the effects of expansions on the Mach 3 turbulent boundary layer subjected to four expansion regions (centered and gradual expansions of 7° and 14°). An examination of the compressible vorticity transport equation and estimates of the perturbation impulses attributable to streamline curvature, acceleration and dilatation both confirm dilatation to be the primary stabilizer.

Experiments showed that the large-scale structures of the outer portions of the boundary layer maintained their identity and increased in scale across the expansions and the structure angle also appeared to increase, suggesting small-scale motions were quenched and consequently resulting in a more intermittent boundary layer, consistent with the observations by Lewis *et al* [112]. However, the large-scale structures weakened downstream of the expansion regions supported by the reduction of the Reynolds shear stress which is mainly associated

with large-scale structures.

Turbulence levels were observed to decrease across the expansion and the reductions increased in severity as the wall is approached since the turbulence activity is associated with small-scale motions near the wall which are significantly quenched. This observation seems to agree with the results of Dussauge and Gaviglio [122] and Smith and Smits [123], where sharp reductions in near wall turbulence were encountered across the expansions. Additionally, the severity of the reductions increased with expansion angle. Downstream of the two 14° expansions, the reductions are more severe and reverse transition is indicated by sharp reductions in turbulent kinetic energy levels and a change in sign of the Reynolds shear stress, while the two 7° expansions are not strong enough to cause complete reversion.

For all of the expansions, reductions in the Reynolds shear stress levels occur more rapidly than decreases in the turbulence levels. The Reynolds shear stress in part of the top half of the boundary actually changes sign, indicating that the usual extraction of energy from the mean flow by the turbulence has ceased and the turbulent motions are decaying. Furthermore, reductions in the turbulent transport of turbulent kinetic energy in the normal direction occur more rapidly than reductions for the turbulent transport in the streamwise direction, as indicated by the fact that streamwise skewness and flatness profiles were not altered significantly, but the normal skewness was reduced and the normal flatness was decreased.

The recovery process is not only associated with the regions of the boundary layer [122], but also with the quantities measured. Experiment showed that the mean velocity profiles would recover the equilibrium profile more quickly than the turbulence profiles. Indications of recovery appear nearer the expansion regions for the 7° expansions than for the 14° expansions. Bradshaw [131] suggested that a suitable response time for the stress-containing eddies is the ratio of the turbulence energy k to its rate of production ($t = k/(\overline{u'v'}\frac{\partial u}{\partial y})$, where the stress ratio $a = \frac{\overline{u'v'}}{k}$ and the typical value is 0.3). A corresponding relaxation length X is u times this response time. In the middle of the layer, using a $1/7$ th power law, $u/\frac{\partial u}{\partial y} \simeq 3$ and therefore $X \approx 10\delta_0$. It is generally true that the outer layer responds very slowly to a disturbance. As the wall is approached, X tends to zero; that is, the flow adjusts very quickly in the inner region. The relaxation length also depends on the quantity measured. This occurs largely because of the increasing sensitivity of the turbulence terms as they increase in order. For example, the shear stress may take longer than the mean velocity to relax, partly because it becomes self-preserving at roughly the same rate as $\partial u/\partial y$.

Dawson *et al* [108] studied the response of a Mach 3 fully developed compressible turbulent boundary layer at $Re_\theta = 2.5 \times 10^4$ to centered and gradual ($R/\delta_0 = 50$) expansions, both of 7° and 14° deflection. High-frequency-response miniature pressure transducers were used to acquire multi-point fluctuating surface pressure measurements in the same equilibrium

and perturbed boundary layers. Normalized power spectra showed the pressure fluctuations to be much more concentrated at low frequencies just downstream of the expansions relative to the pre-expansion flow. The elevated low-frequency levels were accompanied by sharp decreases at high frequencies. This indicated that small-scale motions were quenched essentially immediately after the expansion.

Lu and Chung [132] proposed a scaling law to identify a downstream influence of the expansion corner based on the mean surface pressure distribution. The downstream influence of the corner is estimated as the horizontal distance from the corner to the intersection of the tangent through the downstream pressure data with the inviscid downstream pressure. The scaling parameter is chosen to be hypersonic similarity parameter $K = M_\infty \alpha$, where M_∞ is incoming Mach number and α is the corner deflection angle in radians. The downstream influence distance increases with K . This scaling law is validated for Mach 1.76 to Mach 8 for K up to 1.

Chung and Lu [133] study experimentally the effect of the expansion on surface pressure fluctuations. Surface pressure fluctuations of Mach 8 turbulent flow past a 2.5° and a 4.25° expansion corner maintained a Gaussian distribution but were severely attenuated by the expansion process. The surface pressure fluctuations four boundary-layer thickness downstream of the corner damped to only 37% and 21% of the incoming value for the 2.5° and a 4.25° corners. The pressure fluctuations did not recover to the level corresponding to an equilibrium turbulent flow even though the mean pressure downstream reached the inviscid value within four to six boundary layer thicknesses. The space-time correlation study of the surface pressure fluctuations showed that the fluctuations were convected with a velocity comparable to that on a flat plate and these fluctuations maintained their identities longer for stronger expansions.

Chung [134] performed experiments for the incoming flow past 5° , 10° and 15° expansion corners at $M = 1.28$ and the unit Reynolds number of $2.57 \times 10^7 \text{m}^{-1}$. The study showed that the downstream influence for a lower supersonic expansion-corner flow at $M_\infty = 1.28$ is insensitive to the corner deflection angle ($\alpha = 5^\circ, 10^\circ$ and 15°). The downstream influence was measured by the mean surface pressure and the surface pressure fluctuation. The downstream influence is less than one boundary-layer thickness based on the mean surface pressure distribution. This agrees with the discussion of Narasimha and Sreenivasan [135]. The surface pressure fluctuations are normalized by upstream dynamic pressure. The distributions indicated that the intensity of pressure fluctuations decreases and reaches the minimum downstream of expansion corners. The final equilibrium pressure fluctuation levels are obtained with three- to five-boundary layer thickness, which indicates a larger interaction region than obtained from the mean surface pressure distribution. Thus the interaction region scaling of the expansive flows may be further refined based on the distribution of surface pressure fluctuation.

Zheltonovodov *et al* [24] performed a combined experimental and numerical study of a supersonic turbulent flow over an expansion corner followed by a compression corner at different Mach numbers and deflection angles. The effects of the expansion corner on the separation properties were thoroughly studied. It was shown that the basic characteristics of the flow regimes are 1) attached flow for small values of α , 2) the appearance of a local separation zone in the compression corner with a free separation point at moderate values of α , 3) formation of large-scale separated flow with a fixed separation point when α becomes large enough. A range of the dimensionless separation length is plotted *vs* Reynolds number in Fig. 50 where the characteristic length (L_c) is defined in (1) with δ and M_∞ evaluated downstream of the expansion fan and upstream of the compression corner. As shown by Zheltonovodov *et al* [23, 24], the increase of the velocity profile "fullness" in the boundary layer after the expansion fan can increase its resistance to separation compared to an isolated compression corner case (see Fig. 7). The monotonic increase in the separation length with the decrease in Reynolds number is observed in Figs. 7 and 50. This can be explained by a decrease in the effective viscosity near the wall due to the fact that the turbulent fluctuations of the expansion waves become more suppressed as the Reynolds number decreases. This is in accordance with the conclusion of Goldfeld *et al* [128] regarding the Reynolds number effects on relaminarization of the turbulent boundary layer behind a convex corner.

Zheltonovodov *et al* [136] analyzed the relaxation processes in the disturbed turbulent boundary layer in the vicinity of expansion-compression corner configuration at different surface inclination angles 8, 25 and 45 degrees on the basis of the velocity profiles and surface skin friction measurements at Mach 3 and 4. The appearance of the distinct Görtler type vortices has been ascertained by the surface pattern visualization in the vicinity of the 45 deg configuration. A comparison of these data with similar results for the compression-expansion corner configuration at the same surface inclination angles has been performed to determine the complex nature of the dependence of the relaxation process on the shock wave and expansion fan positions.

Zheltonovodov *et al* [37, 39, 40, 41] performed measurements of surface heat transfer distribution in the vicinity of 25 degree expansion-compression corner Mach 2, 3 and 4. As shown by the experiments, the decrease in Mach number caused an increase in the length of the separation zone in the compression corner after the expansion fan and the heat transfer level in it, as well as an increase of the heat transfer level on the plate downstream of the attachment line. The heat transfer distribution for such configuration has been compared with similar data for the 25 deg compression-expansion corner case. As shown on the basis of analysis of the hot-wire measurements of the mass flow, density and velocity fluctuations, the higher heat transfer level downstream of the compression/expansion corner comparing with the expansion/compression configuration is associated with a higher turbulence level downstream of the disturbances in the first case. Zheltonovodov *et al* [39, 40] and Borisov

et al [48] demonstrated the possibility of prediction of the heat transfer distribution in the vicinity of such configurations on a basis of the asymptotic turbulent boundary layer theory by Kutateladze-Leontiev in the framework of the "new-layer" concept with the use of generalized experimental turbulence data.

Zheltovodov *et al* [24], Borisov *et al* [48, 137], Horstman and Zheltovodov [64, 138] used the experimental data for the 8, 25 and 45 deg expansion-compression corner flows at Mach 3 and 4 to validate RANS simulations with different turbulence models ($k-\epsilon$ by Jones and Launder and its two layer modification by Rodi, $q-\omega$ by Coakley). Additional review of these studies has been performed by Zheltovodov [3, 47]. It was concluded that the mean flowfield structure, surface pressure and, sometimes, skin friction distribution can be accurately predicted. Nevertheless, surface heat transfer distribution cannot be accurately predicted by the the turbulence models used.

In the following section, an LES of the expansion-compression corner is presented. Mean quantities represent combined time and spanwise averages.

3.1 Case 1: Mach 3, $\alpha = 25^\circ$

Knight *et al* [139] simulated a Mach 2.88 expansion compression corner at $Re_\delta = 2 \times 10^4$ and adiabatic wall conditions. Experimental data of Zheltovodov *et al* [23, 24, 37, 39, 40, 41, 136, 138] is available for $\alpha = 25^\circ$ at $M_\infty = 2.9$ and $Re_\delta = 4.1 \times 10^4$ to 1.95×10^5 . The flow conditions are shown in Table 12. The inviscid pressure ratio across the expansion is $p_2/p_1 = 0.098$, and the Mach number downstream of the expansion is $M_2 = 4.59$. Across the subsequent compression, the pressure ratio is $p_3/p_2 = 8.60$ and the downstream Mach number $M_3 = 2.43$.

Details of the computation are presented in Table 13. An unstructured grid LES algorithm using the MILES model [88] was utilized. The inflow profile is the same as Case 1 of the 2-D compression corner.

The computed flowfield structure is shown in Figs. 51 and 52 which display the mean static pressure and streamlines (S is separation, A is attachment). The flow expands around the first corner, and recompresses at the second corner. The shock wave turbulent boundary layer at the second corner is sufficiently strong to separate the boundary layer as evident in Fig. 52. The flowfield structure is in good agreement with the results of Zheltovodov and his colleagues [3, 23, 24, 37, 40, 41, 136] which are shown qualitatively in Fig. 3.

Mean velocity profiles in the x -direction are shown in Fig. 53 at $x = 2\delta$ and $x = 6\delta$, where x is measured from the inflow along the direction of the inflow freestream velocity (Fig. 51). The abscissa is the component of velocity locally parallel to the wall, and the ordinate is the distance measured normal to the wall. The first profile is upstream of the expansion corner (which is located at $x = 4\delta$). The second profile is downstream of the expansion fan and

upstream of the separation point. The computed mean velocity profile at the first location is slightly fuller than the experiment. This is consistent with the experimentally observed dependence of the exponent n in the power-law $U/U_\infty = (y/\delta)^{1/n}$ on the Reynolds number. The second profile shows a significant acceleration of the flow in the outer portion of the boundary layer due to the expansion.

The surface pressure is displayed in Fig. 54. The surface pressure drops rapidly at the first corner. The shock boundary layer interaction at the second corner causes separation of the boundary layer and a concomitant plateau in the surface pressure [67]. The experiments display an increase in the size of the pressure plateau region with decreasing Reynolds number. The computed results for $Re_\delta = 2 \times 10^4$ are in good agreement with the experimental data at the lowest Reynolds number ($Re_\delta = 4.1 \times 10^4$) for the location, extent and magnitude of the pressure plateau. Also, the shape of the experimental pressure plateau shows little variation for $Re_\delta \leq 6.8 \times 10^4$, thus suggesting that the computed pressure plateau region (for $Re_\delta = 2 \times 10^4$) is accurate. The computed recovery of the surface pressure is more rapid than in the experiment, however.

The computed and experimental mean skin friction coefficient $c_f = \tau_w / \frac{1}{2} \rho_\infty U_\infty^2$ are shown in Fig. 55. The skin friction coefficient increases rapidly downstream of attachment. The computed results at $Re_\delta = 2 \times 10^4$ are in close agreement with the experimental data at $Re_\delta = 8.0 \times 10^4$ and 1.94×10^5 in the region downstream of reattachment.

Zheltonovodov and Schülein [23] have correlated experimental data for the scaled separation length L_{sep}/L_c defined by (2) for the expansion-compression corner where δ is the incoming boundary layer thickness (upstream of the expansion corner), p_2 is the pressure after the shock in inviscid flow, and p_{pl} is the plateau pressure from the empirical formula of Zukoski [25] $p_{pl} = p_e(\frac{1}{2}M_e + 1)$ where p_e and M_e are the static pressure and freestream Mach number upstream of the compression corner and downstream of the expansion fan. In the computation, the location is taken to be $x = 6\delta$. The values of M_e and p_2 have been computed using inviscid theory. Also, $Re_{\delta_e} = 1.8 \times 10^4$ for LES ($Re_{\delta_e} = \rho_e U_e \delta_e / \mu_e$, where ρ_e , U_e and μ_e are computed using inviscid theory). The experimental data correlation and the computed result [139] for the scaled separation length is shown in Fig. 50. The computed value is consistent with a linear extrapolation of the experimental data.

In summary, the following conclusions can be made:

- The LES accurately reproduces the mean surface pressure and rapid recovery of the skin friction downstream of attachment to a level close to the undisturbed upstream in agreement with experiment
- The LES predicts a mean separation length consistent with a linear extrapolation of the experimental data

4 3-D Single Fin

The 3-D single fin/plate configuration (Fig. 4) is a standard CFD validation case for a swept shock wave turbulent boundary layer interaction. An equilibrium supersonic turbulent boundary layer, developed along a plate, approaches a semi-infinite fin of angle α , attached normally to the plate. The deflection of the flow by the fin generates a swept shock system. The increase in pressure through the shock is diffused on the plate and a disturbed flow pattern is observed for a considerable distance both upstream and downstream of the shock position predicted for inviscid flow. If the shock is strong enough to cause the boundary layer to separate, the topology of the flow changes significantly. The intensity of the interaction depends on the flow conditions (Mach number, fin angle), and on the geometry of the fin (swept or not).

In this section we review the most critical features of the single fin flow field. A more detailed review has been done by Panaras [140]. Additional reviews are presented in Settles and Dolling [141, 142], Zheltovodov and Schülein [143], Bogdonoff [144], Zheltovodov [3] and Knight [1]. In general the interaction domain in these types of flows is quasi-conical, *i.e.*, it grows almost linearly in the downstream direction. Various manifestations of the conical nature of the flow have been observed experimentally, even in the early 70's, when the available experimental techniques were limited. Nevertheless, it was very recently that strong evidence was provided for the existence of quasi-conical vortices in swept shock/boundary layer interactions.

The existence of pressure gradients in the transverse direction as well as along the external streamline direction is the essential characteristic, which distinguishes a 3-D flow from a 2-D or axisymmetric one. The boundary layer responds to the transverse gradient by the development of a crossflow or secondary flow. Though the crossflow may be small near the outer edge of the boundary layer, it may be substantially close to the surface where the momentum deficit is large. Thus the velocity vectors close to the surface can progressively rotate resulting in a "skewing" of the boundary layer. When the distance from the surface tends to zero the velocity vectors reach a limiting direction, which is co-linear with the skin friction vectors. At the same time the streamlines tend to a limiting position, which is also a trajectory of the skin friction lines. For this reason they are called "limiting streamlines". In general, the limiting streamlines in 3-D flows follow paths that are different in direction from the external streamlines. Limiting streamlines originate at nodal points of attachment, and after circumscribing the body surface disappear into nodal points of separation.

In the case of the fin/plate configuration the footprint of the flow (turbulent or laminar) on the surface of the plate consists also of a separation line, lying ahead of the inviscid position of the shock, and of a reattachment line close to the corner. Token [145] proposed the first flow model of the fin-plate configuration in 1974. For explaining the high heat-transfer peak

measured on the flat plate near the root of the fin, he suggested that a separation conical vortex appears between the separation and the reattachment lines. Kubota and Stollery [146] improved the flow model of Token based on their own experiments. The separated flow in their model is characterized by two counter-rotating vortices - a tight, vigorous, roughly circular one in the corner with a weak, very elongated one above it (Fig. 56). Kubota and Stollery, in addition to the separation vortices, investigated the structure of the shock system. Of paramount importance for the development of the flow model is the appearance or absence of the λ -foot bifurcation of the fin shock at the region of its interaction with the boundary layer, exactly as it happens in a strong 2-D shock-wave/boundary layer interaction. For resolving this question Kubota and Stollery applied the vapour-screen technique to their Mach 3 tests. According to their vapour-screen pictures, when the angle of the fin is smaller than the one required for the appearance of separation, there exists no λ -shock, but for larger angles, when the corresponding oil-flow picture suggests a separated flow, there is evidence of the shock splitting into a λ -shape near the edge of the boundary layer.

In the early 1990's non-intrusive experimental techniques were available that produce very clear pictures of the cross-section of the flowfield in the normal to the shock direction, and provide quantitative data, such as the skin friction distribution, which are suitable for direct comparison with computational predictions. Also, the efficiency of computers permitted the use of high-resolution grids and more advanced codes. The new numerical simulations verified all the critical elements of the flow structure of a swept shock/turbulent-boundary-layer interaction, some of which up to then were objects of speculation.

An important consequence of the quasi-conical nature of the fin/plate flows is the presumption that their features can be projected upon the surface of a sphere whose origin is the conical origin. Zubin and Ostapenko [147] and Alvi and Settles [148] have demonstrated this feature of the conical flow by using conical shadowgraphy. Focusing a light beam at the origin of the approximately conical flowfield and aiming it such that the resulting conical light beam coincided with the rays of the swept interaction, they obtained clear pictures of the flowfield of fin/plate interactions. Alvi and Settles [149] combined their conical flow images with previous wall pressure and skin-friction measurements to construct a physical flowfield model. An example is shown in Fig. 57 for a $M_\infty = 3$, $\alpha = 16^\circ$ test case. The cross-section of the flow is normal to the shock. It is seen that on top of the separation bubble lies a well-bifurcated shock. From the shock triple-point a shear layer emanates and moves towards the corner. Below the flowfield map the corresponding surface distributions of static pressure and skin friction are plotted in the same conical-angle scale. Alvi and Settles [149] observed that the inviscid air processed between the triple-point and the separation vortex is curved downwards and impinges upon the flat plate. This is accomplished by reflected Prandtl-Meyer expansion and compression fans. The authors call it an "impinging-jet" and attribute to it the peak heating, pressure and skin friction, observed in the corner region.

Clear 3-D images of the swept shock/turbulent-boundary-layer interaction were provided by Panaras [150], who calculated a $M_\infty = 3.0$, $\alpha = 20^\circ$ fin/plate flow, using a RANS code based on the Baldwin and Lomax [151] algebraic turbulence model. Fig. 58 from Panaras [150] includes all the critical elements of the swept shock/turbulent-boundary-layer interaction. The vortices that are expected to appear in this type of flow are visualized in the 3-D space by the contours of the eigenvalues of the velocity gradient field. In addition, three cross-sections have been drawn on which the density contours are displayed (visualization of shock waves). It is observed that, as expected, the flow is dominated by a large vortical structure, which lies on the flat plate and whose core has a remarkable conical shape with a flattened elliptical cross-section. Also on the flat plate, on the side of the main vortex, a thin vortex has developed in the direction of the flow. This is not an independent vortex, but the core of the vorticity sheet which lifts-off the surface, along the separation line, and rolls up to form the conical vortex. Along the vertical fin and close to the corner, the longitudinal vortex, mentioned by Zheltovodov [152, 153] and Kubota and Stollery [146], is seen. It also develops quasi-conically, but with a smaller rate of increase, compared to the prime conical structure. In the lower part of the figure, a cross-section of the vortices is shown. There, it is indicated that indeed the flat ground vortex constitutes the initial part of the primary conical vortex.

In the conical projections of Alvi and Settles [149] the flow seems to be quasi-conical rather than conical. Then the question arises, what causes this deviation? In this context Panaras [150] observes that the different rate of thickening of the conical vortex and of the boundary layer of the plate is expected to affect the conical similarity adversely. For studying this effect Panaras [150] projected conically the sections (i) and (ii) shown in Fig. 58 on the outflow section (iii). The iso-Mach lines have been used as visualization parameters. The results of that correlation are shown in Fig. 59. It is observed in Fig. 59b, where section (i) is conically projected on the outflow section, that while good coincidence is observed between the separation bubbles, the swept shocks and the shock triple-point, the feet of the λ -shocks are fairly correlated, especially the separation shocks, while there is no equivalence at all between the boundary layers in the two cross-sections. More particularly, the boundary layer of the first cross-section is about 40% thicker than the boundary layer of the third section. This large difference in the scaling is due to the lower rate of development of the boundary layer, compared to that of the vortex.

The deviation from the conical behaviour is smaller if the two cross-sections that are conically correlated are closer. This is demonstrated in Fig. 59c, where section (ii) is conically projected on section (iii). Panaras [150], has also presented quantitative data which verify the observation done in Fig. 59b that the deviation from conical similarity is greater at the part of the flow between the separation shock and the plate.

In addition to the development of the flow model depicted in Fig. 57, Alvi and Settles

[148] have also discovered some peculiar features of the phenomenon of secondary separation in a single fin flow. Indeed, while in a strong swept shock laminar boundary-layer interaction, a secondary reattachment line appears between the primary separation and reattachment lines, their experiments indicated that no secondary reattachment line is visible in a turbulent interaction. In addition to this difference, between laminar and turbulent flows, Zheltovodov [152, 153, 154], Zubin and Ostapenko [147] and Alvi and Settles [148] report another one, which perhaps is more fundamental. While in laminar flows the secondary separation phenomenon appears progressively with increasing shock strength, in the turbulent fin/plate flows the existence of a secondary separation line in the surface flow pattern has been detected only in interactions of moderate strength and it disappears in stronger ones. A typical skin-friction pattern for a single fin flow with secondary separation is shown in Fig. 60, after Panaras and Stanewsky [155]. In this figure it is demonstrated that the secondary vortex is gradually formed along the secondary separation line. No secondary reattachment line is observed. We note in Fig. 60 that in the surface flow pattern the separation and the reattachment lines are curved and not straight close to the apex. The initial region of deviation from conical behavior has been called the "inception zone".

A reasonable explanation of the strange behavior of the secondary separation in a single fin flow has been given by Zheltovodov *et al* [154, 156]. According to them, the secondary separation line first appears once the interaction has achieved a certain strength, showing up in the conical region but not in the inception zone. Its spanwise extent grows with increasing shock strength but then diminishes again, eventually appearing only in the inception zone and then disappearing altogether. Secondary separation then reappears in the strongest interaction observed to date ($M_\infty = 4$, $\alpha = 30.6^\circ$), but in a different position, closer to the fin than previously. The experimental results of Zheltovodov *et al* [156] demonstrate that the initial behaviour of secondary separation is related to laminar, transitional and then turbulent reverse flow in the swept separation bubble. They also ascribe the reappearance of secondary separation to the development of supersonic turbulent reverse flow in the separated region with an imbedded normal shock wave of critical strength (with the pressure ratio $p_2/p_1 \geq 1.5 - 1.6$) for turbulent flows to specify the conclusion by Zubin and Ostapenko [147] regarding the reason of disappearance and the condition of reappearance of secondary separation. Regarding the secondary reattachment line, Zheltovodov *et al* [156] obtained evidence of its existence only in the aforementioned extremely strong interaction (very close to the secondary separation line). The work of Zheltovodov's group is summarized in Fig. 61. They have identified six regimes for the 3-D single fin flowfield depending on the strength of the shock wave. In Regime I, the boundary layer is unseparated and no convergence of surface streamlines is observed. In Regime II, the streamlines turn approximately parallel to the inviscid shock but do not form a line of coalescence. In Regime III, a primary separation line (S1) forms corresponding to the coalescence of the surface streamlines. An attachment line

(R1) forms near the fin-plate junction. A line of secondary separation (S2) appears located between the primary separation and attachment lines. In Regimes IV to VI, the secondary separation (S2) and attachment lines (R2) disappear and finally reappear. Using sand-grain roughness mounted along the primary attachment line $R1$, Zheltovodov *et al* [156] showed experimentally that the secondary separation can be suppressed by such way in the regimes III and IV, but not in the regime VI. These experiments support the conclusion regarding the critical strength of the imbedded normal shock wave which causes the reappearance of secondary turbulent separation in the regime VI.

Though the numerical simulations have considerably contributed to the verification of the early hypotheses regarding the structure of the single fin flows, the accuracy of the predictions was not exceptional in the early 90's. The capability of numerical simulation of 3-D shock-wave/turbulent boundary-layer interactions has been assessed by Knight [157], who, to that purpose, examined five specific configurations (sharp fin, blunt fin, cylinder/flare, swept compression corner and crossing shocks) at Mach numbers from two to eight. Knight [157] concluded that the pitot pressure, yaw angle and surface pressure are predictable with reasonable accuracy using algebraic or two-equation turbulence models, however the surface heat transfer is not accurately predicted in strong interactions. In the particular case of the sharp-fin/plate configuration, Kim *et al* [158] have performed a joint experimental and computational study of skin friction in weak-to-strong interactions at $M_\infty = 3$ and 4. In their Navier-Stokes calculations they tested algebraic turbulence models and the $k-\epsilon$ model, integrated to the wall or employing the wall-function technique. They have found that their computations agree well with the data for moderate interaction strengths, but systematically underpredict the data with increasing interaction strength. Also, the secondary separation line, which, according to the experimental data, exists in the surface flow-pattern has not been predicted in their calculations.

In a recent work Panaras [2] studied the structure of the separation vortex in a strong swept shock-wave/turbulent boundary-layer interaction, for the purpose of explaining why current turbulence models fail to predict accurately this type of flow. One of the sharp-fin/plate flows examined by Kim *et al* [158] was used as model. After the validation of the results, by comparison with appropriate experimental data, he studied the flowfield by means of stream surfaces which start at the inflow plane, within the undisturbed boundary layer, and which are initially parallel to the plate. Each of these surfaces has been represented by a number of streamlines.

Calculation of the spatial evolution of some selected stream surfaces has revealed that the inner layers of the undisturbed boundary layer, where the eddy viscosity is high, wind around the core of the vortex. However, the outer layers, which have low turbulence, rotate over the vortex and penetrate into the separation bubble at the reattachment region forming a low turbulence tongue, which lies along the plate, underneath the vortex (Fig. 62). The

intermittency of the air that constitutes the tongue and the outer layers of the vortex, is very small, *i.e.*, the flow is almost laminar there. At the initial stage of development the conical vortex is completely composed of turbulent air, but gradually downstream, as it grows linearly, the low turbulence tongue is formed. Panaras [2] observed that an increase of the strength of the interaction results in the folding of higher layers around the vortex, which are purely inviscid. For example, in the very strong interaction shown in Fig. 63a, the external layers of the separation vortex and a major part of the tongue are purely inviscid. In the other extreme, in a weak interaction no low-turbulence tongue is formed (Fig. 63b). The existence of the low-turbulence tongue underneath the conical separation vortex of a strong swept shock/turbulent boundary layer interaction creates a mixed-type separation bubble: turbulent in the vicinity of the separation line and almost laminar between the reattachment line and the secondary separation vortex. This type of separation is difficult to be simulated accurately, since current turbulence models are based on the physics of 2-D flows, where in a separation bubble the whole recirculation region is turbulent.

For improving the accuracy of the numerical predictions of swept shock-wave/turbulent boundary-layer interactions, Panaras [159] considered the aforementioned physical feature in the derivation of a new equation for the calculation of the eddy-viscosity coefficient in the region of the separation vortex. He followed the Baldwin-Lomax [151] formulation, because it is easily implemented in a Navier-Stokes computation scheme. The modified turbulence model was used for the computation of some of the test cases compiled by Settles and Dodson [8]. The agreement with the experimental evidence was very good. In addition, the results were given to Knight and Degrez [1] who compared them with similar calculations, contributed by other researchers, employing different turbulence models, in order to assess the capability for numerical simulation of 3-D shock wave turbulent boundary layer interactions. The turbulence modeling proposed by Panaras [159] was the only one that predicted secondary separation.

In principle, the eddy viscosity equation developed by Panaras [159] is appropriate for applications to other 3-D flows characterized by the appearance of extensive crossflow separation (generation of crossflow vortices), like in subsonic or supersonic flows about slender bodies or delta wings at high incidence. Very good agreement with the experiments was observed for the Mach 2.0 flow about an ogive-cylinder at $\alpha = 10^\circ$ and 20° , and the subsonic flow about a 6:1 ellipsoid at incidence $\alpha = 30^\circ$ as described in Panaras [160].

Very recently, Thivet *et al* [161] in an effort to reduce the high level of turbulent kinetic energy observed within the separation vortex of a swept shock turbulent boundary-layer interaction, included in a standard $k-\omega$ model the non-linear correction of Durbin [162]. According to this correction in regions of high strain the eddy viscosity is reduced. Thivet *et al* [161] found that this correction improves considerably the results of simulation of single fin flows. Their results are included in this review and are presented in the next section.

Herein we just note that according to their results, the turbulent kinetic energy within the separation vortex is considerably smaller than that given by the standard $k-\omega$ model, resulting in a vortex of larger size. It is remarkable that near the wall, between the primary attachment and the secondary separation, the turbulent energy is almost zero, exactly as it should be according to the flow model of Panaras [2]. Indeed, comparison of the flow model shown in Fig. 63a and the cross-section of the turbulent kinetic energy calculated by Thivet (Fig.76) reveals a remarkable similarity. In both cases almost laminar flow exists near the wall underneath the separation vortex, and in both cases the separation vortex, outside of the core, consists of air of small intermittency or of small turbulence, respectively. Their only difference is the core itself. In the model of Panaras, the core includes the inner turbulent part of the incoming boundary layer, while in Thivet's results the core has almost zero turbulent kinetic energy. However, since the core occupies a small part of the separation vortex, its effect on the overall flowfield is small. In conclusion, the comparison of Figs. 63a and 76 supports the view that actually the weakly nonlinear Wilcox-Durbin model, applied by Thivet *et al* [161], predicts a flowfield that basically is similar to that proposed by Panaras [2].

4.1 Cases 1-3: Mach 3, $\alpha = 15^\circ$ and Mach 4, $\alpha = 20^\circ$ and 30.6°

Thivet [161] simulated three different configurations of the 3-D single fin. The flow conditions are listed in Table 14. Experimental data of Zheltovodov *et al* [143, 154] and Kim *et al* [158] is available for Cases 1,3 and 2, respectively. The computations were performed at the same flow conditions as the experiment. The inviscid pressure ratio p_2/p_1 is 2.82, 5.21 and 9.5 for Cases 1 to 3, respectively.

Details of the computation are presented in Table 15. Two different turbulence models were examined, namely, the linear Wilcox $k-\omega$ model [163] (WI) and a weakly nonlinear Wilcox $k-\omega$ model [164] (WD+). The WD+ model is an extension to compressible flows of the nonlinear correction of Durbin [162]. In the WD+ model, the coefficient c_μ in the turbulent eddy viscosity $\mu_t = \rho c_\mu k/\omega$ is defined as $c_\mu = \min(c_\mu^o, \sqrt{c_\mu^o}/s)$ where $s = S/\omega$, $S = \sqrt{2S_{ij}S_{ij} - \frac{2}{3}S_{kk}S_{kk}}$ and $S_{ij} = \frac{1}{2}(\partial U_i/\partial x_j + \partial U_j/\partial x_i)$. Computations were performed using the GASPex code [165]. Inviscid fluxes are computed to third order using the Roe scheme with MUSCL reconstruction and a min-mod limiter. Viscous and heat transfer terms are computed using second order central differences. A typical grid is shown in Fig. 64.

The surface streamlines are displayed in Figs. 65 (WI), 66 (experiment) and 67 (WD+) for Case 1, and in Figs. 68 (WI), 69 (experiment) and 70 (WD+) for Case 3. The angle of the primary separation line S_1 is underestimated by the linear (WI) model by 1.4° to 4° , and overestimated by the weakly nonlinear (WD+) model by 1.4° to 2.5° . The angle of the

primary attachment line R_1 is accurately predicted by both models. In Case 1 (Regime III), the weak secondary separation S_2 observed in the experiment (Fig. 66) is absent in the computations with WI model (Fig. 65). For the WD+ model (Fig. 67), the distinct changes in the curvature of surface streamlines occurring midway between the fin and primary separation line are similar to incipient secondary separation conditions which occurred in the experiment at a lower fin angle. In Case 3 (Regime VI), the strong secondary separation S_2 and attachment R_2 lines observed in the experiment (Fig. 69) are evident in the WD+ model (Fig. 70) but are entirely absent in the WI model (Fig. 68). This is a significant achievement of the WD+ model.

The computed and experimental pressure distributions are displayed in Figs. 71 to 73. The WD+ model shows a significant improvement compared to the WI model, and, in particular, accurately predicts the appearance of the secondary shock wave associated with the secondary separation. As is seen from Figs. 70 and 73, the reappearance of the secondary separation in the regime VI has been achieved in the computations with WD+ model when the strength of the imbedded normal shock wave was $p_2/p_1 = 2$, as in the experiment. This value is higher compared to the critical value $p_2/p_1 = 1.5 - 1.6$ which is necessary to cause the appearance of turbulent separation.

The computed and experimental skin friction coefficient for Case 2 is shown in Fig. 74. The peak skin friction for the WD+ model is reduced by 35% compared to the WI model. Two series of measurements are shown, where the solid symbols • correspond to corrected values of the skin friction [166]. The WD+ model displays significantly better agreement with experiment than the WI model. In accordance with the surface skin friction prediction (Fig. 74) as well as the surface pressure distribution considered by Thivet *et al* [161] for regime IV ($M = 4, \alpha = 30.6^\circ$), secondary separation didn't exist in the computations, as in experiments, when the strength of the embedded shock wave was smaller than the critical value for the turbulent separation.

The improvement achieved by the WD+ model is associated with a significant reduction in the peak k within the primary separation vortex core and in the near wall flow penetrating to the place of formation of the secondary separation line. Figs. 75 and 76 display computed turbulence kinetic energy contours for the WI and WD+ models, respectively. The WD+ model reduces the peak k within the core by more than a factor of two, thereby increasing the size of the interaction. These results also support the conclusion of Zheltovodov *et al* [143, 156, 154] that the turbulence amplification in the reversed flow may be the reason for the disappearance of the secondary separation in the regime IV - V (Fig. 61).

In summary, the following conclusions can be made:

- The weakly nonlinear Wilcox-Durbin (WD+) model provides a significant improvement in prediction of the 3-D single fin interaction in comparison with the Wilcox (WI)

model. In particular,

- The secondary separation/attachment and secondary shock are captured for the Mach 4, $\alpha = 30.6^\circ$ configuration (Regime VI). The linear Wilcox model does not predict secondary separation/attachment and the secondary shock for this case.
- The surface pressure distribution is in close agreement with experiment for all three cases, except for the position of upstream influence (*i.e.*, the location of initial pressure rise) for the strongest interaction.
- The improvement in prediction by the Wilcox-Durbin model is associated with a reduction in the computed turbulence kinetic energy k in the separation vortex.

5 3-D Double Fin

The 3-D double fin interaction (also known as the crossing shock wave / turbulent boundary layer interaction) shown in Fig. 5 is a canonical validation case for CFD modeling of 3-D shock wave turbulent boundary layer interactions. An equilibrium supersonic turbulent boundary layer approaches a channel defined by two semi-infinite fins of angles α_1 and α_2 separated by a distance W_e at the entrance. Additional geometric parameters include the minimum (throat) width W_t and the offset (if any) of the midpoint of the throat relative to the midpoint of the entrance.

The first numerical-experimental studies of such configuration with small and moderate fin inclination angles were conducted more than a decade ago by Mee, Stalker and Stollery [167]. Since that time, interest in this problem has greatly increased due to its relationship to scramjet propulsion since the crossing shock interaction constitutes a geometrical simplification of a hypersonic sidewall compression inlet. Symmetric interactions (*i.e.*, $\alpha_1 = \alpha_2$) have been studied by [6, 159, 164, 168, 169, 170, 171, 172, 173, 174, 175, 176, 177, 178, 179, 180, 181, 182, 183, 184, 185, 186, 187, 188, 189, 190, 191, 192, 193, 194, 195, 196, 197, 198, 199, 200, 201, 202, 203, 204, 205, 206, 207, 208, 209]. Asymmetrical interactions (*i.e.*, $\alpha_1 \neq \alpha_2$) have been studied by [6, 164, 167, 169, 171, 172, 173, 174, 179, 187, 192, 193, 196, 197, 198, 199, 202, 203, 204, 208, 209, 210, 211, 212, 213, 214, 215, 216, 218]. These studies cover the Mach number range from 1.85 to 8.3 and fin angles from -3° to 15° . Special emphasis in most papers is on the analysis of the pressure distribution and the structure of the limiting streamlines on the plate surface (surface flow pattern) in the interaction region.

The most complete cycle of experimental research of the symmetrical interaction between crossing shock waves with a turbulent boundary layer for $M_\infty = 3$ and 4 is presented in [172, 174, 177, 178, 184, 185, 186]. In addition to the patterns of the limiting streamlines

and pressure distribution on the plate surface, these papers present the data on the distribution of the skin friction coefficient, total pressure fields and local angles of flow direction, as well as the optical visualization of the 3-D flowfield. Similarly, fairly complete measurements of surface pressure distribution and heat transfer together with fields of various parameters under the conditions of symmetrical interaction are analyzed for two situations ($M_\infty = 8.3, \alpha = 10^\circ$ and 15°) in [179, 180, 181, 182]. Additional systematic information about the surface heat transfer together with surface pressure distribution and limiting streamlines pattern was obtained at $M_\infty = 4$ for different cases of symmetrical and asymmetrical interactions in [187, 194, 196, 216]. The pioneering study [219] of a symmetrical interaction for $M_\infty = 3.85$ near the $\alpha = 15^\circ$ fins mounted on the surface of a 2-D compression corner ($\alpha = 10^\circ$) is also noted. The data on the gas dynamic structure of this more complex flow obtained on the basis of optical visualization and the limiting streamlines on the surface are important for testing the up-to-date calculations and searching for effective configurations of inlets with 3-D compression.

Studies dealing with unsteady effects are infrequent, but nonetheless extremely important. Batcho *et al* [168] were apparently the first to measure the pressure and temperature fluctuations on the surface for the case of symmetrical interaction. These measurements allowed the authors to assume the existence of a relationship between the fluctuations of these parameters and heat transfer intensity fluctuations. More detailed measurements of pressure fluctuations were performed later in [169, 172].

It should be noted that fins with flat internal faces that form a converging half-channel were used in most experiments, except for [179, 180, 181, 182, 187, 194, 196, 216]. There was only one intersection of shock waves because of the threat of half-channel blockage, and the downstream region of investigation on the plate was limited. In the above papers, the side faces had inflected generatrices with a constant-width channel behind the inflection (see Fig. 5). Specific features of the flow in these conditions are determined by the boundary layer interaction with a sequence of crossing shocks and expansion waves.

Advanced numerical studies of these flows are based on the numerical solution of the full Reynolds averaged Navier-Stokes equations (RANS) with the use of various turbulence models: algebraic (Baldwin-Lomax and its modifications) and differential models ($k-\epsilon$, $k-\omega$, $k-l$ and their modifications), and also the full Reynolds stress equations. The calculations conducted for symmetrical [159, 164, 170, 174, 175, 176, 177, 180, 181, 182, 183, 184, 186, 188, 189, 190, 191, 192, 193, 199, 200, 201, 202, 203, 204, 205, 206, 208, 209, 210, 213, 214] and asymmetrical [164, 187, 192, 193, 197, 199, 202, 203, 204, 208, 209, 211, 212, 213, 214, 215, 216, 218] interactions and for symmetrical fins mounted on the compression surface [190, 219]. As it follows from review of investigations of the flow for symmetrical and asymmetrical interactions, the advanced RANS calculations with various turbulence models (algebraic or two-parameter differential models, and also Reynolds stress equations) allow a correct

prediction of only some properties of these flows. For example, the numerical results are in good agreement with experimental data for the shock-wave structure formed in the half-channel under the conditions of viscous-inviscid interaction, the fields of various parameters of the mean flow, the pressure distribution on the surface only for limited range of the crossing shock wave strength (under the conditions of weak- and moderate-strength). This agreement, however, significantly decreases as the strength of crossing shock waves increases. The accurate prediction of surface heat transfer and skin friction remains a challenging problem.

To characterize some specific features of the crossing shock wave/turbulent boundary layer interaction Fig. 77 shows a 3-D perspective view of the flowfield model with schematic images of the interaction structure at some specific cross sections (I to III) in the vicinity of symmetrical $15^\circ \times 15^\circ$ double fin configuration at $M_\infty = 4$ developed by Garrison and Settles [173, 177, 178] on a basis of experimental planar laser scattering images. Based on the inherent symmetry of the crossing-shock interaction, only half of interaction is shown in the figure. Cross section I occurs upstream of the intersection of the two single fin interactions meet and thus represents two separate single fin interactions. Incident separation (1), rear (2) and “inviscid” (3) shocks with a slip line (4) penetrating from the triple point to a fin side/plate cross line as well as separation vortex (5) under the bifurcated shock system are visible in this cross section. Cross section II occurs downstream of the intersection of the two separation shocks. To understand the intersection of the two separate single fin interactions, the vertical plane of symmetry is considered an inviscid reflection plane. For the symmetrical crossing shock wave interaction, shock waves that intersect this plane must reflect from it to satisfy continuity. It is evident that in cross section II the incident separation shock reflection from the symmetry plane is an irregular (*i.e.*, Mach) reflection. The Mach reflection results in a straight shock segment, the Mach stem (7), which spans the interaction centerline, a reflected portion of the separation shock (6), and newly formed triple point (10). As it is seen from the perspective view and cross section III, the entire incident λ -shock structure reflects from the center plane in an irregular manner and remains intact, though somewhat distorted, propagating away from the center toward the fin surface. The additional cross sections that characterize details of the complex shock crossings between the cross sections I and III are considered in [173, 177, 178]. As shown in cross section III, two additional shock segments and two triple points are observed to form a result of this crossing. One centerline segment (12) spans the interaction centerline between the reflected inviscid shock waves (9), and the second “bridge” segment (13), connects the reflected inviscid shock (9) to the reflected separation (6) and rear (8) shocks. A “mushroom-shaped” separation structure (5) is formed in the vicinity of the centerline in the last cross section from the twin single-fin separations which begin the crossing-shock interaction.

An example of the flowfield for a $M_\infty = 4$, $15^\circ \times 15^\circ$ symmetric double fin interaction is

shown in Fig. 78 by the stream ribbons together with the footprint of each regime (coherent feature) (Fig. 79) in accordance with RANS computations by Gaitonde and Shang [189] and Gaitonde *et al* [192, 193, 197] performed for the test configuration investigated experimentally by Garrison and Settles [178] and Zheltovodov *et al* [187, 194]. The turbulence model employed to derive the eddy viscosity μ_t is based on the $k-\epsilon$ equations [220, 221] with low Reynolds number terms and incorporates a compressibility correction. As pointed out by Gaitonde and Shang, different coherent features, or regimes, can be identified in the flow. For example, it is evident from Fig. 78 [189, 193, 197, 218] that the incoming boundary layer separates at the line of coalescence $S1$ and its symmetric counterpart $S2$ (not marked). This regime does not reattach thus setting up an open structure with no “trapped” fluid. Flow attaching near the fin-plate corners at $R1$ and its symmetric counterpart $R2$ (not marked) (see also Fig. 79) can be categorized into several regimes, the first of which is a Vortex Interaction (VI), characterized by off-surface stagnation points [192, 200, 201, 206] and which separates from the downstream side of $S1$. Fluid attaching further downstream forms the entrainment flow (EF) which brings high speed fluid near the plate. This regime separates prior to reaching the symmetry plane, and two Centerline Vortices (CV) are formed.

The several lines of coalescence and divergence observed in Fig. 79 have direct counterparts in experimental observation, as documented previously [173, 177, 178, 187, 194, 196, 205, 206]. For example, in accordance with experiments by Zheltovodov *et al* [187, 194, 196] the primary separation lines S_1 and S_2 , the secondary separation lines S_3 and S_4 and the primary attachment lines R_1 and R_2 are specific for $15^\circ \times 15^\circ$ double-fin case at $M_\infty = 4$ (Fig. 80a). The distinct separation region is formed in the throat behind the centerline singular saddle point S_o^1 and bounded by the separation lines S_5 and S_6 . The centerline node point N_o^1 was observed further downstream. The line S_3 is very close to merge with S_5 (and so is S_4 with S_6 on the opposite side) approximately in the middle of the central separated zone.

The topology of surface flow pattern computed by Gaitonde and Shang on a basis of the $k-\epsilon$ turbulence model [192, 205, 206] is somewhat different (Fig. 80b,c). The primary separation lines intersect at the centerline node N_o^2 , and therefore no fluidic throat forms but in the experiment another centerline node N_o^1 is observed. (This is more clearly shown in an enlarged fragment in Fig. 80c). The unsteady intermittent nature of the experimental flow upstream of the singular separation point S_o^1 [194, 217], not predicted by computations, may explain this discrepancy. Additional features, which were not observed in the experiment, are two saddle points S_1 and S_2 located symmetrically about the centerline (Fig. 80c). As shown by Schüle and Zheltovodov [195] these symmetric saddle points appear as a result of the complex evolution of the flow at higher shock waves strength.

The calculations do not reveal the signs of the secondary separation lines S_3 and S_4 , and the central separated zone is more compressed by the flows propagating from the fins and

noticeable smaller in width comparing with experiment (Fig. 80a,b). As result, the computed surface pressure is noticeably overestimated in the vicinity of the channel centerline for $X = x/d > 17$ (Fig. 80d). As was concluded in [198, 205, 206], this discrepancy may be related to a difference in the turbulence level in the near wall region of the secondary flows between the primary attachment (R_1 and R_2) and separation (S_1 and S_2) lines in experiment and computation.

This conclusion is supported by the computations of Panaras [159] (Fig. 81b) who has used his modification of the Baldwin-Lomax turbulence model to predict a similar $M_\infty = 4$, $15^\circ \times 15^\circ$ crossing shock wave turbulent boundary layer interaction investigated by Garrison and Settles [177, 178, 184, 186] (Fig. 81a). The resultant pattern of the limiting streamlines (Fig. 81b) is a good reproduction of the specific features of the behavior of the secondary separation lines S_3 and S_4 under the conditions of the laminar secondary flow, the scale of the central separation region, the centerline pressure distribution (Fig. 81c) and skin friction distribution (Fig. 81c), which were observed by Garrison and Settles in their experiments. At the same time, the computed surface flow pattern is associated with the node in the apex of the centerline separation zone and two symmetrical saddle points as in the computations by Gaitonde and Shang considered above which was not observed in the experiment at such conditions.

Gaitonde *et al* [192, 193, 197, 218] performed RANS computations with the $k-\epsilon$ model and described the evolution of the flow model with interaction strength and asymmetry. An attempt was made in [193, 201, 218] to inhibit the transition of the sidewall boundary layer by limiting the production of turbulent kinetic energy in a $k-\epsilon$ model. It resulted in a rectification of the discrepancies between the flowfield visualization and simulations in the sidewall/shock-vortex interaction region but no significant effect on the bottom wall.

Recent studies [159, 192, 193, 197, 199, 206, 211, 216] distinctly demonstrate obvious limitations of various turbulence models to correctly predict different properties of symmetric and asymmetric crossing shock wave turbulent boundary layer interaction for a wide range of crossing shock strength. They have stimulated new attempts to analyze the possibilities of two-equation $k-\omega$ and $k-\epsilon$ turbulence models and some of their modifications, as well as modifications of the algebraic Baldwin-Lomax model by Panaras for predicting the properties of such flows over a wide range of crossing shock wave strength [6, 164, 200, 201, 202, 203, 204, 205, 208, 209, 210, 218].

5.1 Case 1: Mach 4, $\alpha_1 = 15^\circ$, $\alpha_2 = 15^\circ$

Thivet[164, 202, 204, 209] simulated two configurations of the 3-D double fin⁶. Experimental data of Zheltovodov *et al* [187, 194, 196, 216] is available for both cases. The flow conditions are listed in Table 16. The computations were performed at the same flow conditions as the experiment. The experimental configuration for Case 1 is shown in Fig. 5. The fins were 100 mm high and 192 mm long. Their leading edges were located at a distance of 210 mm from a leading edge of the plate. The boundary layer thickness upstream of the channel entrance $d = 3.5$ mm. The entrance width $W_e = 79.1$ mm and the throat width $W_t = 32$ mm.

Details of the computations⁷ are presented in Table 17. Five different turbulence models were considered, namely, the (linear) Wilcox $k-\omega$ (WI) model[163], and four variants of the Wilcox model based on the requirement for weak realizability[222] of the computed Reynolds stresses⁸. The variants are the Wilcox-Moore (WM), Wilcox-Durbin (WD) and two modifications thereof (WM+ and WD+). Details of the models are presented in Thivet *et al* [164]. A detailed grid refinement study [164] was performed to quantify the uncertainty in the computations.

The surface flow pattern topology, skin friction lines and heat-transfer coefficient lines computed by Thivet [164, 204, 209] using the WI and WM+ models are presented in Fig. 82. The computed primary separation lines S_1 and S_2 intersect at the node point and the fluidic throat does not exist between these lines (compared with the experiment where the saddle point has been revealed in the throat between these lines, see Fig.77). The secondary separation lines S_3 and S_4 are not predicted and additional separation lines S_5 and S_6 , which bound the central separation region, appear much closer to the centerline than in the experiment. Nevertheless, the width of this separation zone is wider comparing with one in the computations by Gaitonde and Shang (Fig. 80b,c).

The computed and experimental surface pressure and heat transfer coefficient on the Throat Middle Line⁹ (TML) for Case 1 are shown in Fig. 83 for the WI and WM+ models. In the case under consideration, two computations were carried out with WM+ model on fine and very fine grids. All three computations with different models underestimate the location of the pressure rise immediately following the plateau and overestimate the peak pressure. The subsequent expansion (associated with the corner of the fins) is more accu-

⁶A third configuration ($M_\infty = 4$, $\alpha_1 = 7^\circ$, $\alpha_2 = 7^\circ$) is not presented here, as it is a weaker interaction. It is accurately predicted by general RANS models.

⁷Data are shown for the finest grid.

⁸Realizability implies that the normal kinematic Reynolds stresses $\overline{u'u'}$, $\overline{v'v'}$ and $\overline{w'w'}$ are non-negative, and the Reynolds shear stresses $\overline{u'v'}$, $\overline{u'w'}$ and $\overline{v'w'}$ are bounded by the Schwartz inequality, *e.g.*, $(\overline{u'v'})^2 \leq \overline{u'u'} \overline{v'v'}$.

⁹The Throat Middle Line is the streamwise datum through the center of the throat.

rately predicted by the WI model. The realizability correction does not modify the computed topology so that the features of the heat transfer distribution remain the same. Nevertheless, the levels are significantly modified, essentially because of the lower turbulence levels in the WM+ solution, which allow an earlier appearance (*i.e.*, farther from TMP) of the separation lines S_5 and S_6 than in the WI solution, yielding a wider central separation region and a lower heat transfer between the maxima. The computed peak heat transfer significantly overestimates the experiment for all models.

In summary, the following conclusions can be made:

- The surface pressure is predicted with reasonable accuracy, although some discrepancies between computed and experimental surface pressure are evident.
- The peak heat transfer is not accurately predicted by any of the models.

5.2 Case 2: Mach 4, $\alpha_1 = 7^\circ$, $\alpha_2 = 11^\circ$

An example of the mean streamline structure is shown in Fig. 84 from Thivet *et al* [164] for a Mach 4, $7^\circ \times 11^\circ$ double fin interaction. The principal features include the separated boundary layer, vortex, and entrained flow. The computed surface heat transfer coefficient contours and surface streamlines are shown in Fig. 85 and the corresponding experimental surface streamline pattern in Fig. 86. The primary separation lines (denoted S_1 and S_2 in Fig. 86) are evident in both computation and experiment, and correspond to the liftoff of the streamlines from the surface in Fig. 84. The attachment lines (denoted R_1 and R_2 in Fig. 86) correspond to the impingement of the streamlines which demarcate the boundaries of the counter-rotating vortex pair formed by the separated flow. Secondary separation lines (S_3 and S_4 in Fig. 86) and attachment line (denoted R_3 in Fig. 86) are also evident.

The computed and experimental surface pressure and heat transfer coefficient¹⁰ on the TML for Case 2 are shown in Fig. 87. The surface pressure is accurately predicted by all models with only slight differences in the plateau pressure at $x = 80 - 100$ mm. Similar good agreement with experiment and insensitivity of the predictions to the turbulence model are observed in the spanwise pressure distributions at three streamwise locations (Fig. 88). This is consistent with previous results [1] which showed a marked insensitivity of the computed surface pressure to the turbulence model employed.

The computed surface heat transfer coefficient on the TML (Fig. 87) and at three streamwise locations (Fig. 89) significantly overpredicts the peak experimental value for all models. This is similar to previous results using other RANS models which did not incorporate a specific realizability effect [1].

¹⁰The heat transfer coefficient $c_h = q_w / \rho_\infty U_\infty c_p (T_w - T_{aw})$ where T_{aw} is the adiabatic wall temperature.

Thivet examined the effect of imposing the turbulence length scale limitation proposed by Coakley and Huang [223]. The turbulent eddy viscosity $\mu_t = \rho c_\mu k^{1/2} \ell$ and the turbulence length scale ℓ is defined by

$$\ell = \min [\ell_{\log}, k^{1/2}/\omega]$$

where

$$\ell_{\log} = \frac{\kappa}{c_\mu^{3/4} d}$$

where $\kappa = 0.41$ is von Karman's constant and d is the distance normal to the wall. The dissipation term in the transport equation for k is modeled using $\omega = k^{1/2}/\ell$. Fig. 90 displays the ratio of the computed turbulence length scale ℓ (without the Coakley and Huang correction) to the logarithmic expression ℓ_{\log} for Case 2 at $x = 46$ mm for six spanwise locations. The transverse location z_r is zero at the fin and unity at the location corresponding to the inviscid shock generated by the 11° fin. It is evident that the ratio does not significantly exceed unity, thereby implying that the Coakley and Huang correction would have little effect on the computed solution.

Thivet also examined the effect of incorporating a compressibility correction [163] in the $k-\omega$ model¹¹. The threshold value of the turbulence Mach number $M_t = \sqrt{2k/a}$ (where a is the local speed of sound) is 0.25 for the compressibility correction. Below this value, the correction is inoperative. The maximum value of M_t using the WI model is 0.3 yielding an increase of only 4% in the dissipation term, thereby implying that this correction (if implemented) would have negligible effect on the computation using the WI model. The values of M_t for the WD, WD+ and WM+ models are everywhere below the threshold, and therefore the compressibility correction (if implemented) would have no effect on these results.

In summary, the following conclusions can be made:

- The computed surface pressure is accurately predicted by the five different turbulence models for Case 1 ($\alpha_1 = 7^\circ$, $\alpha_2 = 11^\circ$).
- The peak heat transfer is not accurately predicted by any of the models.
- The proposed length scale correction of Coakley and Huang [223], and the compressibility modifications of Zeman [224] or Sarkar [225], would not significantly change the computed flowfields.

¹¹The compressibility correction concept, introduced by Zeman [224] and Sarkar [225] to account for the observed decrease in the spreading rate of compressible mixing layers, leads to an undesirable reduction in skin friction for turbulent boundary layers [163, 223, 226].

5.3 Case 3: Mach 5, $\alpha_1 = 18^\circ$, $\alpha_2 = 18^\circ$

Schmisser and Gaitonde [200] and Panaras [227] simulated a Mach 5, $\alpha_1 = \alpha_2 = 18^\circ$ double fin at $Re_\delta = 1.4 \times 10^5$ and isothermal wall conditions ($T_w/T_{aw} = 0.76$). Experimental data of Schülein and Zheltovodov [195, 207] (an additional description is presented in Zheltovodov and Maksimov [228]) is available for this case. The flow conditions are shown in Table 18. The computations were performed at the same flow conditions as the experiment. The experimental configuration is shown in Fig. 91.

Details of the computations are presented in Table 19. Schmisser and Gaitonde utilized the $k-\epsilon$ model [220, 221] with low Reynolds number and compressibility corrections. Panaras [2] employed a modified Baldwin-Lomax model.

The experimental surface oil flow is presented in Fig. 92, and the computed surface streamlines in Fig. 93 (Schmisser and Gaitonde) and Fig. 94 (Panas). The experiment displays a complex structure of separation (S) and attachment (R) lines. The initial separation lines (S_1 and S_2) generated by the individual fin shock boundary layer interactions coalesce to form a node at the centerline. Corresponding attachment lines (R_1 and R_2) are located near the fins. Additional separation (S_3 to S_6) and attachment lines (R_3 to R_6) form downstream. The central point (S_o^1) is a saddle point in the experiment. In the same region, the computation of Schmisser and Gaitonde (Fig. 93) displays a node (N_1), while the computation of Panaras (Fig. 94) appears in closer agreement with experiment. Nonetheless, both computed surface streamline plots show overall good agreement with experiment.

The computed and experimental surface pressure on the centerline is displayed in Fig. 95 (Schmisser and Gaitonde) and Fig. 96 (Panas). The experimental pressure profile displays a rise due to the crossing shock interaction, and a subsequent drop beginning at $x = 42\delta$ due to the expansion originating from the corners C in Fig. 91. The subsequent pressure rise is associated with the reflection of the shocks from the fin surfaces. The computed surface pressure of Schmisser and Gaitonde shows significant deviation from experiment beginning at the initial plateau in surface pressure. The computed surface pressure of Panaras shows good agreement up to the beginning of the decrease in pressure at $x/\delta = 42$. However, a significant discrepancy appears thereafter.

The computed and experimental surface pressure at three streamwise locations are shown in Figs. 97 to 102. The results of Schmisser and Gaitonde are presented in Figs. 97, 99 and 101, and the results of Panaras in Figs. 98, 100 and 102. Both computations show good agreement with experiment at $x = 26.6\delta$ (Figs. 97 and 98). This location is upstream of the interaction of the crossing shocks, and thus represents individual single fin interactions. At $x = 37.1\delta$ (located at approximately the second focal point N^2 as indicated in Fig. 93) both computed profiles show good agreement with experiment, except for a overshoot in centerline pressure in Fig. 99 (Schmisser and Gaitonde). At $x = 52.9\delta$ (see Fig. 93), both

computations show generally good agreement with experiment except for an overshoot in pressure at the centerline.

In summary, the following conclusions can be made:

- The computed surface streamlines are in good agreement with experiment. The detailed structure of separation, attachment and foci are generally accurately reproduced in the simulations.
- The computed surface pressure shows general agreement with experiment during the initial portion of the interaction and off centerline throughout the entire interaction. However, significant differences between computed and experimental surface pressure are evident on the centerline of the interaction.

5.4 Case 4: Mach 5, $\alpha_1 = 23^\circ$, $\alpha_2 = 23^\circ$

Schmisser and Gaitonde [200, 201, 205, 208] and Panaras [227] simulated a Mach 5, $\alpha_1 = \alpha_2 = 23^\circ$ double fin at $Re_\delta = 1.4 \times 10^5$ and isothermal wall conditions ($T_w/T_{aw} = 0.76$). Experimental data of Schülein and Zheltovodov [195, 207] (an additional description is presented in Zheltovodov and Maksimov [228]) is available for this case. The flow conditions are shown in Table 20. The computations were performed at the same flow conditions as the experiment. The experimental configuration is shown in Fig. 103.

Details of the computations¹² are presented in Table 21. Schmisser and Gaitonde utilized the $k-\epsilon$ model [220, 221] with low Reynolds number and compressibility corrections. Panaras [2] employed a modified Baldwin-Lomax model.

The experimental surface oil flow is presented in Fig. 104, and the computed surface streamlines in Figs. 105 (Schmisser and Gaitonde) and 106 (Panas). Good agreement is observed between the computations and experiment.

The computed and experimental surface pressure on the centerline is displayed in Fig. 107 (Schmisser and Gaitonde) and Fig. 108 (Panas). The experimental profile is similar to the $18^\circ \times 18^\circ$ configuration except for the absence of the second shock reflection on the centerline due to the limited length of the flat plate. The computed profile by Schmisser and Gaitonde shows good agreement with experiment up to the peak experiment pressure, but significantly overestimates experiment downstream. The computed profile by Panaras also shows good agreement with experiment up to the peak pressure, but does not display the expansion region¹³ observed in the experiment.

¹²Schmisser and Gaitonde performed a grid refinement study using meshes of $91 \times 72 \times 52$, $181 \times 143 \times 103$ and $229 \times 179 \times 129$ and confirmed that the finest grid solution was grid converged.

¹³A separate coarse grid computation was performed by Panaras [227] wherein the effect of the finite plate

The computed and experimental surface pressure at three streamwise locations are shown in Figs. 109 to 114. The results of Schmisser and Gaitonde are shown in Figs. 109, 111 and 113, and the results of Panaras in Figs. 110, 112 and 114. Both computations are in close agreement with the available experimental data at $x = 22.1\delta$ which is upstream of the crossing shock interaction (see Figs. 107 and 108). At $x = 32.6\delta$, located in the midst of the crossing shock interaction, both computations show close agreement with experiment, although somewhat overestimating the centerline pressure. At $x = 48.4\delta$, the agreement between computation and experiment is good except in the immediate vicinity of the centerline where the pressure is overestimated.

In summary, the following conclusions can be made:

- The computed surface streamlines display good agreement with experiment
- The computed surface pressure shows general agreement with experiment during the initial portion of the interaction and off centerline throughout the entire interaction. However, significant differences between computed and experimental surface pressure are evident on the centerline, similar to Case 3.

6 Conclusions

An evaluation of the CFD capability for prediction of shock wave turbulent boundary layer interaction was performed under the auspices of NATO RTO Working Group 10. Five separate configurations were considered, namely, the 2-D compression corner, 2-D shock impingement, 2-D expansion-compression corner, 3-D single fin and 3-D double fin. Recent DNS, LES and RANS simulations were solicited. The computed results were compared with experimental data where available. The following conclusions may be drawn:

- DNS and LES
 - DNS and LES of shock wave turbulent boundary layer interaction is an active area of research. In the previous review of shock wave turbulent boundary layer interaction by Knight and Degrez [1] published in 1998, there were no DNS or LES results available. The present paper includes several DNS and LES results for 2-D shock wave turbulent boundary layer interactions.

length was approximated by adding a divergent section to the flat plate. The computed centerline pressure displayed significantly better agreement with experiments, but the spanwise extent of the central structure was smaller than in the experiment.

- A comprehensive assessment of the capability of DNS and LES was not possible for two reasons. First, the DNS and LES simulations have been performed at lower Reynolds numbers Re_δ than the experiment for all cases except one (*i.e.*, the 2-D shock impingement). Second, the DNS and LES have been performed for nominally 2-D flows. Both reasons are attributable to the computational cost of DNS and LES.
- Although the set of comparisons between DNS and LES with experiment was limited, nevertheless it is clear that significant progress has been achieved in the prediction of shock wave turbulent boundary layer interaction using DNS and LES. In several cases, the computations were performed at Reynolds numbers close to the experiment (and, in one case, equal to experiment), and good agreement with experimental data was achieved. Detailed comparisons included surface pressure, skin friction, velocity, temperature and turbulence profiles. However, some significant discrepancies are evident, due possibly to the differences in Reynolds number.
- No DNS or LES results for surface heat transfer in shock wave turbulent boundary layer interaction were available. This is particularly disappointing, since prior RANS simulations of strongly separated shock wave turbulent boundary layer interactions have failed to accurately predict heat transfer [1].

- RANS

- New ideas in modeling have reinvigorated RANS simulations for shock wave turbulent boundary layer interaction. These new ideas include realizability (weak nonlinearity) and specific physical models which incorporate known flowfield behavior.
- The weakly nonlinear Wilcox-Durbin model successfully predicts secondary separation for the 3-D single fin in agreement with experiment.
- The linear and weakly nonlinear Wilcox-based models fail to accurately predict surface heat transfer for the separated 3-D double fin.
- The surface streamline pattern for the 3-D double fin Case Nos. 3 and 4 is predicted by both the conventional $k-\epsilon$ and Baldwin-Lomax-Panaras models.
- The surface pressure for the 3-D double fin is accurately predicted by the conventional $k-\epsilon$ and Baldwin-Lomax-Panaras models only in the initial region of the interaction. Significant differences between the computational and experimental centerline pressure are evident downstream.

7 Future Needs

The following research needs for shock wave turbulent boundary layer interaction may be identified:

- DNS and LES simulations are needed at Reynolds numbers corresponding to the experiment. This is essential to end speculation regarding the reasons for discrepancy between simulation and experiment.
- DNS and LES simulations are needed for 3-D configurations. All DNS and LES results to date have been for nominally 2-D flows.
- DNS and LES simulations are needed to compare with experimental data for heat transfer. Neither DNS, LES nor RANS models to date have successfully predicted surface heat transfer in strongly separated shock wave turbulent boundary layer interactions.
- RANS modeling needs continued emphasis on weakly nonlinear corrections to two equation models, and continued development of configuration-specific modifications to simple models.

8 Acknowledgments

This research is supported by AFOSR under Grant No. F49620-99-1-0008 monitored by Drs. Robert Herklotz, L. Sakell, J. Schmisser and Steve Walker, by the SCOPES 2000-2003 Program under Project No. 7SUPJ062351 and by the Russian Foundation of Basic Research under Grant No. 97-01-00885.

References

- [1] Knight D, Degrez G. Shock Wave Boundary Layer Interactions in High Mach Number Flows – A Critical Survey of Current CFD Prediction Capabilities. AGARD AR-319, Volume 2, 1998.
- [2] Panaras A. The Effect of the Structure of Swept Shock Wave Turbulent Boundary Layer Interactions on Turbulence Modeling, *Journal of Fluid Mechanics*, 1997; 338:203–230. Also published as DLR-IB-223-96 A 21.
- [3] Zheltovodov A. Shock Waves / Turbulent Boundary Layer Interactions - Fundamental Studies and Applications. AIAA Paper 96-1977, 1996.

- [4] Muylaert J (Ed). Technologies for Propelled Hypersonic Flight. EWP NR. 2122, European Space Agency, May 2001.
- [5] Knight D. Overview of NATO RTO WG 10 SG 3: CFD Validation for Propelled Hypersonic Flight. AIAA Paper 2002-0433, Jan 2002.
- [6] Knight D, Yan H, Panaras A, Zheltovodov A. RTO WG 10: CFD Validation for Shock Wave Turbulent Boundary Layer Interactions. AIAA Paper 2002-0437, 2002.
- [7] <http://www.cs.rutgers.edu/~knight/wg10>
- [8] Settles G, Dodson L. Hypersonic Shock Boundary Layer Interaction Database. NASA CR-117577, 1991.
- [9] Haase W, Chaput E, Elshotz E, Leschziner M, Müller U. ECARP - European Computational Aerodynamics Research Project: Validation of CFD Codes and Assessment of Turbulence Models, Friedr. Vieweg & Sohn Verlagsgesellschaft mbH, Braunschweig/Wiesbaden, 1997.
- [10] Petrov G, Likhusin V, Nekrasov I, Sorkin L. Influence of Viscosity on the Supersonic Flow with Shock Waves. Proceedings of CIAM, No. 224, 1952, 28 pp. (in Russian).
- [11] Chapman D, Kuehn D, and Larson H. Investigation of Separated Flows in Supersonic and Subsonic Streams with Emphasis on the Effect of Transition. NACA Report 1356, 1957.
- [12] Gogish L, Stepanov G. Turbulent Separated Flows, Moscow Nauka, 1979, 367 pp. (in Russian).
- [13] Green J. Interactions Between Shock Waves and Turbulent Boundary Layers. Progress in Aerospace Sciences 1970;11:235–341.
- [14] Charwat A. Supersonic Flows with Imbedded Separated Regions. Advances in Heat Transfer 1970; 6:1–132.
- [15] Stanewsky E. Shock-Boundary Layer Interaction in Transonic and Supersonic Flows, in Transonic Flows in Turbomachinery, Von Karman Institute, Rhodes Saint-Genese, Belgium, Lecture Series No. 59, May 1973, 198 pp.
- [16] Delery J, Marvin J. Turbulent Shock-Wave/Boundary Layer Interaction. AGARDograph No. 280, E. Reshotko (Ed), February 1986, 224 pp.

- [17] Holden M. Shock Wave-Turbulent Boundary-Layer Interaction in Hypersonic Flow. AIAA Paper 72-74, 1972.
- [18] Law C. Supersonic Turbulent Boundary-Layer Separation. AIAA Journal, 1974; 12(6):794–797.
- [19] Shang J, Hankey W, Law C. Numerical Simulation of Shock Wave Turbulent Boundary Layer Interaction. AIAA Journal, 1976; 14(10):1451–1457.
- [20] Smits A, Dussauge J.-P. Turbulent Shear Layers in Supersonic Flow. American Institute of Physics, Woodbury, NY, 1996.
- [21] Andreopoulos Y, Agui H, Briassulis G. Shock Wave - Turbulence Interactions. Annual Review of Fluid Mechanics 2000; 32:309–345.
- [22] Delery J. Shock Wave/Turbulent Boundary Layer Interaction and Its Control. Progress in Aerospace Sciences, 1985; 22:209–280.
- [23] Zheltovodov A, Schülein E. The Peculiarities of Turbulent Separation Development in Disturbed Boundary Layers. Modelirovaniye v Mekhanike, 1988; 2(1):53–58 (in Russian).
- [24] Zheltovodov A, Schülein E, Horstman C. Development of Separation in the Region Where a Shock Interacts with a Turbulent Boundary Layer Perturbed by Rarefaction Waves. Journal of Applied Mechanics and Technical Physics, 1993; 34(3):346–354.
- [25] Zukoski E. Turbulent Boundary Layer Separation in Front of a Forward Facing Step. AIAA Journal, 1967; 5(10):1746–1753.
- [26] Albertson C, Ash R. Compressible Equilibrium Turbulent Boundary Layers at Nonadiabatic Wall Conditions. AIAA Journal, 1991; 29(10):1573–1580.
- [27] Johnson C, Bushnell D. Power-Law Velocity Profile-Exponent Variation with Reynolds Number, Wall Cooling, and Mach Number in a Turbulent Boundary Layer. NASA TN D-5753, April 1970.
- [28] Settles G. An Experimental Study of Compressible Turbulent Boundary-Layer Separation at High Reynolds Number. PhD Thesis, Aerospace and Mechanical Sciences Department, Princeton University, 1975.

- [29] Settles G, Perkins J, Bogdonoff S. Upstream Influence Scaling of 2D and 3D Shock/Turbulent Boundary Layer Interactions at Compression Corners. AIAA Paper 81-0334, 1981.
- [30] Adamson T, Messiter A. Analysis of Two-Dimensional Interactions Between Shock Waves and Boundary Layers. *Annual Review of Fluid Mechanics*, 1980; 12:103–138.
- [31] Stewartson K, Williams P. Self-induced Separation. *Proceedings of the Royal Society of London Series A*, 1969; 312:181–206.
- [32] Neiland V. Theory of Laminar Boundary Layer Separation in Supersonic Flow. *Mekhanika Zhidkosti i Gaza*, 1969, 4:53–57 (in Russian). Translated in *Fluid Dynamics* 1969; 4(4):33–35.
- [33] Agrawal S, Messiter A. Turbulent Boundary Layer Interaction with a Shock Wave at a Compression Corner. *Journal of Fluid Mechanics* 1984; 143:23–46.
- [34] Zheltovodov A. Peculiarities of Development and Modeling Possibilities of Supersonic Turbulent Separated Flows. In *Separated Flows and Jets*, IUTAM Symposium, Novosibirsk, USSR, Springer-Verlag, Berlin, July 1990, pp. 225–236.
- [35] Zheltovodov A, Yakovlev V. Stages of Development, Flowfield Structure and Turbulence Characteristics of Compressible Separated Flows in the Vicinity of 2-D Obstacles. Preprint No. 27-86, Institute of Theoretical and Applied Mechanics, USSR Academy of Sciences, Novosibirsk, 1986, 56 pp. (in Russian).
- [36] Zheltovodov A, Schülein E, Yakovlev V. Development of Turbulent Boundary Layer under Conditions of Mixed Interaction with Shock and Expansion Waves. Preprint No. 28-83, Institute of Theoretical and Applied Mechanics, USSR Academy of Sciences, Novosibirsk 1983, 51 p. (In Russian).
- [37] Zheltovodov A, Trofimov V, Schülein E, Yakovlev V. An Experimental Documentation of Supersonic Turbulent Flows in the Vicinity of Forward- and Backward-Facing Ramps. Report No. 2030, Institute of Theoretical and Applied Mechanics, USSR Academy of Sciences, 1990.
- [38] Zheltovodov A, Pavlov A, Schulein E, Yakovlev V. Interconnectionship Between the Flow Separation and the Direct and Inverse Transition at Supersonic Speed Conditions. In *Laminar-Turbulent Transition*, IUTAM Symposium Novosibirsk/USSR 1984, Kozlov V (Ed). Springer-Verlag Berlin Heidelberg 1985, pp. 503-508

- [39] Zheltovodov A, Zaulichniy E, Trofimov V, Yakovlev V. The Study of Heat Transfer and Turbulence in Compressible Separated Flows. Preprint No. 22-87, Institute of Theoretical and Applied Mechanics, USSR Academy of Sciences, Novosibirsk, 1987, 48 pp. (in Russian).
- [40] Zheltovodov A, Zaulichniy E, Trofimov V. Development of Models for Calculations of Heat Transfer under Conditions of Supersonic Turbulent Separated Flows. *Prikladnaya Mekhanika i Tekhnicheskaya Fizika* 1990; 4:96–104 (in Russian).
- [41] Zheltovodov A, Trofimov V, Filippova E, Yakovlev Y. Influence of Turbulence Change on the Heat Exchange Under the Conditions of Supersonic Separated Flows. In Abstracts: IUTAM Symposium on Separated Flows and Jets, USSR Academy of Sciences, Siberian Division, Novosibirsk, 1990, pp. 273–274.
- [42] Dolling D. High-Speed Turbulent Separated Flows: Consistency of Mathematical Models and Flow Physics. *AIAA Journal* 1998; 36:725–732.
- [43] Dolling D. Fifty Years of Shock Wave Boundary Layer Interaction Research: What Next? *AIAA Journal* 2001; 39:1517–1531.
- [44] Adams N. Direct Simulation of the Turbulent Boundary Layer Along a Compression Ramp at $M = 3$ and $Re_\theta = 1685$. *Journal of Fluid Mechanics* 2000; 420:47–83.
- [45] Zheltovodov A, Schülein E, Yakovlev V. Investigation of Development of Compressible Turbulent Boundary Layer in the Vicinity of Compression/Expansion Corner Combination. Report No. 1397, Institute of Theoretical and Applied Mechanics, USSR Academy of Sciences, 1983, 127 pp. (in Russian)
- [46] Zheltovodov A, Yakovlev V. The Study of Turbulence Characteristics in Compressible Close to Separation and Separation Flows. Part II, Report No. 1418, Institute of Theoretical and Applied Mechanics, USSR Academy of Sciences, 1984, 100 pp. (in Russian).
- [47] Zheltovodov A. Investigation of Supersonic Turbulent Separated Flows. In Experimentation, Modeling and Computation in Flow, Turbulence and Combustion, Vol. 1, Desideri, J, Chetverushkin, B, Kuznetsov, A, Periaux, J, and Stoufflet, B, (Eds), 1996, John Wiley & Sons Ltd, 1996, pp. 337–350.
- [48] Borisov A, Zheltovodov A, Trofimov V, Schülein E, Yakovlev V. Analysis of Turbulent separated Flows in the Vicinity of Two-Dimensional Obstacles Under Supersonic

- Speeds Conditions. In Separated Flows and Jets, IUTAM Symposium, Novosibirsk, USSR, Springer-Verlag, Berlin, July 1990, pp. 333–336.
- [49] Dolling D, Murphy M. Unsteadiness of the Separation Shock Wave Structure in a Supersonic Compression Ramp Flowfield. *AIAA Journal* 1983; 12:1628–1634.
- [50] Dolling D, Or C. Unsteadiness of the Shock Wave Structure in Attached and Separated Compression Ramp Flows. *Experiments in Fluids* 1985; 3:24–32.
- [51] Andreopoulos J, Muck K. Some New Aspects of the Shock Wave Boundary Layer Interaction in Compression-ramp Flows. *Journal of Fluid Mechanics* 1987; 180:405–428.
- [52] Erengil M, Dolling D. Unsteady Shock Wave Structure Near Separation in a Mach 5 Compression Ramp Interaction. *AIAA Journal* 1991; 29:728–735.
- [53] Erengil M, Dolling D. Correlation of Shock Motion with Pressure Fluctuations in the Incoming Boundary Layer. *AIAA Journal* 1991; 29:1868–1877.
- [54] Dolling D. Fluctuating Loads in Shock Wave Turbulent Boundary Layer Interaction: Tutorial and Update. *AIAA Paper* 93-0284, 1993.
- [55] Bibko V, Efimtsov B, Kuznetsov V. Spectrums of the Surface Pressure Upstream of Internal Compression Corners. *Uchenie Zapiski TSAGI (Scientific Notes of TsAGI)*, 1989; 20(4):112–117 (in Russian).
- [56] Bibko V, Efimtsov B, Korkach B, Kuznetsov V. About the Fluctuations of Shock Wave Induced by the Boundary Layer Separation. *Fluid Mechanics*, 1990; 4:168–170.
- [57] Glotov G The Features of Incipieny and Development of the Re-circulated Zones in the Supersonic Layers of Supersonic Flows. *Applied Mechanics and Technical Physics* 1998; 36(5):30–39 (in Russian).
- [58] Wu P, Miles R. Megahertz Visualization of Compression Corner Shock Structures. *AIAA Journal*, 2001; 39(8):1542–1546.
- [59] Yan H, Knight D, Zheltovodov A. Large Eddy Simulation of Supersonic Compression Corner Using ENO Scheme. *Third AFOSR International Conference on DNS and LES*, Arlington, Texas, August 2001.
- [60] Shang J, Hankey W, Jr. Numerical Solution for Supersonic Turbulent Flow over a Compression Corner. *AIAA Journal*, 1975; 13(10):1368–1375.

- [61] Horstman C, Hung C. Reynolds Number Effects on Shock-Wave Turbulent Boundary-Layer Interaction - A Comparison of Numerical and Experimental Results. AIAA Paper 77-42, 1977.
- [62] Visbal M, Knight D. The Baldwin-Lomax Turbulence Model for Two-Dimensional Shock-Wave/Boundary-Layer Interactions. AIAA Journal 1984; 22(7):921–928.
- [63] Ong C, Knight D. Hybrid MacCormack and Implicit Beam-Warming Algorithms for a Supersonic Compression Corner. AIAA Journal 1987; 25(3):401–407.
- [64] Horstman C, Zheltovodov A. Numerical Simulation of Shock Waves/Expansion Fans - Turbulent Boundary Layer Interaction. In International Conference on Methods of Aerophysical Research, Institute of Theoretical and Applied Mechanics, Russian Academy of Sciences, Novosibirsk, Russia, July 1994, Part 2, pp. 118–125.
- [65] Borisov A, Zheltovodov A, Maksimov A, Fedorova N, Shpak S. Verification of Turbulence Models and Computational Methods of Supersonic Separated Flows. In International Conference on Methods of Aerophysical Research, Institute of Theoretical and Applied Mechanics, Russian Academy of Sciences, Novosibirsk, Russia, July 1996, Part 1, pp. 54–61.
- [66] Bedarev I, Zheltovodov A, Fedorova N. Supersonic Turbulent Flows Numerical Model Verification. In International Conference on Methods of Aerophysical Research, Institute of Theoretical and Applied Mechanics, Russian Academy of Sciences, Novosibirsk, Russia, July 1998, Part 1, pp. 30–35.
- [67] Kuehn D. Experimental Investigation of the Pressure Rise Required for Incipient Separation of Turbulent Boundary Layers in Two-Dimensional Supersonic Flow. NASA TM 1-21-59A, 1959.
- [68] Reda D, Murphy J. Shock Wave Turbulent Boundary Layer Interactions in Rectangular Channels. AIAA Paper No. 72-715, 1975.
- [69] Reda D, Murphy J. Shock Wave Turbulent Boundary Layer Interactions in Rectangular Channels, Part II: The Influence of Sidewall Boundary Layers on Incipient Separation and Scale of the Interaction. AIAA Paper 73-234, 1973.
- [70] Law C. Supersonic Shock Wave Turbulent Boundary Layer Interactions. AIAA Paper 75-832, 1975.

- [71] Kussoy D, Horstman C. An Experimental Documentation of a Hypersonic Shock Wave Turbulent Boundary Layer Interaction Flow - With and Without Separation. NASA TM X-62412, 1975.
- [72] Kussoy M, Horstman K. Documentation of Two- and Three-Dimensional Shock Wave Turbulent Boundary Layer Interaction Flows at Mach 8.2. NASA TM 103838, May 1991.
- [73] Zakharov N, Kutuzova A. Dimensions of the Interaction Regions of the Boundary Layer with Shock Waves. Trudi CIAM (Proceedings of CIAM) 1990; 1252:89–100 (in Russian).
- [74] Brazhko V. Periodical Structure of Flow and Heat Transfer in the Region of Attachment of Supersonic Flows. Uchenie Zapiski TSAGI (Scientific Notes of TsAGI) 1979; 10:113–118.
- [75] Rose W, Johnson D. Turbulence in a Shock Wave Boundary Layer Interaction. AIAA Journal 1975; 13(7):884–889.
- [76] Mikulla V, Horstman, C. Turbulence Measurements in Hypersonic Shock-Wave Boundary Layer Interaction Flows. AIAA Journal 1976; 14(5):568–575.
- [77] Modarress D, Johnson D. Investigation of Turbulent Boundary-Layer Separation Using Laser Velocimetry. AIAA Journal 1979; 17(7):747–752.
- [78] Meyer M, Buter T, Bowerson R. Compressible Turbulence Measurements in a Supersonic Boundary Layer with Impinging Shock Wave Interaction. AIAA Paper 97-0427, 1997.
- [79] Fedorova N, Fedorchenko I, Schülein E. Impinging Shock Wave/Flat Plate Turbulent Boundary Layer Interaction at $M = 5$ (Experiments and Computations). Proc. International Conference on the Methods of Aerophysical Research, Part I, Novosibirsk, Publishing House of Siberian Branch of Russian Academy of Sciences, 2000, pp. 71–78.
- [80] Lindbland I, Joganson A, Friedrich R, Lechner L, Krogmann P, Schülein E, Courty J.-C, Ravachol M, Giordano D. A Prediction Method for High Speed Turbulent Separated Flows with Experimental Verification. AIAA Paper 98-2547, 1998.
- [81] Rizzetta D. Evaluation of Explicit Algebraic Reynolds-Stress Models for Separated Supersonic Flows. AIAA Journal 1998; 36(1):24–30.

- [82] Hayashi M, Aso S, Tan A. Fluctuation of Heat Transfer in Shock Wave/Turbulent Boundary-Layer Interaction. *AIAA Journal* 1989; 27(4):399–404.
- [83] Brusniak L, Dolling D. Engineering Estimation of Fluctuating Loads in Shock Wave/Turbulent Boundary-Layer Interactions. *AIAA Journal* 1996; 34(12):2554–2561.
- [84] Holden M, Chadwick K. Studies of Film and Transpiration Cooled Flows in Regions of Shock Interaction. *AIAA Paper* 94-2306, 1994.
- [85] Urbin G, Knight D, Zheltovodov A. Compressible Large Eddy Simulation using Unstructured Grid: Supersonic Turbulent Boundary Layer and Compression Corner. *AIAA Paper* 99-0427, 1999.
- [86] Kannepalli C, Arunajatesan S, Dash S. RANS/LES Methodology for Supersonic Transverse Jet Interactions with Approach Flow. *AIAA Paper* 2002-1139, January 2002.
- [87] White F. *Viscous Fluid Flow*, McGraw-Hill, 1974, New York.
- [88] Boris J, Grinstein F, Oran E, Kolbe R. New Insights into Large Eddy Simulation. *Fluid Dynamics Research* 1992; 10:199–228.
- [89] Muck K, Spina E, Smits A. Compilation of Turbulence Data for an 8 degree Compression Corner at Mach 2.9. Report MAE-1642, Princeton University, Department of Mechanical and Aerospace Engineering, April 1984.
- [90] Adams N. Direct Numerical Simulation of Turbulent Supersonic Boundary Layer Flow. In *Advances in DNS and LES - First AFOSR International Conference on DNS and LES*, Greydon Press, Columbus, OH, 1997, pp. 29–40.
- [91] Adams N. Direct Numerical Simulation of Turbulent Compression Ramp Flow. *Theoretical and Computational Fluid Dynamics* 1998; 12(2):109–129.
- [92] Rizzetta D, Visbal M, Gaitonde D. Direct Numerical and Large Eddy Simulation of Supersonic Flows by a High-Order Method. *AIAA Paper* 2000-2408, January 2000.
- [93] Stolz S, Adams N, Kleiser L. The Approximate Deconvolution Model for Large-Eddy Simulation of Compressible Flows and Its Application to Shock Turbulent Boundary Layer Interaction. *Physics of Fluids* 2001; 13(10):2985–3001.
- [94] Germano M, Piomelli U, Moin P, Cabot W. A Dynamic Subgrid-Scale Eddy Viscosity Model. *Physics of Fluids A* 1991; 3(7):1760–1765.

- [95] VanDriest E. Turbulent Boundary Layers in Compressible Fluids, *Journal of the Aeronautical Sciences* 1951; 18(3):145–160.
- [96] Tennekes H, Lumley J. *A First Course in Turbulence*. The MIT Press, 1972, Cambridge, MA.
- [97] Rizzetta D, Visbal M. Large Eddy Simulation of Supersonic Compression Ramp Flows. *AIAA Paper* 2001-2858, June 2001.
- [98] Settles G, Fitzpatrick T, Bogdonoff S. Detailed Study of Attached and Separated Compression Corner Flowfields in High Reynolds Number Supersonic Flow. *AIAA Journal* 1979; 17(6):579–585.
- [99] Smits A, Muck K. Experimental Study of Three Shock Wave Turbulent Boundary Layer Interactions. *Journal of Fluid Mechanics* 1987; 182:291–314.
- [100] Borisov A, Zheltovodov A, Maksimov A, Fedorova N, Shpak S. Experimental and Numerical Study of Supersonic Turbulent Separated Flows in the Neighborhood of Two-Dimensional Obstacles. *Fluid Dynamics* 2000; 34(2):181–189.
- [101] Garnier E. *Simulation des Grandes Échelles en Régime Transsonique*. Le Grade de Docteur en Sciences de l'Université Paris XI Orsay, 27 October 2000.
- [102] Garnier E. Large Eddy Simulation of Shock Boundary Layer Interaction. In *Third AFOSR International Conference on DNS and LES*, Arlington, TX, August 2001.
- [103] Deleuze J. *Structure d'une couche limite turbulente soumise à une de choc incidente*. Thèse de doctorat, Université Aix-Marseille II, 1995.
- [104] Laurent H. *Turbulence d'une interaction onde de choc / couche limite sur une paroi adiabatique ou chauffée*. Thèse de Doctorat, Université Aix-Marseille II, 1996.
- [105] Sagaut P. *Large Eddy Simulation for Incompressible Flows*. Springer-Verlag, Berlin, 2001.
- [106] Lenormand E, Sagaut P, Ta Phuoc L, Comte P. Subgrid-scale Models for Large-Eddy Simulation of Compressible Wall Bounded Flows. *AIAA Journal* 2000; 38(8):1340–1350.
- [107] Lenormand E, Sagaut P, Ta Phuoc L. Large Eddy Simulation of Subsonic and Supersonic Channel Flow at Moderate Reynolds Number. *International Journal for Numerical Methods in Fluids* 2000; 32:369–406.

- [108] Dawson J, Samimy M, Arnette S. Effects of Expansions on Supersonic Boundary Layer: Surface Pressure Measurements. *AIAA Journal* 1994; 32(11):2169–2177.
- [109] Arnette S, Samimy M, Elliott G. The Effects of Expansion on the Turbulence Structure of a Compressible Boundary Layer. *Journal of Fluid Mechanics* 1998; 367:67–105.
- [110] Morkovin, M. Effects of High Acceleration on a Turbulent Supersonic Shear Layer. *Proceedings of the Heat Transfer and Fluid Mechanics Institute, Stanford University*, 1955.
- [111] Thomann H. Effect of Streamwise Wall Curvature on Heat Transfer in a Turbulent Boundary Layer. *Journal of Fluid Mechanics*, 1968; 33:283–292.
- [112] Lewis J, Gran R, Kubota T. An Experiment on the Adiabatic Compressible Turbulent Boundary Layer in Adverse and Favorable Pressure Gradients. *Journal of Fluid Mechanics* 1972; 51(4):657–672.
- [113] Alber I, Coats D. Analytical Investigation of Equilibrium and Non-Equilibrium Compressible Turbulent Boundary Layers. *AIAA Paper 69-689*, 1969.
- [114] Narasimha R, Sreenivasan K. Relaminarization in Highly Accelerated Turbulent Boundary Layers. *Journal of Fluid Mechanics* 1973; 61:417–447.
- [115] So R, Mellor G. An Experimental Investigation of Turbulent Boundary Layers along Curved Surfaces. *NASA CR-1940*, 1972.
- [116] So R, Mellor G. Experiment on Convex Curvature Effects in Turbulent Boundary layers. *Journal of Fluid Mechanics* 1973; 60:43–62.
- [117] Gillis J, Johnston J, Kays W, Moffatt, R. Turbulent Boundary Layer on a Convex, Curved Surface. Report HMT-31, Thermosciences Division, Stanford University, 1980.
- [118] Gillis J, Johnston J. Turbulent Boundary-Layer Flow and Structure on a Convex Wall and Its Redevelopment on a Flat Wall. *Journal of Fluid Mechanics*, 1983; 135:123–153.
- [119] Smits A, Young S, Bradshaw P. The Effect of Short Regions of High Surface Curvature on Turbulent Boundary Layers. *Journal of Fluid Mechanics* 1979; 94:209–242.
- [120] Dussauge J, Gaviglio J. Bulk Dilatation Effects on Reynolds Stress in the Rapid Expansion of a Turbulent boundary layer at Supersonic Speed. In *Proceedings of the Symposium on Turbulent Shear Flows*, Vol. 2, 1981, pp. 33–38.

- [121] Morkovin M. Effects of Compressibility on Turbulent Flows. *Mecanique de la Turbulence*, CNRS, Paris, 1962.
- [122] Dussauge J, Gaviglio J. The Rapid Expansion of a Supersonic Turbulent Flow: Role of Bulk Dilatation. *Journal of Fluid Mechanics* 1987; 174:81–112.
- [123] Smith D, Smits A. The Rapid Expansion of a Turbulent Boundary Layer in a Supersonic Flow. *Theoretical and Computational Fluid Dynamics* 1991; 2:319–328.
- [124] Adamson T. Effect of Transport Properties on Supersonic Expansion Around a Corner. *Physics of Fluids* 1967; 10(5):953–962.
- [125] Arnette S, Samimy M, Elliott G. The Effect of Expansion on the Large Scale Structure of a Compressible Turbulent Boundary Layer. *AIAA Paper 93-2991*, 1993.
- [126] Page R, Sernas V. Apparent Reverse Transition in an Expansion Fan. *AIAA Journal* 1970; 8:189–190.
- [127] Zakkay V, Toba K, Kuo T. Laminar Transitional and Turbulent Heat Transfer after a Sharp Convex Corner. *AIAA Journal* 1964; 2:1389–1395.
- [128] Goldfeld M, Tyutina E. Relaminarization of a Turbulent Boundary Layer during Rapid Expansion Near a Corner Point. Preprint No. 12-82, Institute of Theoretical and Applied Mechanics, USSR Academy of Sciences, 1982.
- [129] Narasimha R, Viswanath P. Reverse Transition at an Expansion Corner in Supersonic Flow. *AIAA Journal* 1975; 13(5):693–695.
- [130] Arnette S, Samimy M, Elliott G. Structure of Supersonic Turbulent Boundary Layer After Expansion Regions. *AIAA Journal* 1995; 33(3):430–437.
- [131] Bradshaw P. Effects of Streamline Curvature on Turbulent Flow, AGARD AG-169, 1973.
- [132] Lu F, Chung K. Downstream Influence Scaling of Turbulent Flow Past Expansion Corners. *AIAA Journal* 1992; 30(12):2976–2977.
- [133] Chung K, Lu F. Damping of Surface Pressure Fluctuations in Hypersonic Turbulent Flow Past Expansion Corners. *AIAA Journal* 1993; 31(7):1229–1234.
- [134] Chung K. Interaction Region of Turbulent Expansion-Corner Flow. *AIAA Journal* 1998; 36(6):1115–1116.

- [135] Narasimha R, Sreenivasan K. Relaminarization of Fluids Flow. *Advances in Applied Mechanics* 1979; 19:221–309.
- [136] Zheltovodov A, Mecler L, Schülein E. Peculiarities of Development of Separated Flows in Compression Corners After the Expansion Fans. Preprint No. 10-87, Institute of Theoretical and Applied Mechanics, USSR Academy of Sciences, Novosibirsk, 1987, 47 pp. (in Russian).
- [137] Borisov A, Zheltovodov A, Pavlov A, Fedorova N, Shpak S. Experimental and Numerical Studies of Supersonic Turbulent Separation Flows. In *Mathematical Modeling, Aerodynamics and Gasdynamics*, Fomin V (Ed), Novosibirsk, 1995, pp. 107–120 (in Russian).
- [138] Zheltovodov A, Horstman C. Experimental and Numerical Investigation of 2-D Expansion/Shock Wave - Turbulent Boundary Layer Interactions. Preprint No. 2-93, Institute of Theoretical and Applied Mechanics, Russian Academy of Sciences, Novosibirsk, 1993, 25 pp.
- [139] Knight D, Yan H, Zheltovodov A. Large Eddy Simulation of Supersonic Turbulent Flow in Expansion-Compression Corner. In *Third AFOSR International Conference on DNS and LES*, Arlington, TX, Aug 2001.
- [140] Panaras A. Review of the Physics of Swept-Shock / Boundary Layer Interactions. *Progress in Aerospace Sciences* 1996; 32:173–244.
- [141] Settles G, Dolling D. Swept Shock Wave Boundary Layer Interactions. In *Tactical Missile Aerodynamics*, AIAA Progress in Aeronautics and Astronautics, Nielson J (Ed), 1986, pp. 297–379.
- [142] Settles G, Dolling G. Swept Shock Boundary Layer Interactions - Tutorial and Update. AIAA Paper 90-0375, 1990.
- [143] Zheltovodov A, Schülein E. 'Three Dimensional Interaction of Swept Shock Waves with Turbulent Boundary Layer in Corner Configurations. Institute of Theoretical and Applied Mechanics Preprint 34-86, USSR Academy of Sciences, Novosibirsk, 1986, 49 pp. (in Russian).
- [144] Bogdonoff S. Flowfield Modeling of a Three-Dimensional Shock Wave Turbulent Boundary Layer Interaction. In *Separated Flows and Jets*, Kozlov V, Dovgal, A (Eds), IUTAM Symposium Novosibirsk/USSR 1990, Springer-Verlag, Berlin, 1991, pp. 279–302.

- [145] Token K. Heat Transfer Due to Shock Wave / Turbulent Boundary Layer Interactions on High Speed Weapon Systems. AFFDL TR-74-77, 1974.
- [146] Kubota H, Stollery J. An Experimental Study of the Interaction Between a Glancing Shock Wave and a Turbulent Boundary Layer. *Journal of Fluid Mechanics* 1982; 116:431–458.
- [147] Zubin M, Ostapenko N. Structure of the Flow in the Region of Separation for the Interaction of a Normal Shock Wave with a Boundary Layer. *Izvestiya AN SSSR, Mekhanika Zhidkosti i Gasa* 1979; 3:42–50 (in Russian).
- [148] Alvi F, Settles G. Structure of Swept Shock Wave / Boundary Layer Interactions Using Conical Shadowgraphy. AIAA Paper 90-1644, 1990.
- [149] Alvi F, Settles G. A Physical Model of the Swept Shock / Boundary Layer Interaction Flowfield. AIAA Paper 91-1768, 1991.
- [150] Panaras A. Numerical Investigation of the High Speed Conical Flow Past a Sharp Fin. *Journal of Fluid Mechanics* 1992; 236:607–633.
- [151] Baldwin B, Lomax H. Thin Layer Approximation and Algebraic Model for Separated Turbulent Flows. AIAA Paper 78-257, 1978.
- [152] Zheltovodov A. Three Dimensional Interaction of Shock Wave Generated by the Fin-Type Obstacle with Turbulent Boundary Layer. *Fizicheskaya Gazodinamika* (Physical Gas Dynamics) 1976; 6:125–129 (in Russian). Institute of Theoretical and Applied Mechanics, Novosibirsk.
- [153] Zheltovodov A. Physical Features and Properties of Two- and Three-Dimensional Separated Flows at Supersonic Velocities. *Fluid Dynamics* 1979; 3:42–50.
- [154] Zheltovodov A. Regimes and Properties of Three-Dimensional Separation Flows Initiated by Skewed Compression Shocks. *Journal of Applied Mechanics and Technical Physics* 1982; 23(3):413–418.
- [155] Panaras A, Stanewsky E. Numerical Study of Secondary Separation in Glancing Shock / Turbulent Boundary Layer Interactions. AIAA Paper 92-3666, 1992.
- [156] Zheltovodov A, Maksimov A, Schüle E. Development of Turbulent Separated Flows in the Vicinity of Swept Shock Waves. In *The Interactions of Complex 3-D Flows*, Kharitonov A (Ed), Institute of Theoretical and Applied Mechanics, Siberian Branch of the USSR Academy of Sciences, Novosibirsk, 1987, pp. 67–91.

- [157] Knight D. Numerical Simulation of 3-D Shock Wave Turbulent Boundary Layer Interactions. AGARD-R-792, Paper 3, 1993.
- [158] Kim K, Lee Y, Alvi F, Settles G, Horstman C. Skin Friction Measurements and Computational Comparison of Swept Shock Boundary Layer Interactions AIAA Journal 1991; 29(10):1643–1650.
- [159] Panaras A. Algebraic Turbulence Modelling for Swept Shock Wave / Turbulent Boundary Layer Interactions. AIAA Journal 1997; 35(3):456–463.
- [160] Panaras A. Calculation of Flows Characterized by Extensive Cross Flow Separation. Paper 47, Fourth European Symposium on Aerothermodynamics for Space Vehicles, Capua Italy, 15-18 October 2001, ESA SP-487.
- [161] Thivet F, Knight D, Zheltovodov A, Maksimov A. Importance of Limiting the Turbulence Stresses to Predict 3D Shock Wave Boundary Layer Interactions. 23rd International Symposium on Shock Waves, Ft. Worth, TX, July 2001.
- [162] Durbin P. On the $k-\epsilon$ Stagnation Point Anomaly. International Journal of Heat and Fluid Flow 1996; 17(1):89–90.
- [163] Wilcox D. Turbulence Modeling for CFD. DCW Industries, Inc, La Canada, CA, 1993.
- [164] Thivet F, Knight D, Zheltovodov A, Maksimov A. Insights in Turbulence Modeling for Crossing Shock Wave Turbulent Boundary Layer Interactions. AIAA Journal 2001; 39(6):985–995.
- [165] Aerosoft, Inc, General Aerodynamic Simulation Program Version 3 User's Manual. Aerosoft, Inc, Blacksburg, VA, 1996.
- [166] Settles, G, Private Communication.
- [167] Mee D, Stalker R, Stollery J. Glancing Interaction Between Single and Intersecting Oblique Shock Waves and a Turbulent Boundary Layer. Journal of Fluid Mechanics 1986; 170:411–433.
- [168] Batcho P, Ketchum A, Bogdonoff S, Fernando E. Preliminary Study of the Interactions Caused by Crossing Shock Waves and a Turbulent Boundary Layer. AIAA Paper No. 89-0359, 1989.
- [169] Poddar K, Bogdonoff S. A Study of Unsteadiness of Crossing Shock Wave Turbulent Boundary Layer Interactions. AIAA Paper 90-1456, 1990.

- [170] Narayanswami N, Knight D, Bogdonoff S, Horstman C. Crossing Shock Wave / Turbulent Boundary Layer Interactions. AIAA Paper 91-0649, 1991.
- [171] Bogdonoff S, Stokes W. Crossing Shock Wave Turbulent Boundary Layer Interactions: Variable Angle and Shock Generator Length Geometry Effects at Mach 3. AIAA Paper 92-0636, 1992.
- [172] Davis D, Hingst W. Surface and Flow Measurements in a Symmetric Crossing Shock Waves / Turbulent Boundary Layer Interaction. AIAA Paper 92-2634, 1992.
- [173] Garrison T, Settles G. Flowfield Visualization of Crossing Shock Wave / Boundary Layer Interactions. AIAA Paper 92-0750, 1992.
- [174] Garrison T, Settles G, Narayanswami N, Knight D. Interaction Strength and Model Geometry Effects on the Structure of Crossing Shock Wave / Turbulent Boundary Layer Interactions. AIAA Paper 92-3670, 1992.
- [175] Narayanswami N, Knight D, Bogdonoff S, Horstman C. Interaction Between Crossing Oblique Shocks and Turbulent Boundary Layer. AIAA Journal 1992; 30(8):1945–1952.
- [176] Gaitonde D, Shang J. Calculation on a Double Fin Turbulent Boundary Layer Interaction. AIAA Paper No. 93-3432, 1993.
- [177] Garrison T, Settles G, Narayanswami N, Knight D. Structure of Crossing Shock Wave Turbulent Boundary Layer Interactions. AIAA Journal 1993; 31(12):2204–2211.
- [178] Garrison T, Settles G. Interaction Strength and Model Geometry Effects on the Structure of Crossing Shock Wave / Turbulent Boundary Layer Interactions. AIAA Paper 93-0780, 1993.
- [179] Kussoy M, Horstman K. Intersecting Shock Wave / Turbulent Boundary Layer Interactions at Mach 8.3. NASA TM 103909, 1993, 46 pg.
- [180] Kussoy M, Horstman K, Horstman C. Hypersonic Crossing Shock Wave / Turbulent Boundary Layer Interactions. AIAA Journal 1993; 31(12):2197–2203.
- [181] Narayanswami N, Horstman C, Knight D. Numerical Simulation of Crossing Shock / Turbulent Boundary Layer Interaction at Mach 8.3: Comparison of Zero- and Two-Equation Turbulence Models. AIAA Paper 93-0779, 1993.
- [182] Narayanswami N, Horstman C, Knight D. Computation of Crossing Shock / Turbulent Boundary Layer Interaction at Mach 8.3. AIAA Journal 1993; 31(8):1369–1376.

- [183] Bardina J, Coakley T. Three-Dimensional Navier-Stokes Simulations with Two-Equation Turbulence Models of Intersecting Shock Waves / Turbulent Boundary Layer at $M = 8.3$. AIAA Paper 94-1905, 1994.
- [184] Garrison T, Settles G, Narayanswami N, Knight D. Laser Interferometer Skin Friction Measurements of Crossing Shock Wave Turbulent Boundary Layer Interactions. AIAA Journal 1994; 32(6):1234–1241.
- [185] Garrison T. The Interactions Between Crossing Shock Waves and a Turbulent Boundary Layer. Ph.D. Thesis, Dept. of Mechanical Engineering, Pennsylvania State Univ, PA, 1994, 175 pp.
- [186] Garrison T, Settles G, Narayanswami N, Knight D, Horstman C. Comparison of Flow-field Surveys and Computations of a Crossing Shock Wave / Boundary Layer Interaction. AIAA Paper 94-2273, 1994.
- [187] Zheltovodov A, Maksimov A, Shevchenko A, Vorontsov S, Knight D. Experimental Study and Computational Comparison of Crossing Shock Wave Turbulent Boundary Layer Interactions. In International Conference on Methods of Aerophysical Research, Institute of Theoretical and Applied Mechanics, Siberian Branch of Russian Academy of Sciences, Novosibirsk, 1994, pp. 221–230.
- [188] Gaitonde D, Shang J, Visbal M. Structure of a Double Fin Turbulent Interaction at High Speed. AIAA Journal 1995; 33(2):193–200.
- [189] Gaitonde D, Shang J. Structure of a Double Fin Turbulent Interaction at Mach 4. AIAA Journal 1995; 33(12):2250–2258.
- [190] Gaitonde D, Shang J. On 3-D Shock Wave / Turbulent Boundary Layer Interactions at Mach 4. AIAA Paper No. 96-0043, 1996.
- [191] Smith B. Prediction of Hypersonic Shock Wave / Turbulent Boundary Layer Interactions. Journal of Spacecraft and Rockets 1996; 33(5):614–619.
- [192] Gaitonde D, Shang J, Garrison T, Zheltovodov A, Maksimov A. Evolution of the Separated Flowfield in a 3-D Shock Wave/Turbulent Boundary Layer Interaction. AIAA Paper 97-1837, 1997.
- [193] Gaitonde D, Visbal M, Shang J, Zheltovodov A, Maksimov A. Parametric Investigation of Flowfield Structure and Validation Issues in 3-D Crossing-Shock Wave/Turbulent Boundary Layer Interactions. In Proceedings of the International Conference on the Methods of Aerophysical Research, Part 1, Novosibirsk, 1998, pp. 67–76.

- [194] Zheltovodov A, Maksimov A, Shevchenko A. Topology of Three Dimensional Separation Under the Conditions of the Symmetric Interaction of Crossing Shocks and Expansion Waves with Turbulent Boundary Layers. *Thermophysics and Aeromechanics* 1998; 5(3):293–312.
- [195] Schülein E, Zheltovodov A. Development of Experimental Methods for the Hypersonic Flow Studies in Ludweig Tube. In *Proceedings of the International Conference on the Methods of Aerophysical Research: Part 1*, Institute of Theoretical and Applied Mechanics, Novosibirsk, Russia, 1998, pp. 191–199.
- [196] Zheltovodov A, Maksimov A. Symmetric and Asymmetric Crossing-Shock-Waves/Turbulent Boundary Layer Interactions. Final Technical Report, EOARD Contract F61708-97-W0136, Institute of Theoretical and Applied Mechanics, Siberian Branch of Russian Academy of Sciences, Novosibirsk, 1998, 76 pp.
- [197] Gaitonde D, Shang J, Garrison T, Zheltovodov A, Maksimov A. Three-Dimensional Turbulent Interactions Caused by Asymmetric Crossing-Shock Configurations. *AIAA Journal* 1999; 37(12):1602–1608.
- [198] Zheltovodov A, Maksimov A. Hypersonic Crossing Shock Waves Turbulent Boundary Layer Interactions. Final Technical Report, EOARD Contract F61775-98-W091, Russian Academy of Sciences, Novosibirsk, Russia, 1999.
- [199] Knight D, Gnedin M, Becht R, Zheltovodov A. Numerical Simulation of Crossing-Shock-Wave/Turbulent Boundary-Layer Interaction Using a Two-Equation Model of Turbulence. *Journal of Fluid Mechanics* 2000; 409:121–147.
- [200] Schmisser J, Gaitonde D. Numerical Investigation of New Topologies in Strong Crossing Shock Wave Turbulent Boundary Layer Interaction. *AIAA Paper* 2000-0931, 2000.
- [201] Schmisser J, Gaitonde D, Zheltovodov A. Exploration of 3-D Shock Turbulent Boundary Layer Interactions Through Combined Experimental/Computational Analysis. *AIAA Paper No.* 2000-2378, 2000.
- [202] Thivet F, Knight D, Zheltovodov A, Maksimov A. Some Insights in Turbulence Modeling for Crossing-Shock-Wave/Boundary-Layer Interactions. *AIAA Paper No.* 2000-0131, 2000.
- [203] Thivet F, Knight D, Zheltovodov A. Computation of Crossing-Shock-Wave / Boundary Layer Interaction with Realizable Two-Equation Turbulence Models. In *Proceedings*

- of the International Conference on the Methods of Aerophysical Research, Part 1, Novosibirsk, 2000, pp. 195–201.
- [204] Thivet F, Knight D, Zheltovodov A, Maksimov A. Numerical Prediction of Heat Transfer in Supersonic Inlets. European Congress on Computational Methods in Applied Sciences and Engineering, ECCOMAS, Sept. 2000.
- [205] Zheltovodov A, Maksimov A, Schülein E, Gaitonde D, Schmisser J. Verification of Crossing-Shock-Wave / Boundary Layer Interaction Computations with the $k-\epsilon$ Turbulence Model. In Proceedings of the International Conference on the Methods of Aerophysical Research, Part 1, Novosibirsk, 2000, pp. 231–241.
- [206] Zheltovodov A, Maksimov A, Gaitonde D, Visbal M, Shang J. Experimental and Numerical Study of Symmetric Interaction of Crossing Shocks and Expansion Waves with a Turbulent Boundary Layer. *Thermophysics and Aeromechanics* 2000; 7(2):155–171.
- [207] Schülein E, Zheltovodov A. Documentation of Experimental Data for Hypersonic 3-D Shock Waves / Turbulent Boundary Layer Separation. DLR IB 223-99 A 26, Göttingen, 2001, 95 pp.
- [208] Zheltovodov A, Maksimov A, Schülein E, Knight D, Thivet F, Gaitonde D, Schmisser J. Experimental and Computational Studies of Crossing-Shock-Wave/Turbulent Boundary-Layer Interactions. In in Proceedings of the International Conference on Recent Developments in Applied Mathematics and Mechanics: Theory, Experiment, and Practice – Devoted to N. N. Yanenko's 80th Anniversary, Computational Technologies, Special Issue on CDROM, ISSN 1560-7534, Editor-in Chief Academician Y. Shokin, Vol. 6, Part 2, 2001, 10 pp.
- [209] Thivet F, Knight D, Zheltovodov A, Maksimov A. Analysis of Observed and Computed Crossing Shock Wave / Turbulent Boundary Layer Interactions. *Aerospace Science and Technology* 2002; 6(1):3–17.
- [210] Bardina J, Coakley T. The Structure of Intersecting Shock Waves / Turbulent Boundary Layer Interaction Flow. AIAA Paper 95-2215, 1995.
- [211] Knight D, Garrison T, Settles G, Zheltovodov A, Maksimov A, Shevchenko A, Vorontsov S. Asymmetric Crossing Shock Wave / Turbulent Boundary Layer Interaction. *AIAA Journal* 1995; 33(12):2241–2249.

- [212] Knight D, Garrison T, Settles G, Zheltovodov A, Maksimov A, Shevchenko A, Vorontsov S. Asymmetric Crossing Shock Wave / Turbulent Boundary Layer Interaction. AIAA Paper No. 95-0231, 1995.
- [213] Gnedin M, Knight D, Zheltovodov A, Maksimov A, Shevchenko A, Vorontsov S. 3-D Crossing Shock Wave / Turbulent Boundary Layer Interaction. AIAA Paper 96-2001, 1996.
- [214] Gnedin M, Zha G, Knight D, Zheltovodov A, Maksimov A, Shevchenko A, Vorontsov S. 3-D Crossing Shock Wave / Turbulent Boundary Layer Interaction. In Proceedings of the International Conference on the Methods of Aerophysical Research, September 2- 6, 1996, Novosibirsk, Russia. Novosibirsk, 1996, Part 1, pp. 114–122.
- [215] Zha G, Knight D. Computation of 3-D Asymmetric Crossing Shock Wave / Turbulent Boundary Layer Interaction Using a Full Reynolds Stress Equation Turbulence Model. AIAA Paper 96-0040, 1996.
- [216] Zheltovodov A, Maksimov A, Shevchenko A, Knight D. Topology of Three Dimensional Separation Under the Conditions of Asymmetric Interaction of Crossing Shocks and Expansion Waves with Turbulent Boundary Layer. Thermophysics and Aeromechanics 1998; 5(4):483–503.
- [217] Dolling D. Unsteady Phenomena in Shock Wave Turbulent Boundary Layer Interactions. In Turbulent Boundary-Layer Interactions in Supersonic and Hypersonic Flows, Advisory Group for Aerospace Research and Development, Report No. 792, 1993, pp. 4-1 to 4-46.
- [218] Gaitonde D, Visbal M, Shang J, Zheltovodov A, Maksimov A. Sidewall Interaction in an Asymmetric Simulated Scramjet Inlet Configuration. Journal of Propulsion and Power 2001; 17(3):579–584.
- [219] Garrison T, Settles G, Horstman C. Measurements and Computation of the Triple Shock Wave / Turbulent Boundary Layer Interaction. AIAA Paper 94-2274, 1994.
- [220] Jones W, Launder B. The Prediction of Laminarization with a Two-Equation Model of Turbulence. International Journal of Heat and Mass Transfer 1972; 15:301–314.
- [221] Launder B, Sharma B. Application of the Energy Dissipation Model of Turbulence to the Calculation of Flows Near a Spinning Disk. Letters in Heat and Mass Transfer 1974; 1:131–138.

- [222] Shumann U. Realizability of Reynolds Stress Turbulence Models. *Physics of Fluids* 1977; 20(5):721–725.
- [223] Coakley T, Huang, P. Turbulence Modeling for High Speed Flows. AIAA Paper 92-0436, 1992.
- [224] Zeman O. Dilatation Dissipation: The Concept and Application in Modeling Compressible Mixing Layers. *Physics of Fluids* 1990; 2(2):178–188.
- [225] Sarkar S, Erlebacher G, Hussaini M, Kreiss O. The Analysis and Modeling of Dilational Terms in Compressible Turbulence. *Journal of Fluid Mechanics* 1991; 227:473–493.
- [226] Aupoix B, Desmet E, Viala S. Hypersonic Turbulent Boundary Layer Modeling. *Transitional and Turbulent Compressible Flows*, Kral L, Zang T (Eds), FED Vol. 151, American Society of Mechanical Engineers, 1993, pp. 175–182.
- [227] Panaras, A, Private Communication, September 2001.
- [228] Zheltovodov A, Maksimov A. Hypersonic Crossing Shock Waves Turbulent Boundary Layer Interactions. Final Technical Report, EOARD Contract F61775-98-WE091, Russian Academy of Sciences, Novosibirsk, Russia, 1999.

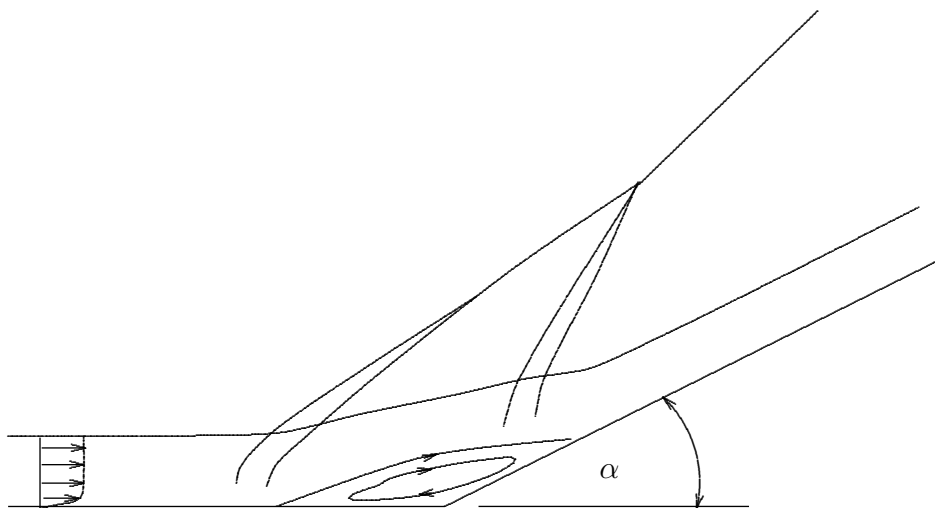


Figure 1: 2-D compression corner

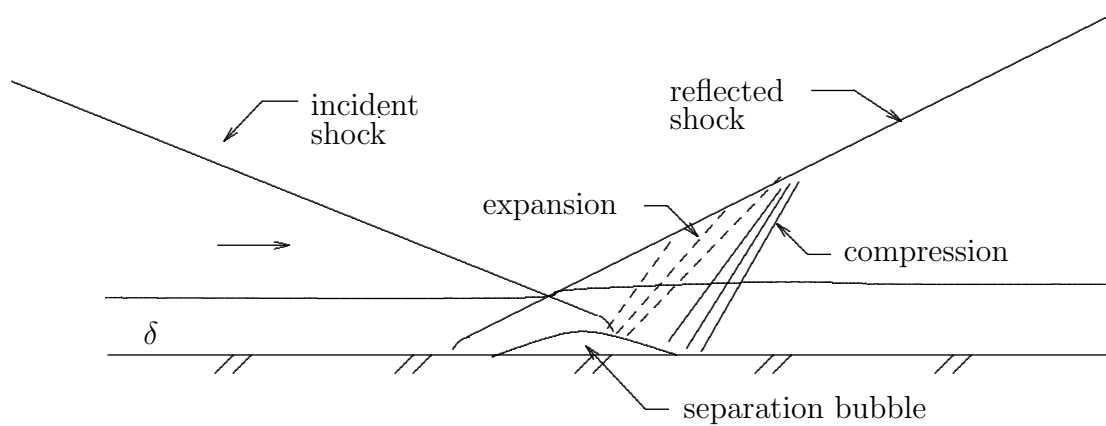


Figure 2: 2-D shock impingement

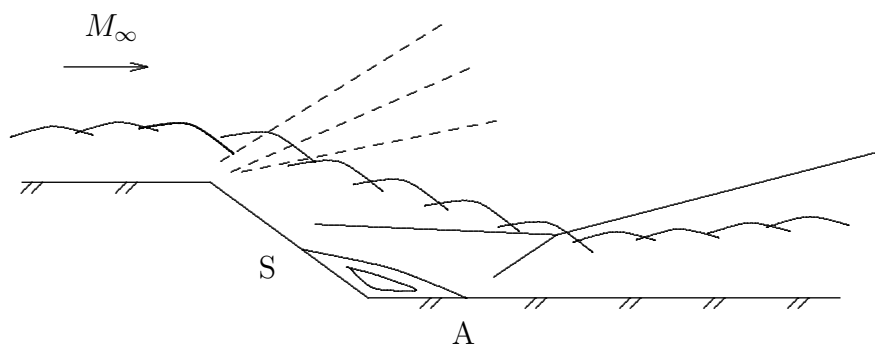


Figure 3: 2-D expansion-compression corner

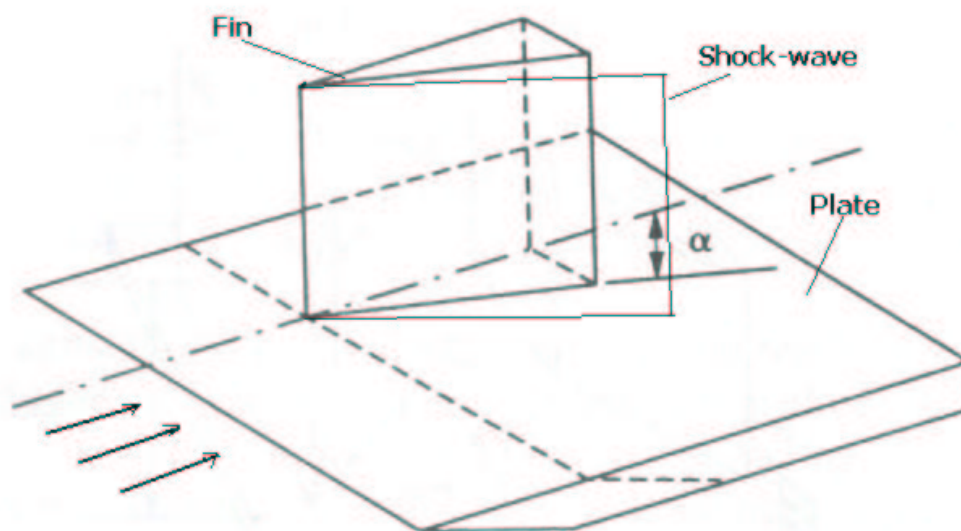


Figure 4: 3-D single fin

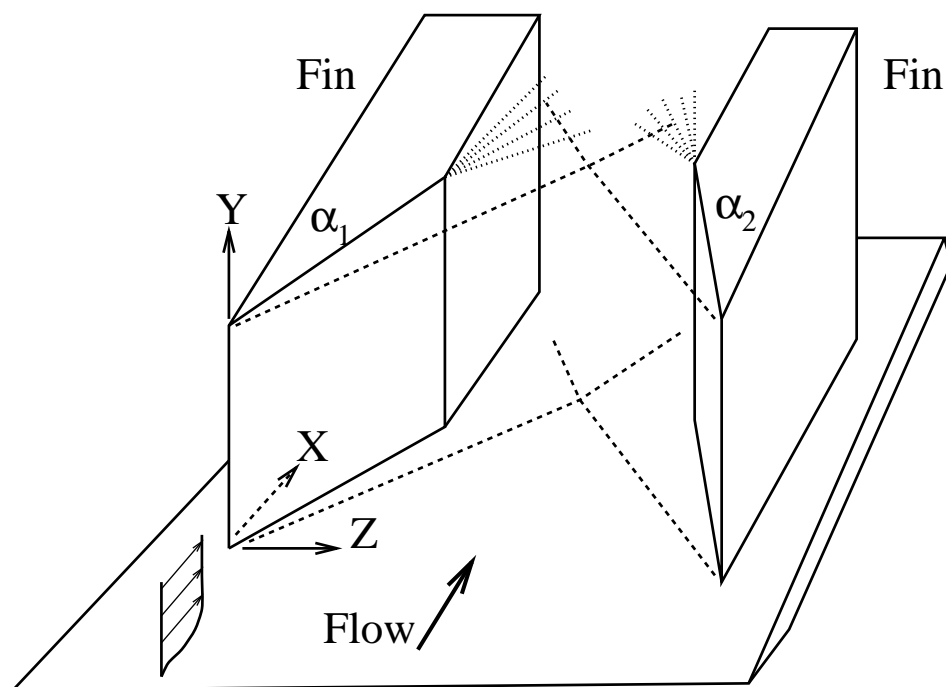


Figure 5: 3-D double fin

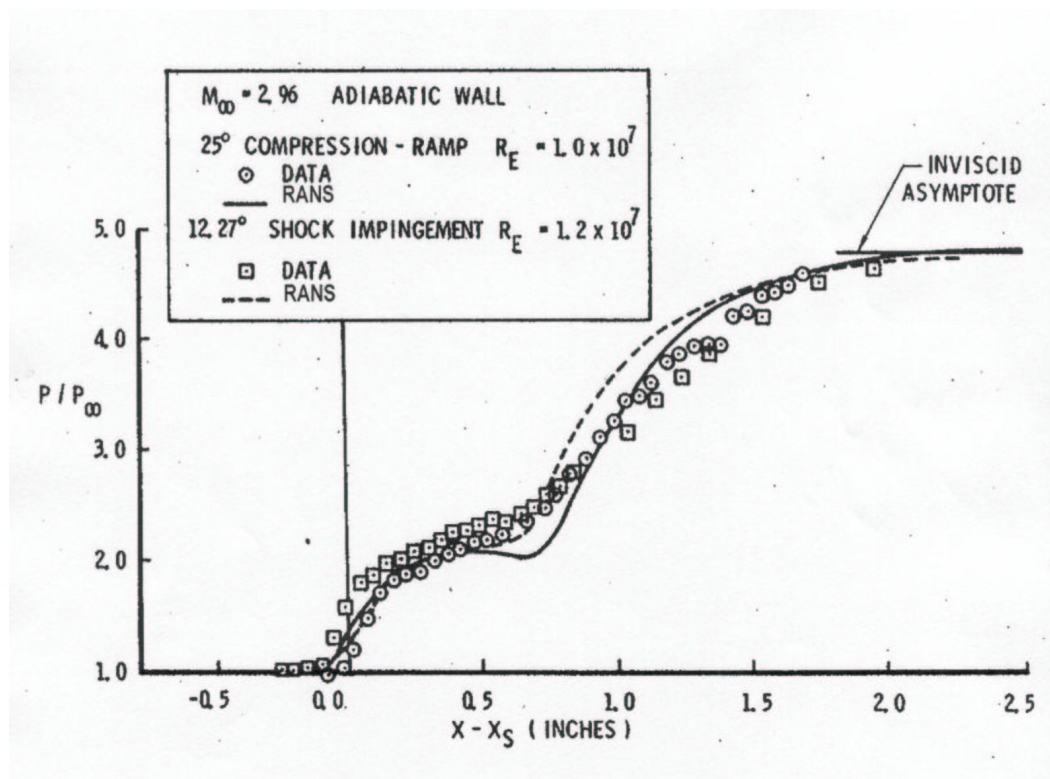


Figure 6: Surface pressure for 2-D compression corner and shock impingement at $M_\infty = 2.96$ and $\alpha = 25^\circ$ [19]

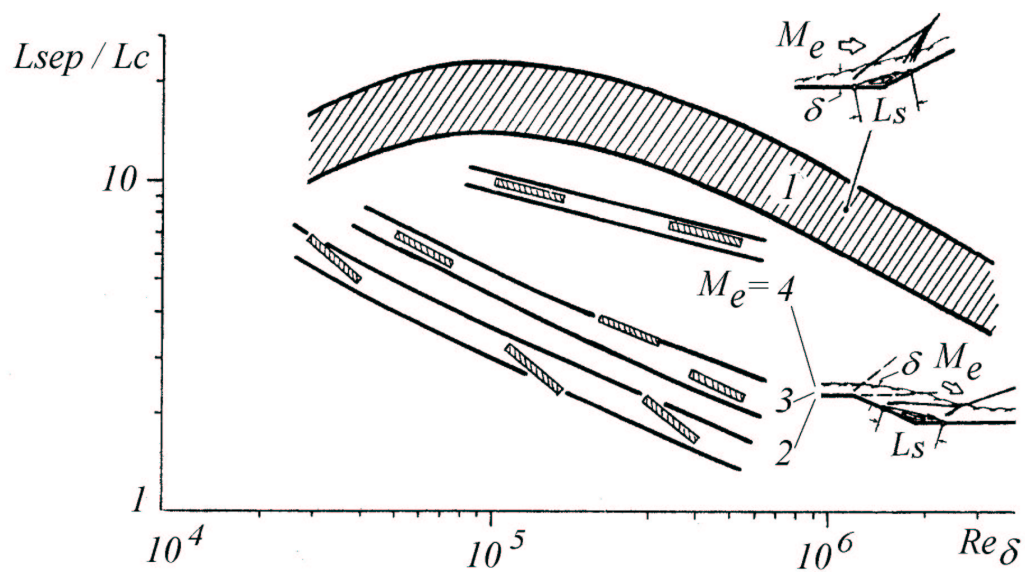


Figure 7: Separation length *vs* Re_δ [24]

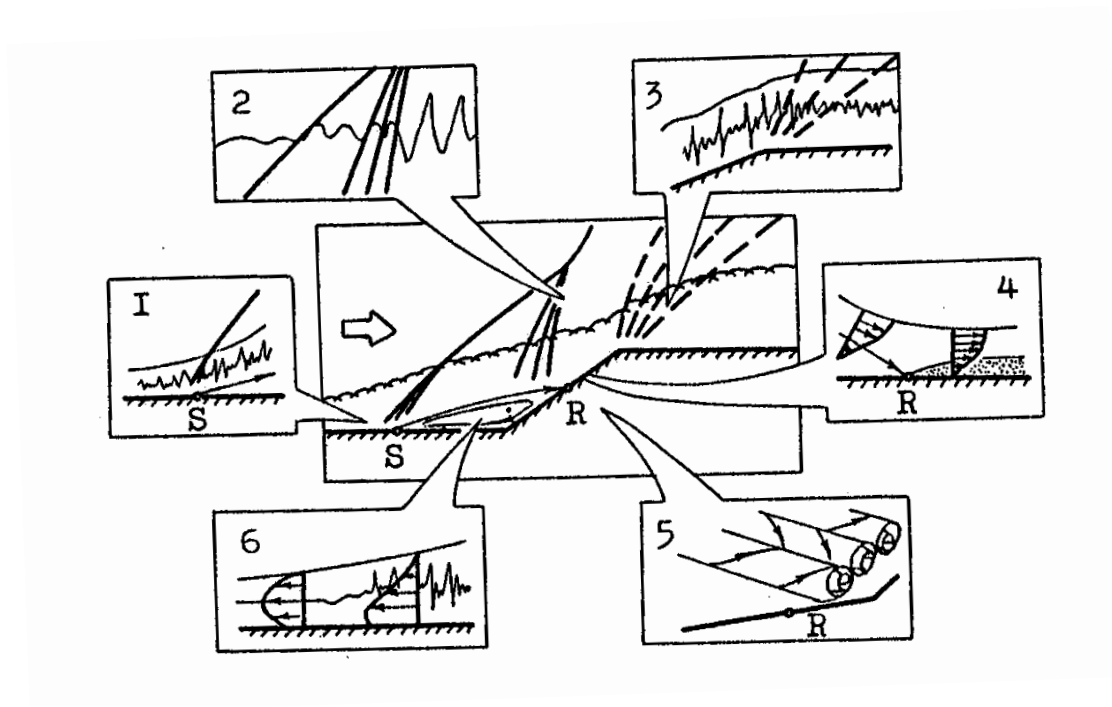


Figure 8: Turbulence structure in 2D compression corner

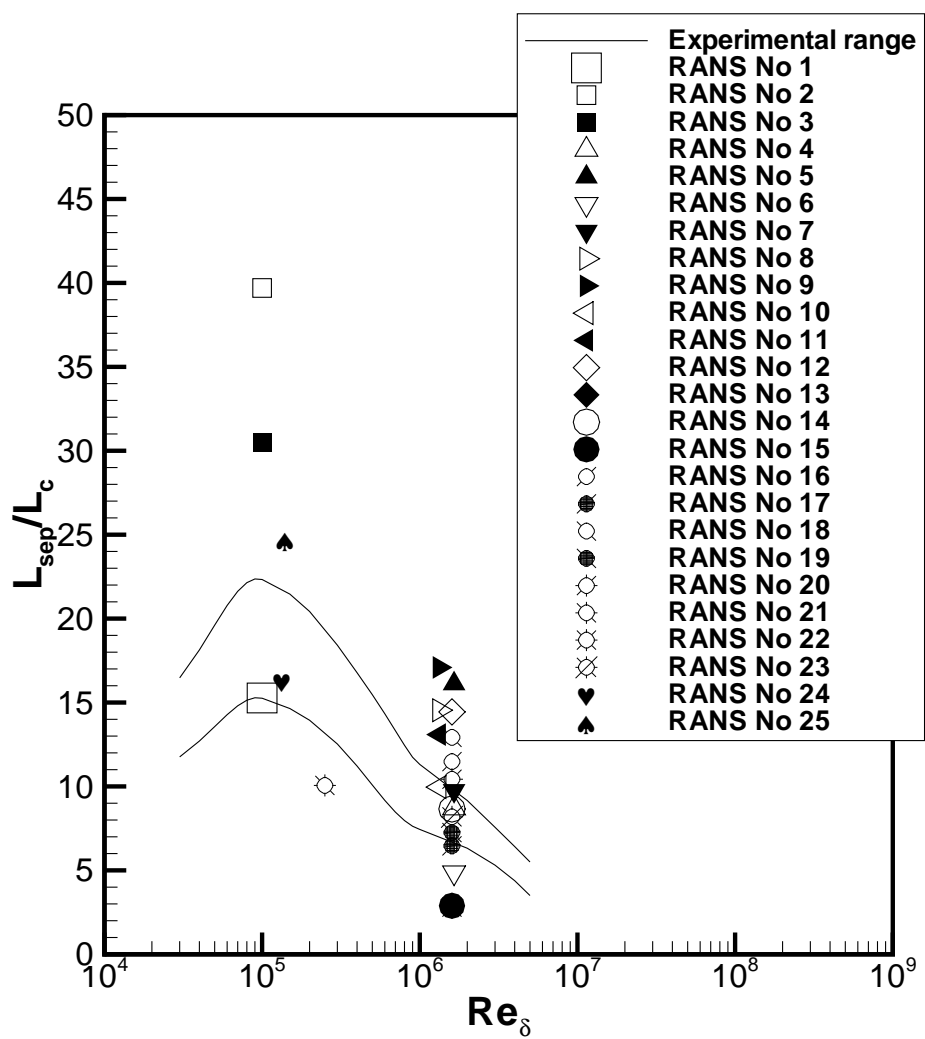


Figure 9: Separation length for RANS

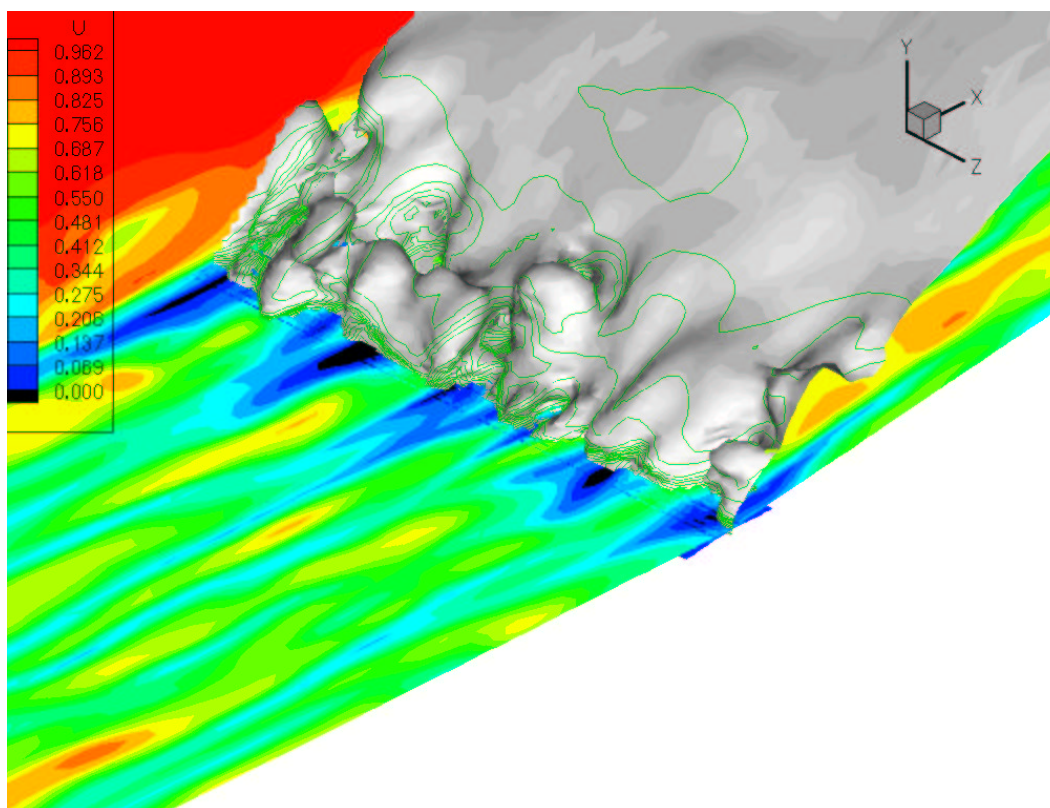


Figure 10: Instantaneous velocity and shock

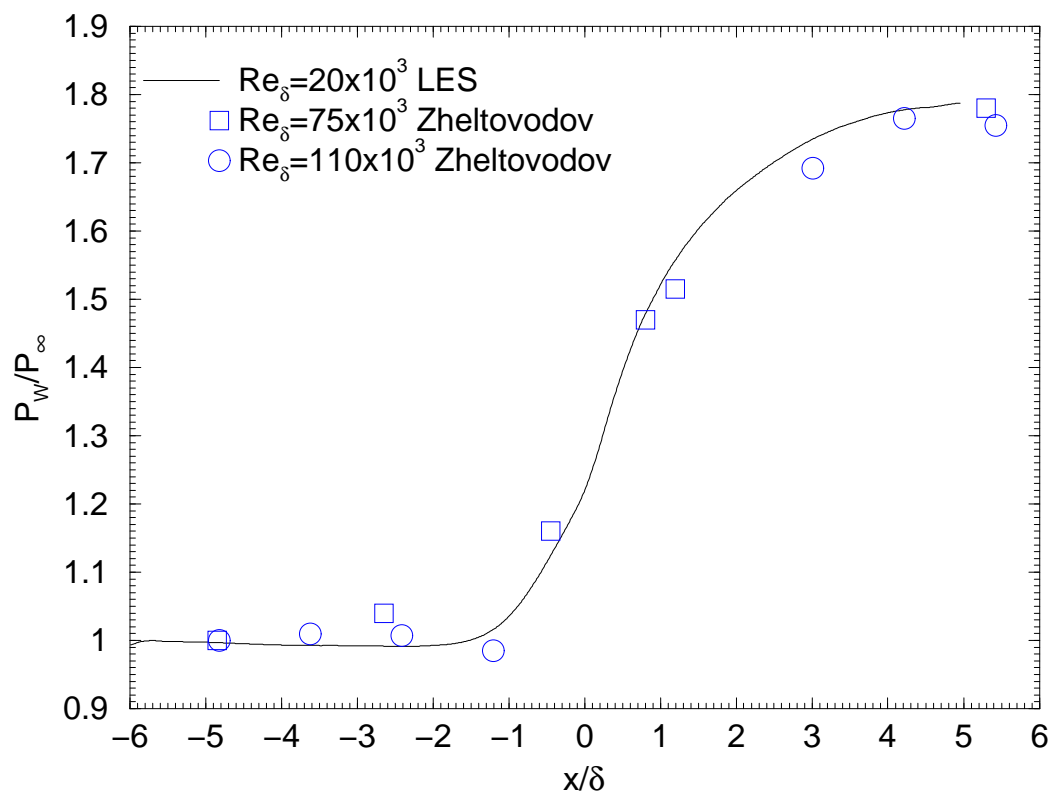


Figure 11: Mean wall pressure

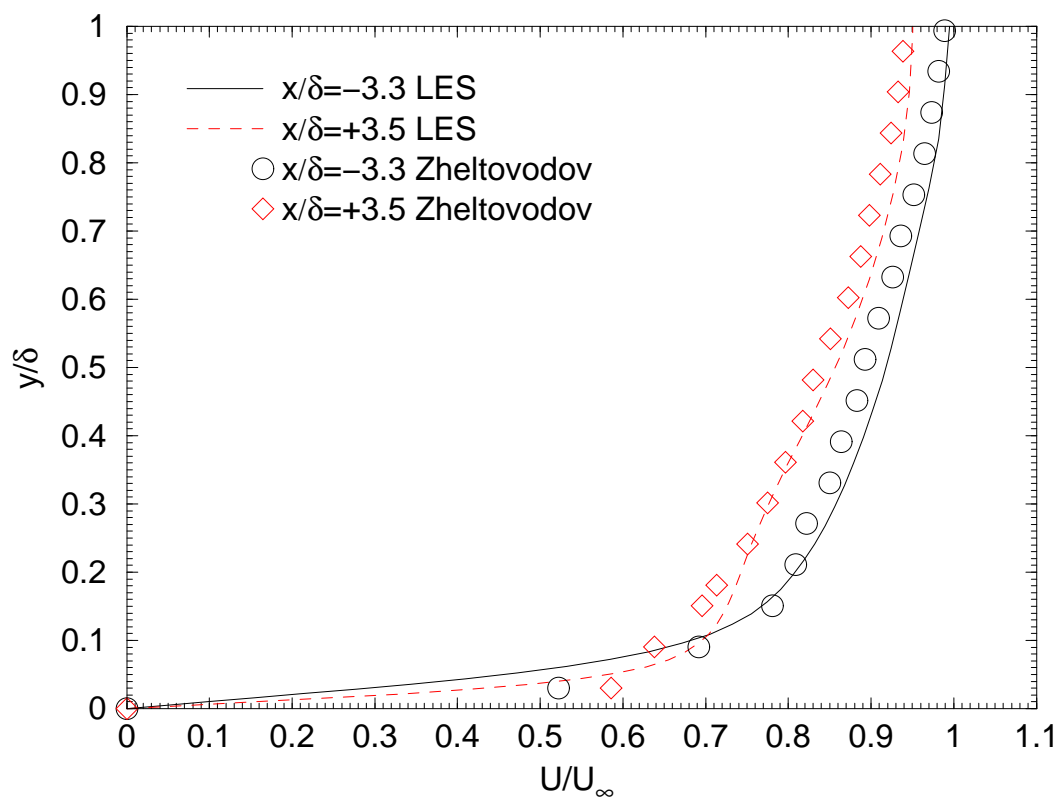


Figure 12: Mean velocity

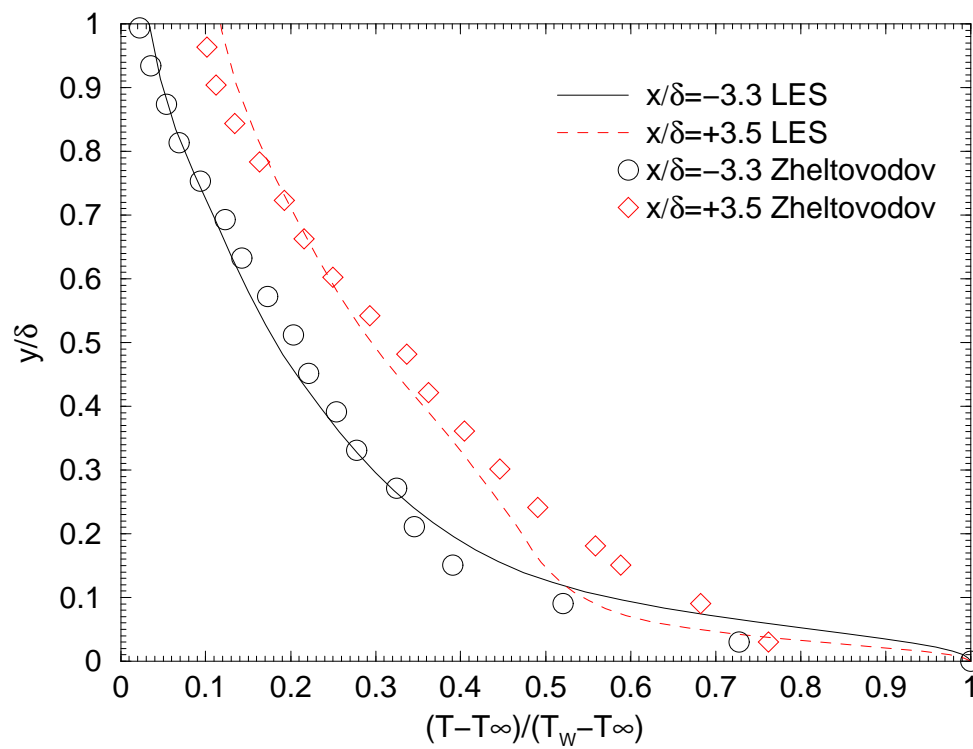


Figure 13: Mean static temperature

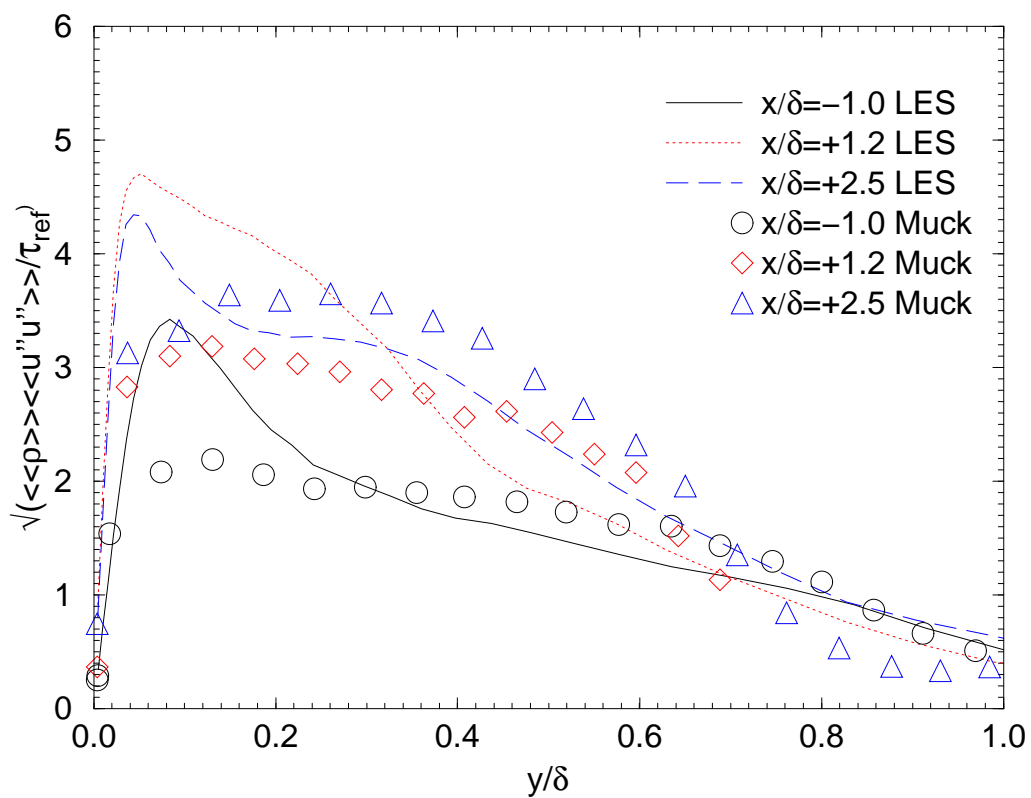


Figure 14: Reynolds streamwise stress

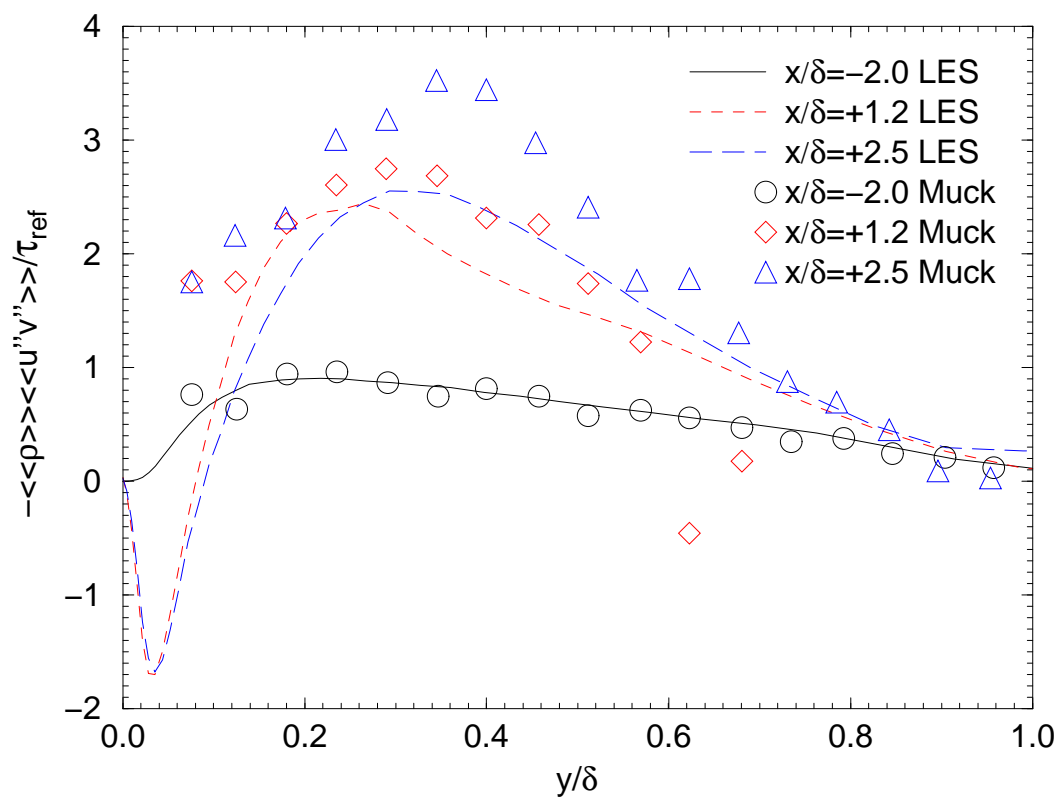


Figure 15: Reynolds shear stress

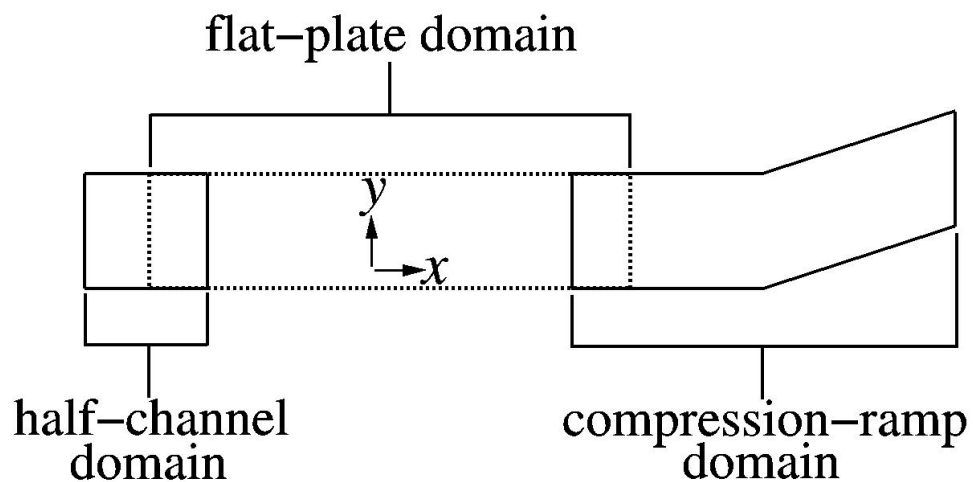


Figure 16: Generation of inflow conditions

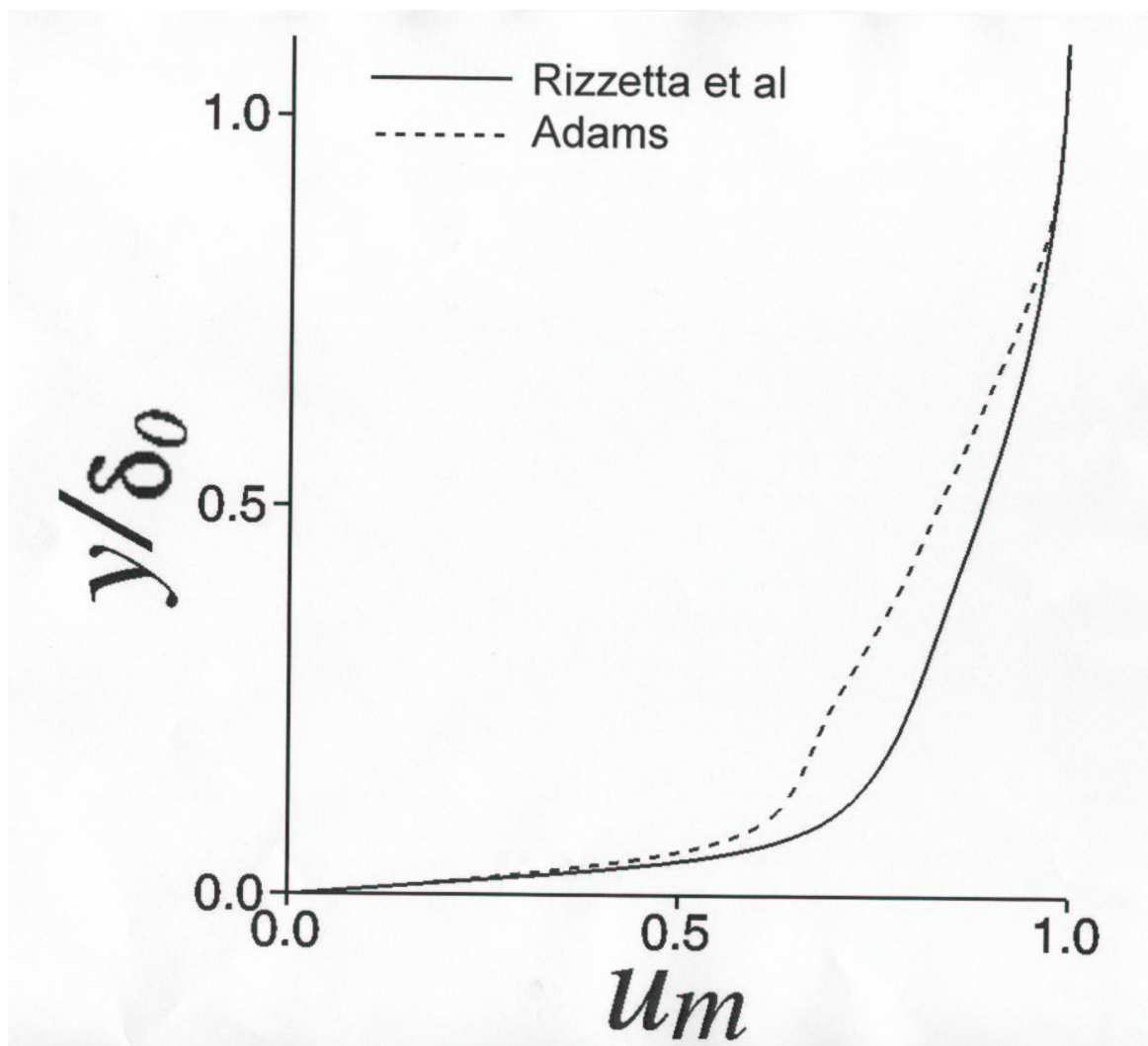


Figure 17: Inflow mean velocity

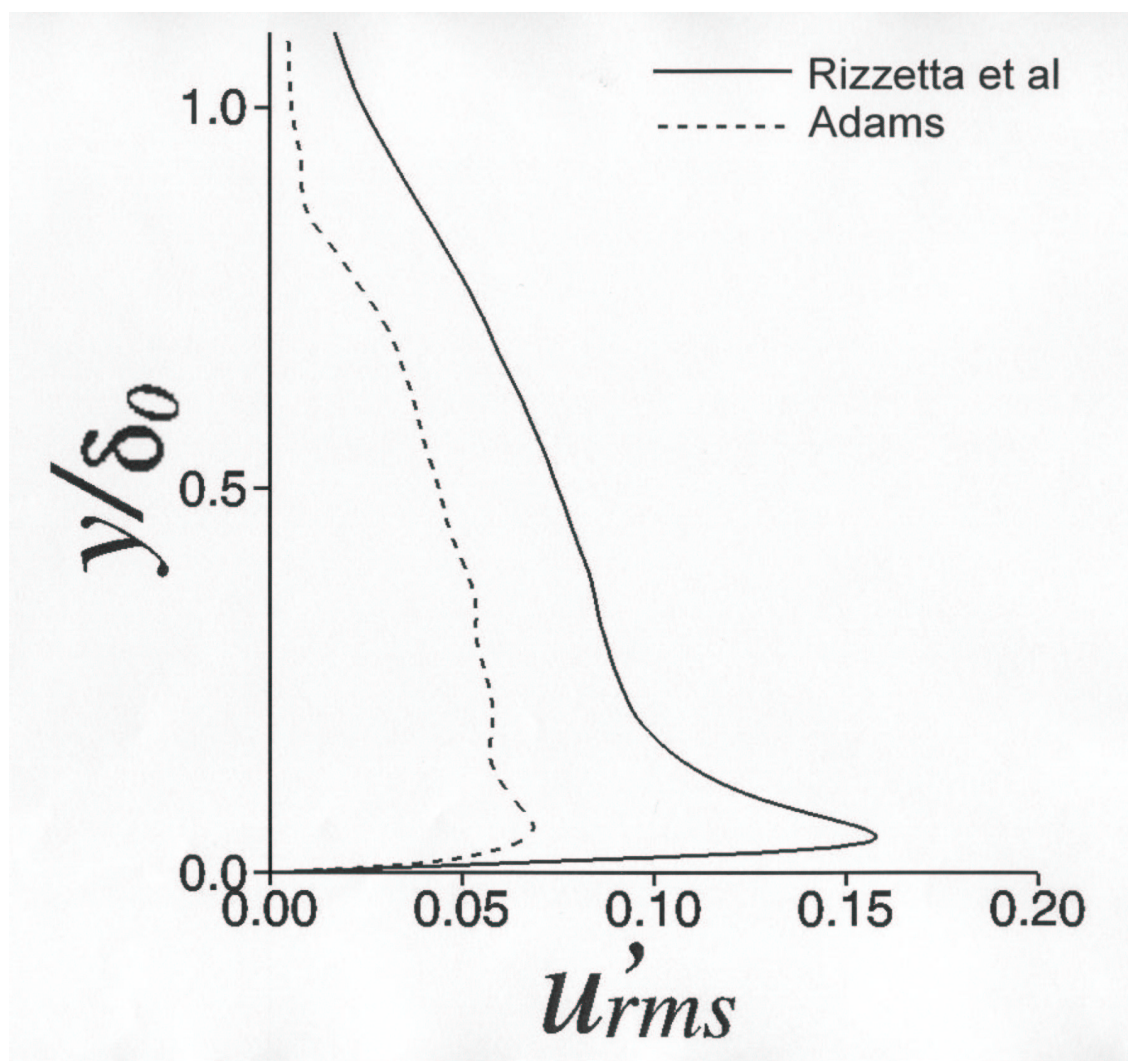


Figure 18: Inflow rms streamwise velocity

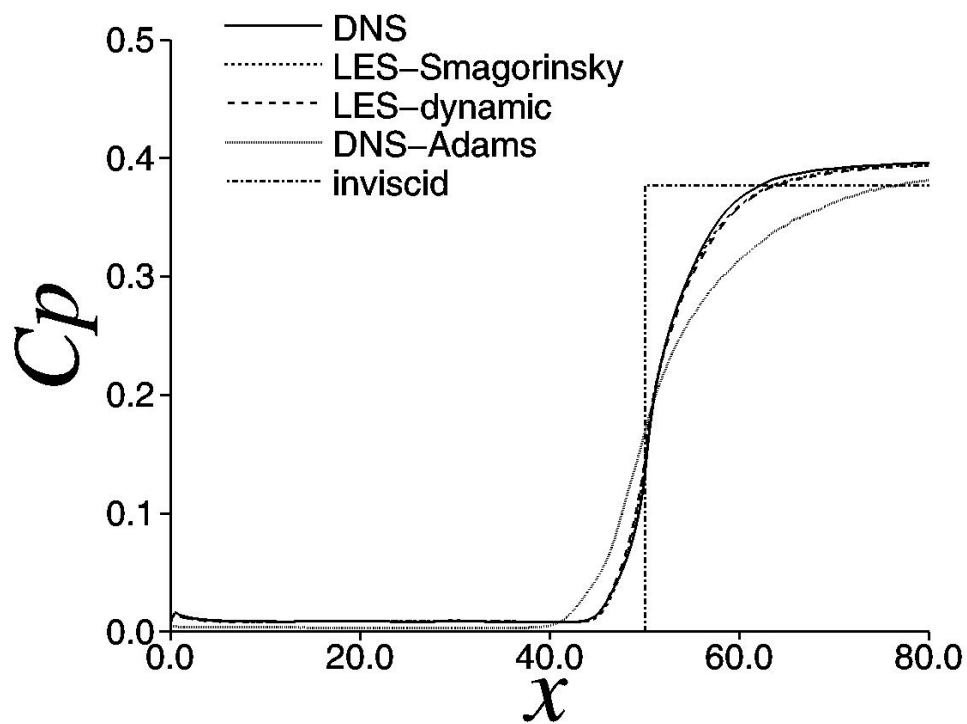


Figure 19: Mean surface pressure

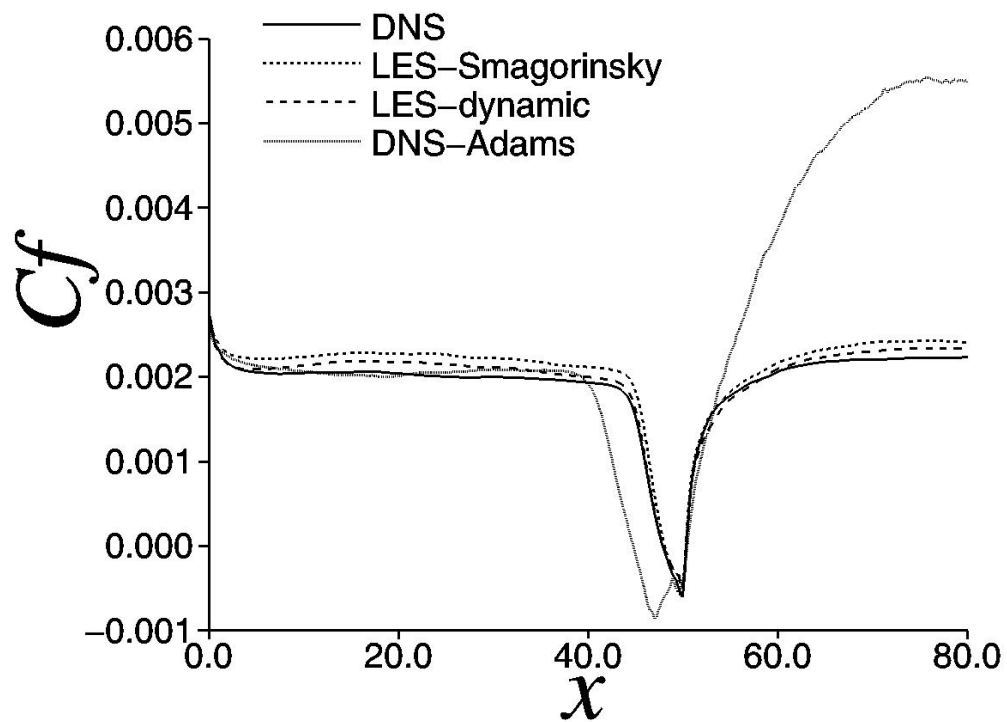


Figure 20: Mean skin friction

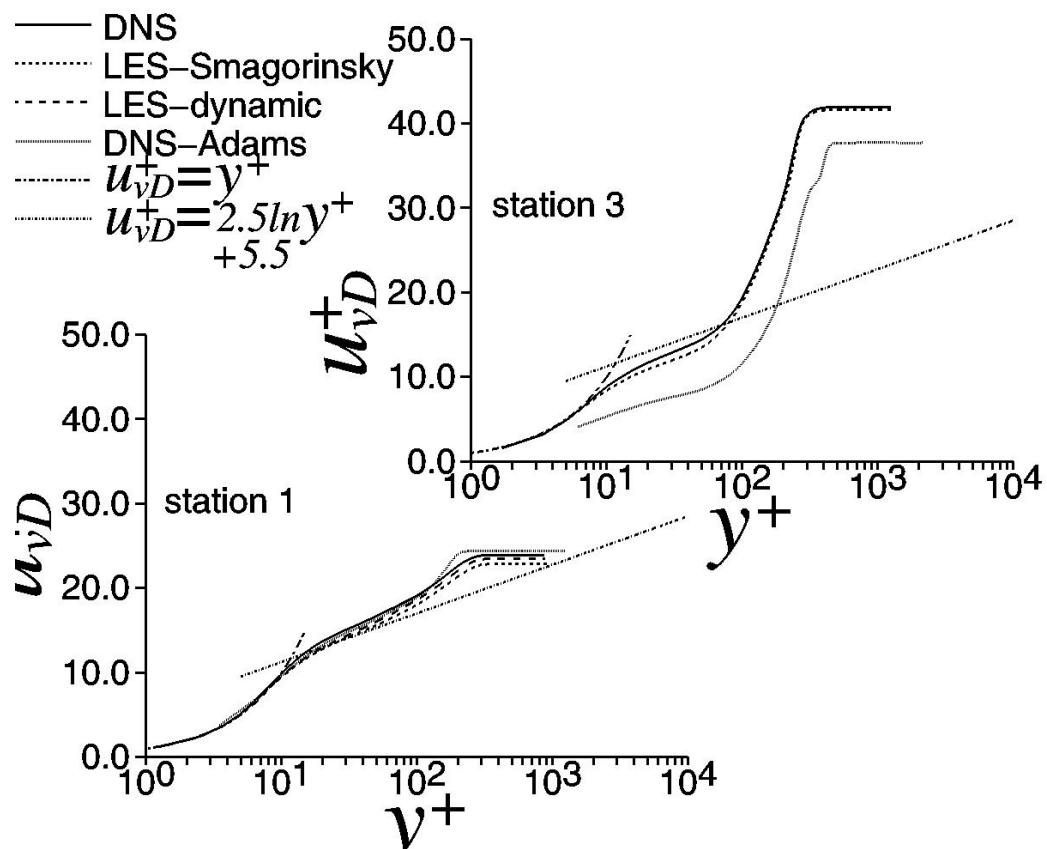


Figure 21: Mean velocity

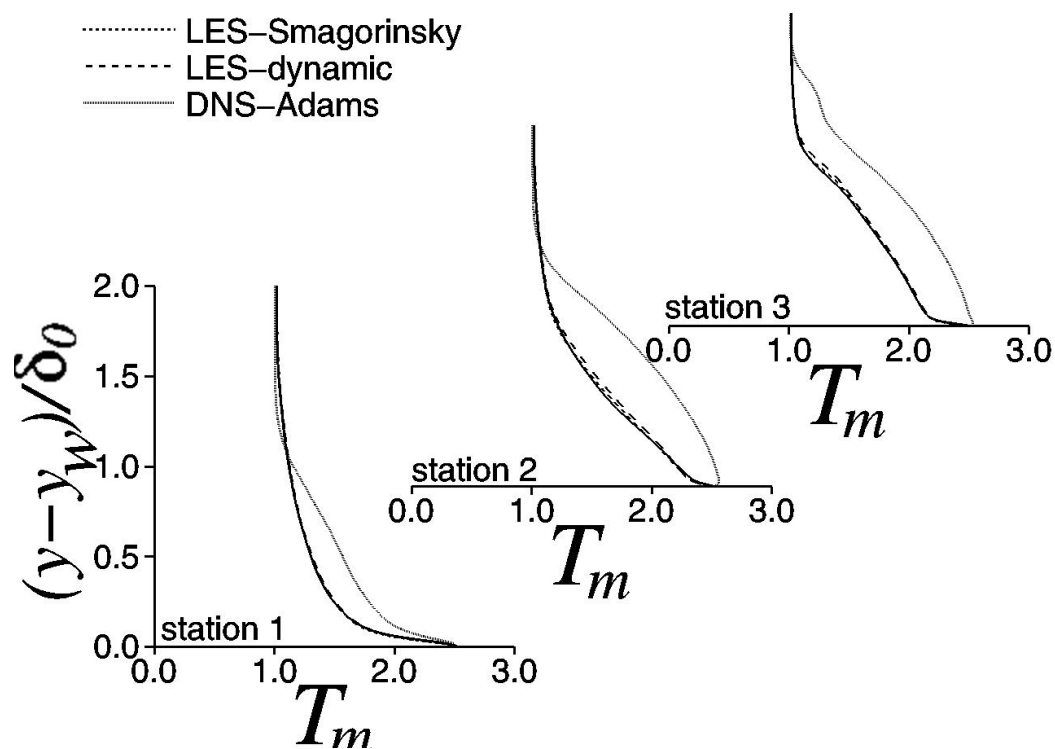


Figure 22: Mean static temperature

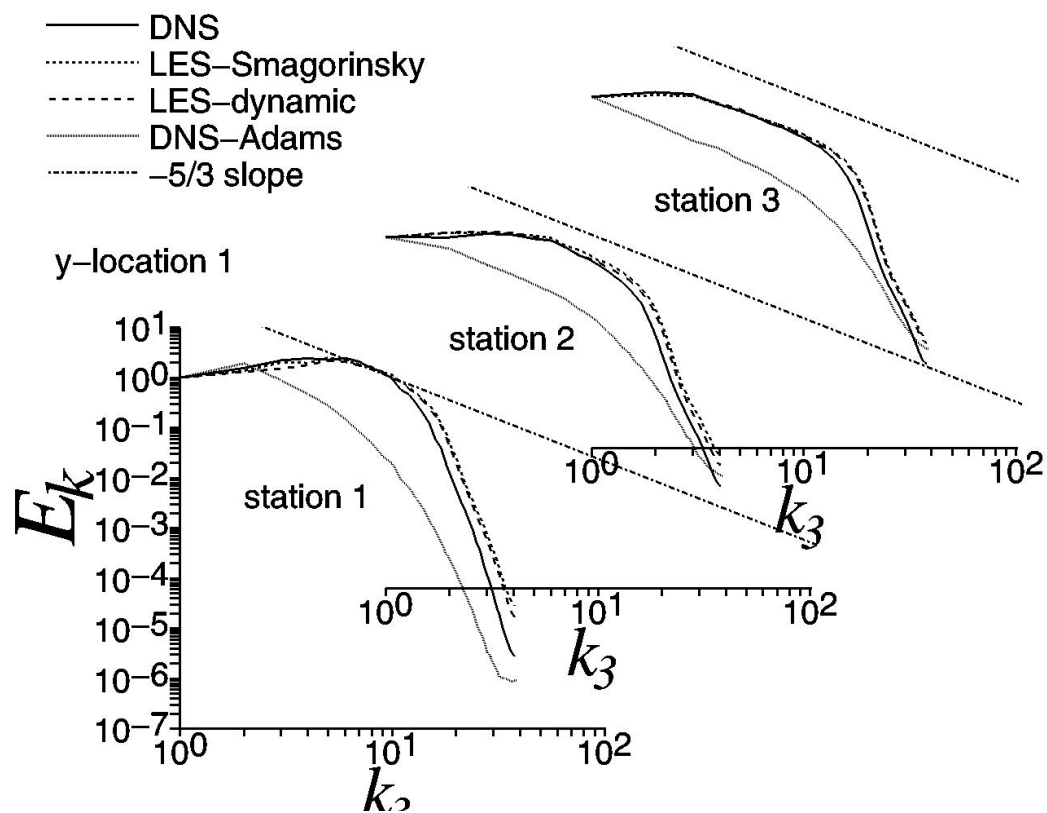


Figure 23: Spanwise TKE spectra at $y^+ = 7.3 (y/\delta = 0.034)$

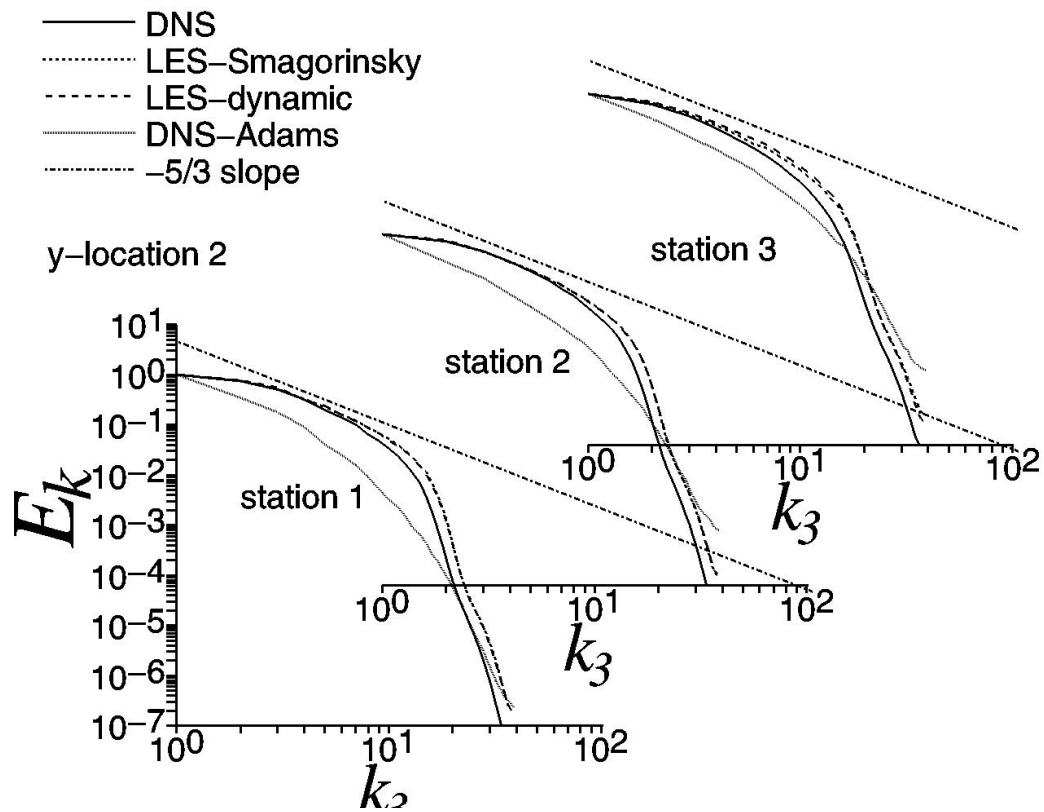


Figure 24: Spanwise TKE spectra at $y^+ = 132 (y/\delta = 0.61)$

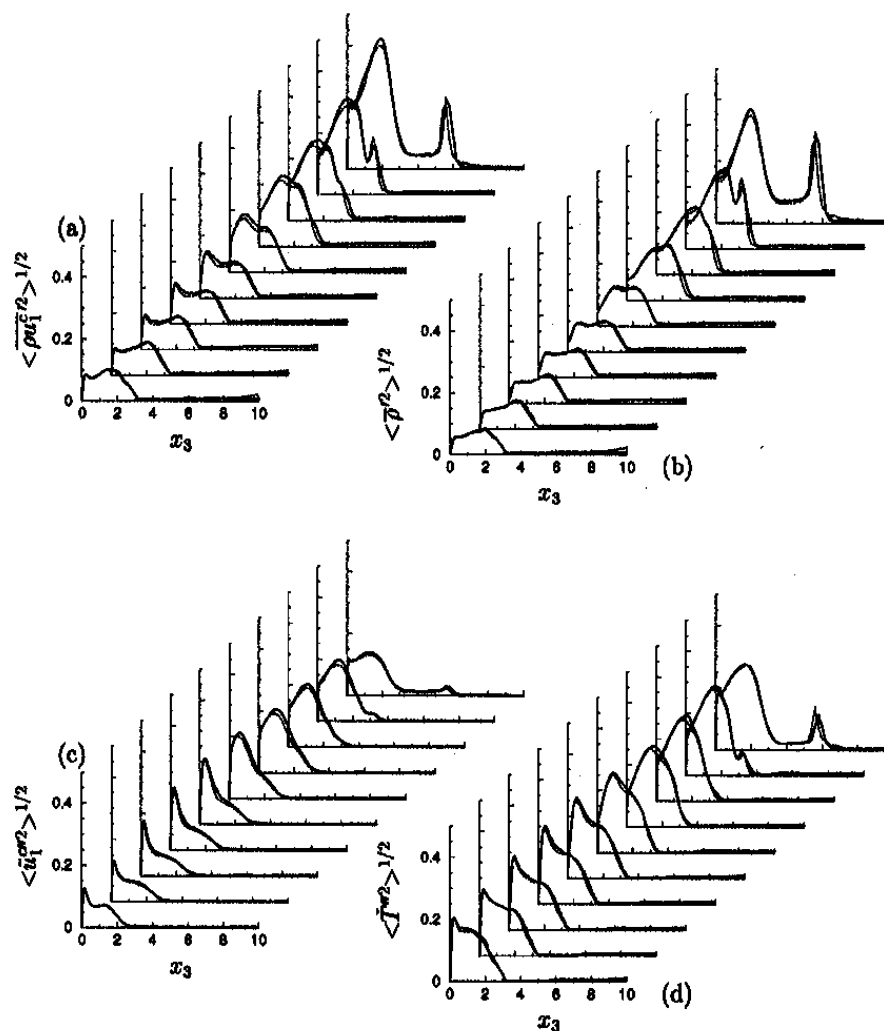


Figure 25: Turbulence statistics (– DNS,... LES (ADM))

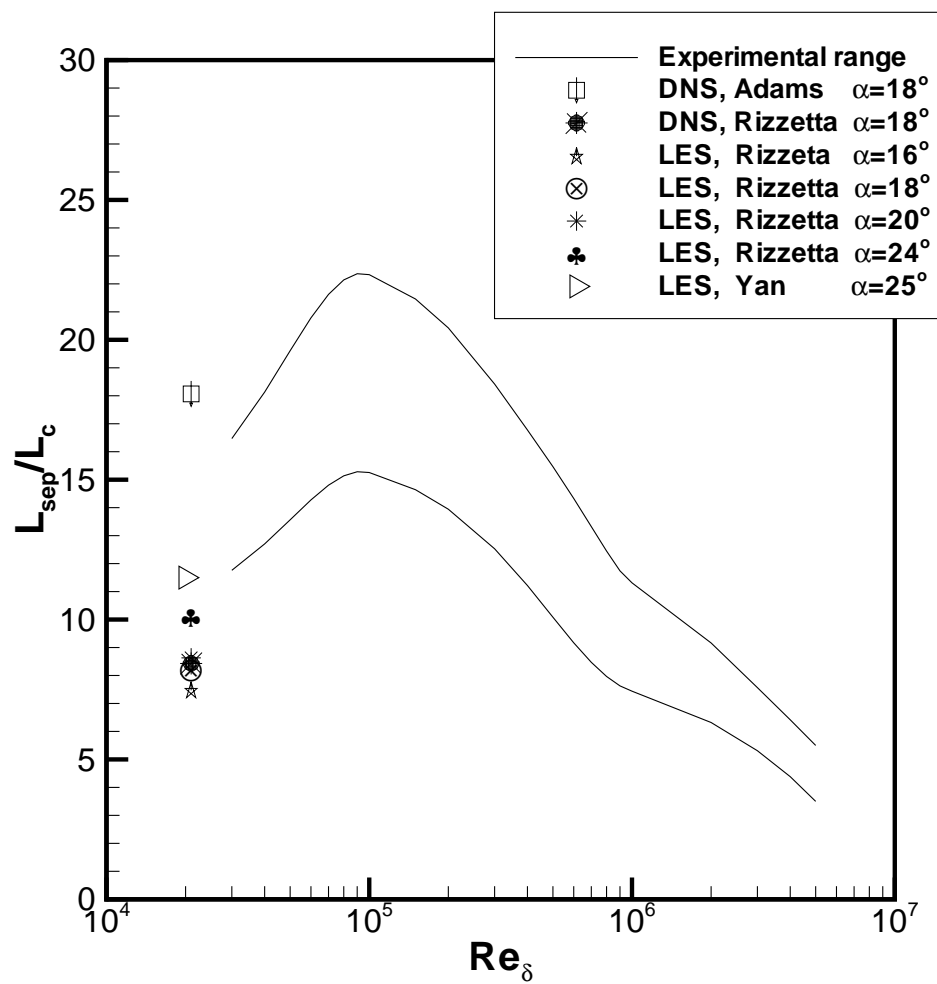


Figure 26: Separation length for DNS and LES

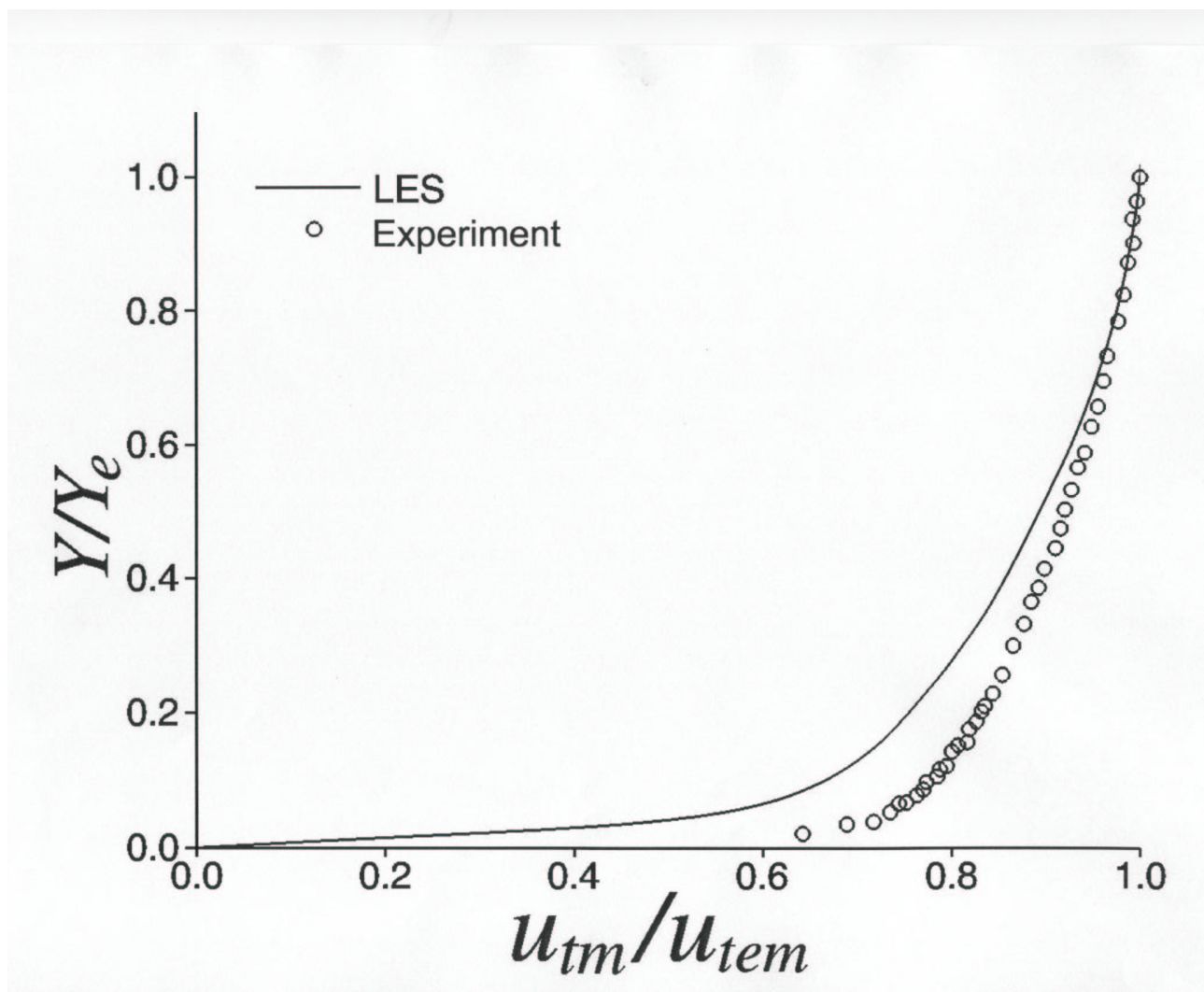


Figure 27: Inflow velocity

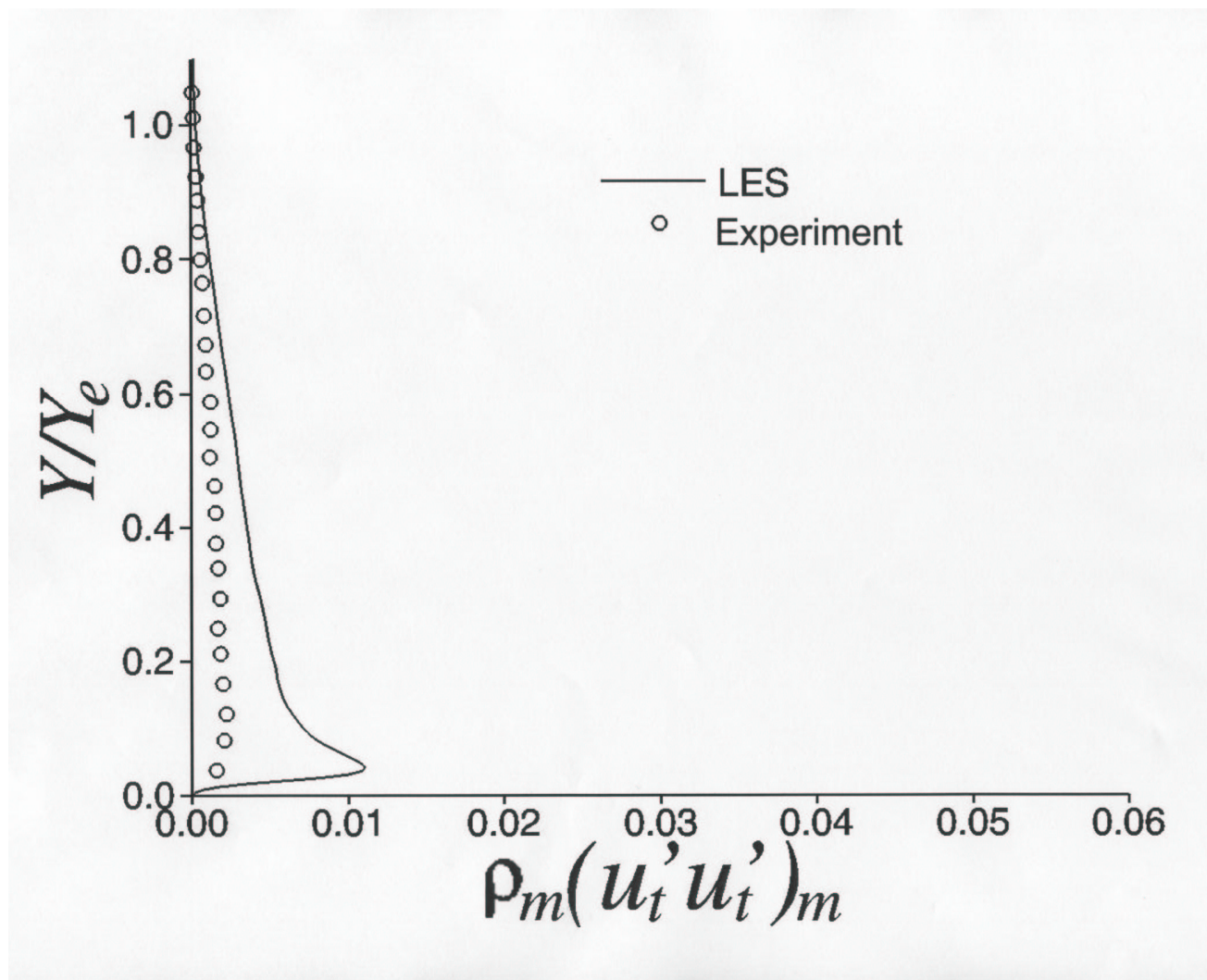


Figure 28: Inflow Reynolds streamwise stress

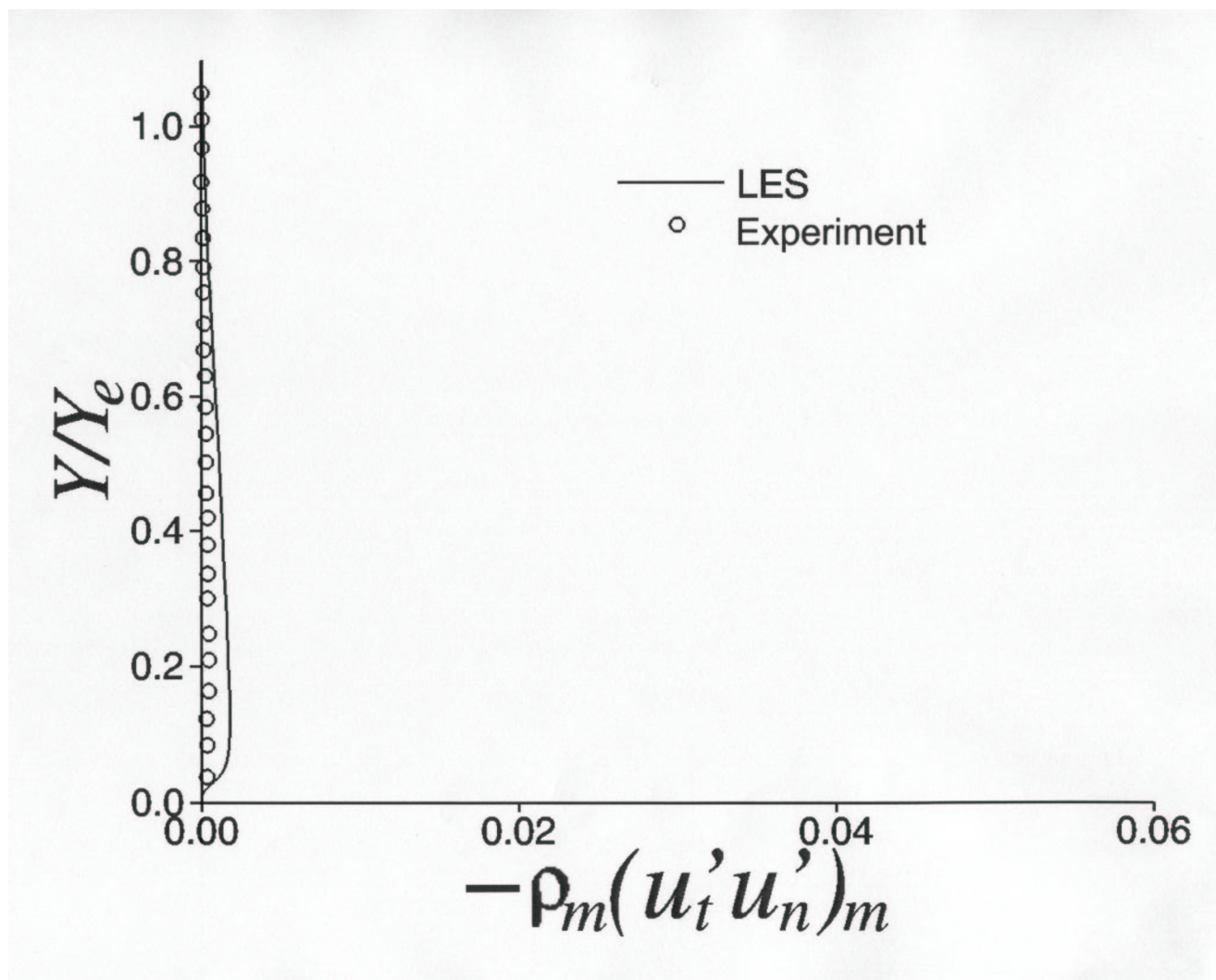


Figure 29: Inflow Reynolds shear stress

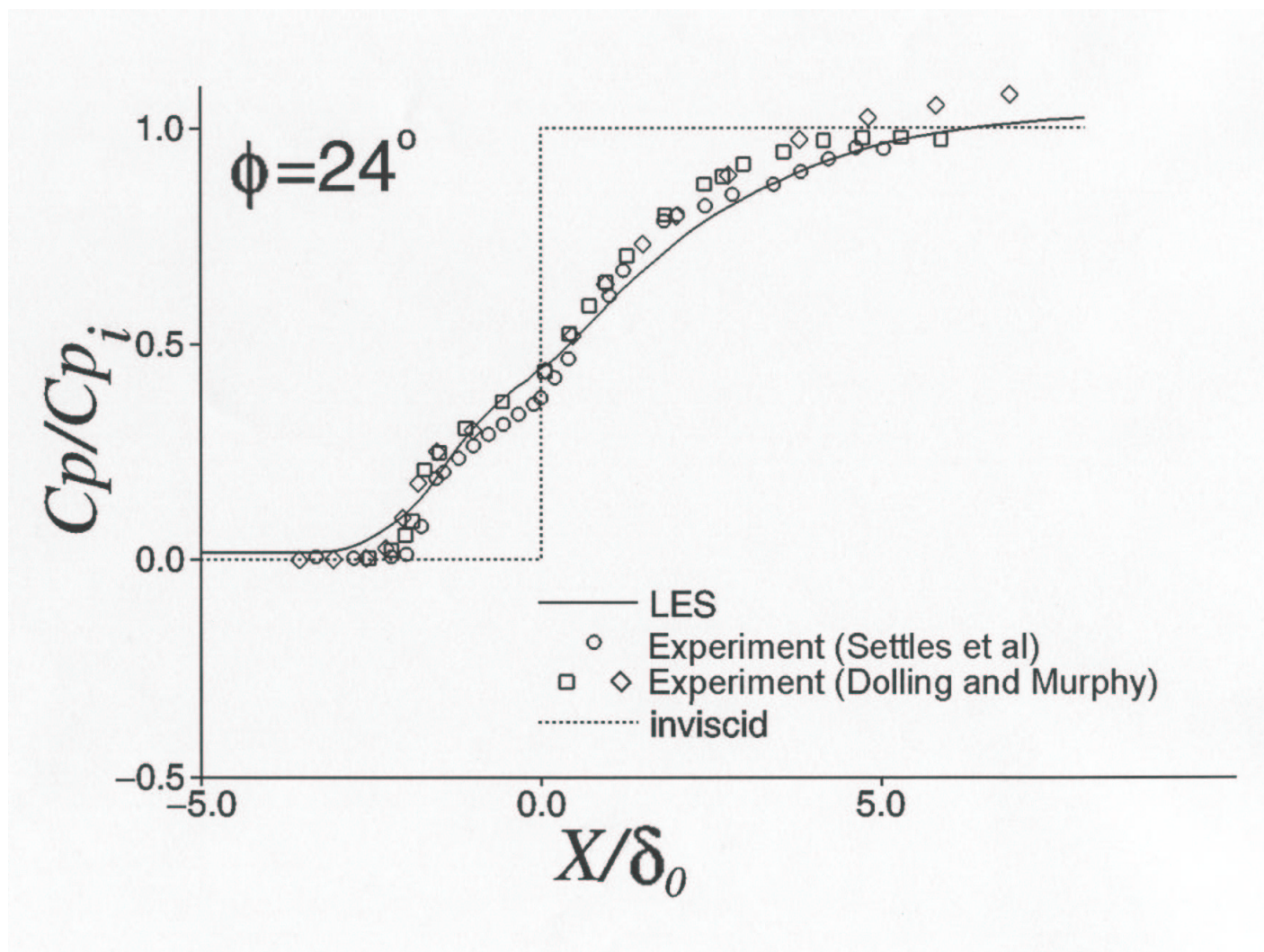


Figure 30: Mean wall pressure

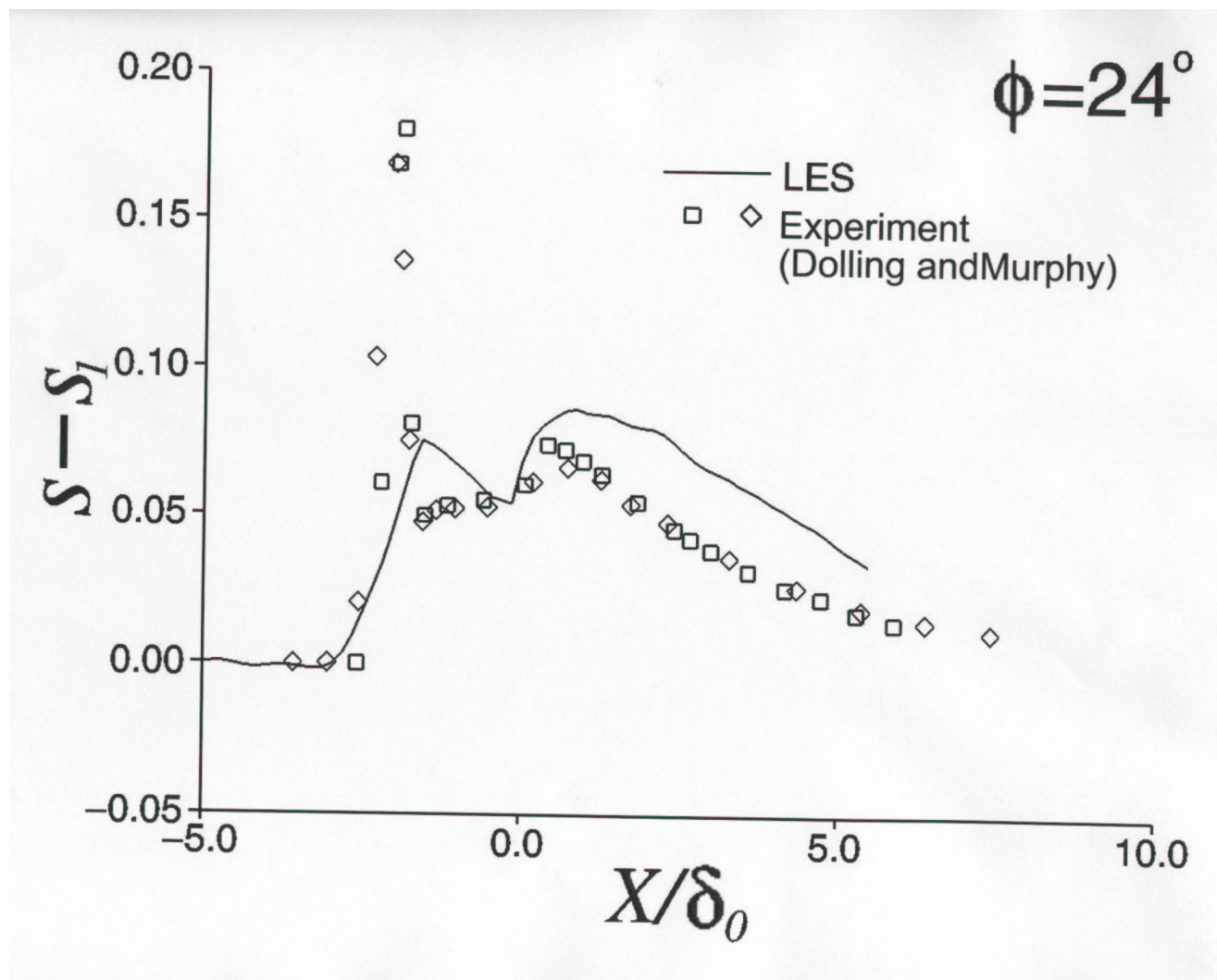


Figure 31: Standard deviation of wall pressure

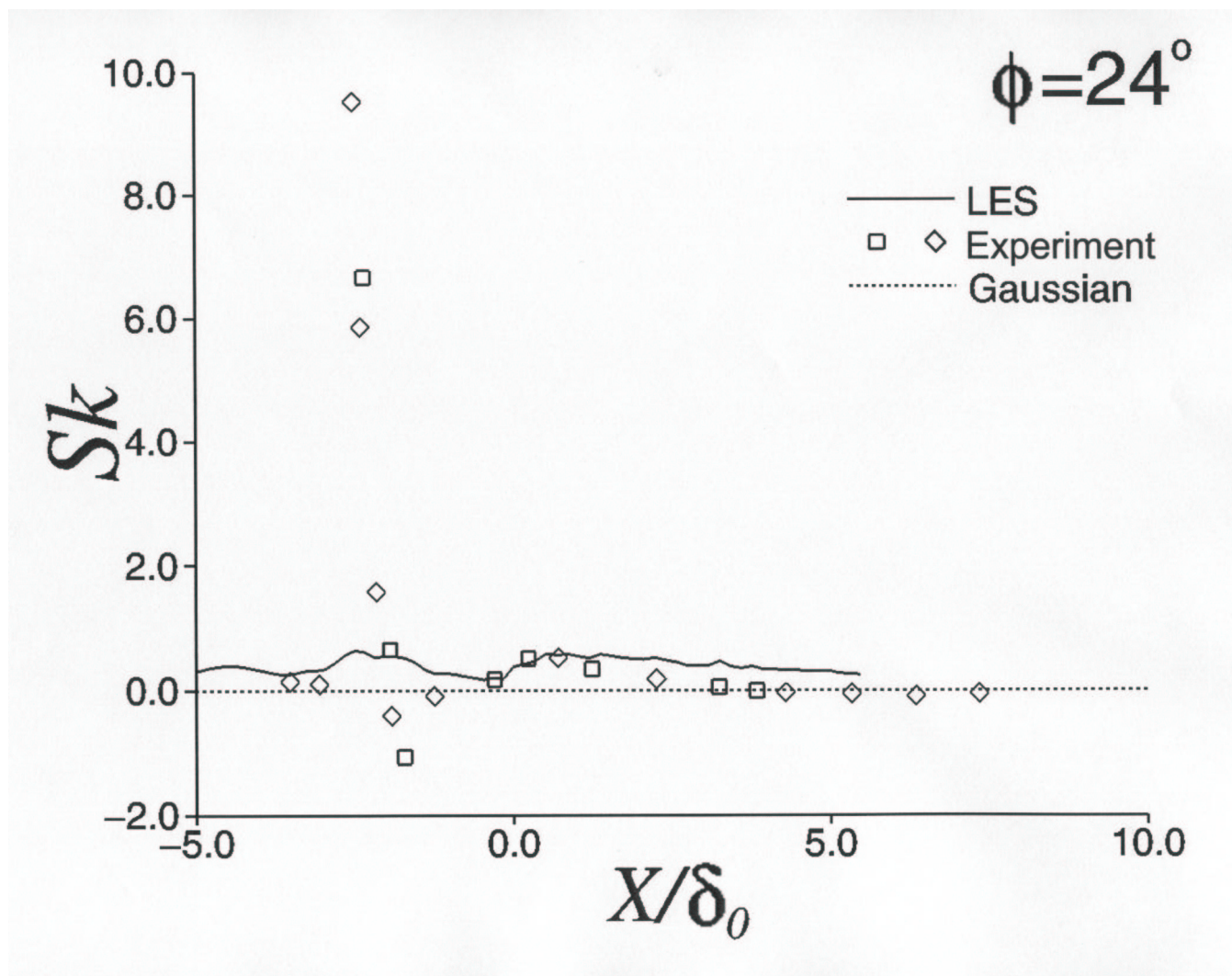


Figure 32: Skewness of wall pressure

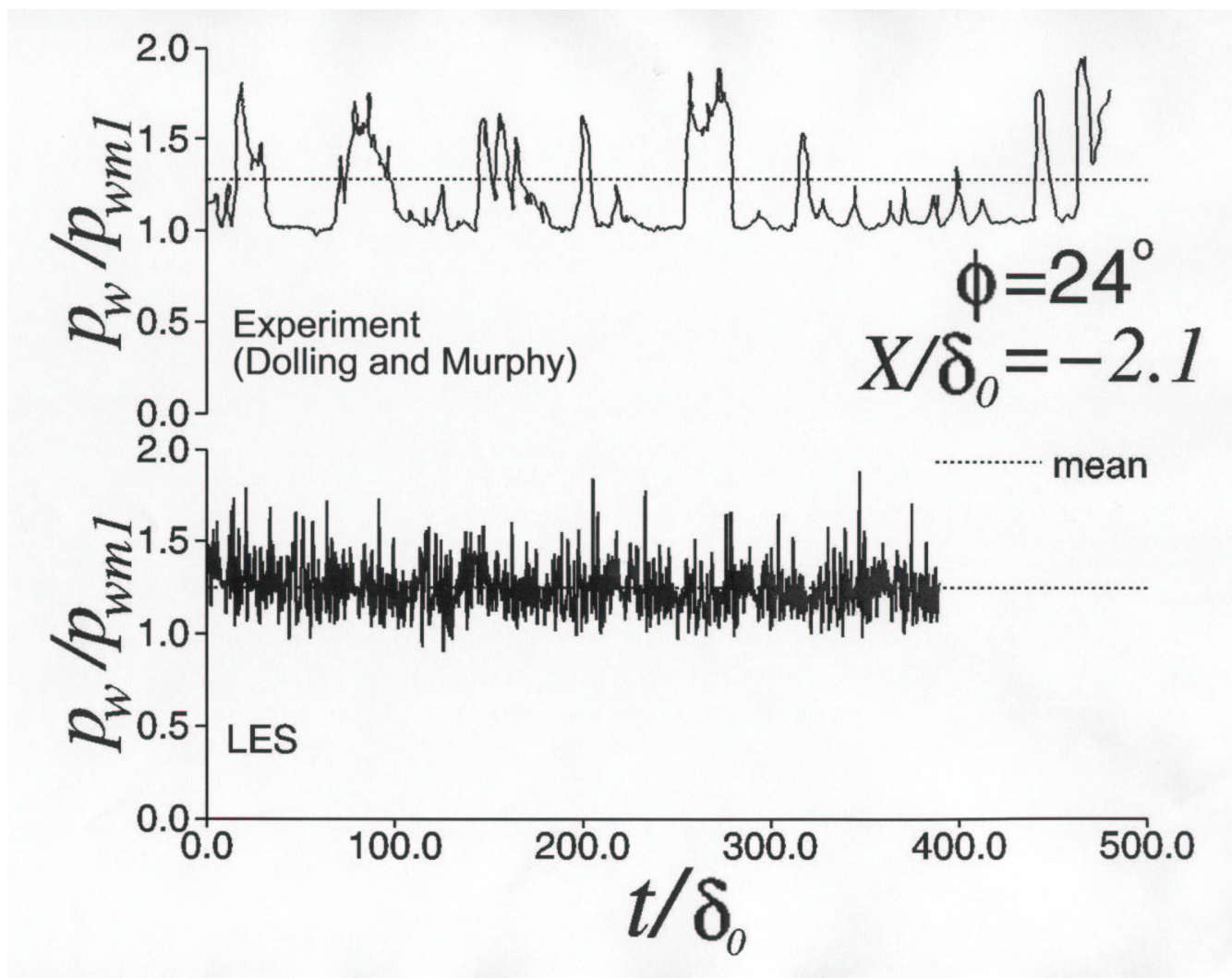


Figure 33: Time history of wall pressure

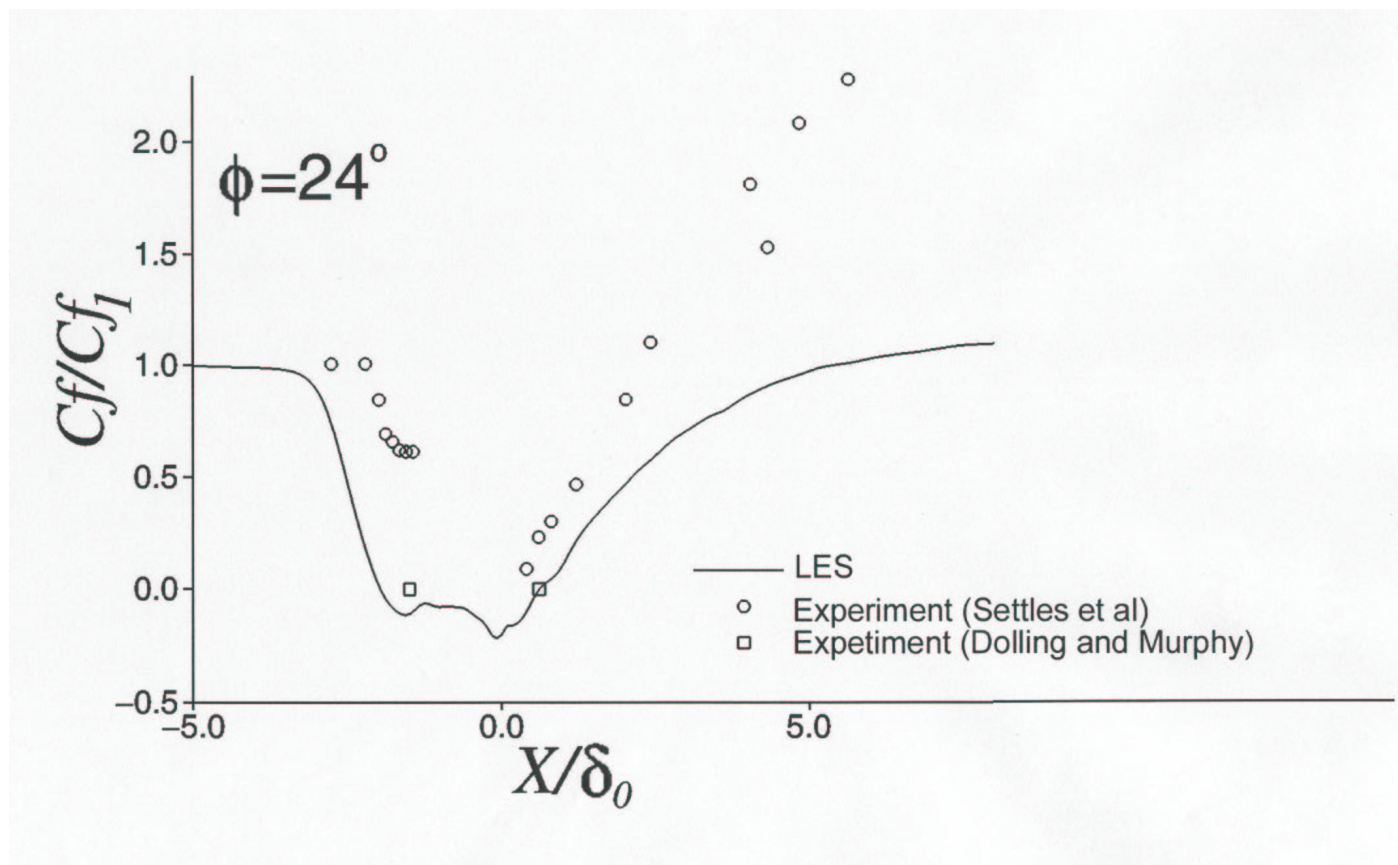


Figure 34: Mean skin friction

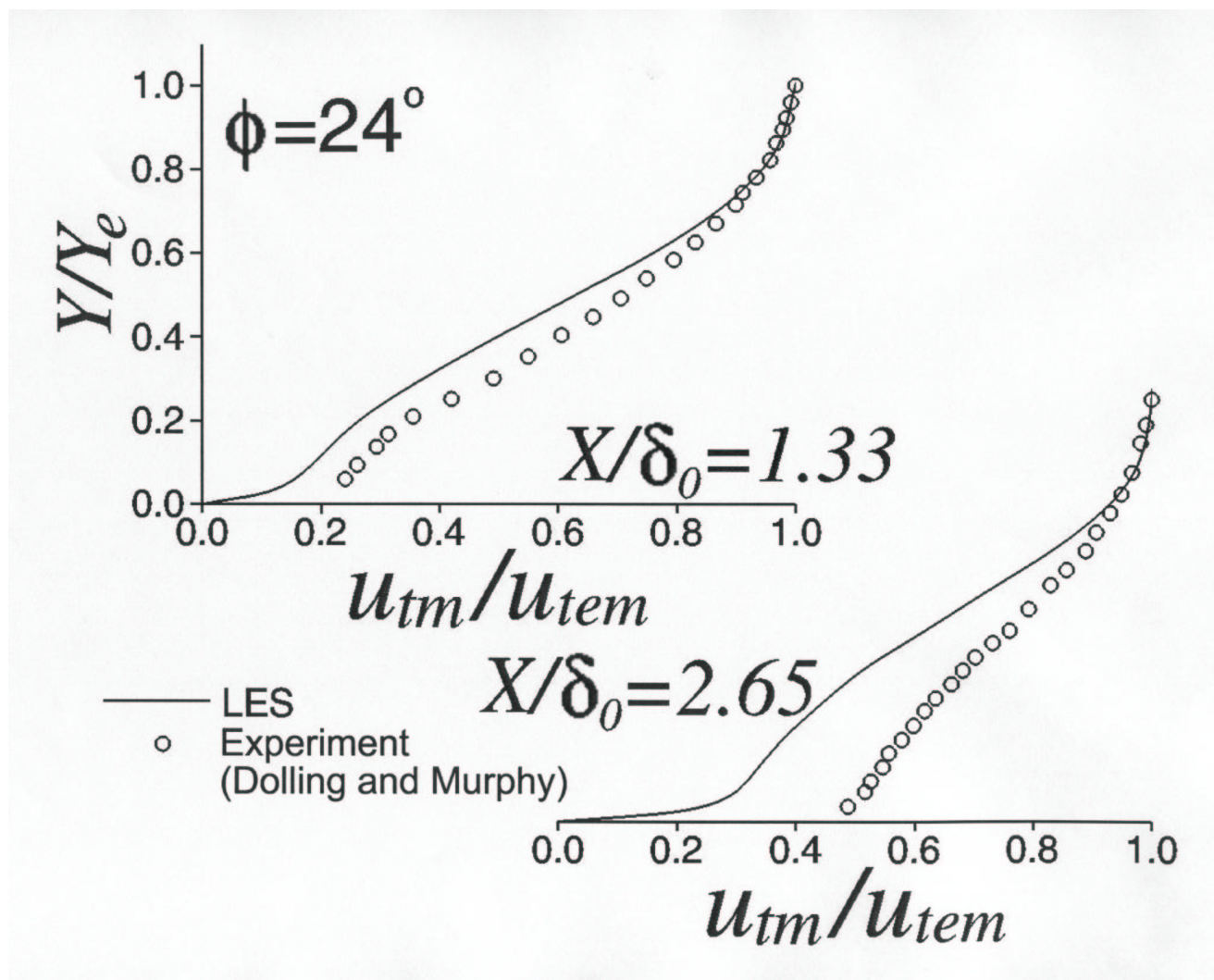


Figure 35: Velocity profiles

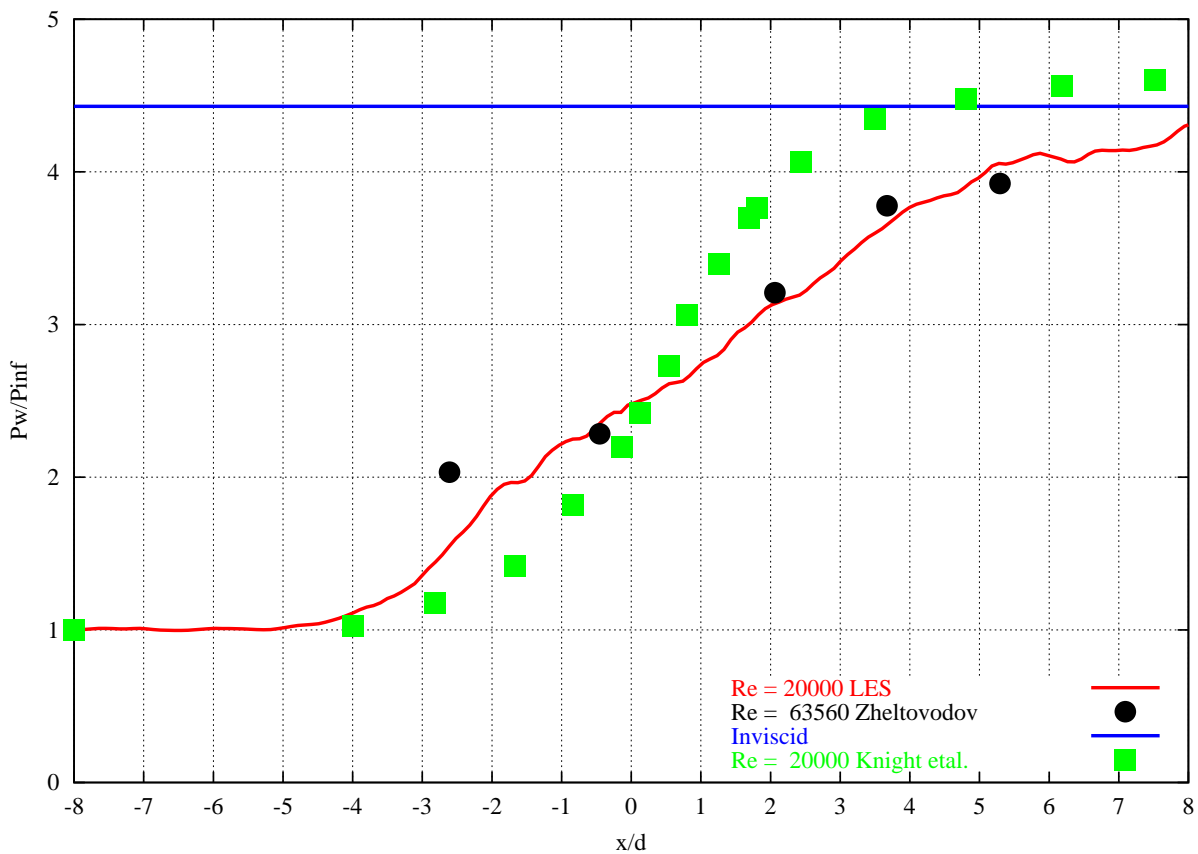


Figure 36: Mean wall pressure

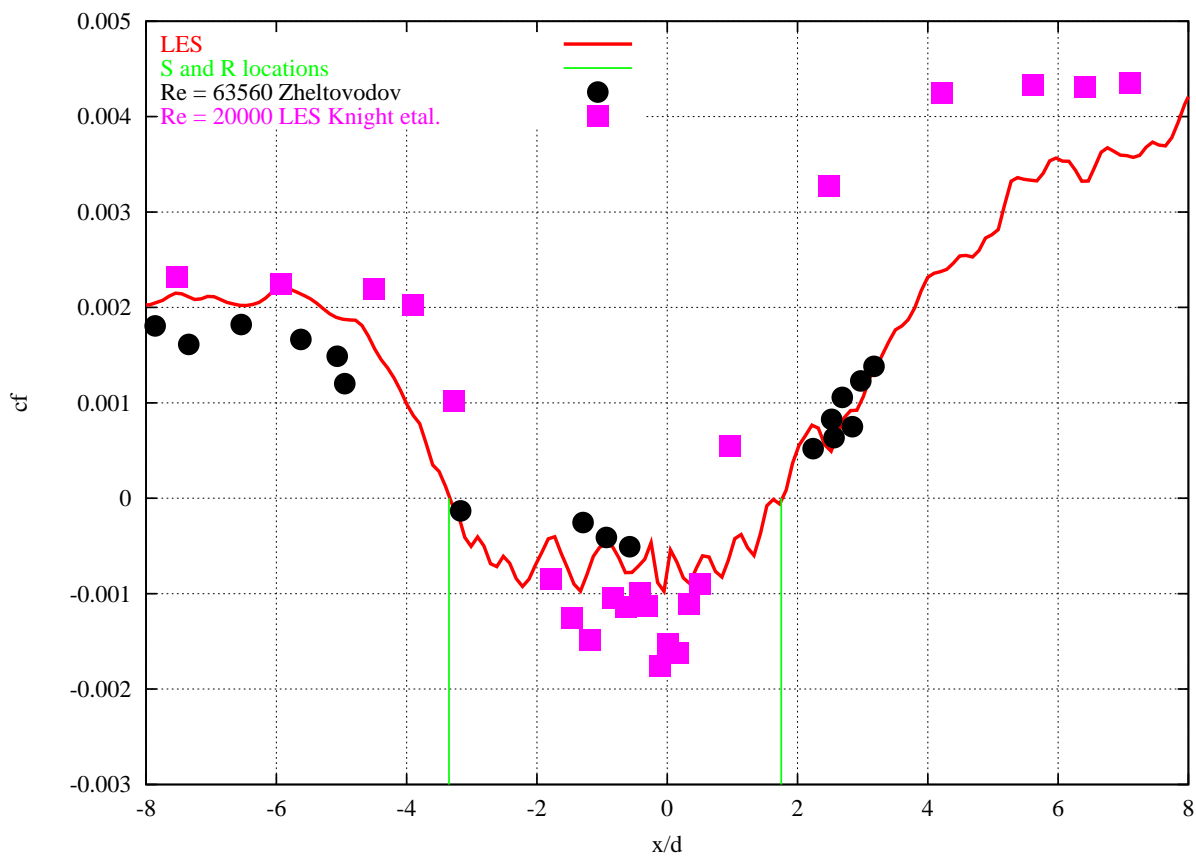


Figure 37: Mean skin friction

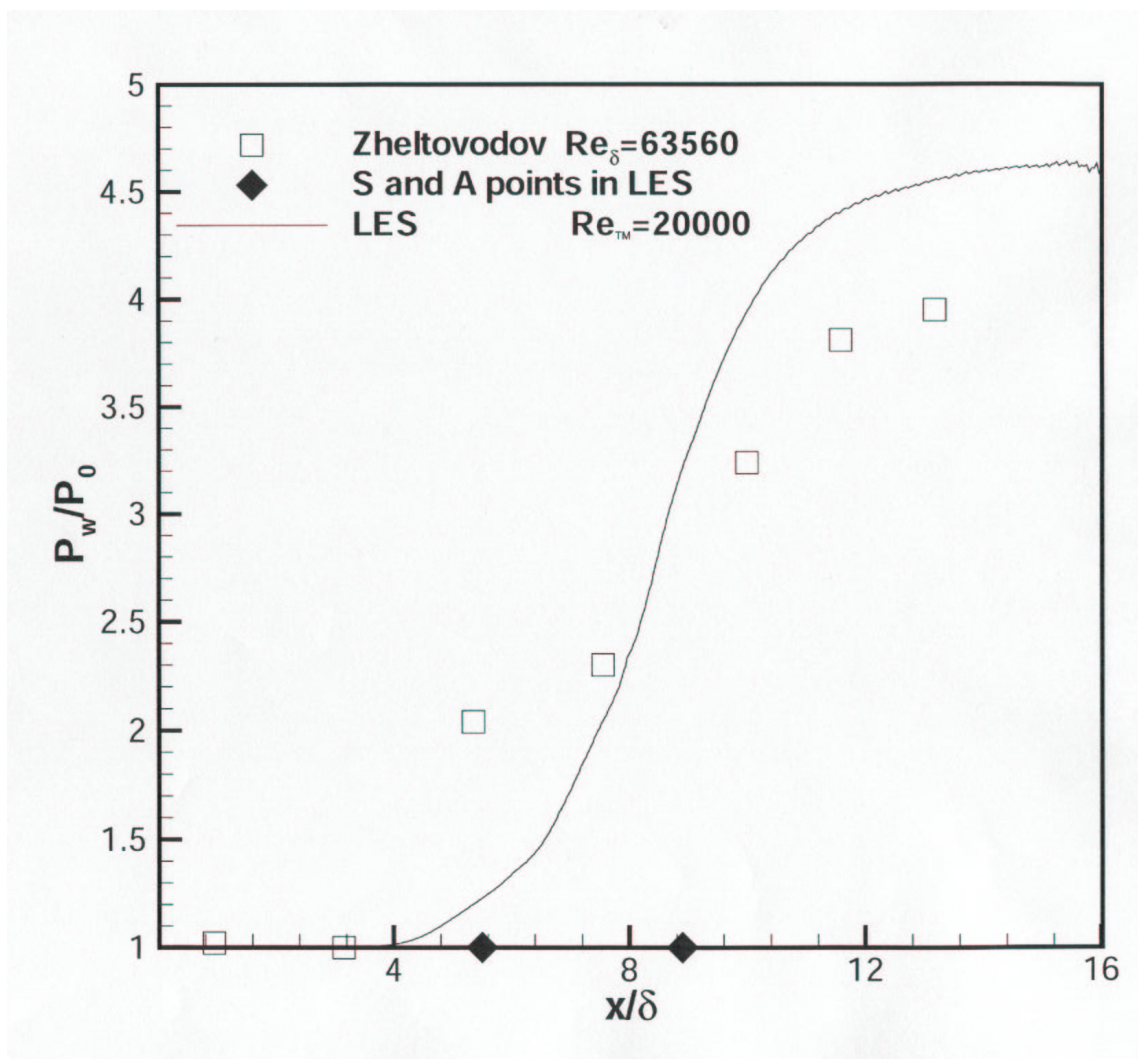


Figure 38: Mean wall pressure

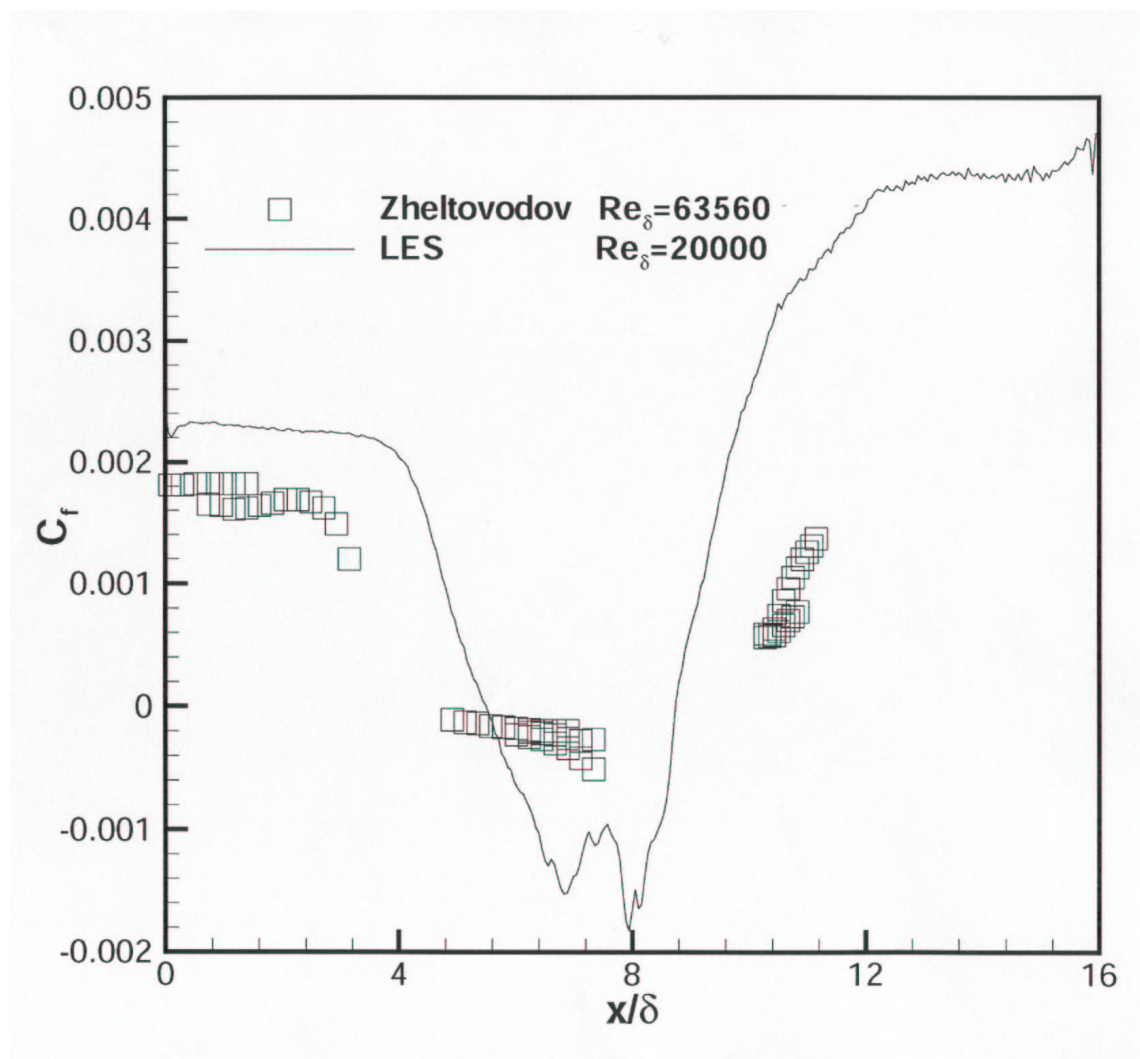


Figure 39: Mean skin friction coefficient

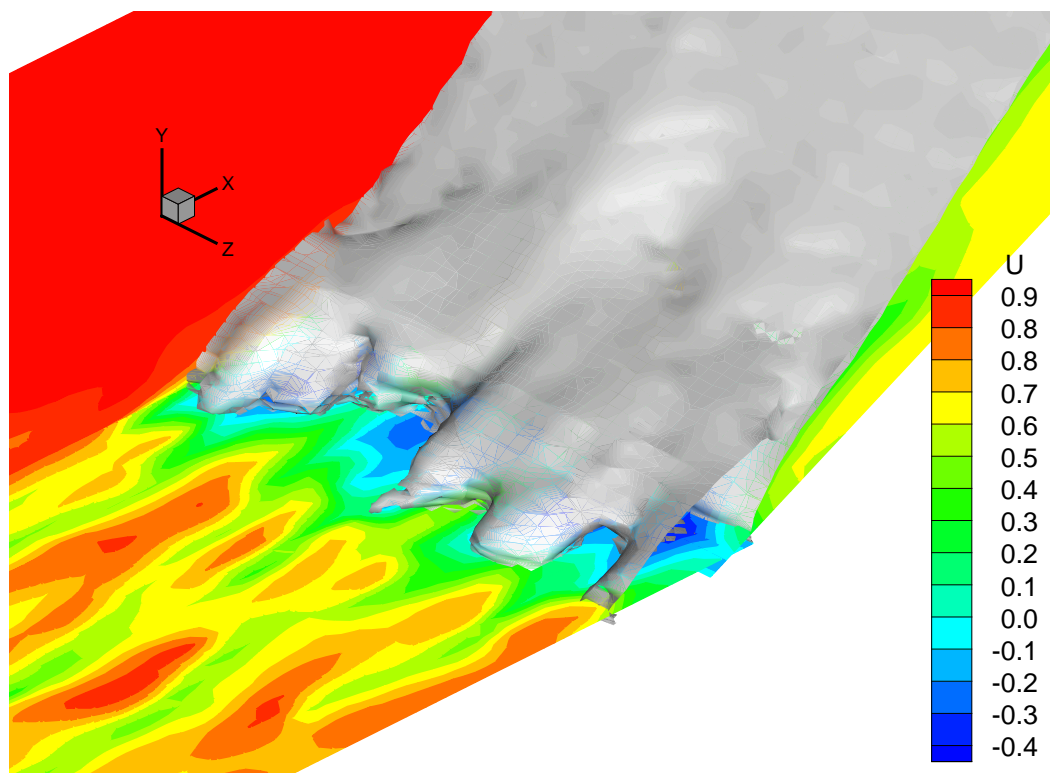


Figure 40: Instantaneous shock structure

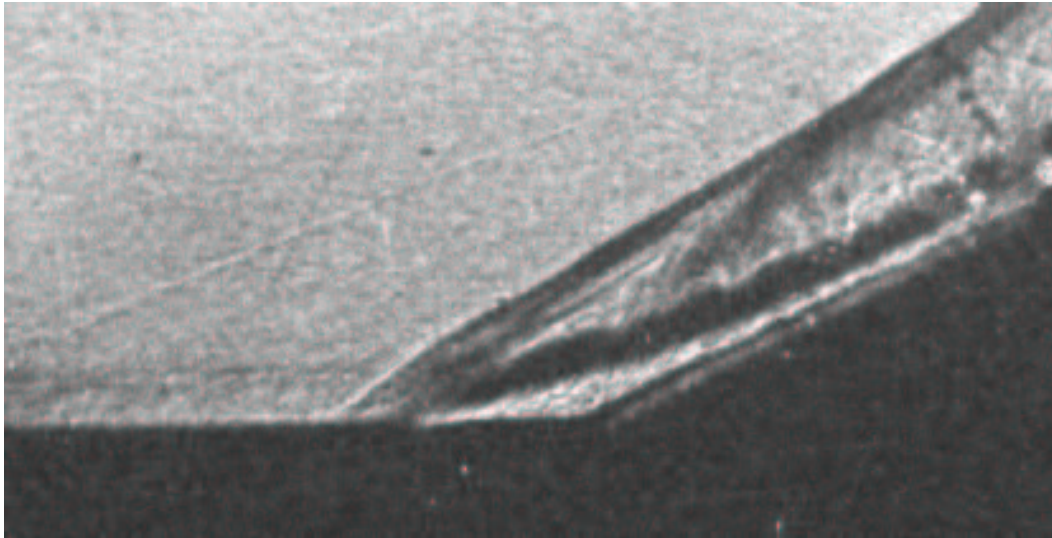


Figure 41: Instantaneous Schlieren image

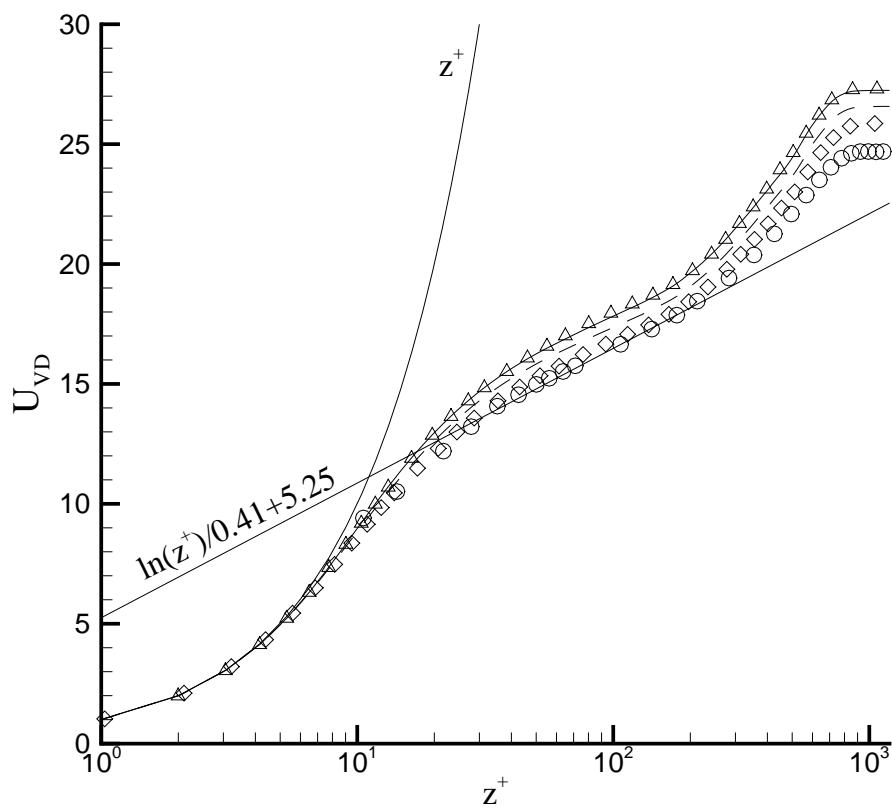


Figure 42: Velocity (A —, B Δ , C —, D \diamond , HWA \circ)

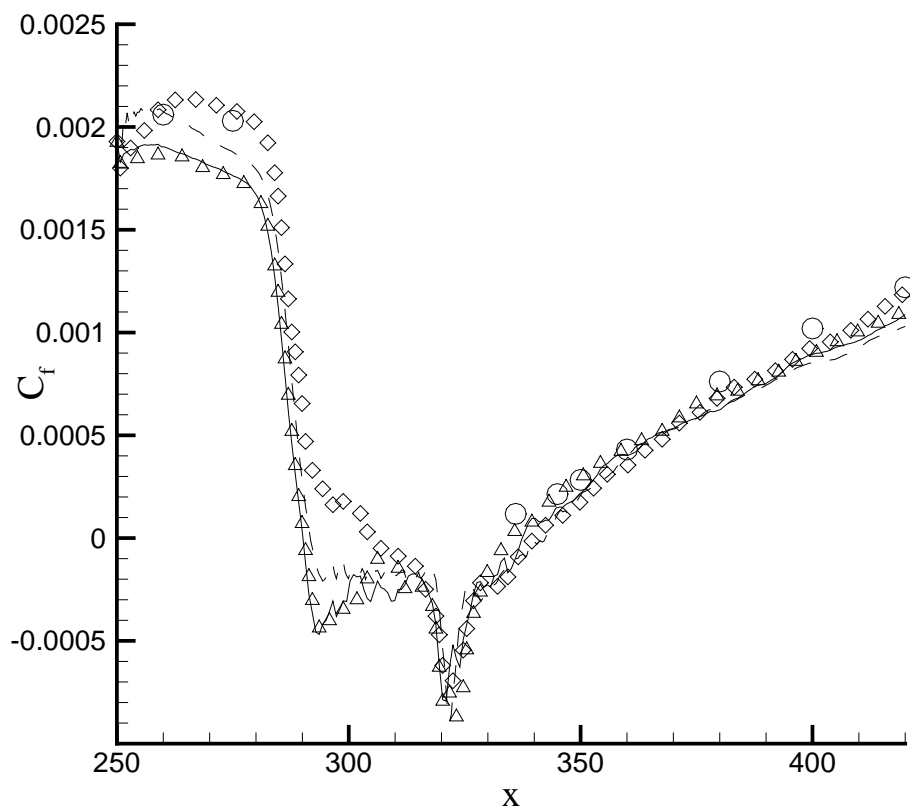


Figure 43: Skin friction (A —, B \triangle , C —, D \diamond , HWA \circ)

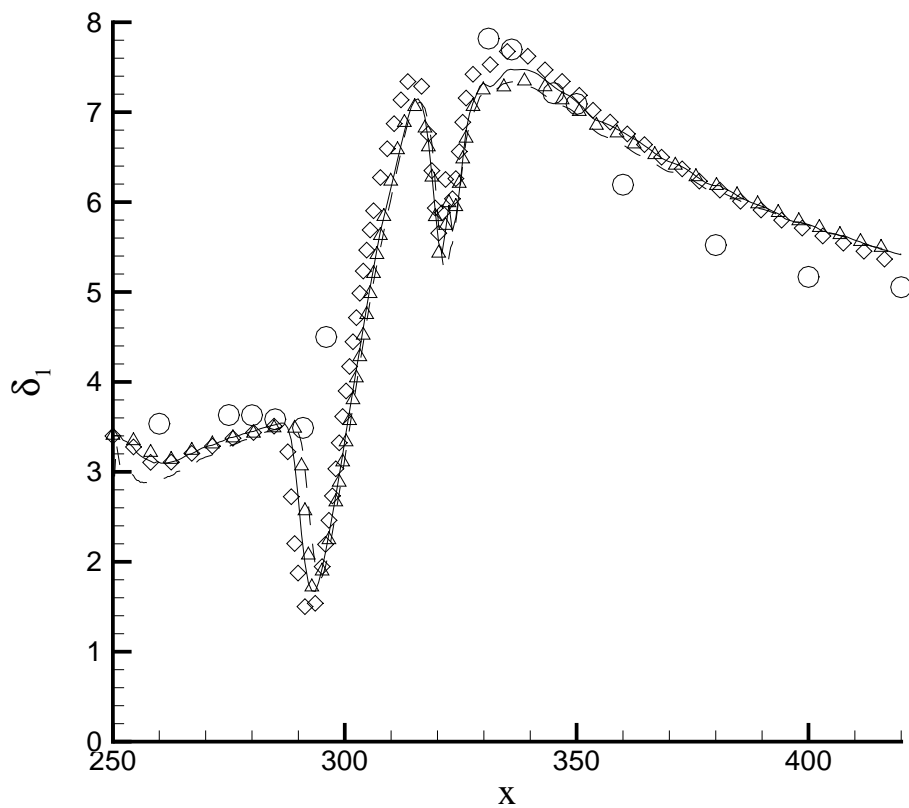


Figure 44: Displacement thickness (A —, B \triangle , C ---, D \diamond , HWA \circ)

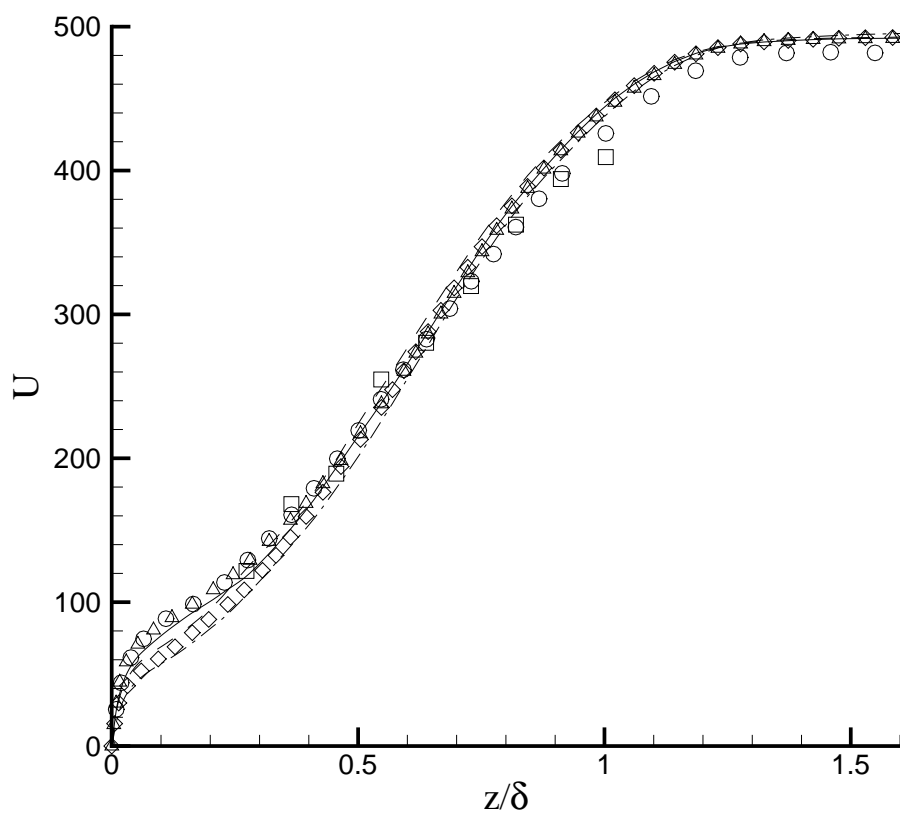


Figure 45: Velocity (A ($x = 351$ mm) —, A ($x = 345$ mm) —●—, B \triangle , C — —, D \diamond , HWA \circ , LDA \square)

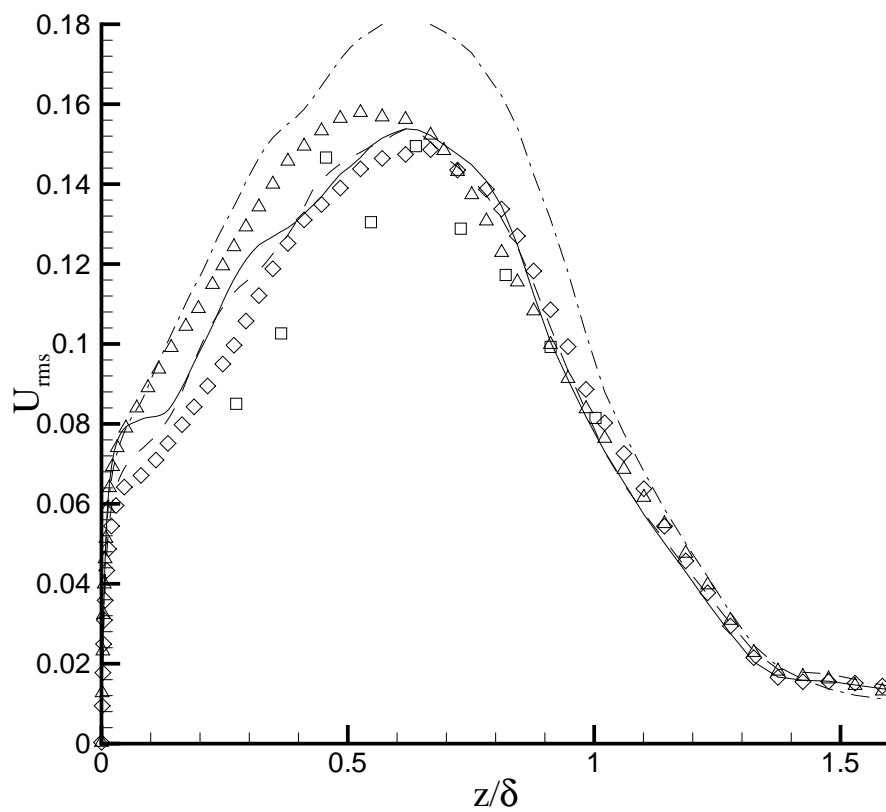


Figure 46: Rms velocity (A ($x = 326$ mm) —, A ($x = 320$ mm) —●—, B \triangle , C —, D \diamond , LDA \square)

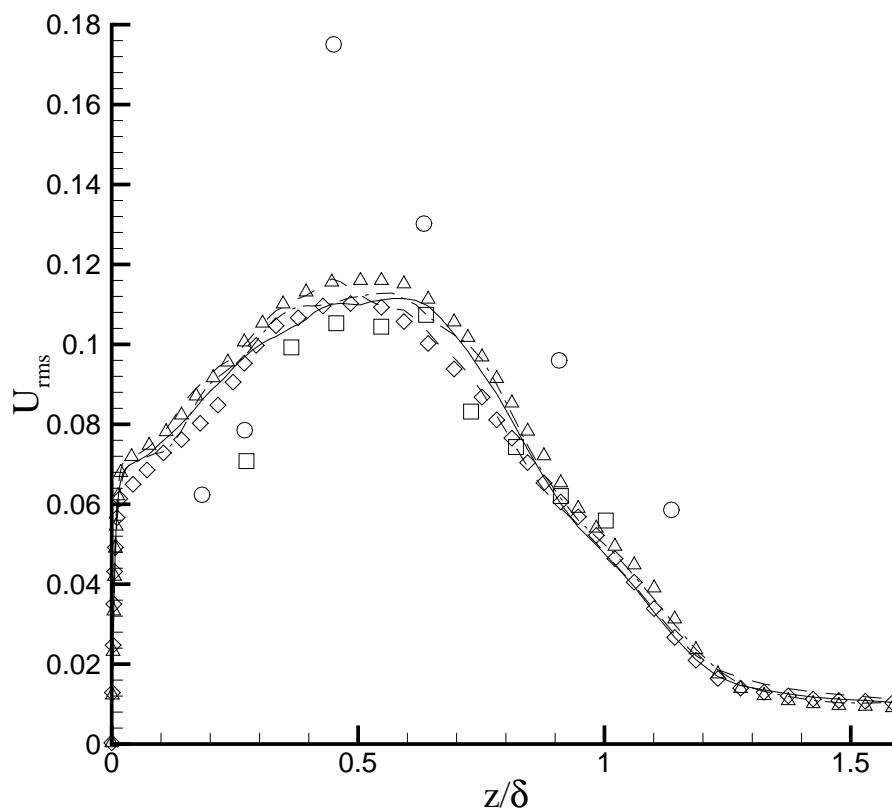


Figure 47: Rms velocity (A ($x = 351$ mm) —, A ($x = 345$ mm) —●—, B \triangle , C —, D \diamond , HWA \circ , LDA \square)

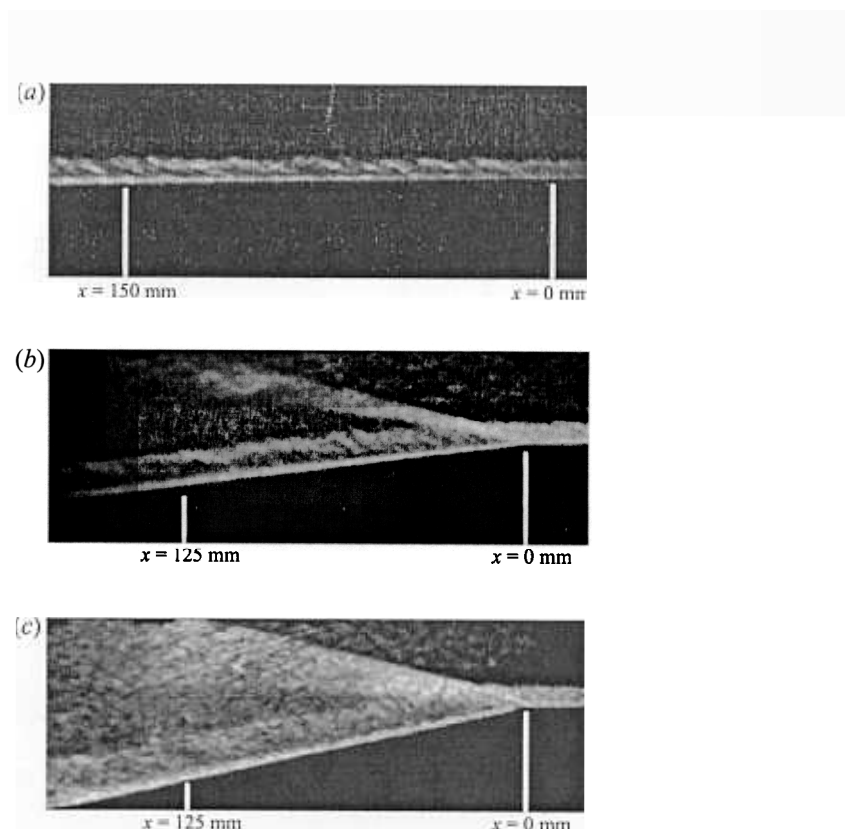


Figure 48: Instantaneous Schlieren images of (a) the flat-plate boundary layer, (b) 7° centered expansion, and (c) 14° centered expansion

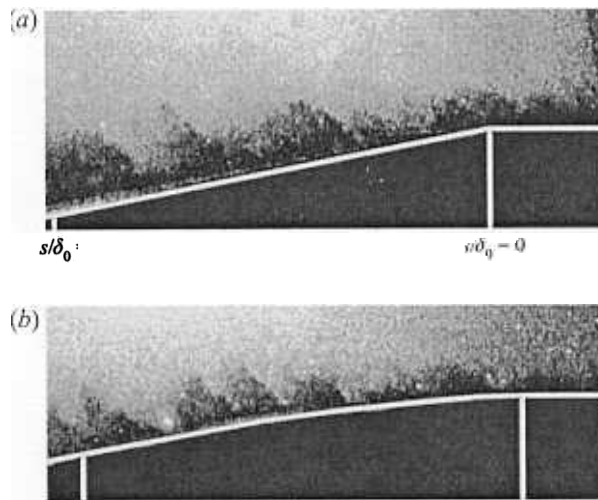


Figure 49: Instantaneous FRS visualization of (a) the 7° centered and (b) gradual expansion regions. The white lines indicate the position of the model surface.

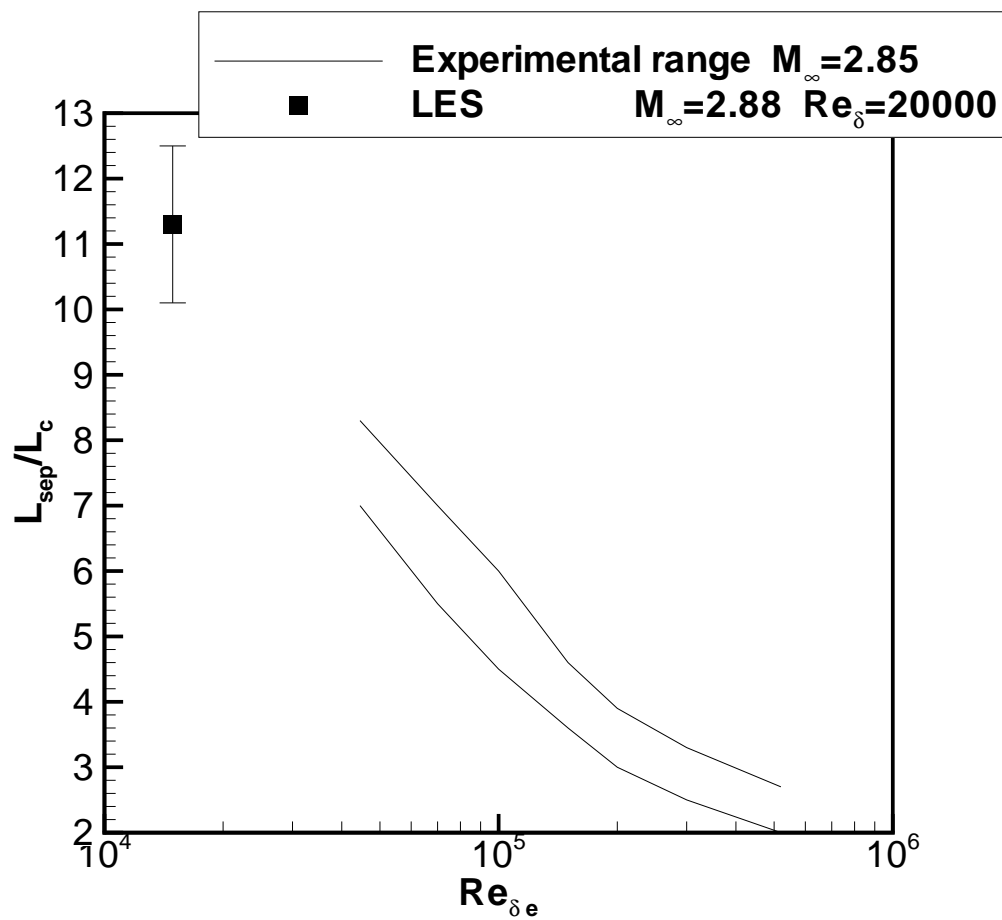


Figure 50: Separation length

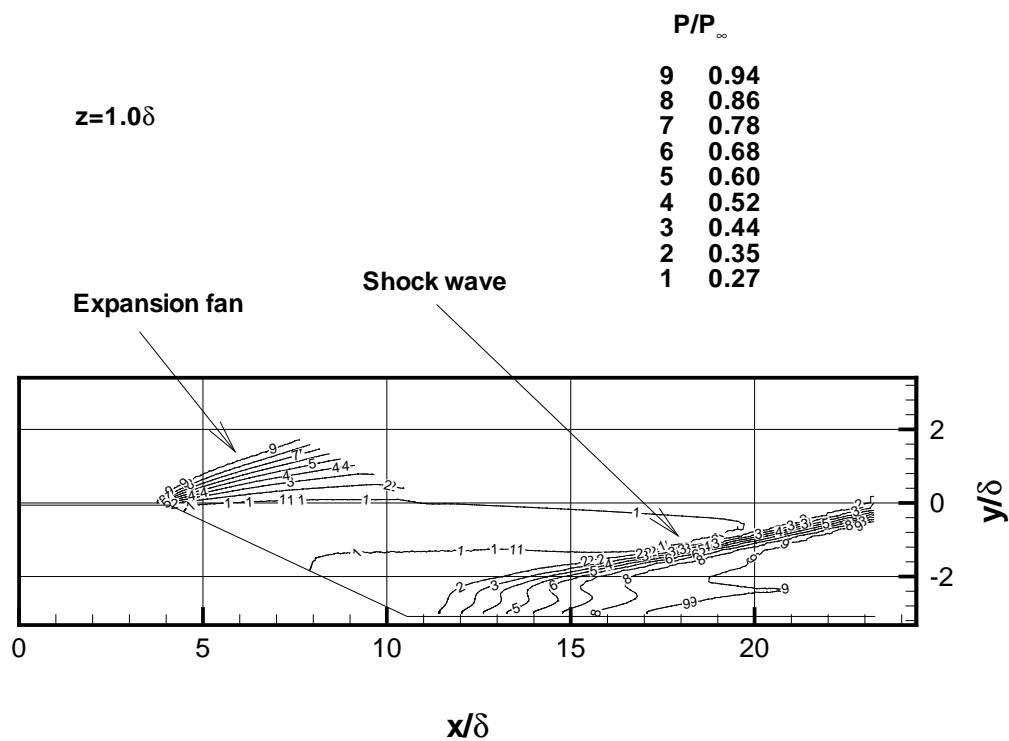


Figure 51: Mean static pressure

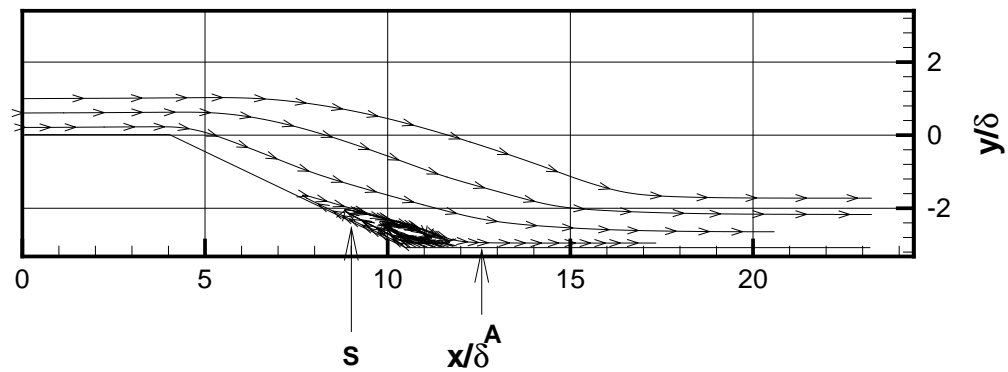


Figure 52: Mean streamlines

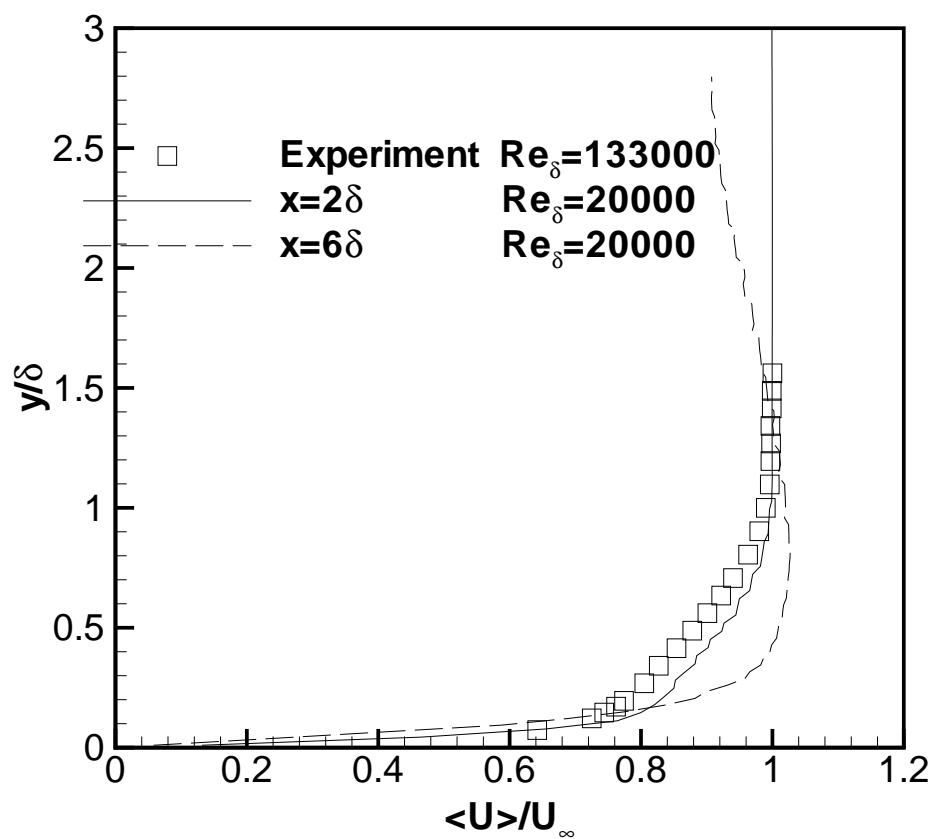


Figure 53: Mean velocity

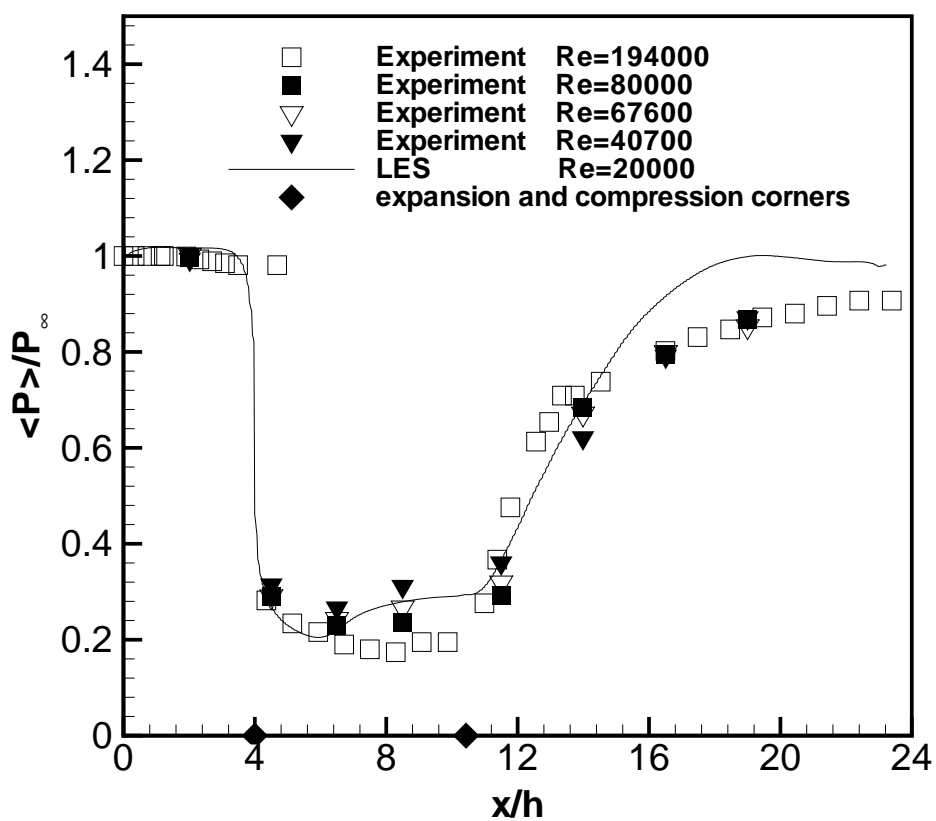


Figure 54: Surface pressure

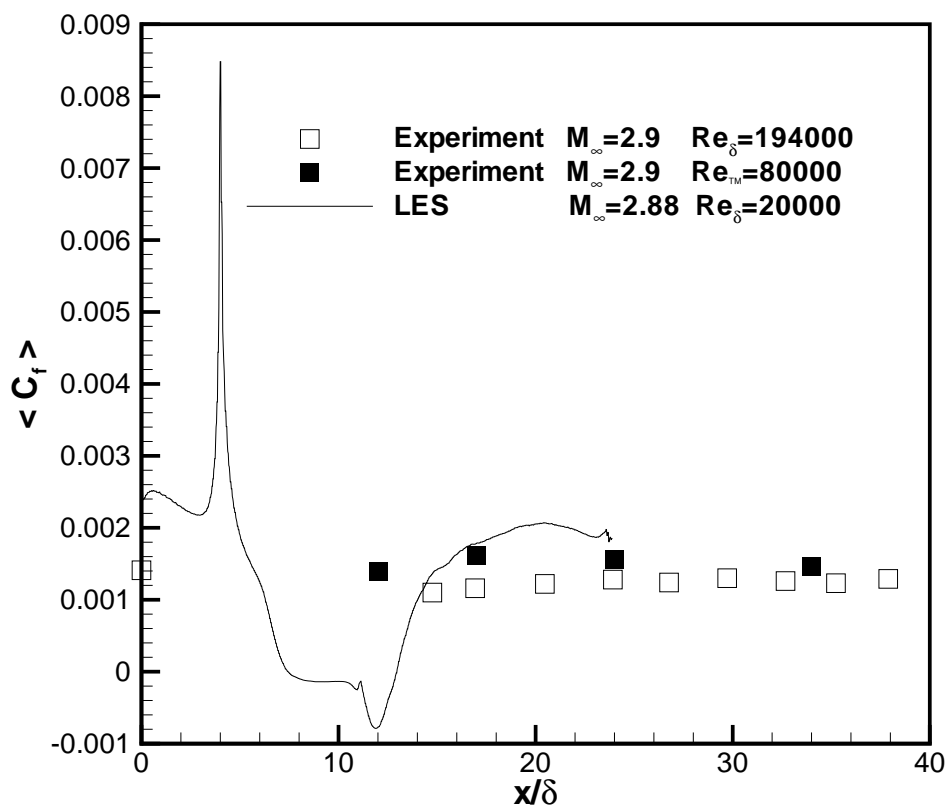


Figure 55: Skin friction coefficient

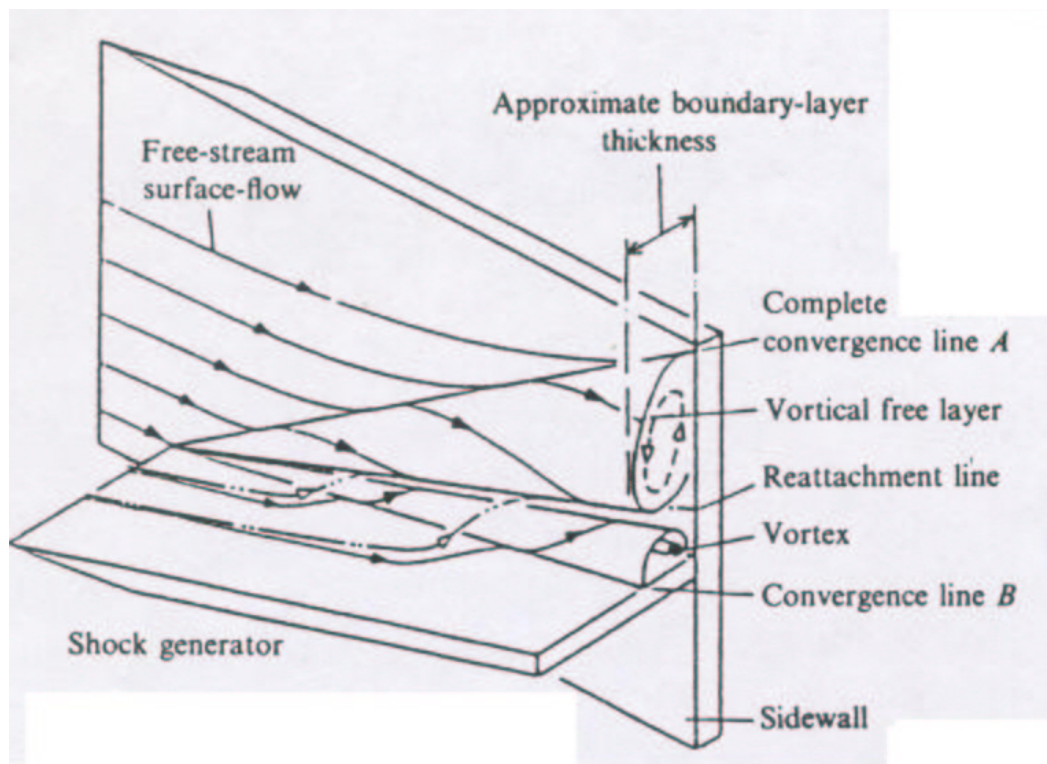


Figure 56: Flow model proposed by Kubota and Stollery[146]

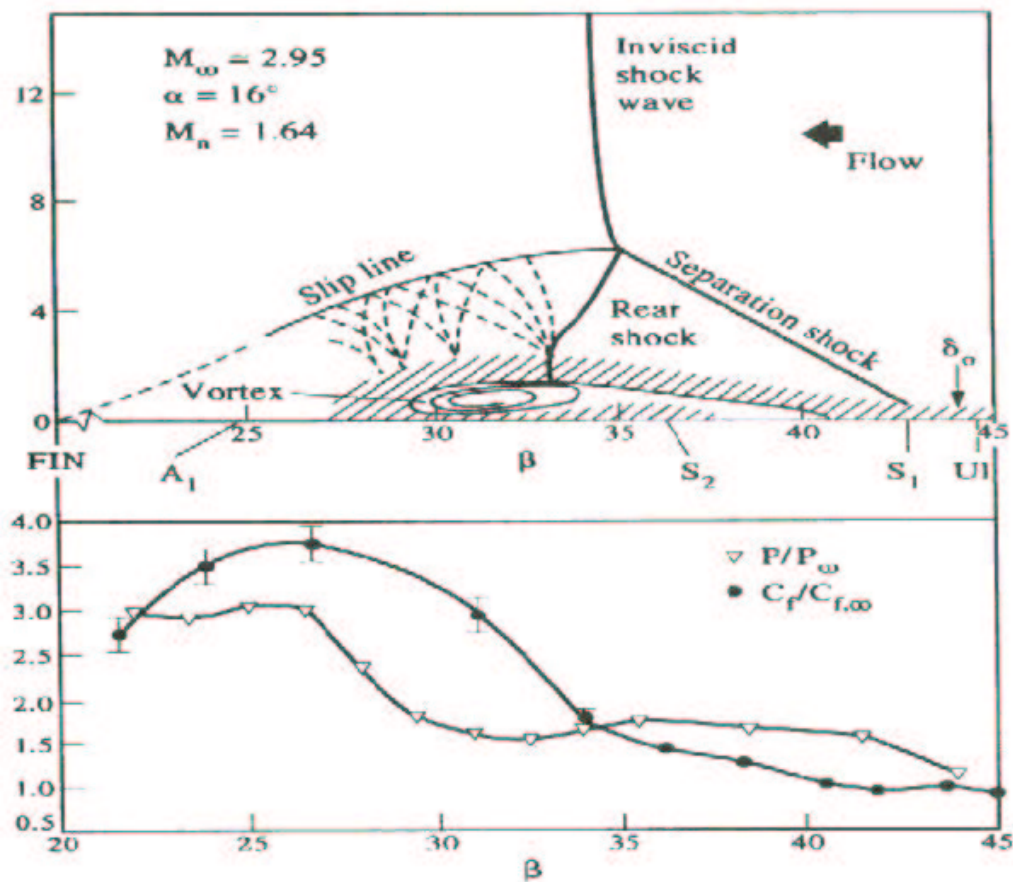


Figure 57: Flow model of Alvi and Settles[148]

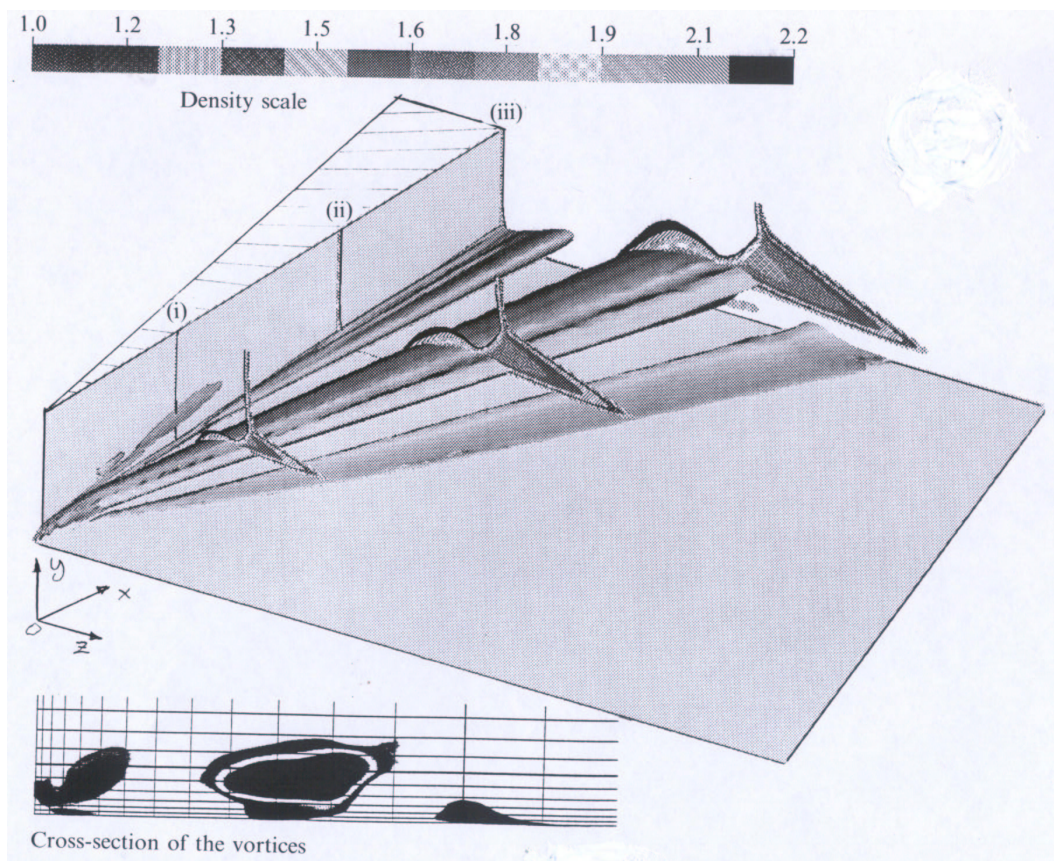


Figure 58: Perspective view of the conical separation vortices and of the shock waves (Panaras [150])

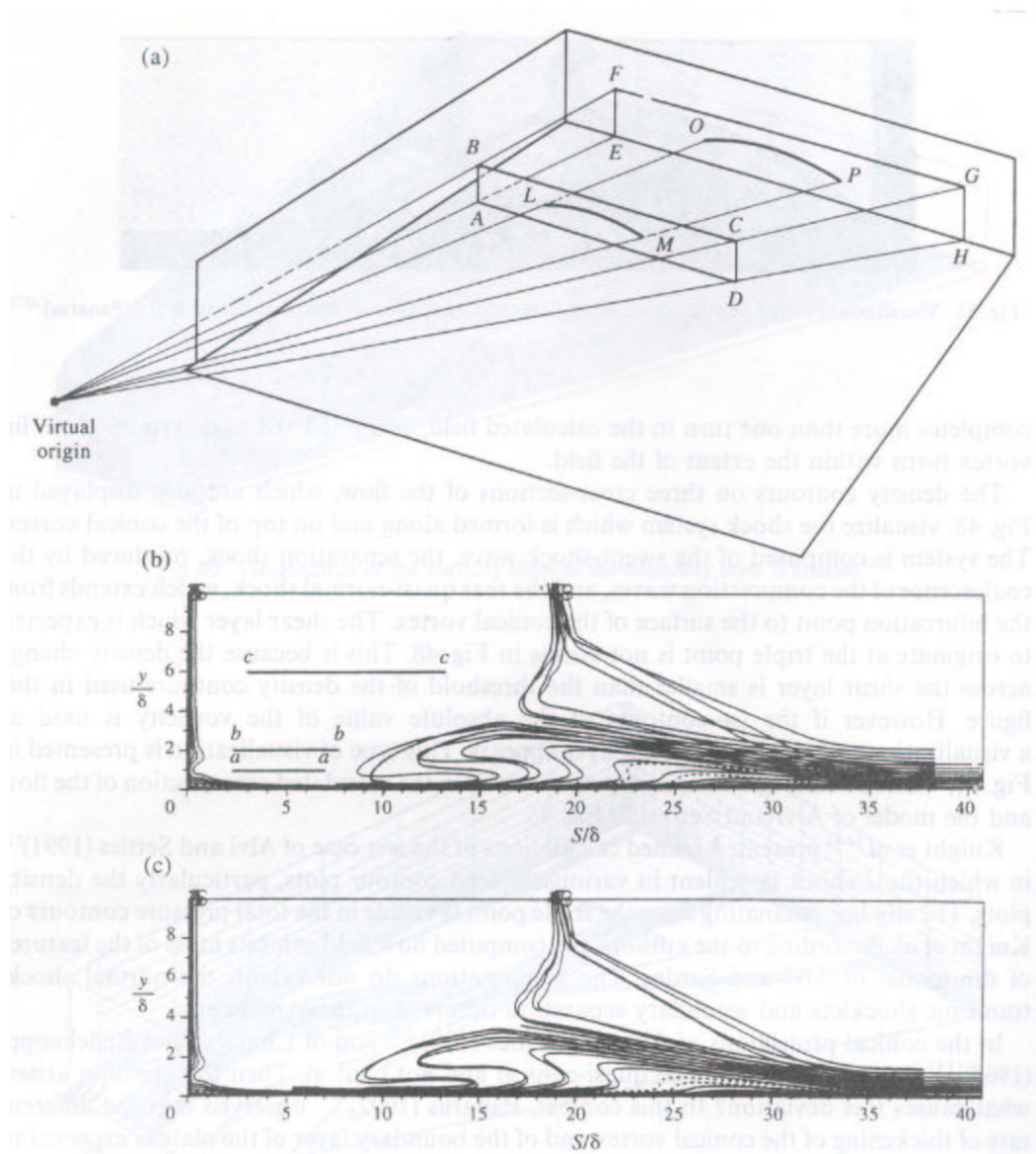


Figure 59: Conical projections of sections of the flow on the outflow plane (Panaras[150])

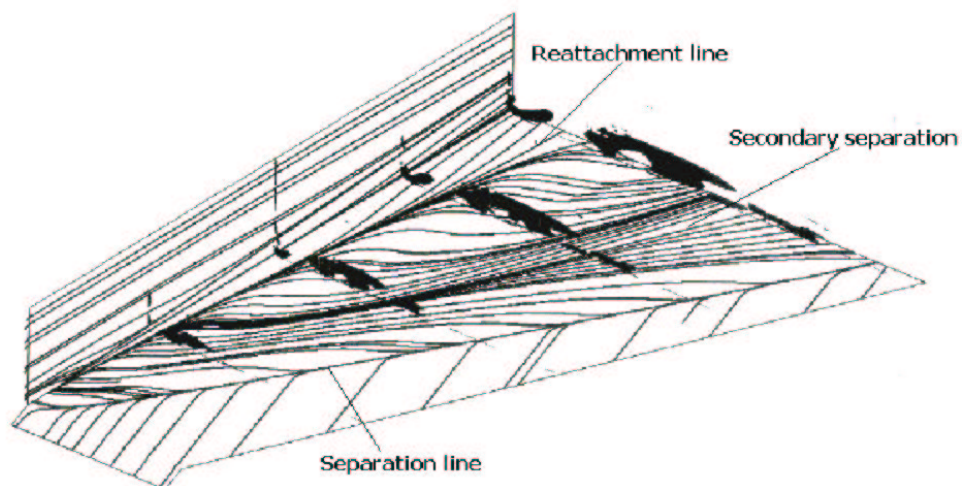


Figure 60: Skin friction lines and cross-section of the vortices (Panaras and Stanewsky[155])

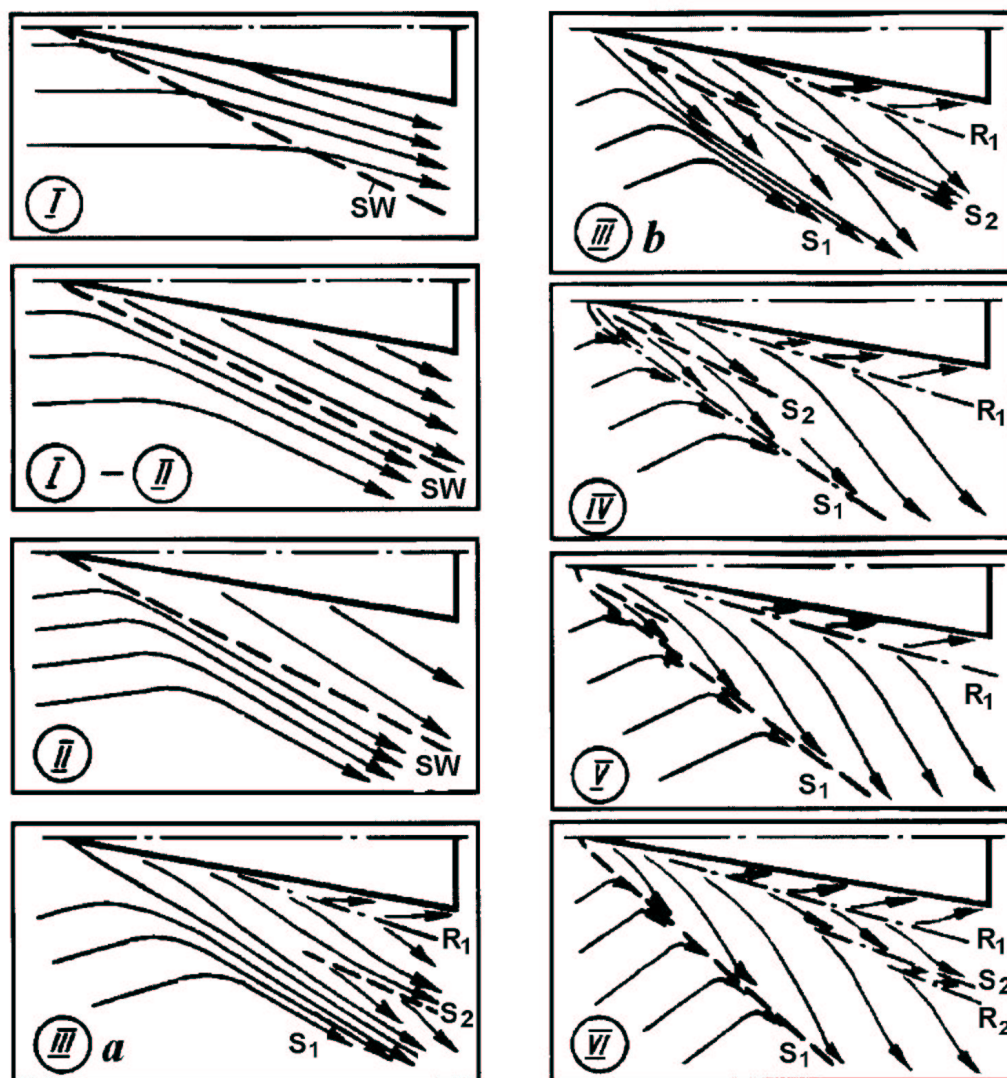
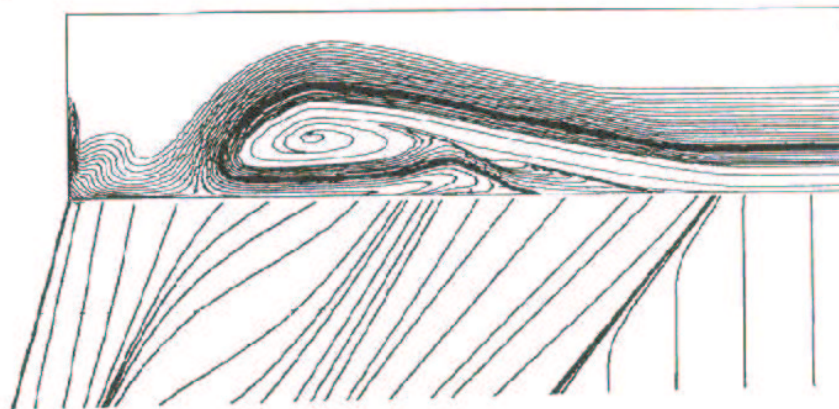
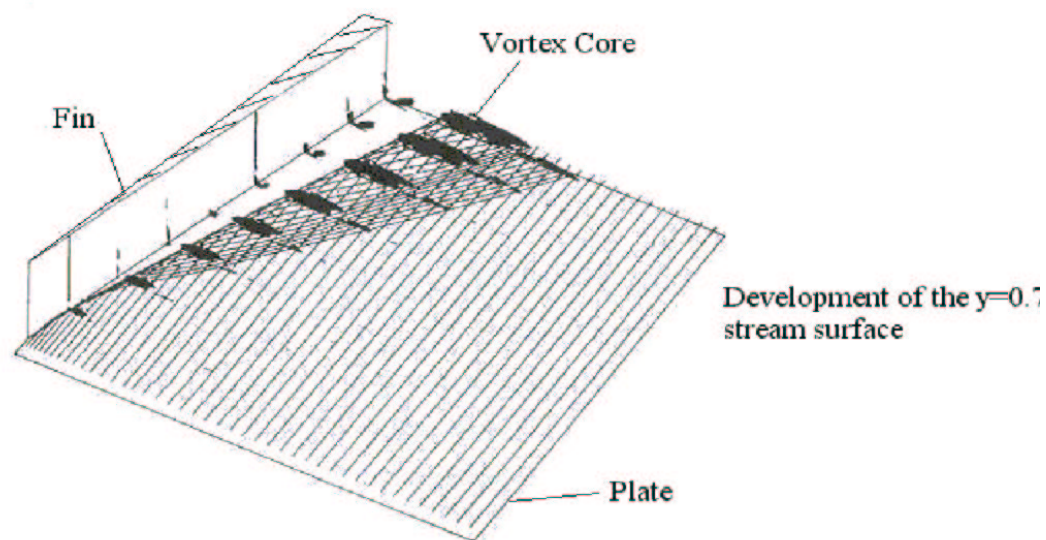


Figure 61: 3-D single fin regimes (Zheltovodov *et al*[156])

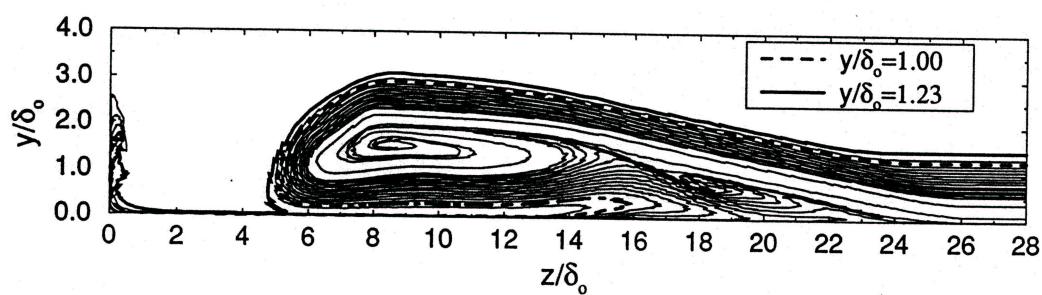


(a) Cross-section of the flow where the thick line denotes the $y = 0.7\delta$ stream line

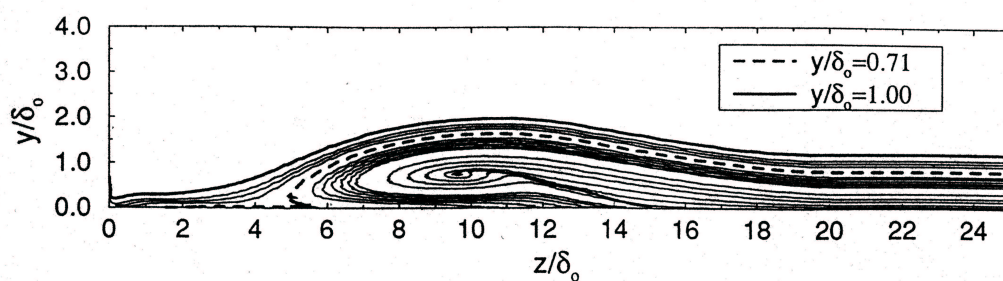


(b) Perspective development of the $y = 0.7\delta$ stream surface

Figure 62: Structure of the separated flow in a swept shock/turbulent boundary-layer interaction



(a) $M_\infty = 4.0$, $\alpha = 20^\circ$



(b) $M_\infty = 3.0$, $\alpha = 10^\circ$

Figure 63: Cross-sections of various flows (Panaras [2])

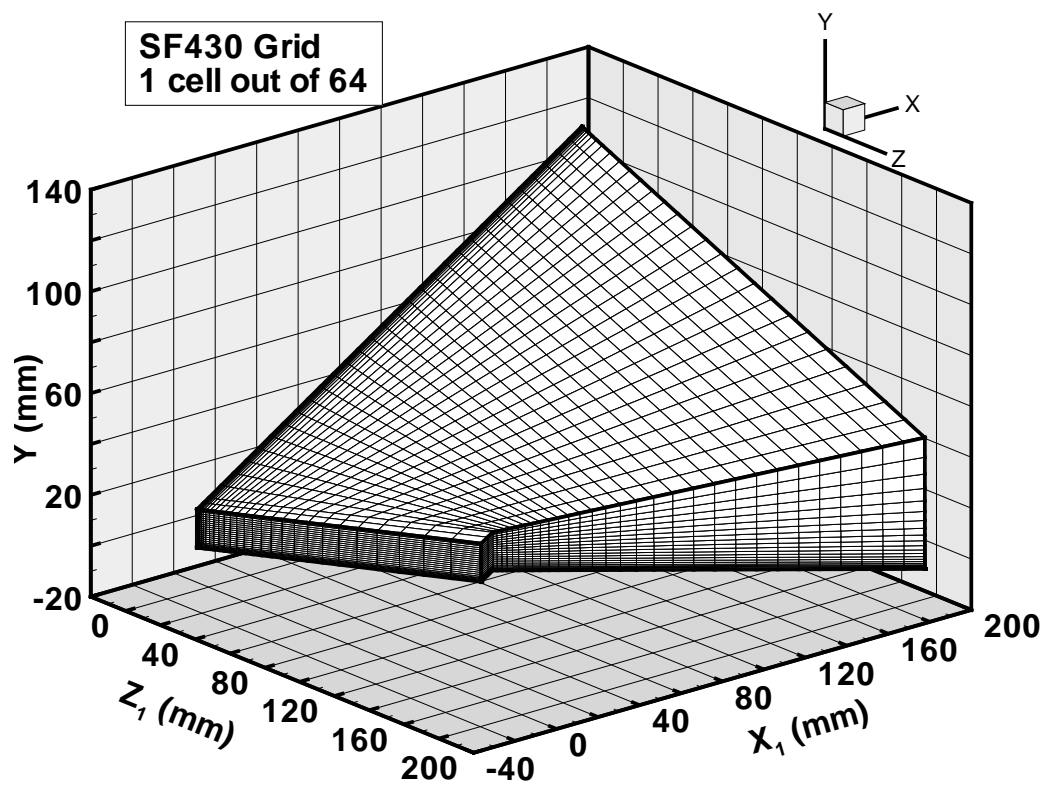


Figure 64: Grid for 3-D single fin

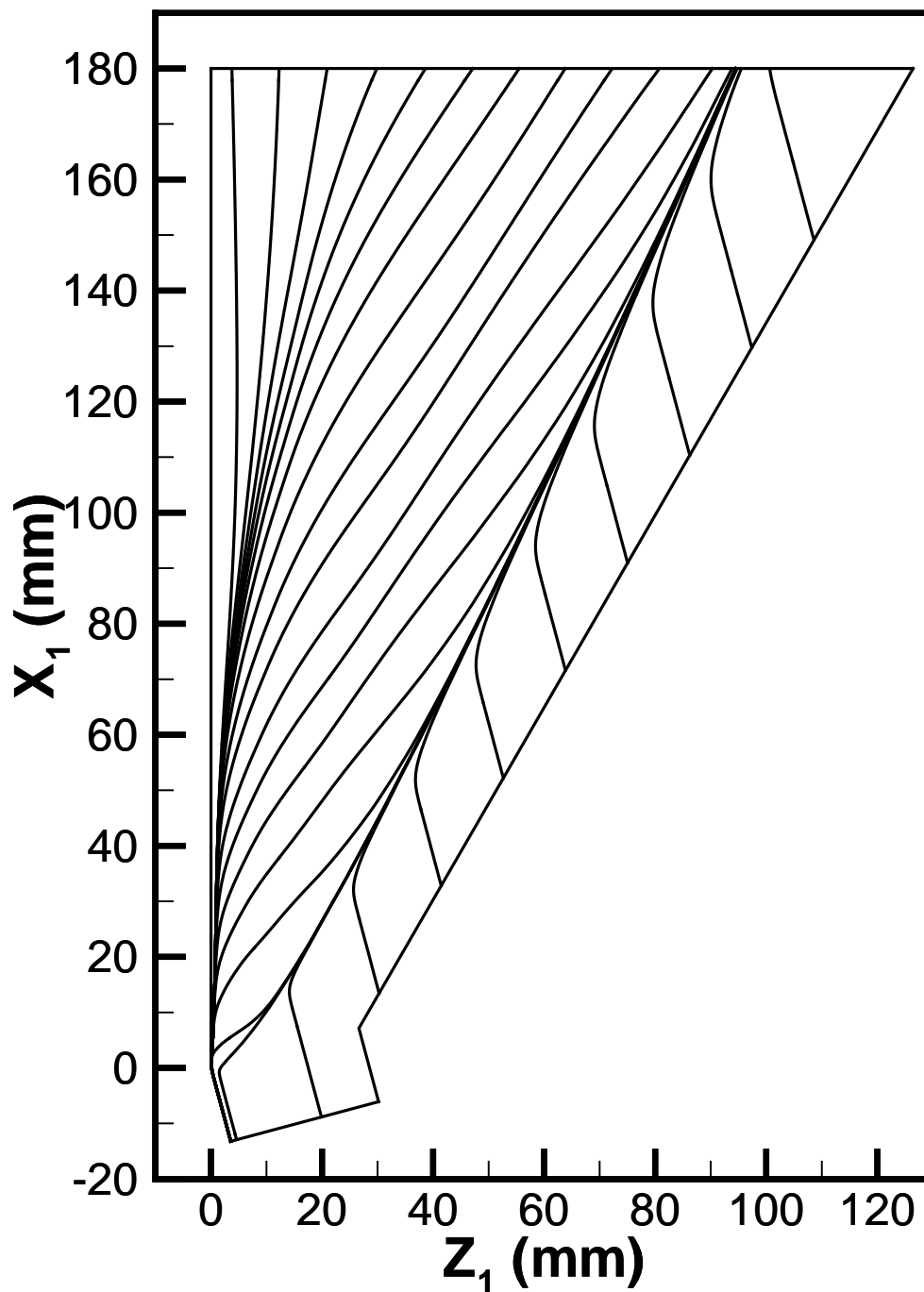


Figure 65: Surface streamlines for Case 1 (WI)

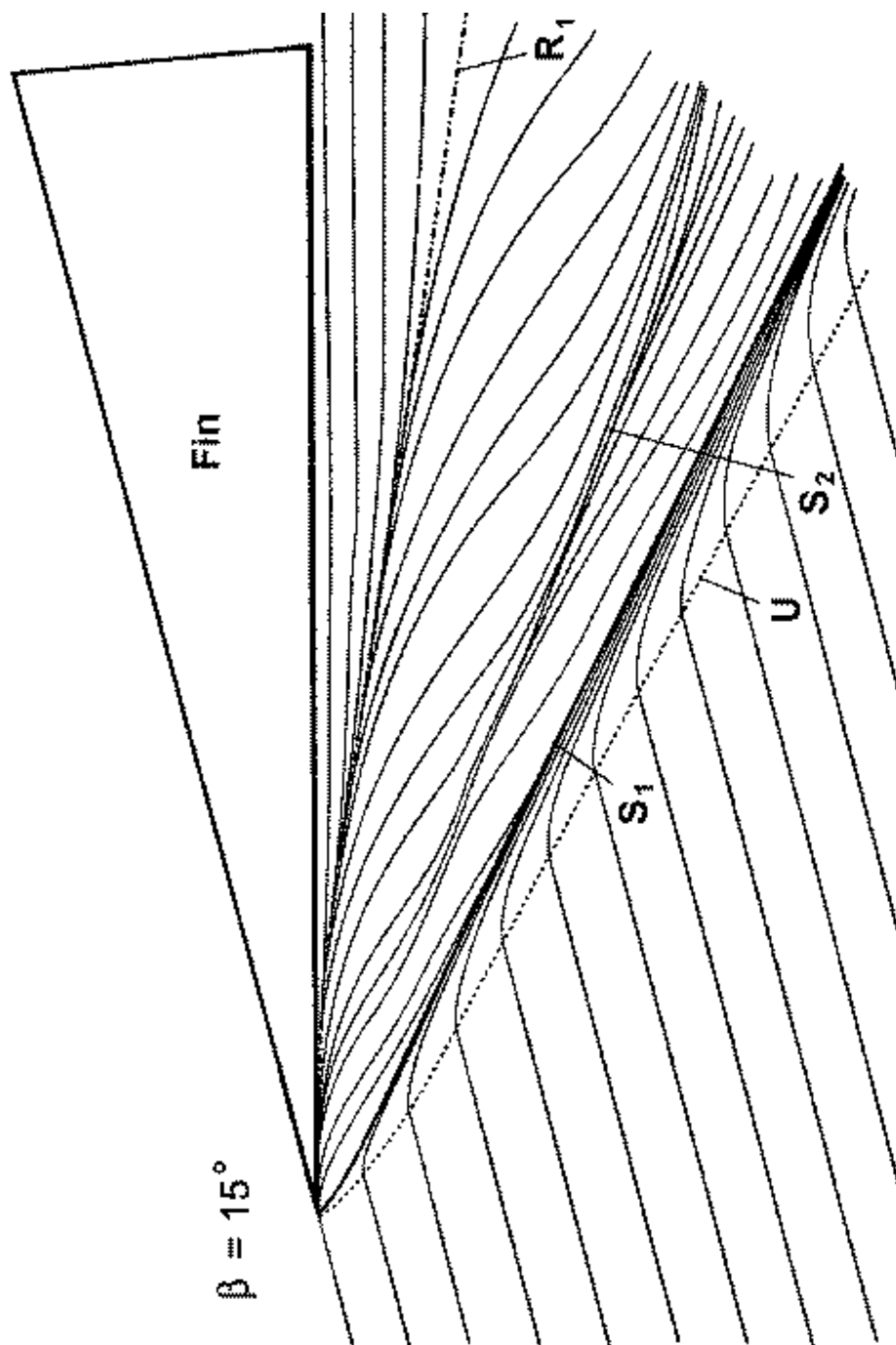


Figure 66: Surface streamlines for Case 1 (exper)

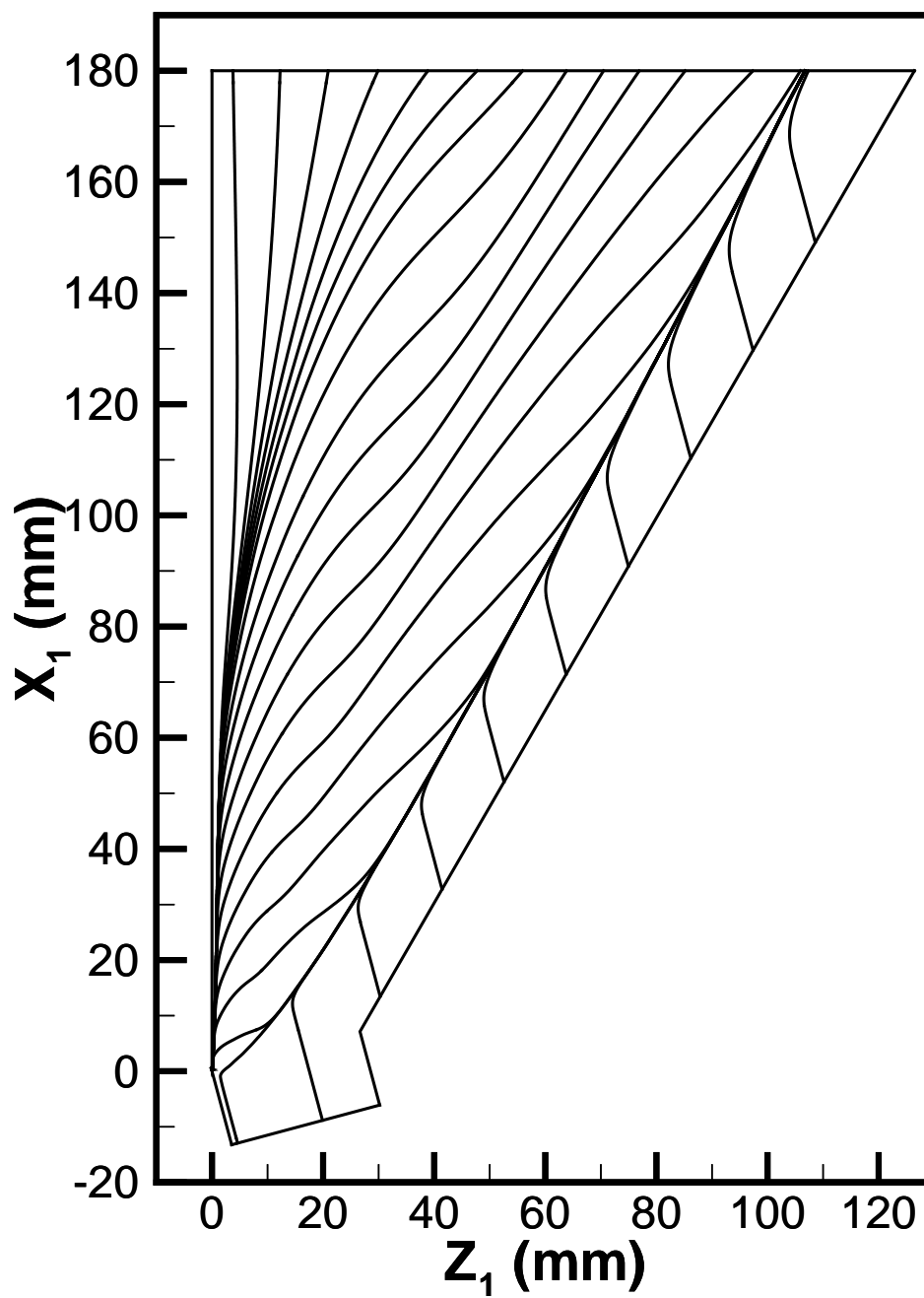


Figure 67: Surface streamlines for Case 1 (WD+)

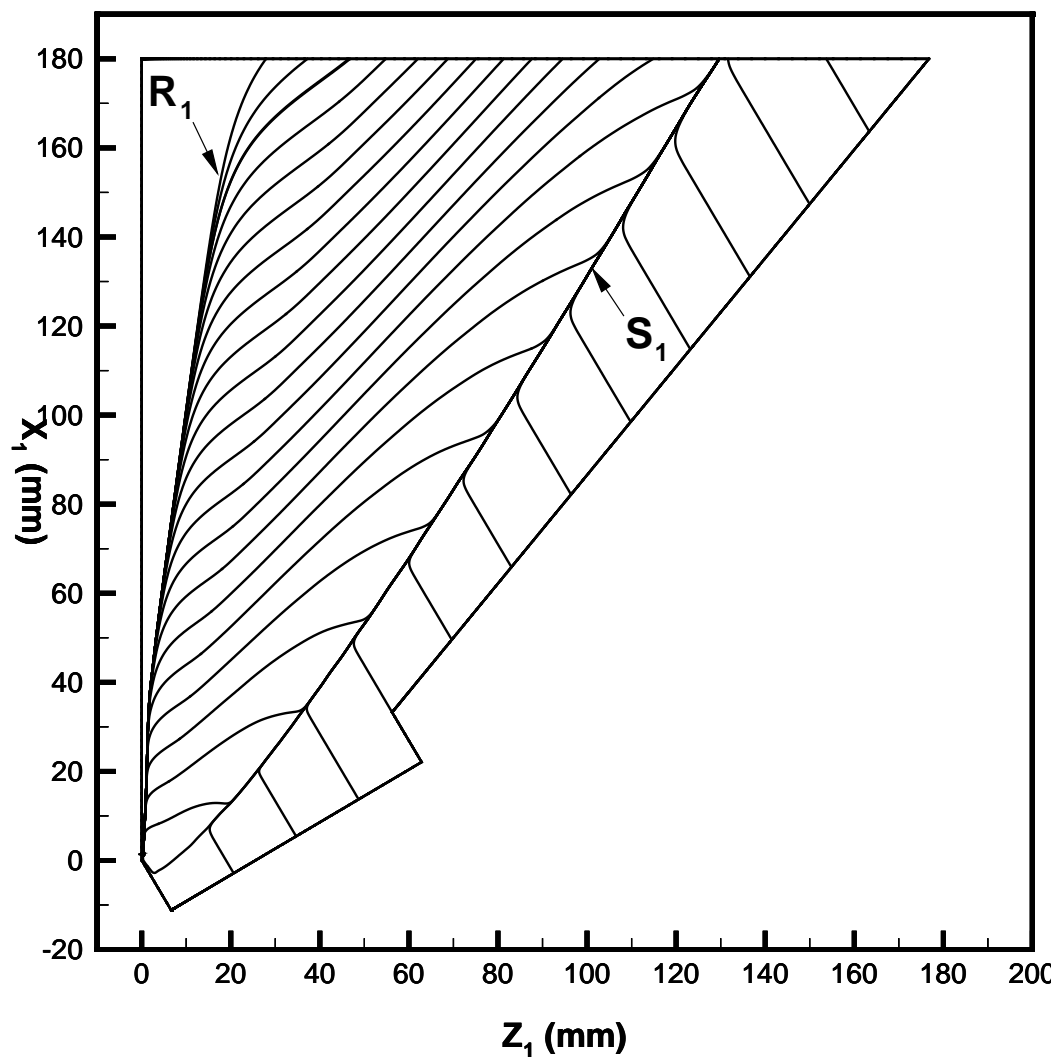


Figure 68: Surface streamlines for Case 3 (WI)

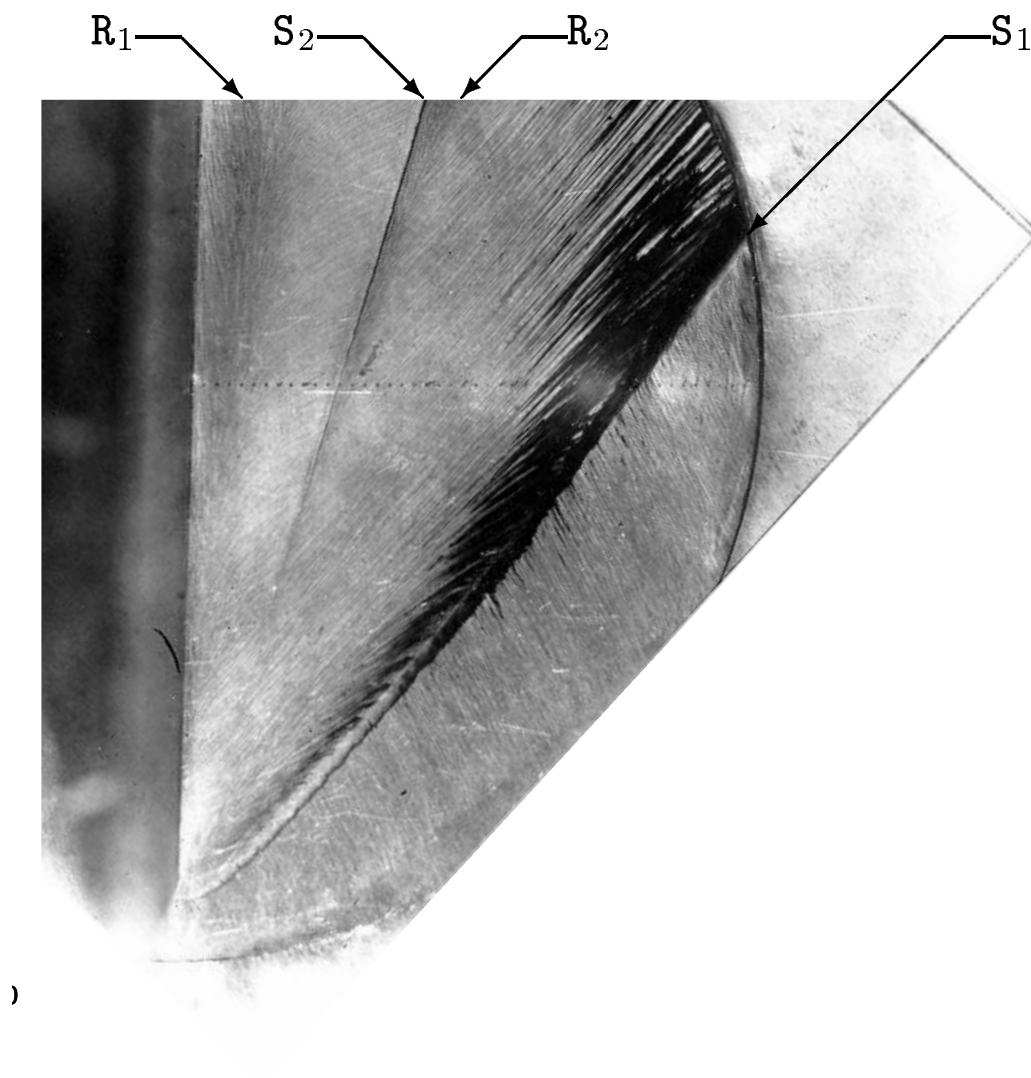


Figure 69: Surface streamlines for Case 3 (exper)

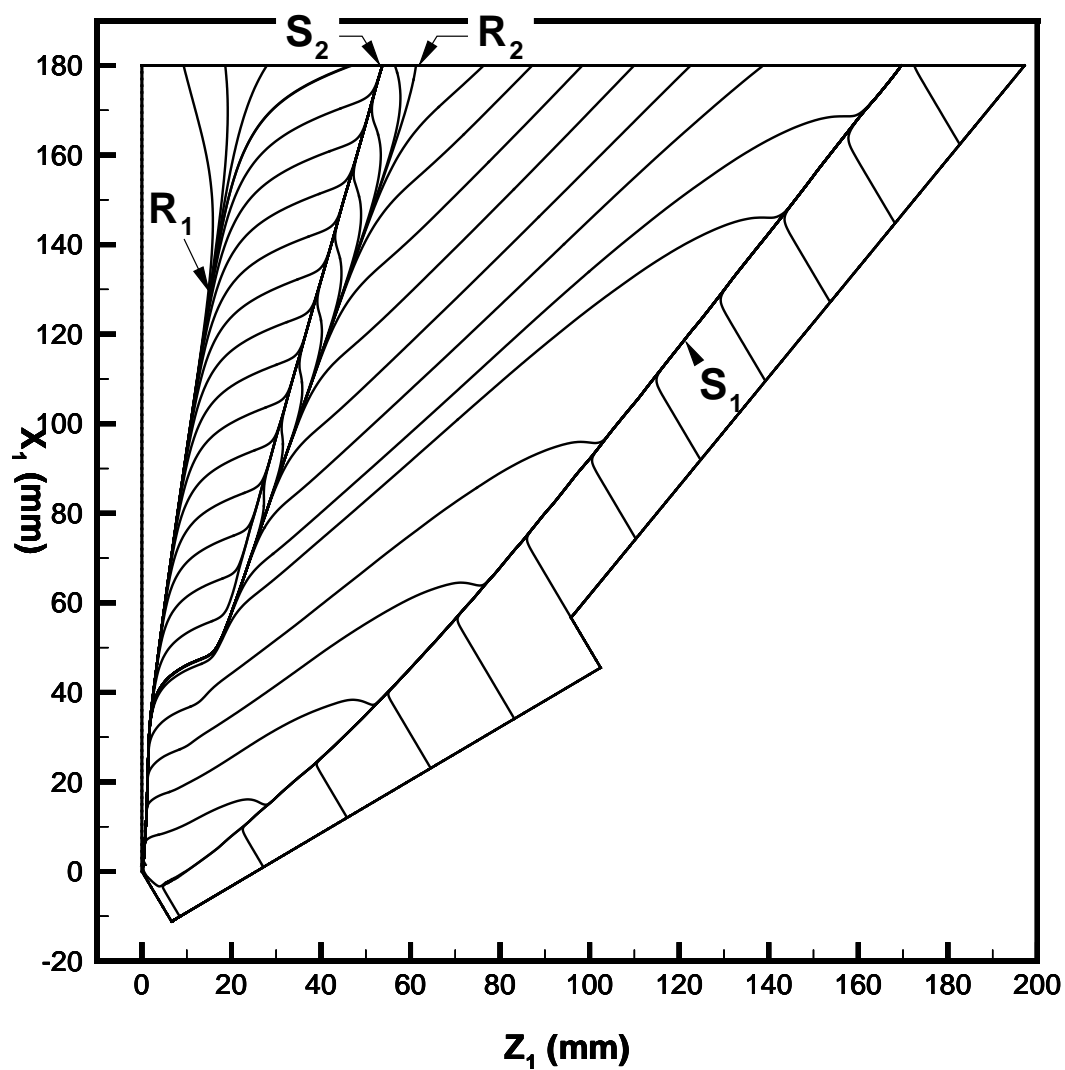


Figure 70: Surface streamlines for Case 3 (WD+)

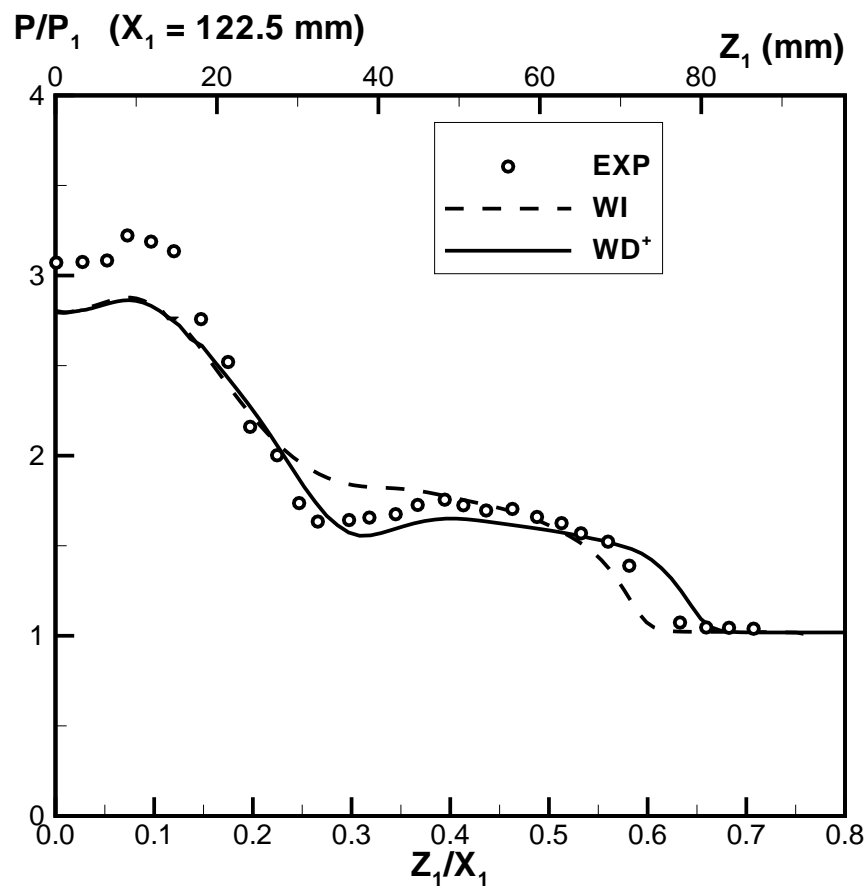


Figure 71: Surface pressure for Case 1

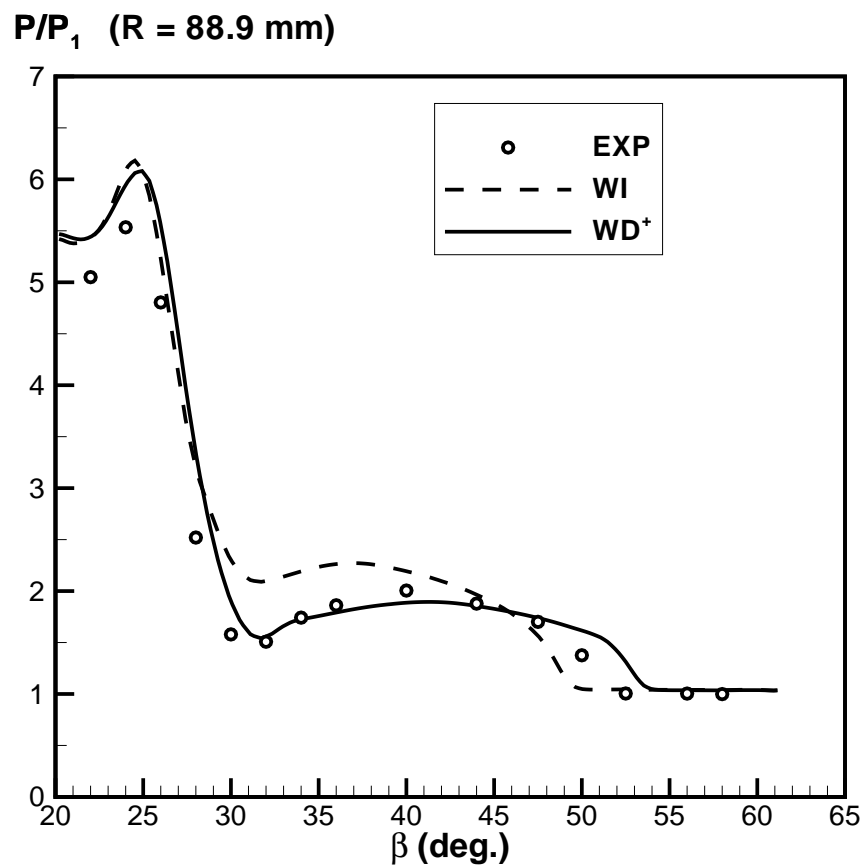


Figure 72: Surface pressure for Case 2

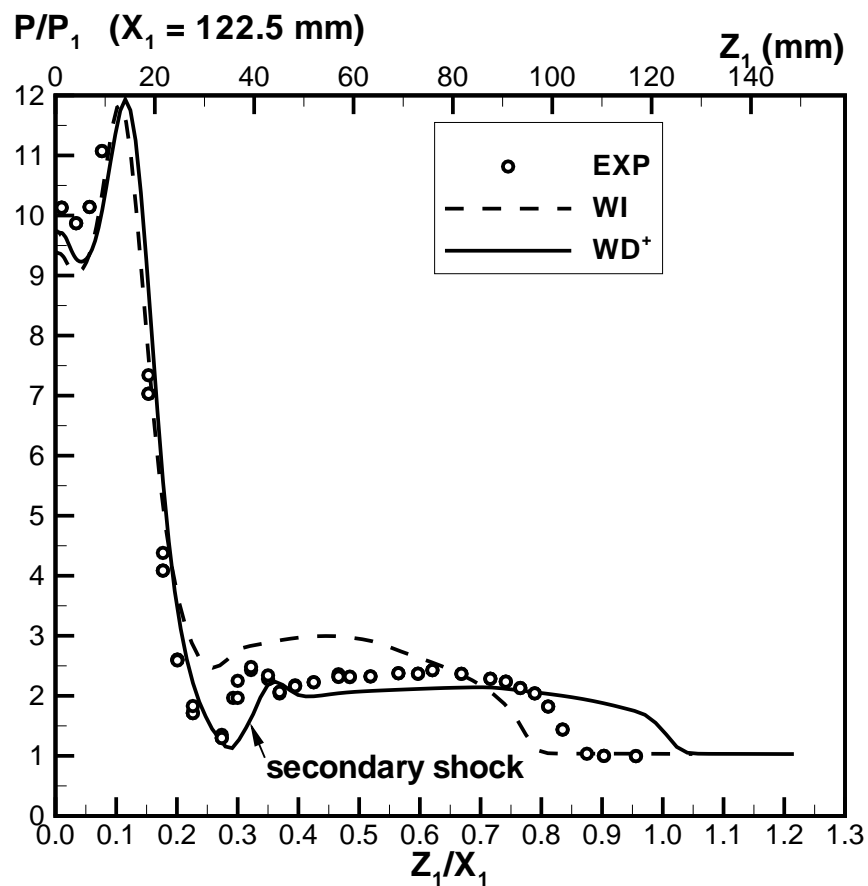


Figure 73: Surface pressure for Case 3

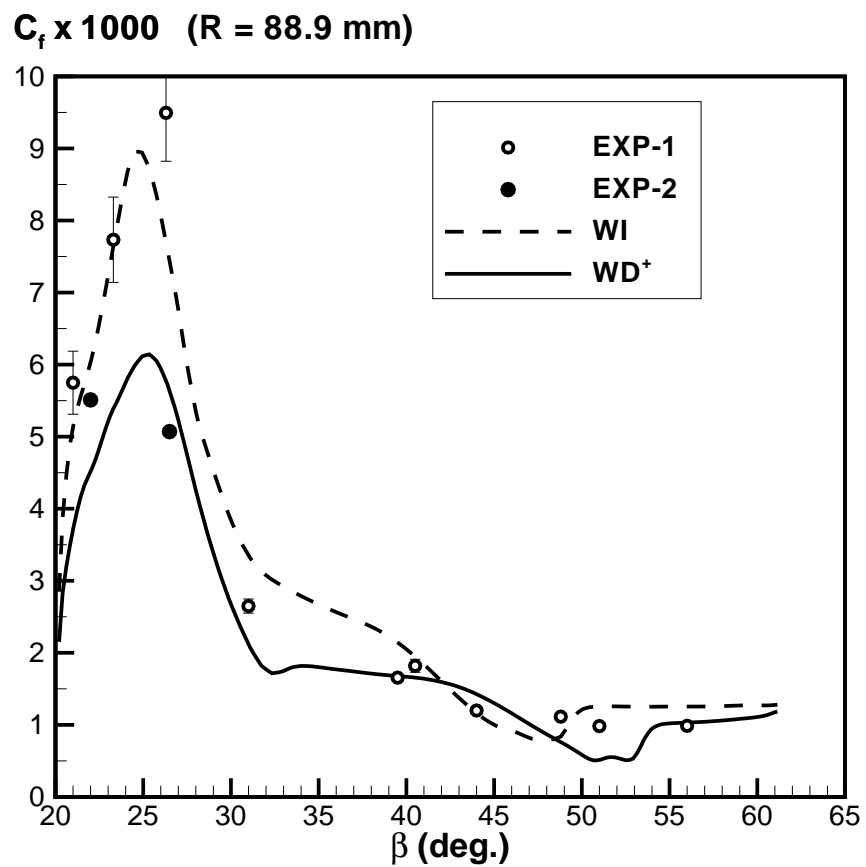


Figure 74: Skin friction for Case 2

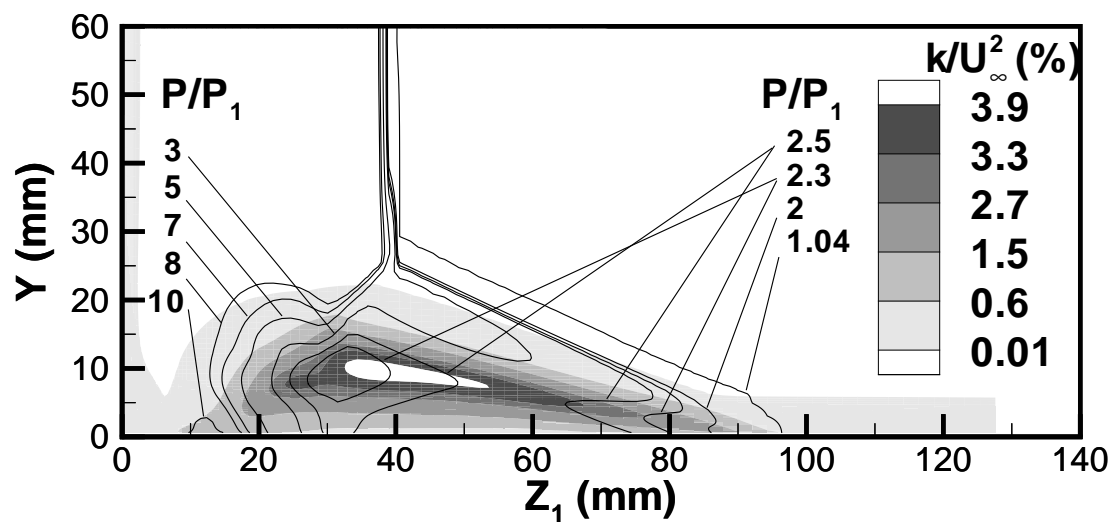


Figure 75: Turbulence kinetic energy for Case 3 (WI)

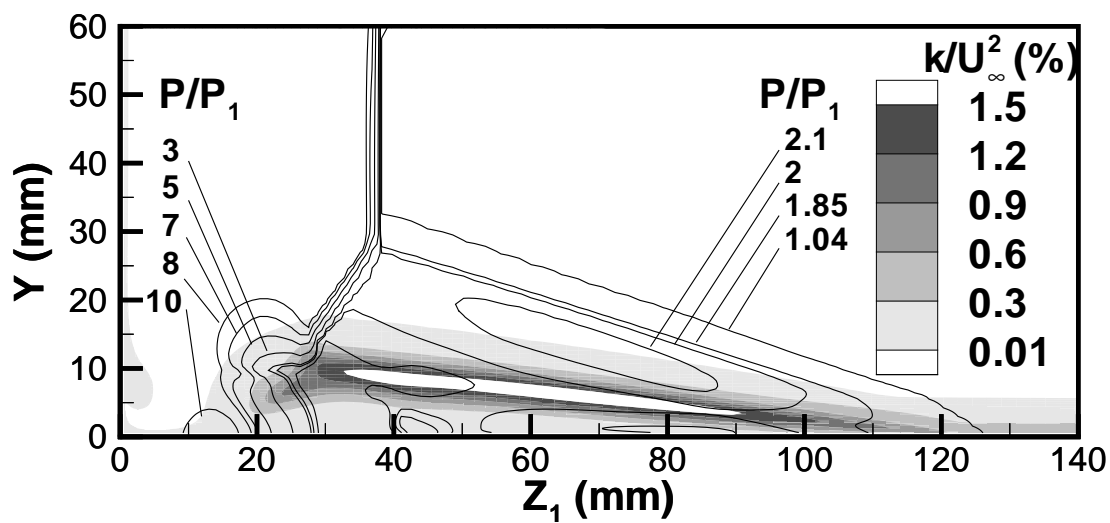


Figure 76: Turbulence kinetic energy for Case 3 (WD+)

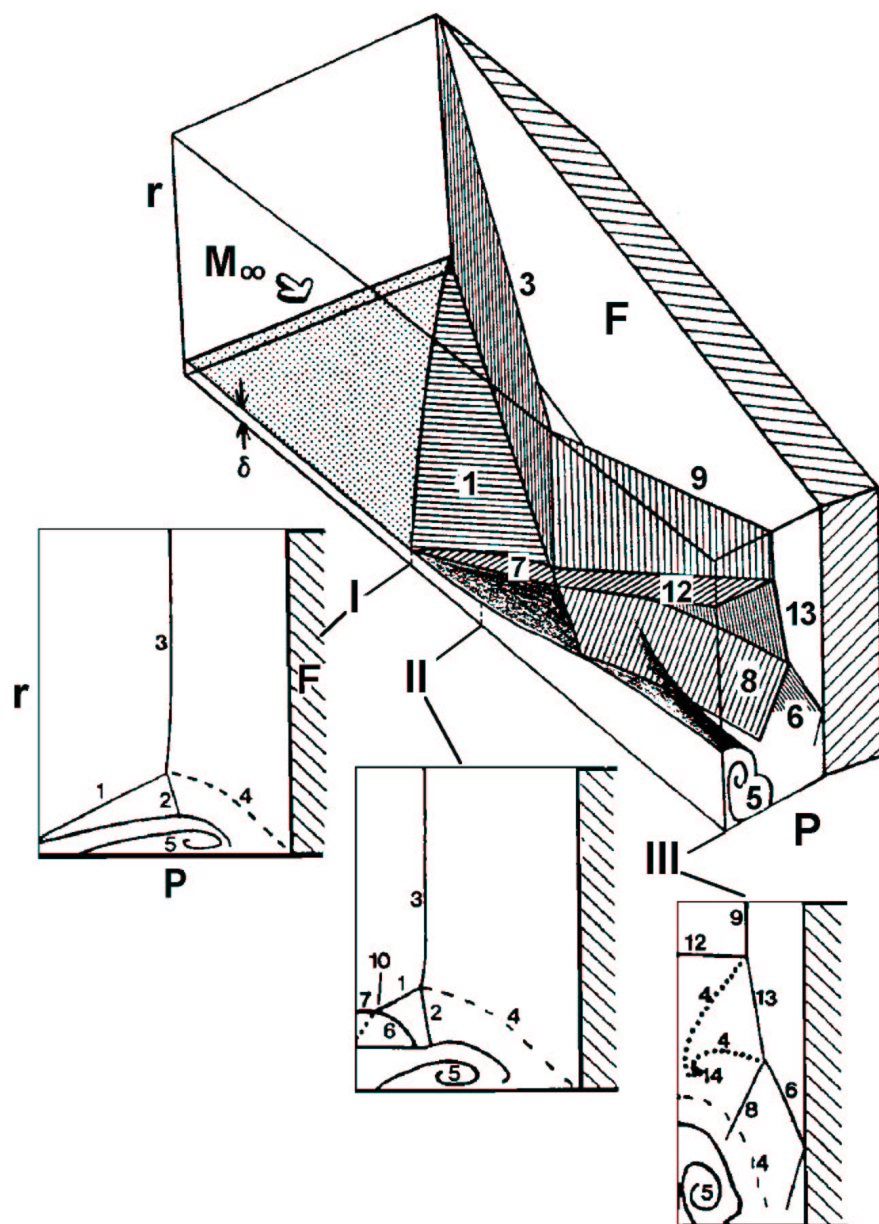


Figure 77: 3-D Double Fin Flow Structure [177, 173, 178]

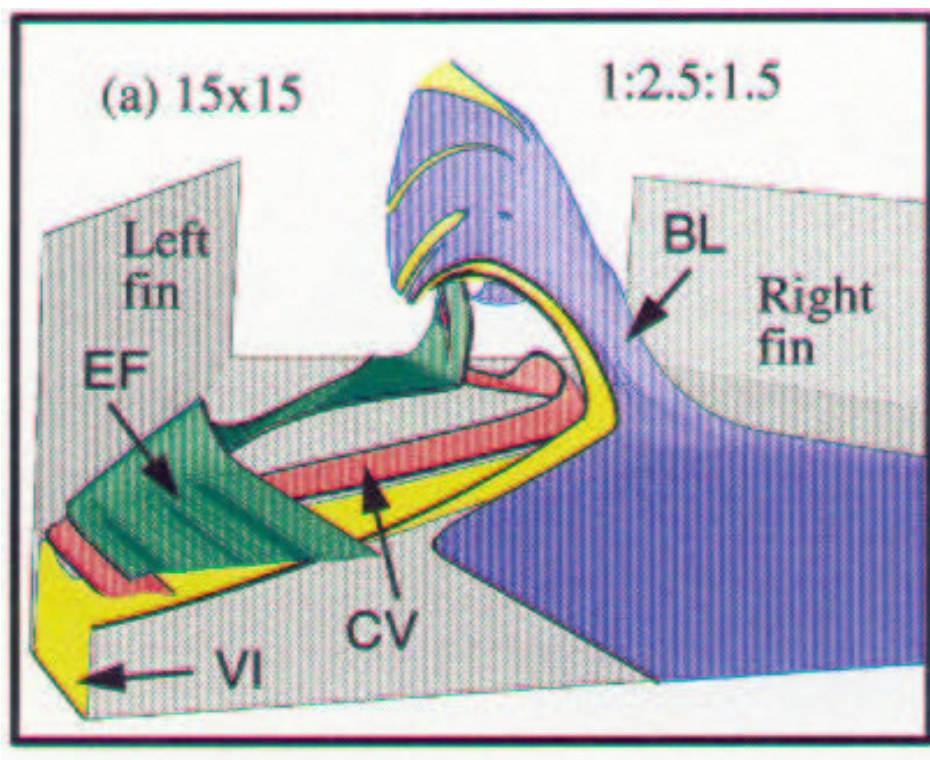


Figure 78: 3-D Double Fin Flow Structure [189, 192, 193, 197]

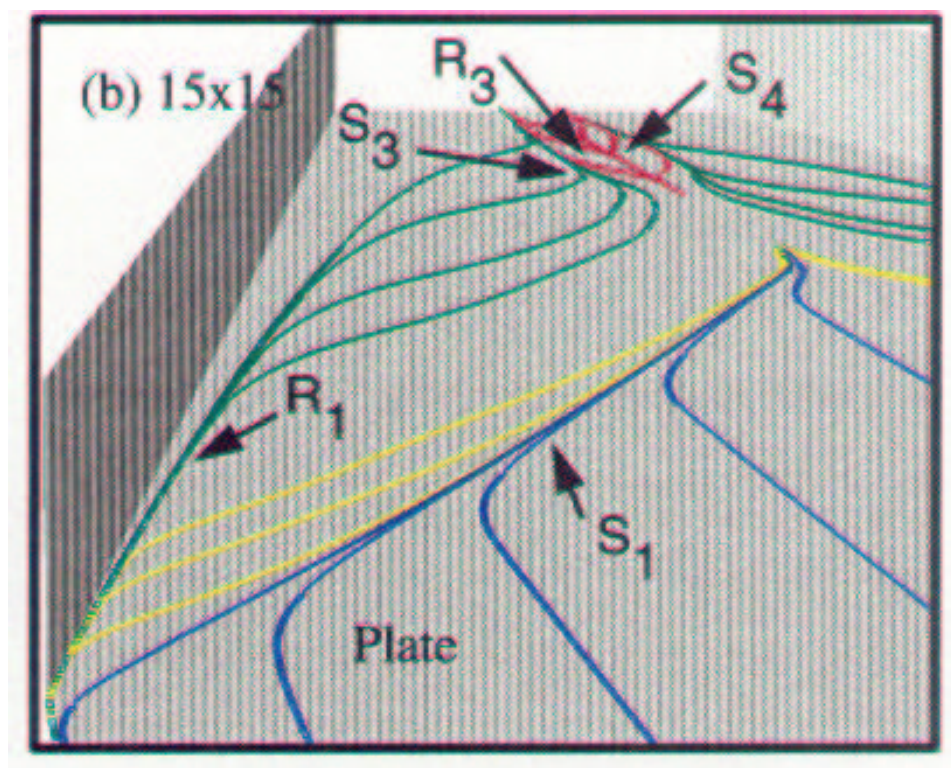


Figure 79: 3-D Double Fin Flow Structure [189, 192, 193, 197]

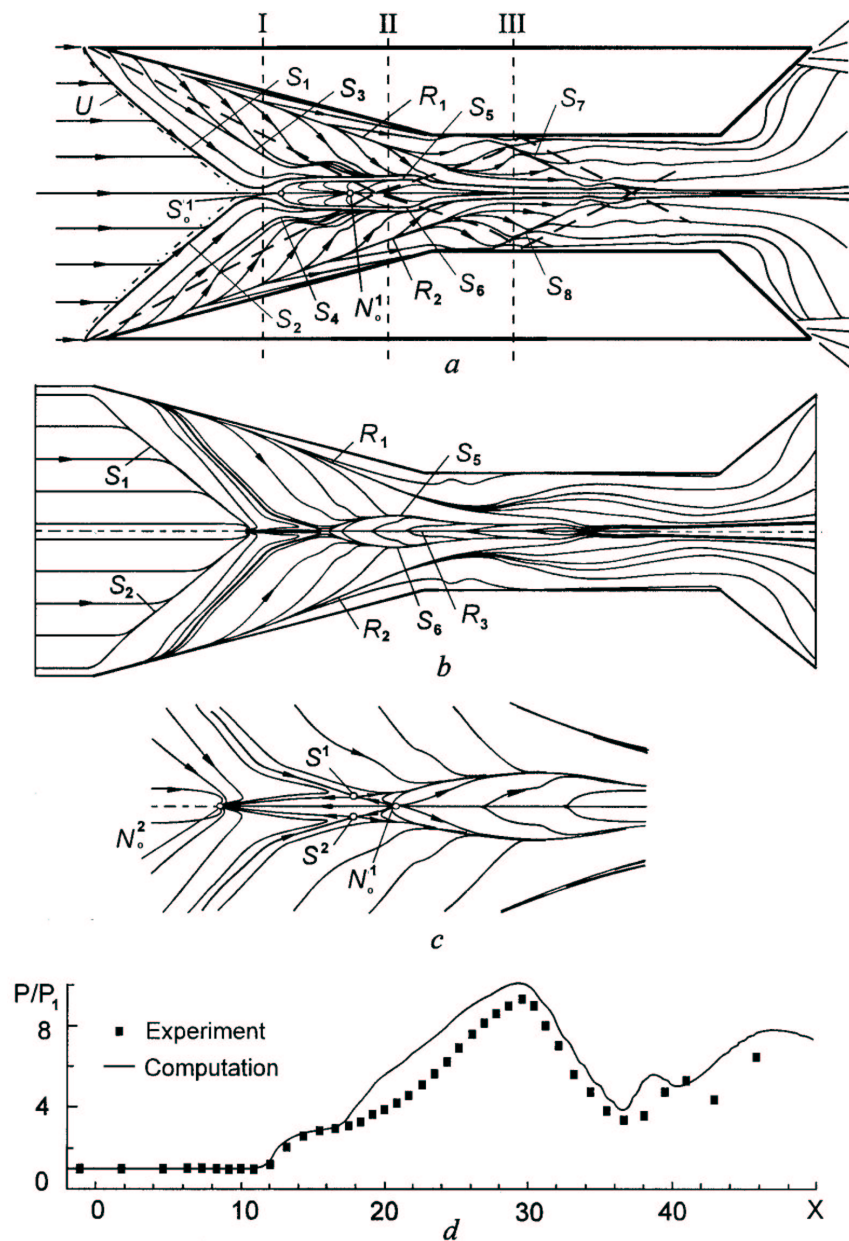


Figure 80: 3-D Double Fin Flow Structure [189, 192, 193, 197]

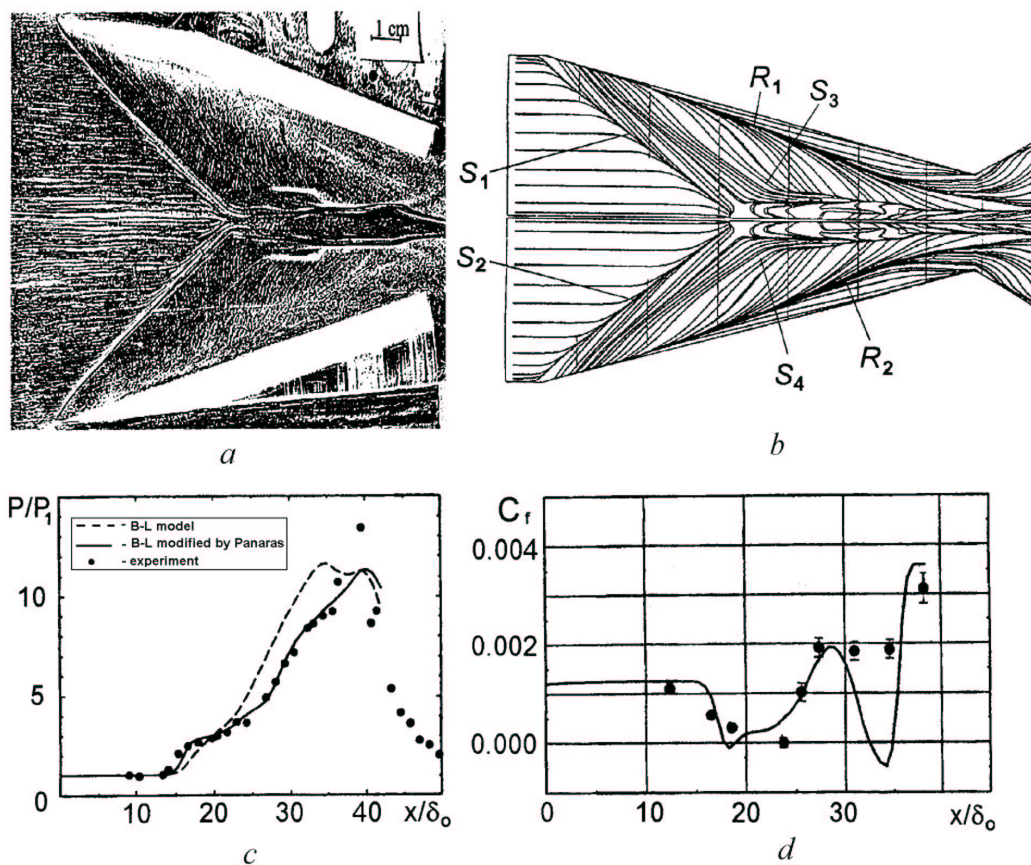


Figure 81: 3-D Double Fin Flow Structure [159]

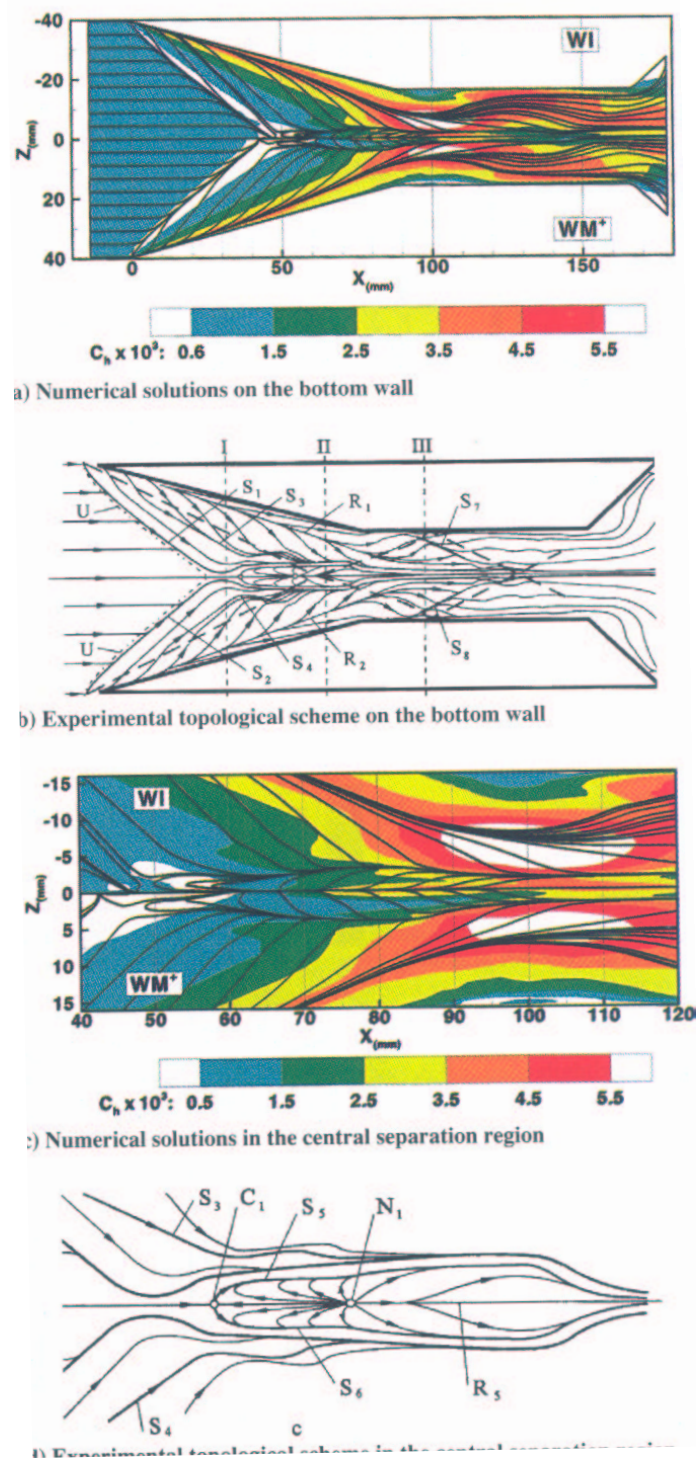


Figure 82: Topology, skin friction and heat transfer

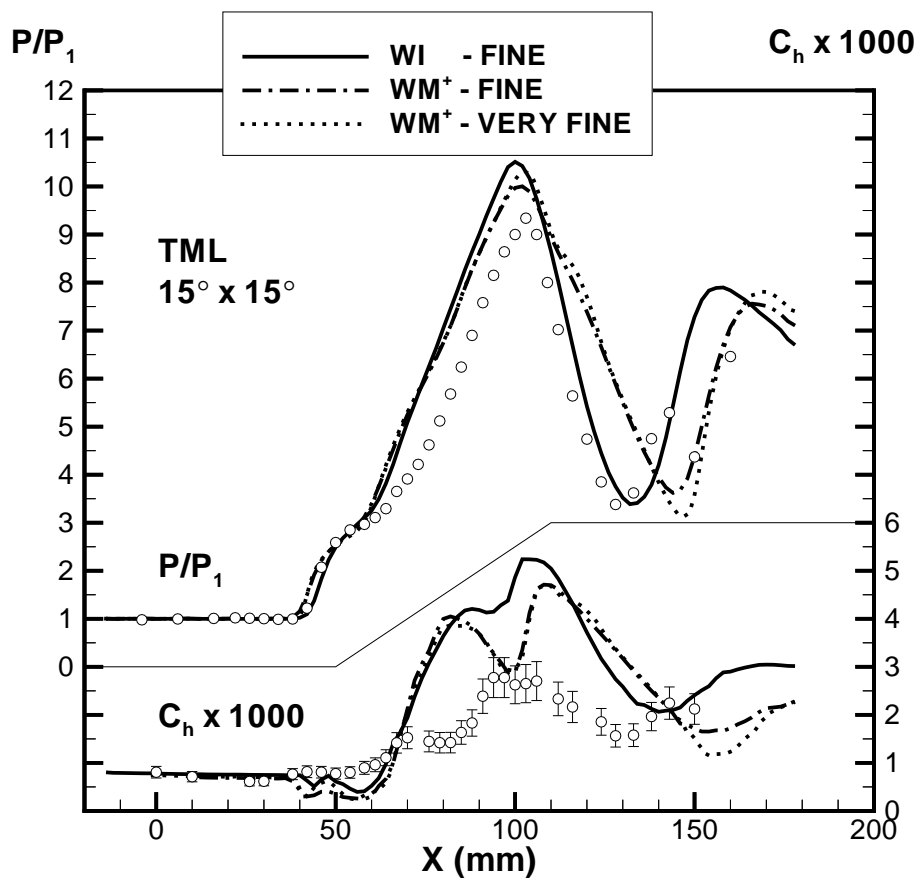


Figure 83: Surface pressure and heat transfer ($\alpha_1 = 15^\circ, \alpha_2 = 15^\circ$)

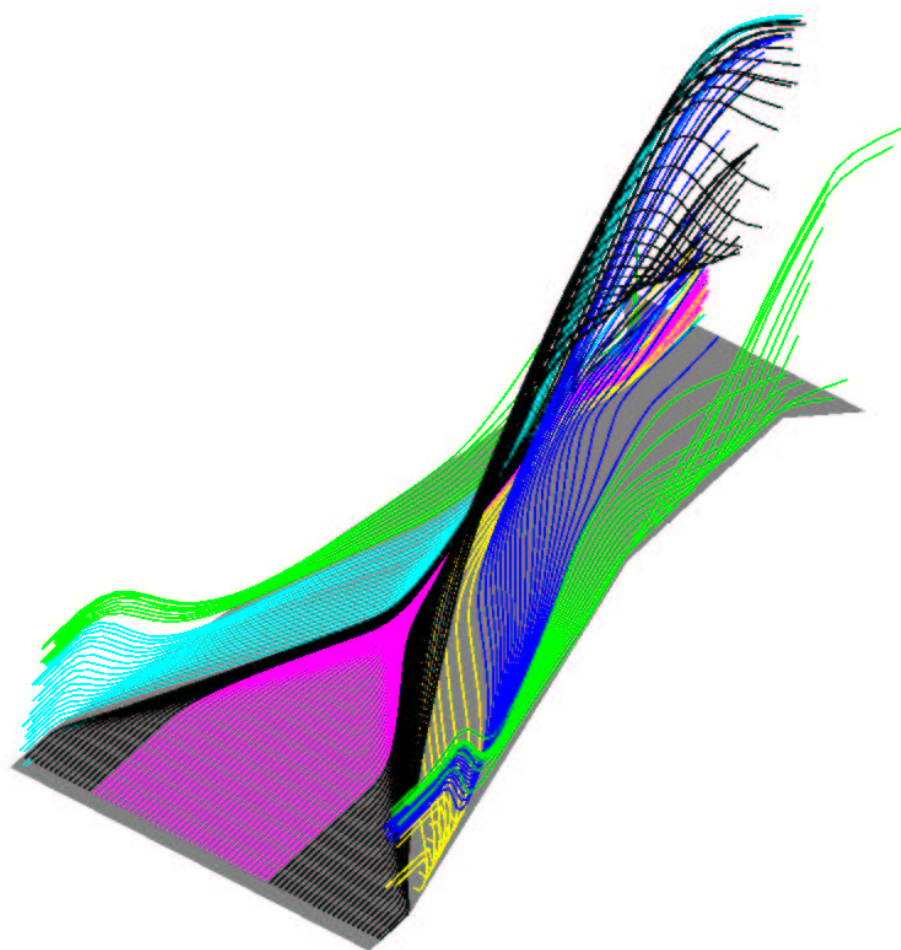


Figure 84: 3-D double fin flow structure

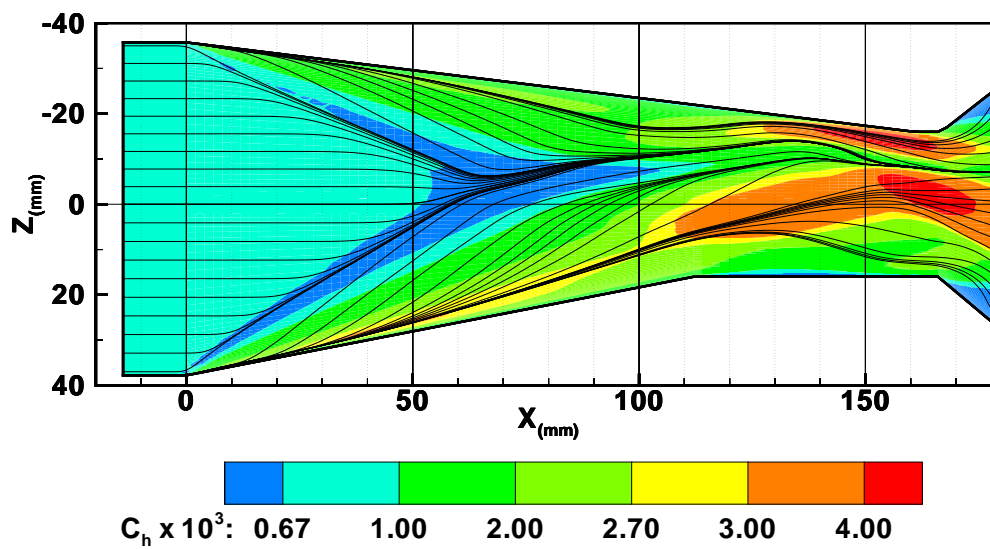


Figure 85: Computed surface heat transfer

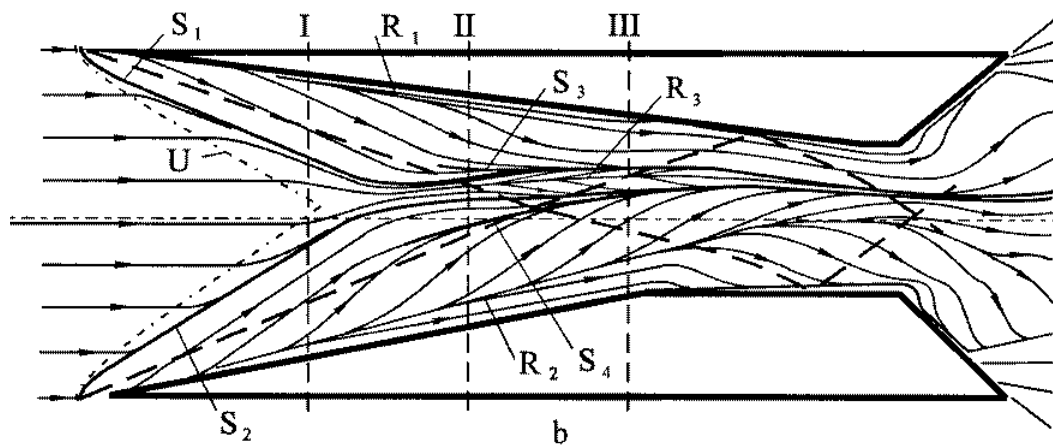


Figure 86: Surface flow visualization

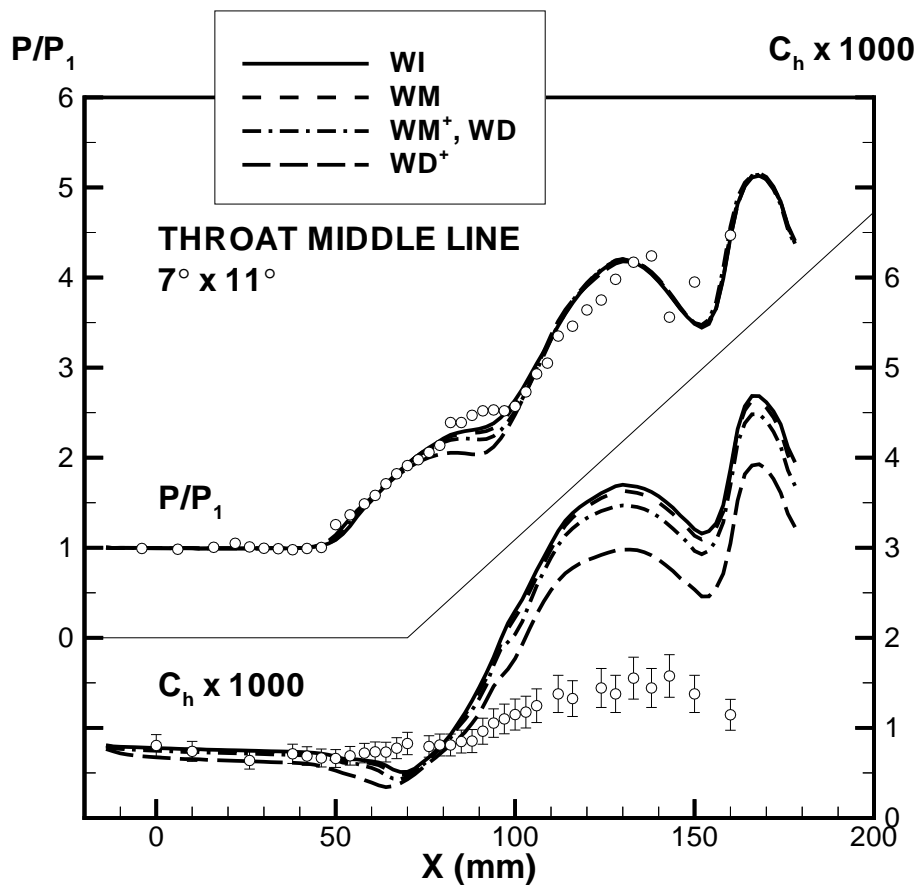


Figure 87: Surface pressure and heat transfer ($\alpha_1 = 7^\circ, \alpha_2 = 11^\circ$)

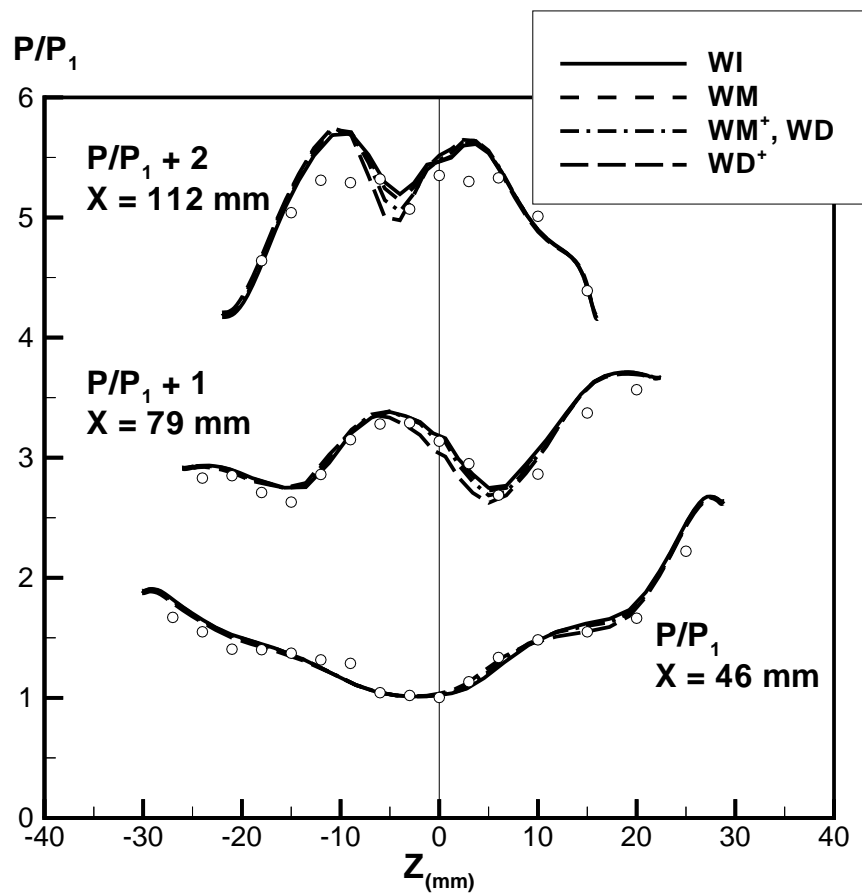


Figure 88: Surface pressure ($\alpha_1 = 7^\circ, \alpha_2 = 11^\circ$)

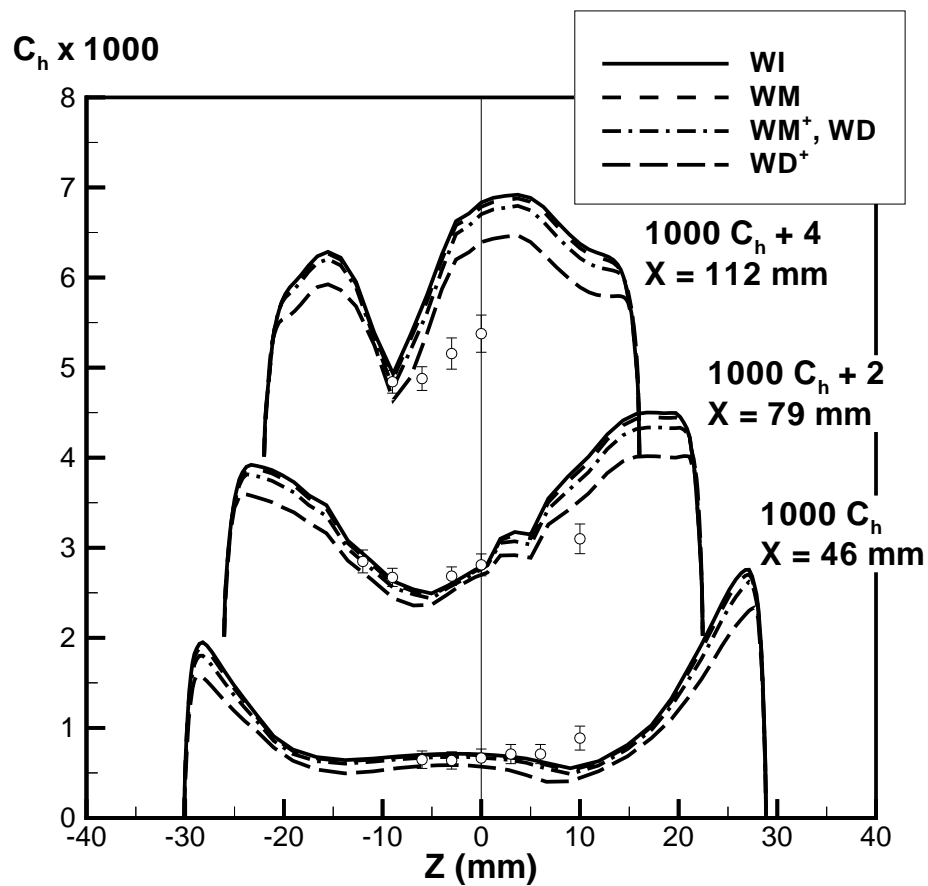


Figure 89: Surface pressure ($\alpha_1 = 7^\circ$, $\alpha_2 = 11^\circ$)

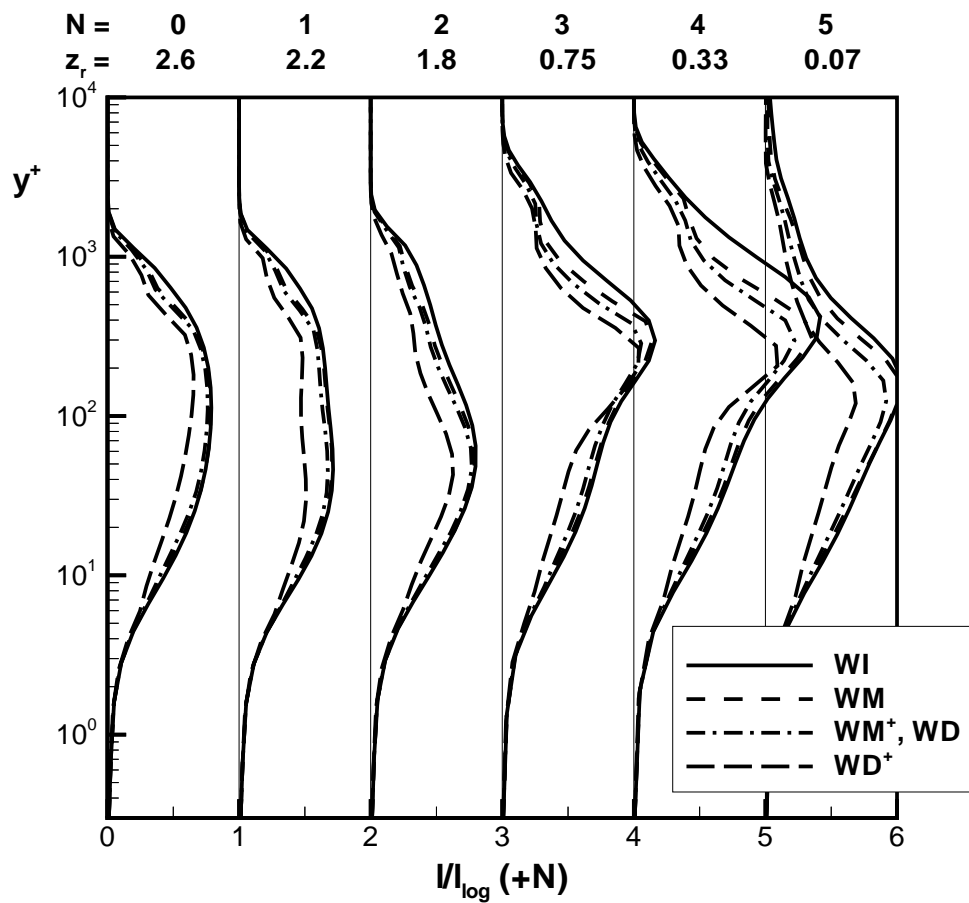


Figure 90: Turbulence length scale ratio ($\alpha_1 = 7^\circ, \alpha_2 = 11^\circ$)

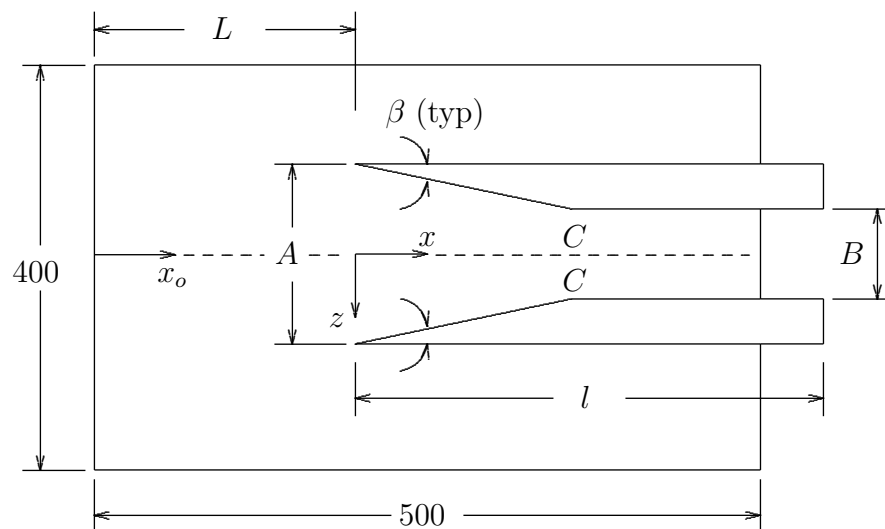


Figure 91: Double fin configuration

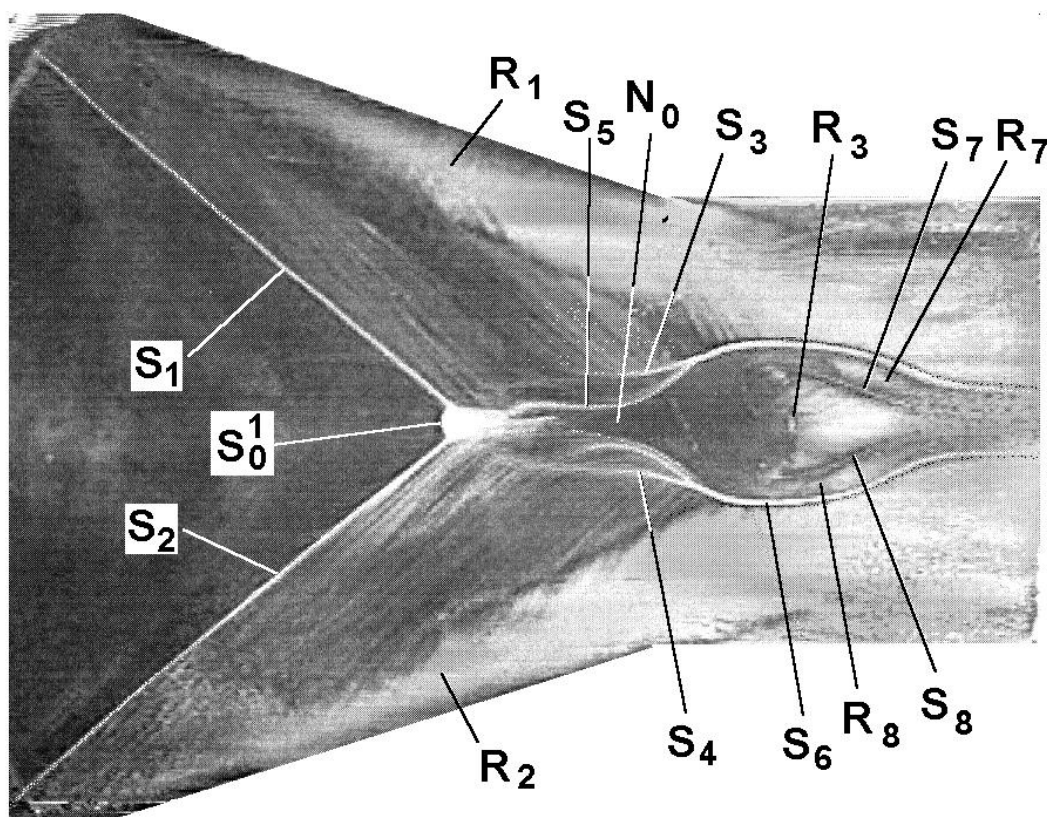


Figure 92: Experimental surface oil visualization

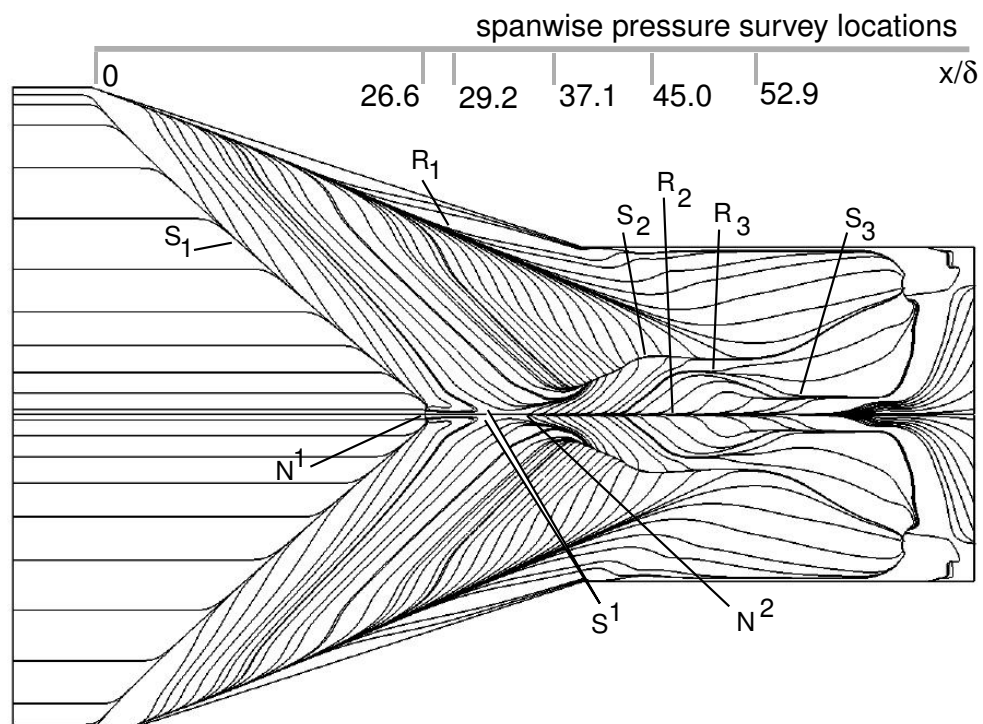


Figure 93: Surface streamlines

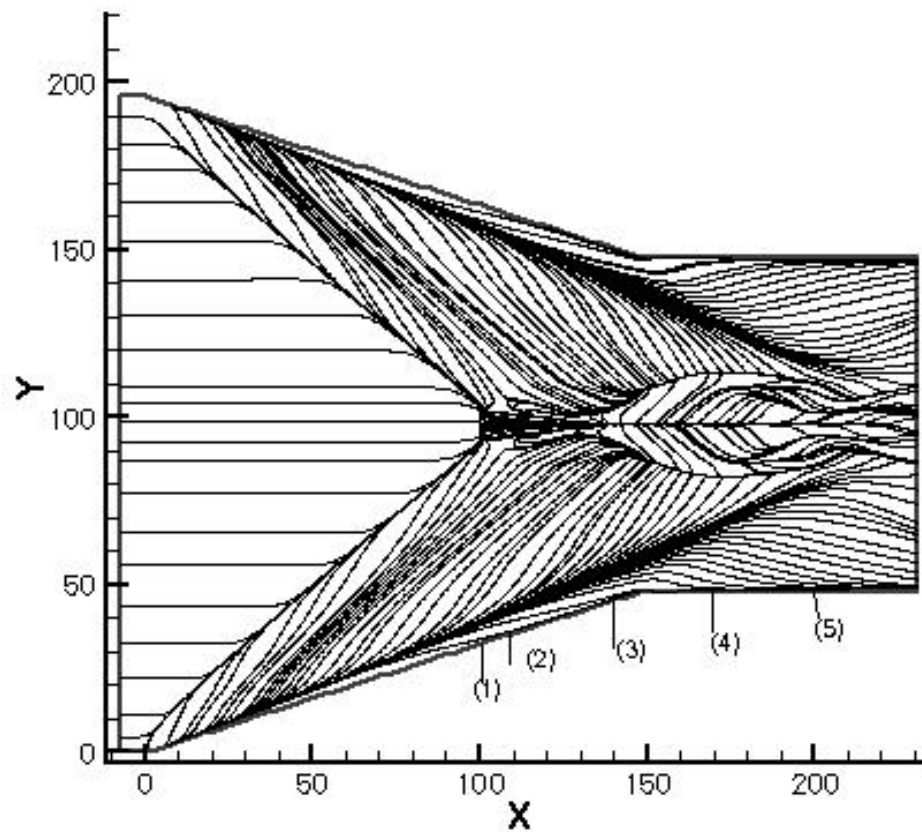


Figure 94: Surface streamlines

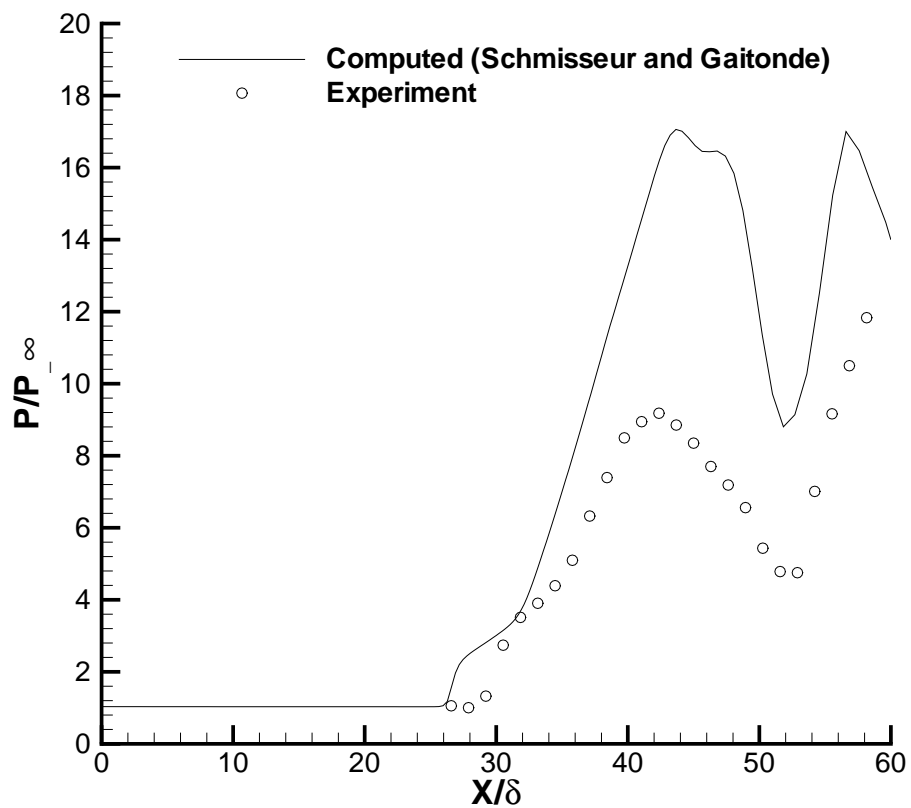


Figure 95: Surface pressure on centerline

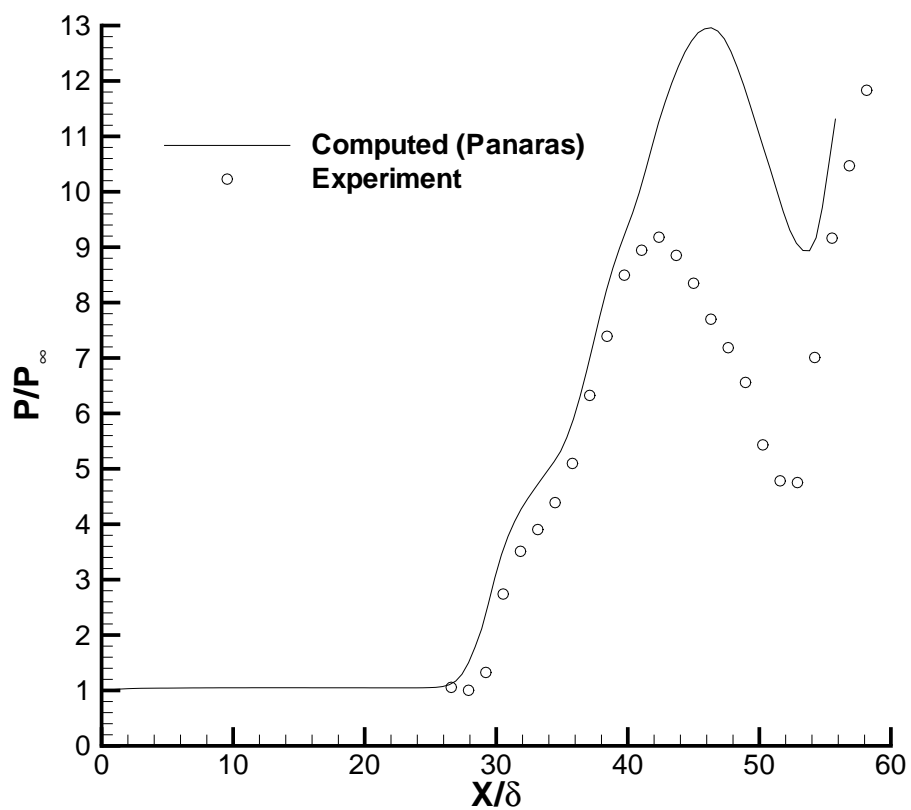


Figure 96: Surface pressure on centerline

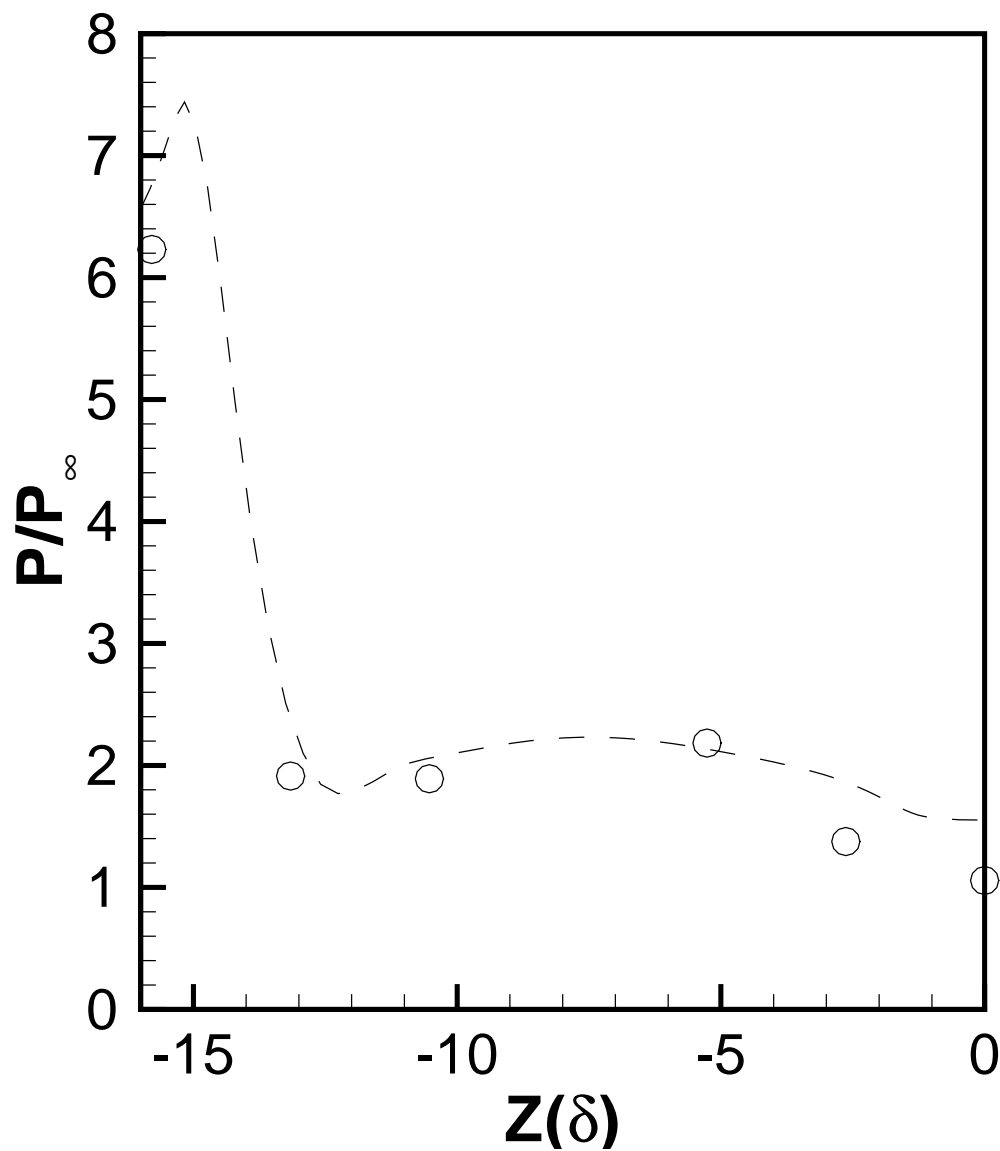


Figure 97: Surface pressure at $x = 26.6\delta$

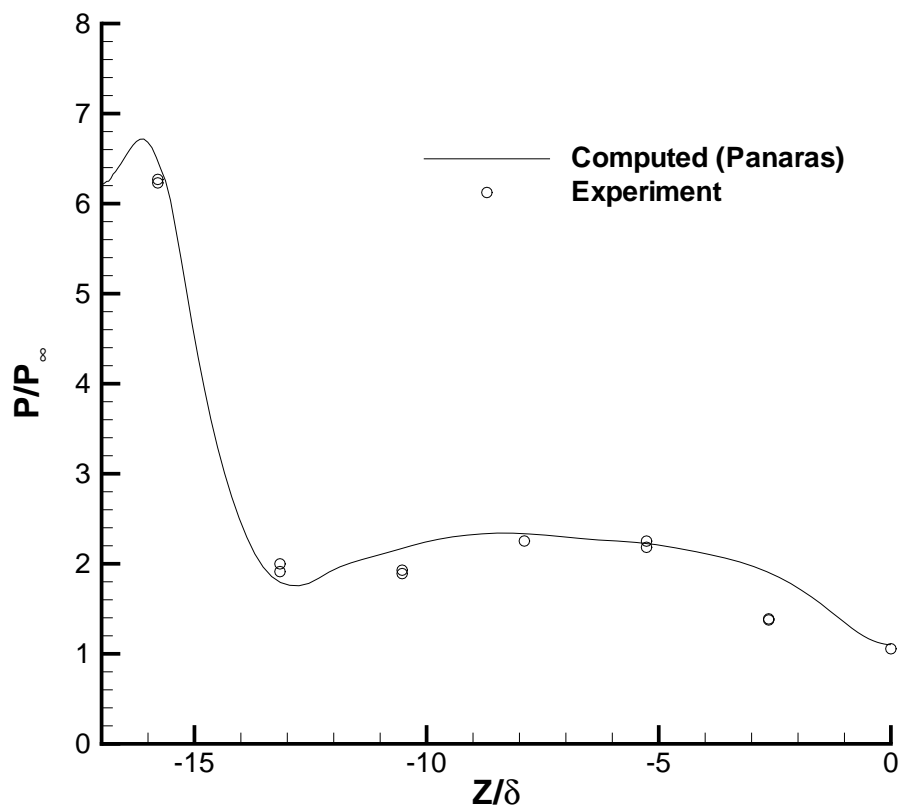


Figure 98: Surface pressure at $x = 26.6\delta$

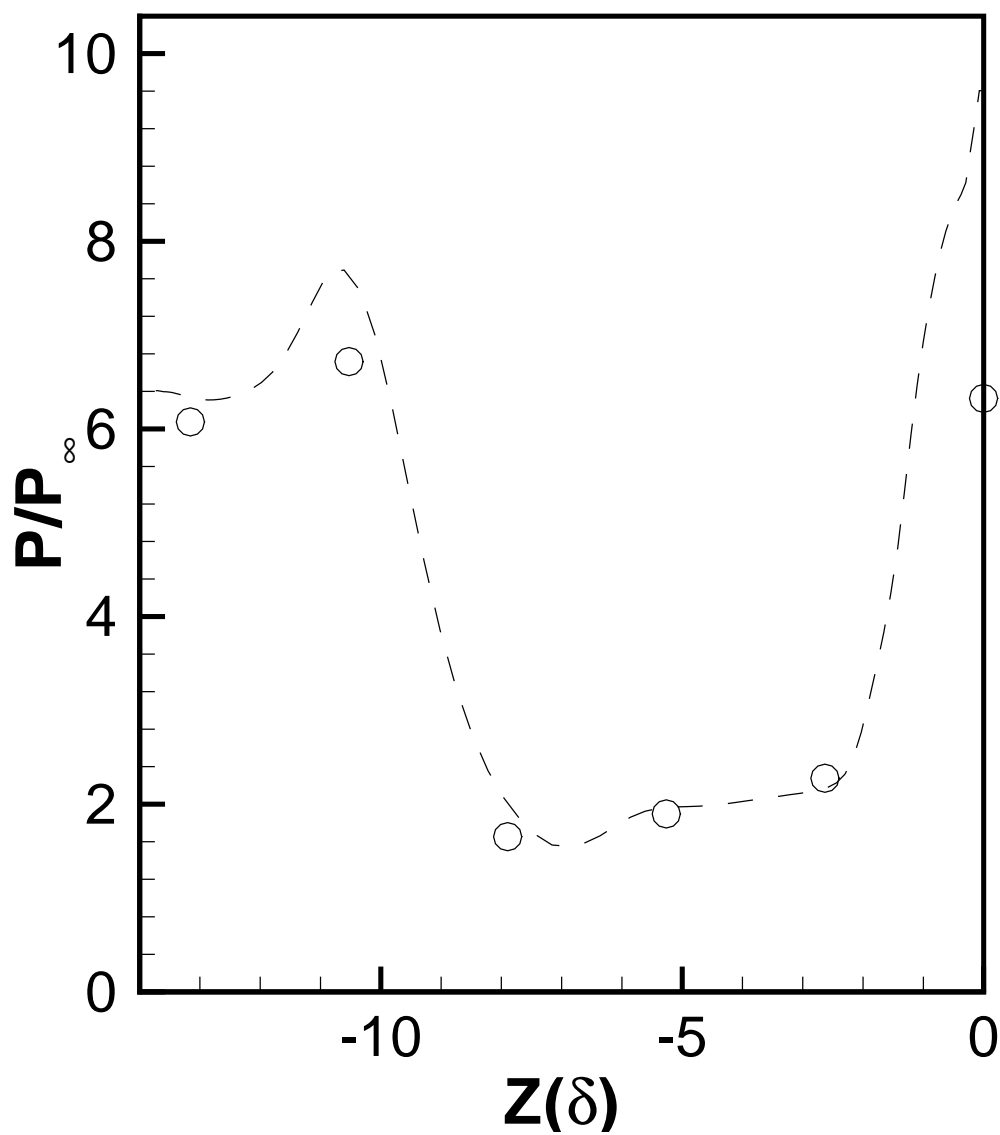


Figure 99: Surface pressure at $x = 37.1\delta$

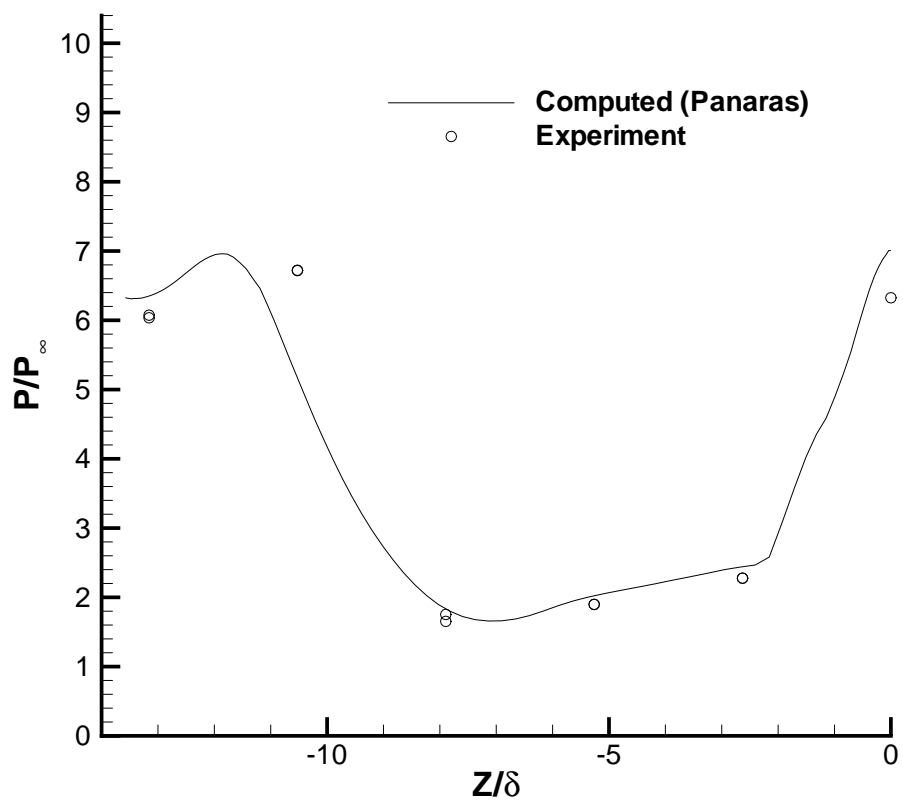


Figure 100: Surface pressure at $x = 37.1\delta$

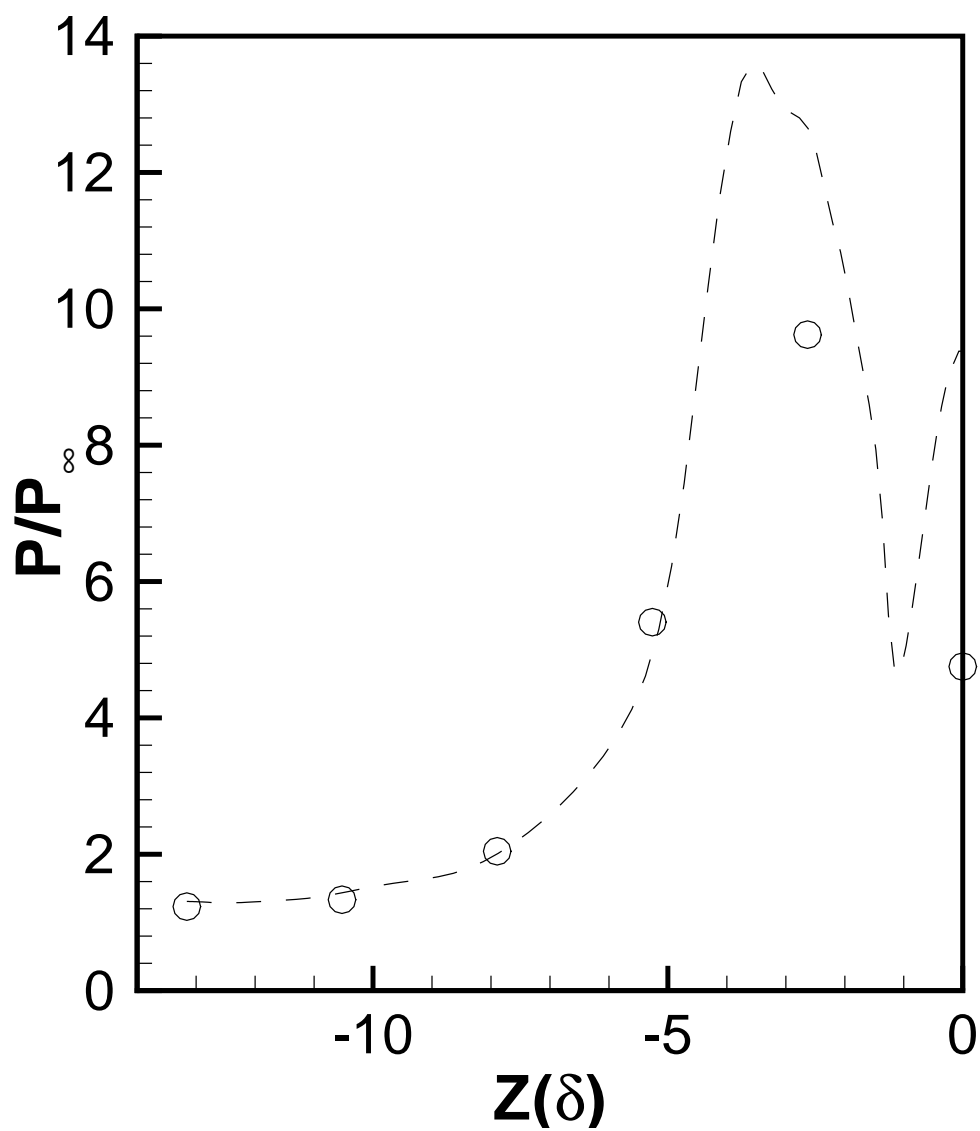


Figure 101: Surface pressure at $x = 52.9\delta$

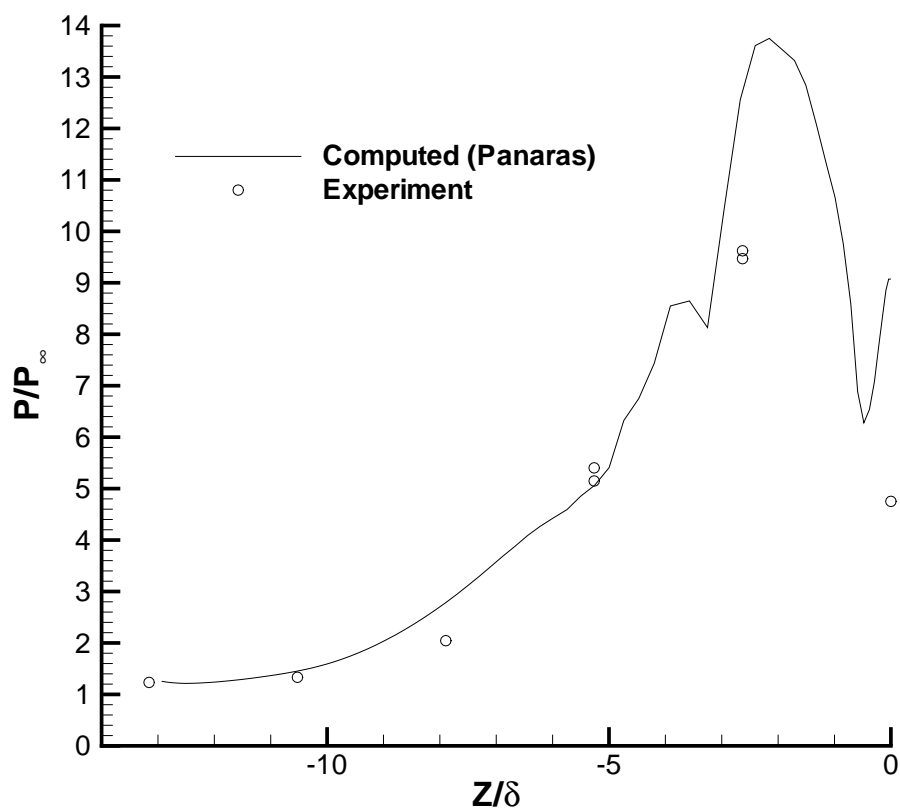


Figure 102: Surface pressure at $x = 52.9\delta$

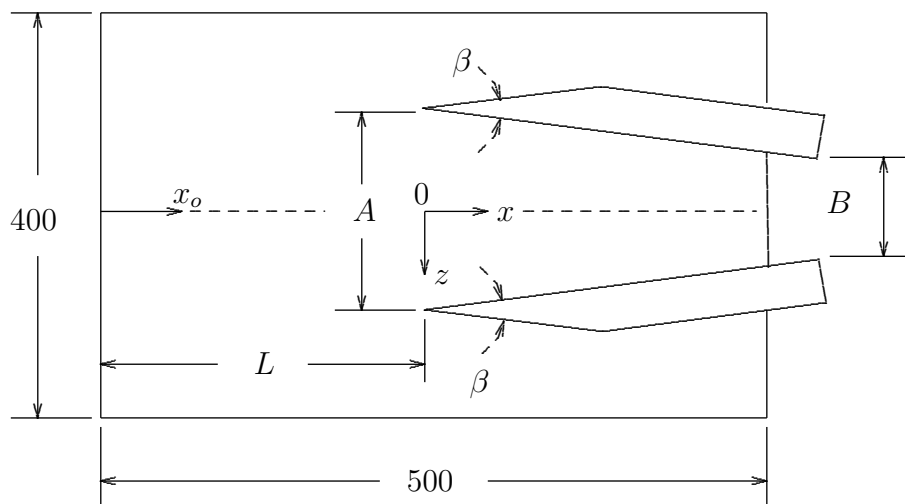


Figure 103: Double fin configuration

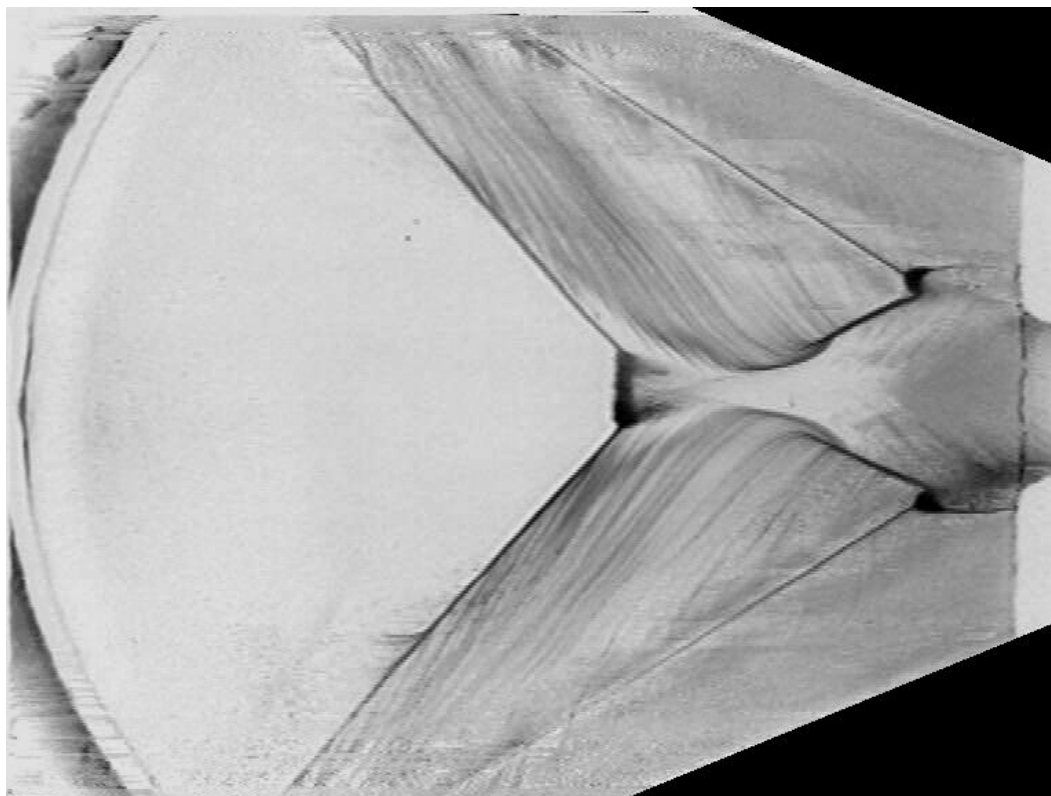


Figure 104: Experimental surface oil visualization

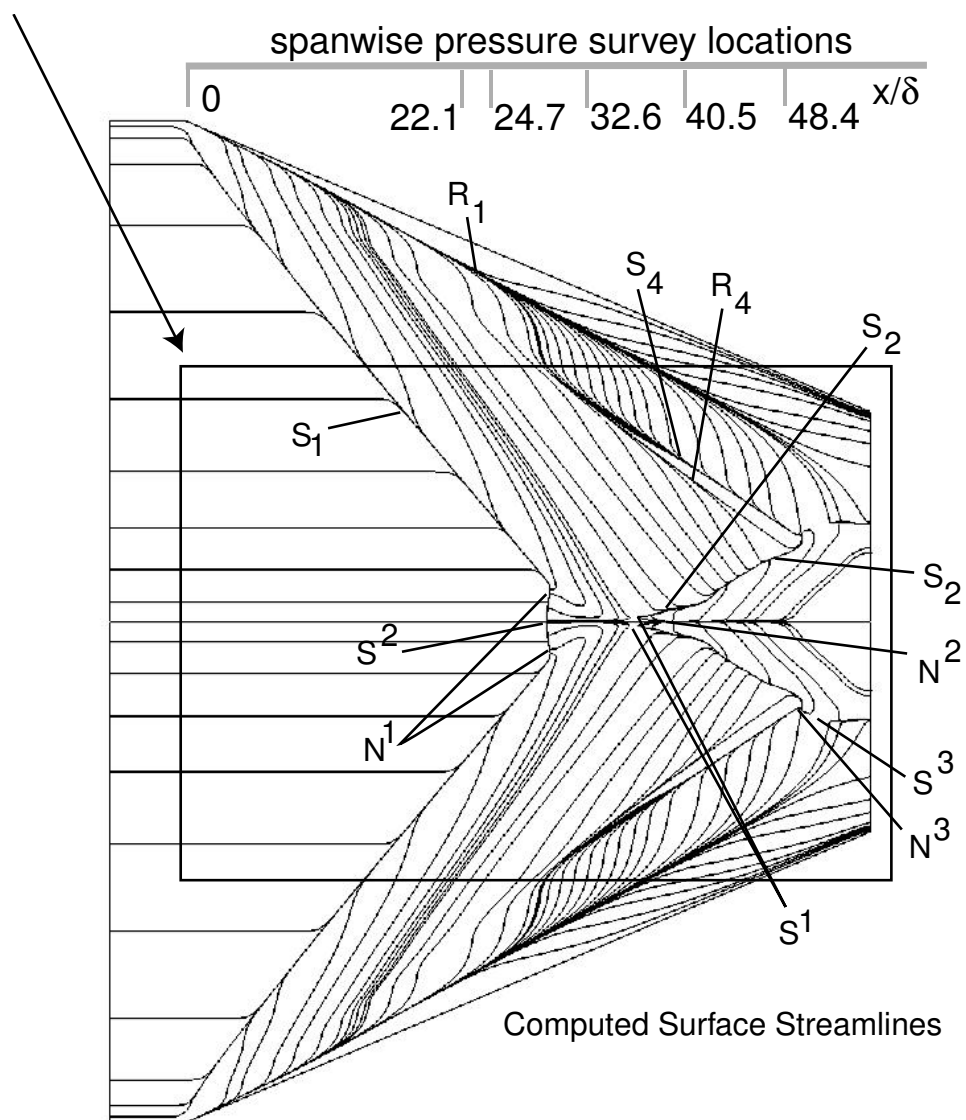


Figure 105: Surface streamlines

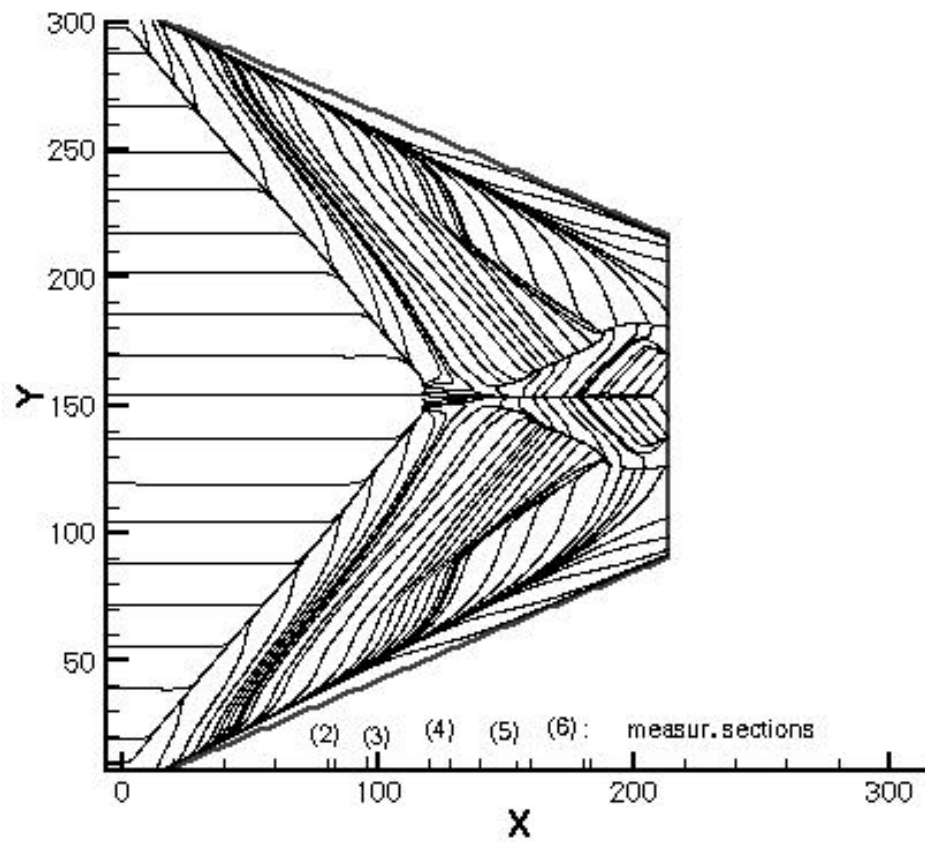


Figure 106: Surface streamlines

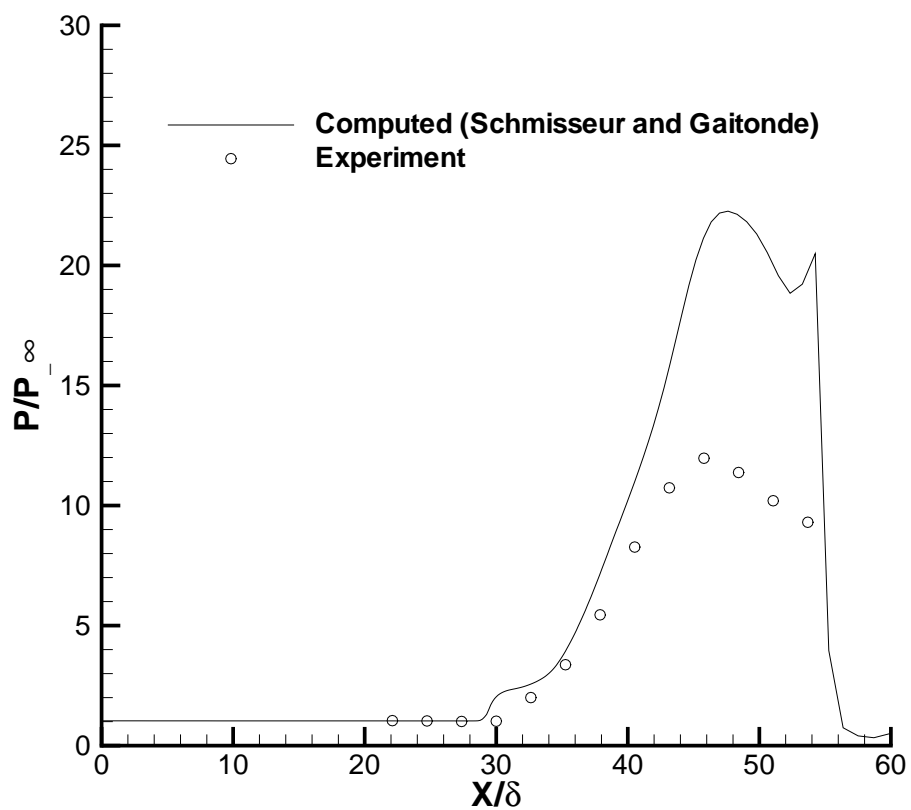


Figure 107: Surface pressure on centerline

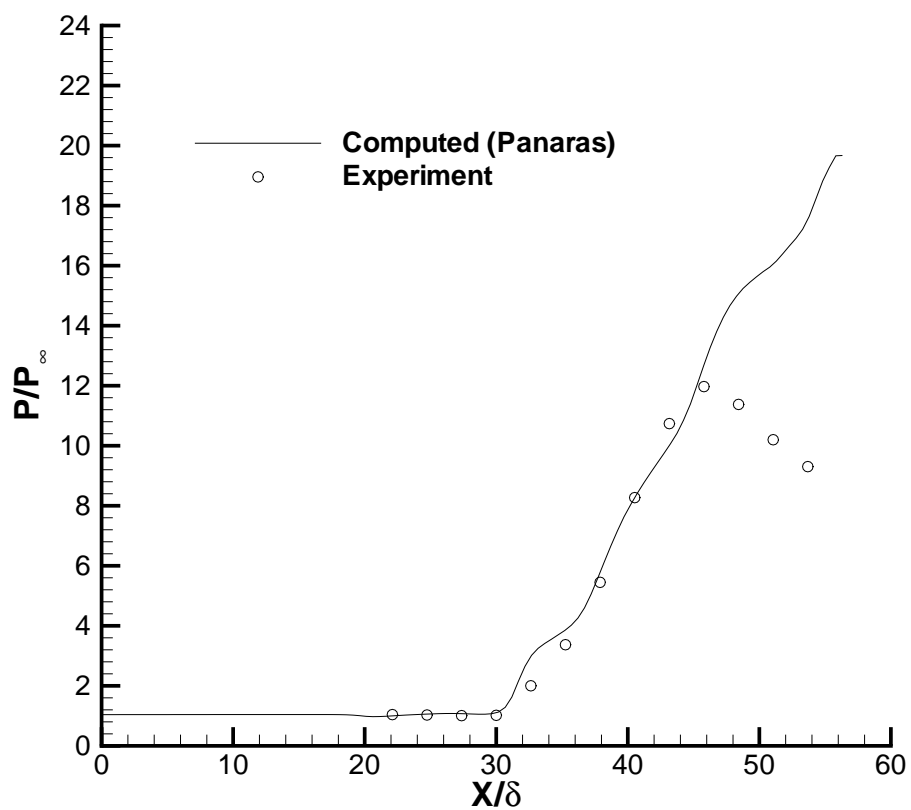


Figure 108: Surface pressure on centerline

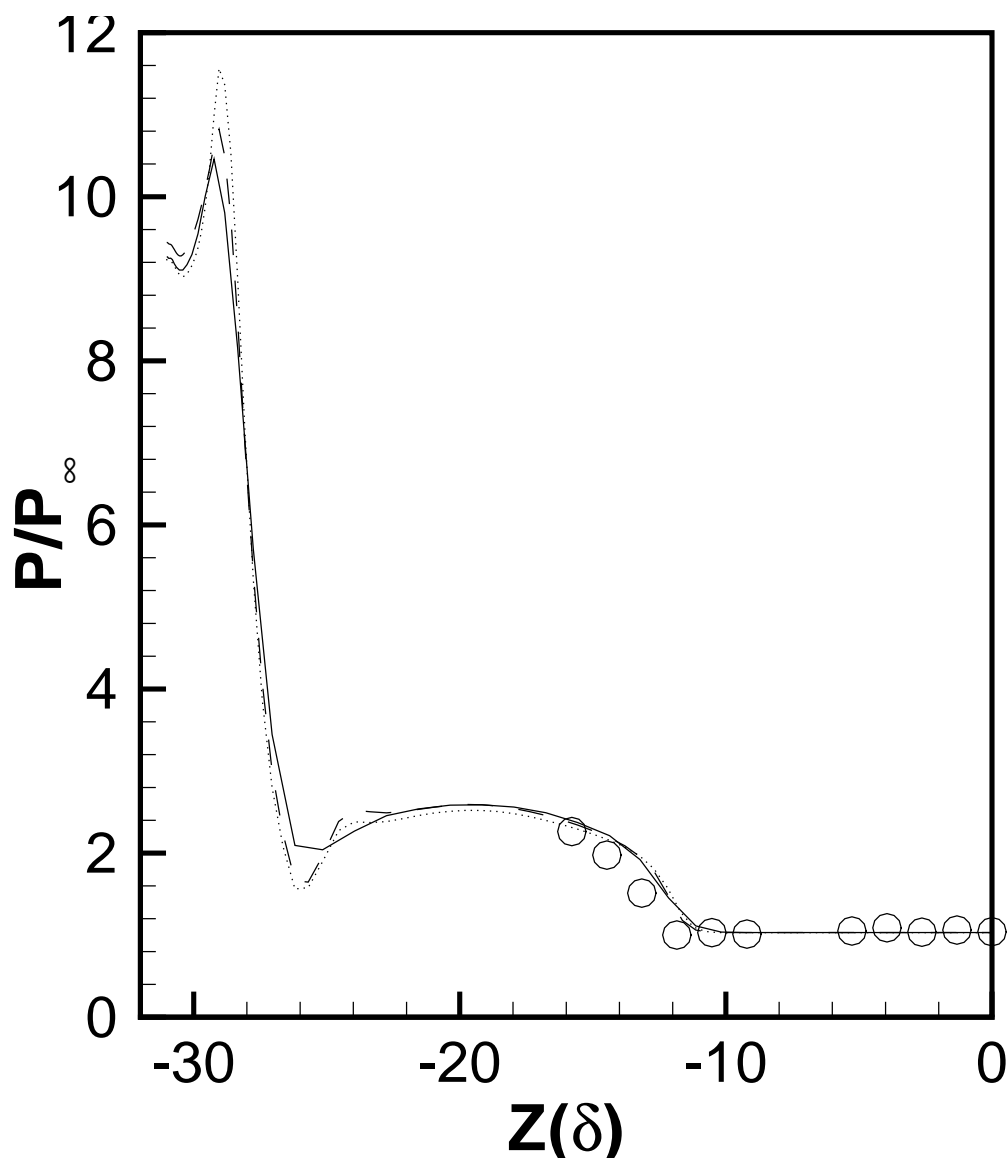


Figure 109: Surface pressure at $x = 22.1\delta$

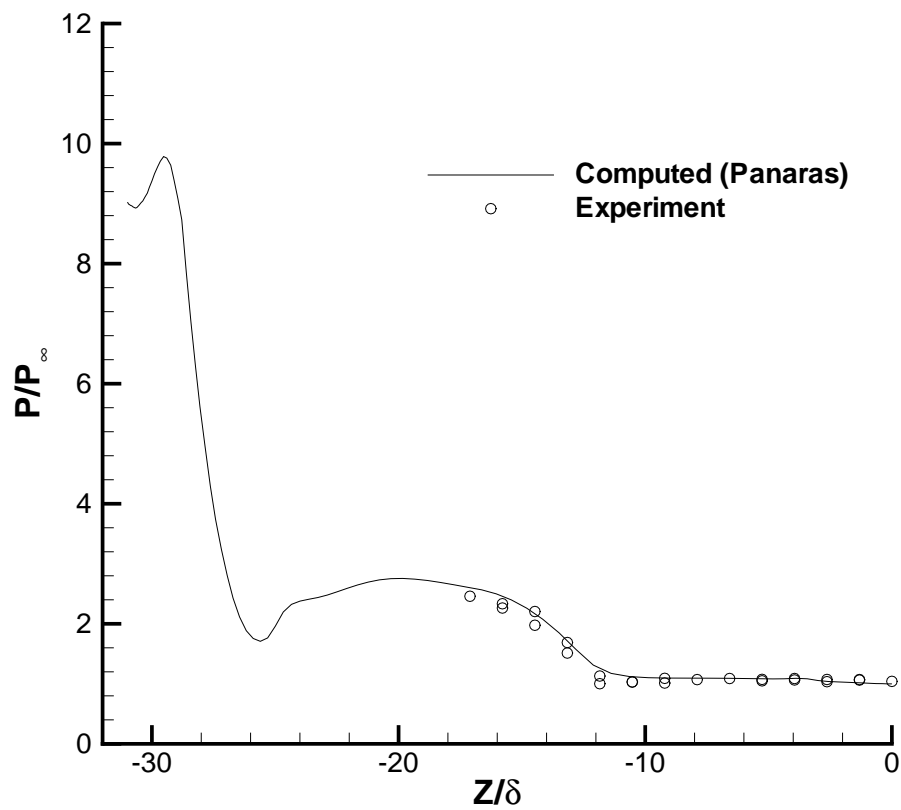


Figure 110: Surface pressure at $x = 22.1\delta$

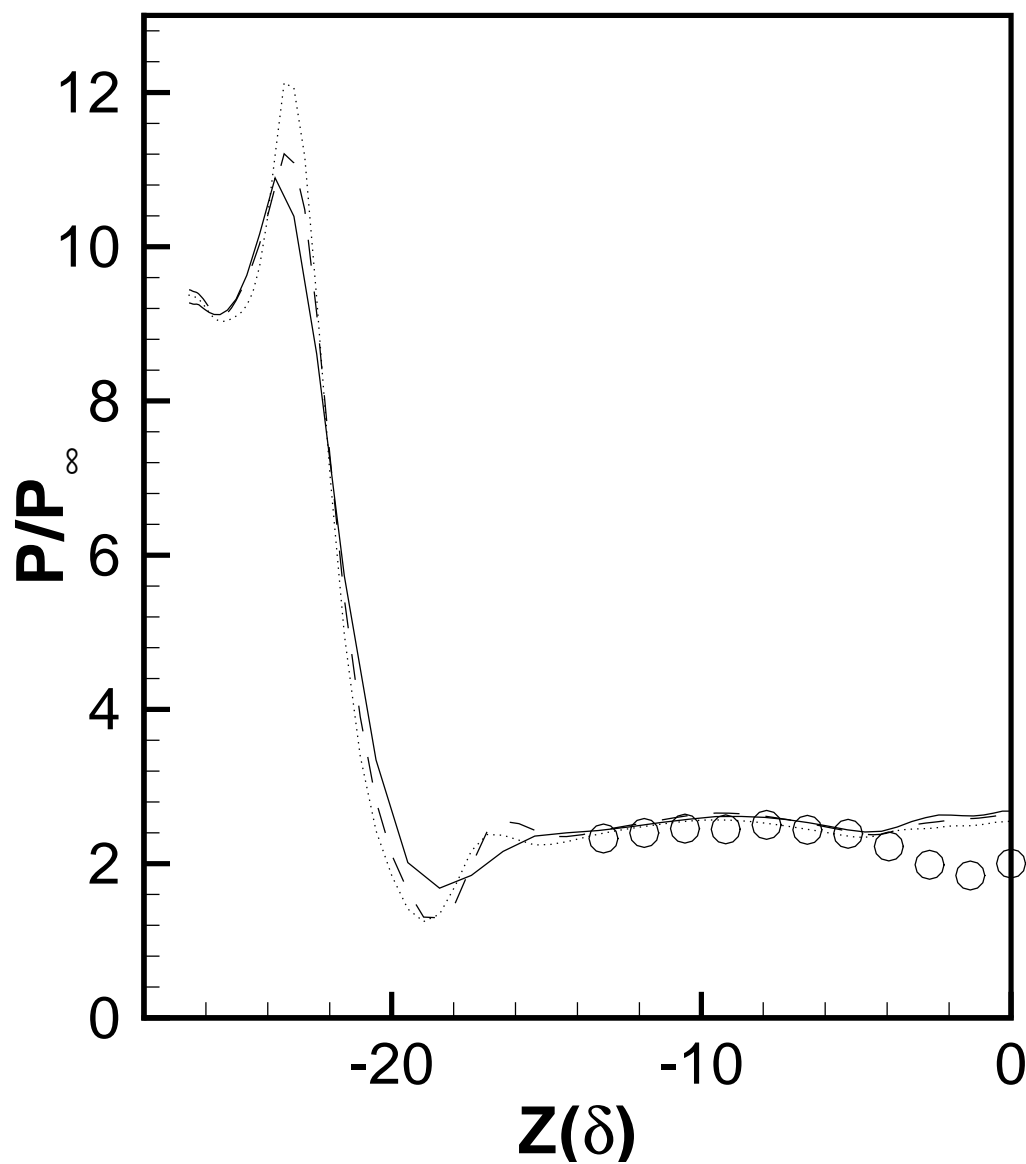


Figure 111: Surface pressure at $x = 32.6\delta$

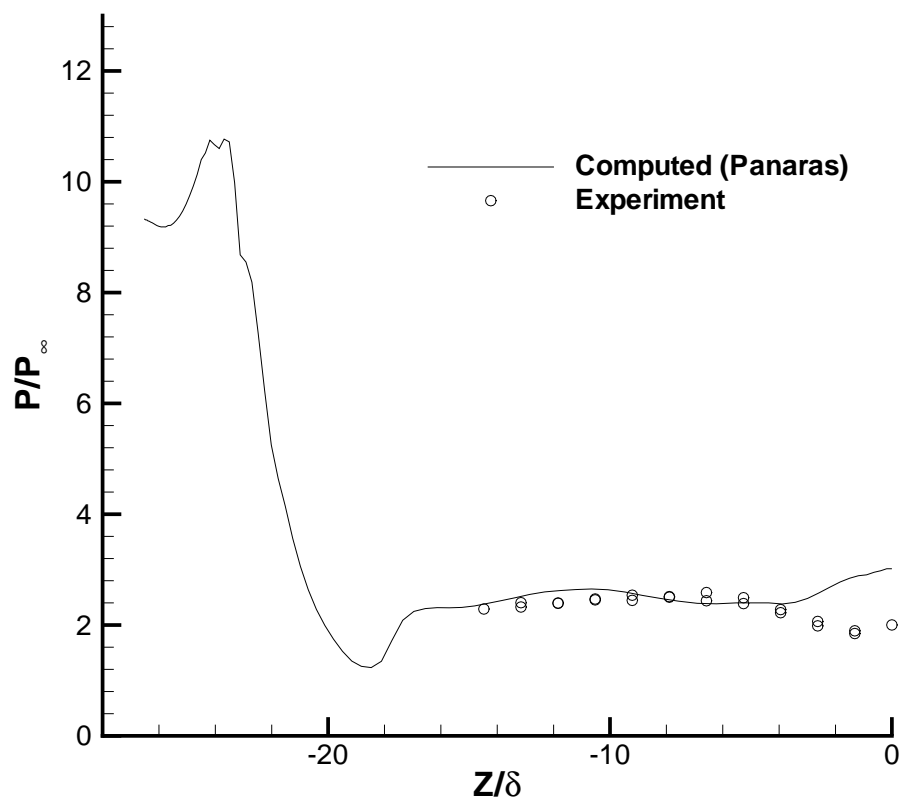


Figure 112: Surface pressure at $x = 32.6\delta$

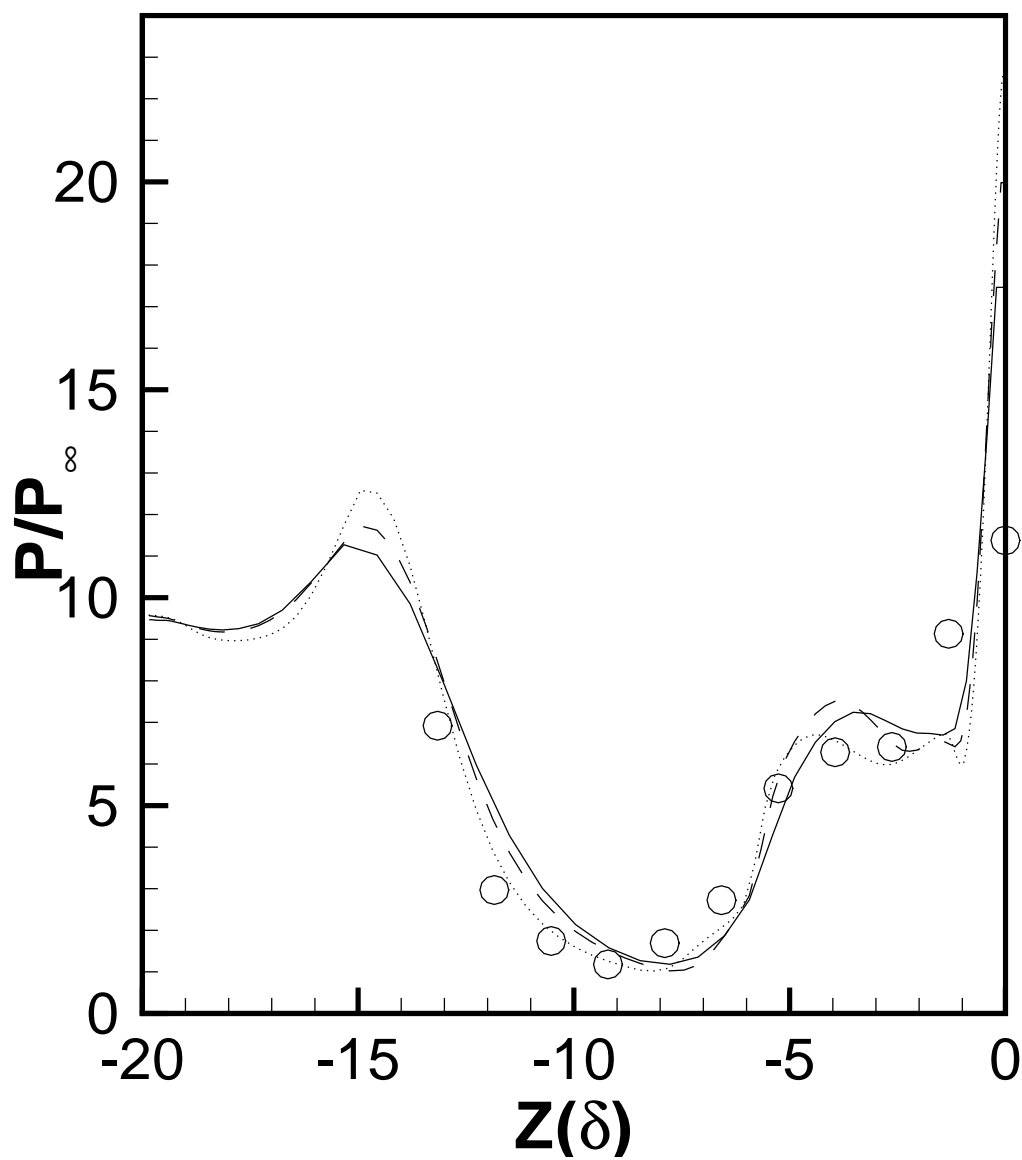


Figure 113: Surface pressure at $x = 48.4\delta$

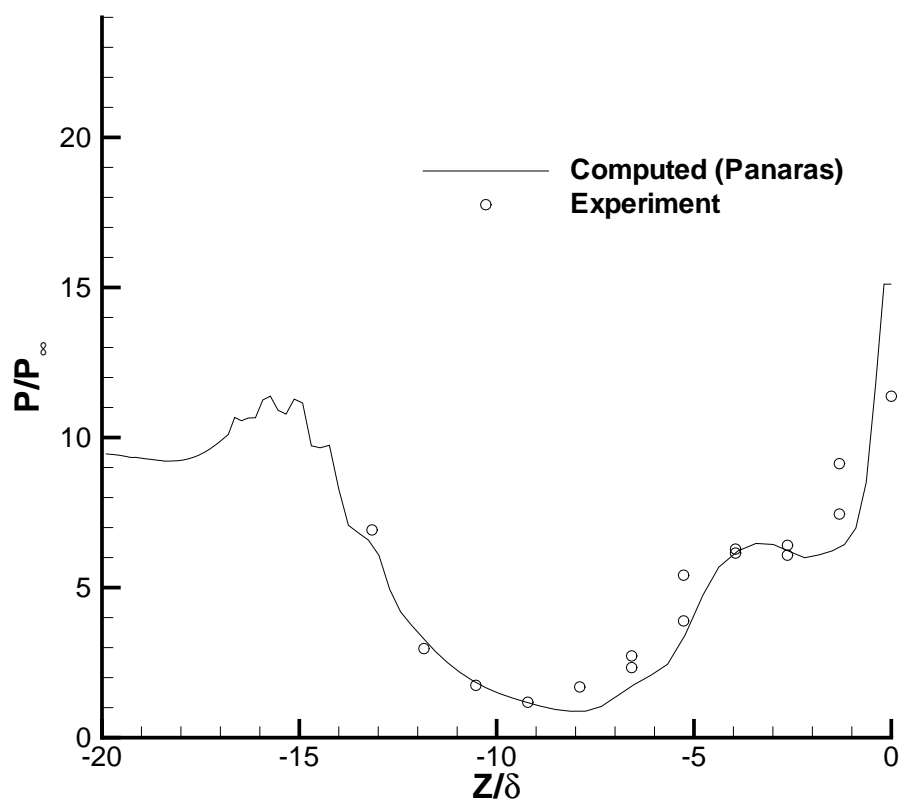


Figure 114: Surface pressure at $x = 48.4\delta$

List of Figure Captions

1. 2-D compression corner
2. 2-D shock impingement
3. 2-D expansion-compression corner
4. 3-D single fin
5. 3-D double fin
6. Surface pressure for 2-D compression corner and shock impingement at $M_\infty = 2.96$ and $\alpha = 25^\circ$ [19]
7. Separation length *vs* Re_δ [24]
8. Turbulence structure in 2D compression corner
9. Separation length for RANS
10. Instantaneous velocity and shock
11. Mean wall pressure
12. Mean velocity
13. Mean static temperature
14. Reynolds streamwise stress
15. Reynolds shear stress
16. Generation of inflow conditions
17. Inflow mean velocity
18. Inflow rms streamwise velocity
19. Mean surface pressure
20. Mean skin friction
21. Mean velocity

22. Mean static temperature
23. Spanwise TKE spectra at $y^+ = 7.3(y/\delta = 0.034)$
24. Spanwise TKE spectra at $y^+ = 132(y/\delta = 0.61)$
25. Turbulence statistics (– DNS, ... LES (ADM))
26. Separation length for DNS and LES
27. Inflow velocity
28. Inflow Reynolds streamwise stress
29. Inflow Reynolds shear stress
30. Mean wall pressure
31. Standard deviation of wall pressure
32. Skewness of wall pressure
33. Time history of wall pressure
34. Mean skin friction
35. Velocity profiles
36. Mean wall pressure
37. Mean skin friction
38. Mean wall pressure
39. Mean skin friction coefficient
40. Instantaneous shock structure
41. Instantaneous Schlieren image
42. Velocity (A —, B \triangle , C —, D \diamond , HWA \circ)
43. Skin friction (A —, B \triangle , C —, D \diamond , HWA \circ)
44. Displacement thickness (A —, B \triangle , C —, D \diamond , HWA \circ)

45. Velocity (A ($x = 351$ mm) —, A ($x = 345$ mm) —●—, B \triangle , C —, D \diamond , HWA \circ , LDA \square)
46. Rms velocity (A ($x = 326$ mm) —, A ($x = 320$ mm) —●—, B \triangle , C —, D \diamond , LDA \square)
47. Rms velocity (A ($x = 351$ mm) —, A ($x = 345$ mm) —●—, B \triangle , C —, D \diamond , HWA \circ , LDA \square)
48. Instantaneous Schlieren images of (a) the flat-plate boundary layer, (b) 7° centered expansion, and (c) 14° centered expansion
49. Instantaneous FRS visualization of (a) the 7° centered and (b) gradual expansion regions. The white lines indicate the position of the model surface.
50. Separation length
51. Mean static pressure
52. Mean streamlines
53. Mean velocity
54. Surface pressure
55. Skin friction coefficient
56. Flow model proposed by Kubota and Stollery[146]
57. Flow model of Alvi and Settles[148]
58. Perspective view of the conical separation vortices and of the shock waves (Panaras [150])
59. Conical projections of sections of the flow on the outflow plane (Panaras[150])
60. Skin friction lines and cross-section of the vortices (Panaras and Stanewsky[155])
61. 3-D single fin regimes (Zheltovodov *et al*[156])
62. Structure of the separated flow in a swept shock/turbulent boundary-layer interaction
63. Cross-sections of various flows (Panaras [2])
64. Grid for 3-D single fin

- 65. Surface streamlines for Case 1 (WI)
- 66. Surface streamlines for Case 1 (exper)
- 67. Surface streamlines for Case 1 (WD+)
- 68. Surface streamlines for Case 3 (WI)
- 69. Surface streamlines for Case 3 (exper)
- 70. Surface streamlines for Case 3 (WD+)
- 71. Surface pressure for Case 1
- 72. Surface pressure for Case 2
- 73. Surface pressure for Case 3
- 74. Skin friction for Case 2
- 75. Turbulence kinetic energy for Case 3 (WI)
- 76. Turbulence kinetic energy for Case 3 (WD+)
- 77. 3-D Double Fin Flow Structure [177, 173, 178]
- 78. 3-D Double Fin Flow Structure [189, 192, 193, 197]
- 79. 3-D Double Fin Flow Structure [189, 192, 193, 197]
- 80. 3-D Double Fin Flow Structure [189, 192, 193, 197]
- 81. 3-D Double Fin Flow Structure [159]
- 82. Topology, skin friction and heat transfer
- 83. Surface pressure and heat transfer ($\alpha_1 = 15^\circ, \alpha_2 = 15^\circ$)
- 84. 3-D double fin flow structure
- 85. Computed surface heat transfer
- 86. Surface flow visualization
- 87. Surface pressure and heat transfer ($\alpha_1 = 7^\circ, \alpha_2 = 11^\circ$)

- 88. Surface pressure ($\alpha_1 = 7^\circ, \alpha_2 = 11^\circ$)
- 89. Surface pressure ($\alpha_1 = 7^\circ, \alpha_2 = 11^\circ$)
- 90. Turbulence length scale ratio ($\alpha_1 = 7^\circ, \alpha_2 = 11^\circ$)
- 91. Double fin configuration
- 92. Experimental surface oil visualization
- 93. Surface streamlines
- 94. Surface streamlines
- 95. Surface pressure on centerline
- 96. Surface pressure on centerline
- 97. Surface pressure at $x = 26.6\delta$
- 98. Surface pressure at $x = 26.6\delta$
- 99. Surface pressure at $x = 37.1\delta$
- 100. Surface pressure at $x = 37.1\delta$
- 101. Surface pressure at $x = 52.9\delta$
- 102. Surface pressure at $x = 52.9\delta$
- 103. Double fin configuration
- 104. Experimental surface oil visualization
- 105. Surface streamlines
- 106. Surface streamlines
- 107. Surface pressure on centerline
- 108. Surface pressure on centerline
- 109. Surface pressure at $x = 22.1\delta$
- 110. Surface pressure at $x = 22.1\delta$

- 111. Surface pressure at $x = 32.6\delta$
- 112. Surface pressure at $x = 32.6\delta$
- 113. Surface pressure at $x = 48.4\delta$
- 114. Surface pressure at $x = 48.4\delta$

Table 1: RANS calculations of 2-D Compression Corner

Number	Ref.	Model	α	Mach	$Re_\delta \times 10^{-6}$	L_{sep}/δ	L_{sep}/L_c
1	Shang [60]	Equilibrium	25°	2.96	0.1	5.0	15.3
2	Shang [60]	Frozen	25°	2.96	0.1	13.0	39.7
3	Shang [60]	Relaxation	25°	2.96	0.1	10	30.5
4	Horstman [61]	Baseline	20°	2.85	1.65	1.45	8.7
5	Horstman [61]	Relaxation	20°	2.85	1.65	2.69	16.1
6	Horstman [61]	Pressure Gradient	20°	2.85	1.65	0.81	4.87
7	Horstman [61]	Relaxation+ Pressure Gradient	20°	2.85	1.65	1.62	9.75
8	Horstman [61]	Baseline	24°	2.85	1.33	4.0	14.5
9	Horstman [61]	Relaxation	24°	2.85	1.33	4.7	17.1
10	Horstman [61]	Pressure Gradient	24°	2.85	1.33	2.74	9.96
11	Horstman [61]	Relaxation+ Pressure Gradient	24°	2.85	1.33	3.6	13.1
12	Visbal,Knight [62]	B-L	16°	2.9	1.6	1.0	14.4
13	Visbal,Knight [62]	Modified B-L	16°	2.9	1.6	0.2	2.89
14	Visbal,Knight [62]	Relaxation	16°	2.9	1.6	0.6	8.66
15	Visbal,Knight [62]	Constant Ymax	16°	2.9	1.6	0.2	2.89
16	Visbal,Knight [62]	B-L	20°	2.9	1.6	1.6	11.5
17	Visbal,Knight [62]	Modified B-L	20°	2.9	1.6	0.9	6.46
18	Visbal,Knight [62]	Relaxation	20°	2.9	1.6	1.8	12.9
19	Visbal,Knight [62]	Modified B-L	24°	2.9	1.6	2.05	7.25
20	Visbal,Knight [62]	Relaxation	24°	2.9	1.6	2.95	10.4
21	Ong,Knight [63]	B-L	16°	1.96	0.25	2.15	10.1
22	Ong,Knight [63]	B-L	16°	2.83	1.6	0.6	2.81
23	Ong,Knight [63]	B-L	20°	2.83	1.6	1.75	8.19
24	Horstman [64]	$k - \varepsilon$	25°	3.0	0.133	4.89	16.3
25	Borisov <i>et al</i> [65]	$k - \omega$	25°	3.0	0.139	7.38	24.8

Table 2: Flow Conditions

<i>Reference</i>	<i>Data</i>	M_∞	$Re_\delta \times 10^{-4}$
Urbin <i>et al</i> [85]	LES	3.0	2.0
Kannepalli <i>et al</i> [86]	LES	2.88	2.0
Zhel'tovodov <i>et al</i> [35, 36, 37]	E	2.9	7.5 – 11

Table 3: Details of Computations

<i>Reference</i>	<i>Type</i>	<i>Cells</i>	SA	TA
Urbin <i>et al</i> [85]	LES	1.6×10^6	2nd	2nd
Kannepalli <i>et al</i> [86]	LES	$300 \times 65 \times 56$	4th	2nd/4th

Table 4: Flow Conditions

<i>Reference</i>	<i>Data</i>	M_∞	$Re_\delta \times 10^{-4}$
Adams[90, 91, 44]	DNS	3	2.1
Rizzetta <i>et al</i> [92]	DNS, LES	3	2.1
Stolz <i>et al</i> [93]	LES	3	2.1

Table 5: Details of Computations

<i>Reference</i>	<i>Type</i>	<i>Grid</i>	SA	TA
Adams[90, 91, 44]	DNS	$1000 \times 180 \times 80$	5th	3rd
Rizzetta <i>et al</i> [92]	DNS	$421 \times 151 \times 81$	6th	2nd
	LES-S	$421 \times 151 \times 81$	6th	2nd
	LES-D	$421 \times 151 \times 81$	6th	2nd
Stolz <i>et al</i> [93]	LES	$334 \times 91 \times 31$	6th	3rd

Table 6: Flow Conditions

<i>Reference</i>	<i>Data</i>	M_∞	$Re_\delta \times 10^{-6}$
Rizzetta <i>et al</i> [97]	LES	3.0	.021
Kannepalli <i>et al</i> [86]	LES	2.88	0.02
Settles <i>et al</i> [98]	E	2.84 – 2.87	1.5 – 1.6
Dolling <i>et al</i> [49]	E	2.90 – 2.95	0.81 – 1.4
Smits <i>et al</i> [99]	E	2.79 – 2.87	1.6
Zhelтоводов <i>et al</i> [3, 35, 36, 37, 100]	E	2.88	0.063

Table 7: Details of Computations

<i>Reference</i>	<i>Type</i>	<i>Grid</i>	SA	TA
Rizzetta <i>et al</i> [97]	LES	$421 \times 151 \times 181$	6th	2nd
Kannepalli <i>et al</i> [86]	LES	$300 \times 65 \times 56$	4th	2nd/4th

Table 8: Flow Conditions

	<i>Reference</i>	<i>Data</i>	M_∞	$Re_\delta \times 10^{-4}$
Yan <i>et al</i> [59]		LES	2.88	2.0
Zhel'tovodov <i>et al</i> [3, 35, 36, 37, 100]		E	2.88	6.4

Table 9: Details of Computations

<i>Reference</i>	<i>Type</i>	<i>Cells</i>	SA	TA
Yan <i>et al</i> [59]	LES	2.0×10^6	2nd	2nd

Table 10: Flow Conditions

<i>Reference</i>	<i>Data</i>	M_∞	$Re_\delta \times 10^{-4}$
Garnier <i>et al</i> [101, 102]	LES	2.3	6.0
Deleuze[103], Laurent[104]	E	2.3	6.0

Table 11: Details of Computations

<i>Reference</i>	<i>Type</i>	<i>Grid</i>	SA	TA
Garnier[101, 102]	LES-X (a)	$255 \times 55 \times 151$	2nd	2nd
	LES-X (b)	$255 \times 110 \times 151$	2nd	2nd
	LES-X (c)	$510 \times 55 \times 151$	2nd	2nd
	LES-M (d)	$510 \times 55 \times 151$	2nd	2nd

Table 12: Flow Conditions

<i>Reference</i>	<i>Data</i>	M_∞	$Re_\delta \times 10^{-4}$
Knight <i>et al</i> [139]	LES	2.88	2.0
Zheltovodov[23, 24, 37, 39, 40, 138, 136, 41]	E	2.88	4.4 – 50.

Table 13: Details of Computations

<i>Reference</i>	<i>Type</i>	<i>Cells</i>	SA	TA
Knight <i>et al</i> [139]	LES	2.4×10^6	2nd	2nd

Table 14: Flow Conditions

<i>Case</i>	<i>Reference</i>	<i>Data</i>	M_∞	α	Re_δ $\times 10^{-5}$
1	Thivet[161]	RANS	3.0	15°	1.9
	Zheltovodov[154, 143]	E	3.0	15°	1.9
2	Thivet[161]	RANS	4.0	20°	2.1
	Kim <i>et al</i> [158]	E	4.0	20°	2.1
3	Thivet[161]	RANS	4.0	30.6°	1.6
	Zheltovodov <i>et al</i> [154]	E	4.0	30.6°	1.6

Table 15: Details of Computations

<i>Case</i>	<i>Reference</i>	<i>Type</i>	<i>Grid</i>	SA	TA
1	Thivet[161]	RANS	$128 \times 160 \times 160$	2nd	SS
2	Thivet[161]	RANS	$128 \times 160 \times 160$	2nd	SS
3	Thivet[161]	RANS	$112 \times 160 \times 160$	2nd	SS

Table 16: Flow Conditions

<i>Case</i>	<i>Reference</i>	<i>Data</i>	M_∞	α_1	α_2	Re_δ $\times 10^{-5}$
1	Thivet[164, 202, 204, 209]	RANS	3.92	15°	15°	3.0
	Zheltonodov <i>et al</i> [187, 194, 196, 216]	E	3.92	15°	15°	3.0
2	Thivet[164, 202, 204, 209]	RANS	3.92	7°	11°	3.0
	Zheltonodov <i>et al</i> [187, 194, 196, 216]	E	3.92	7°	11°	3.0

Table 17: Details of Computations

<i>Case</i>	<i>Reference</i>	<i>Type</i>	<i>Grid</i>	SA	TA
1	Thivet[164]	RANS	$192 \times 200 \times 104$	2nd	SS
2	Thivet[164]	RANS	$96 \times 80 \times 160$	2nd	SS

Table 18: Flow Conditions

<i>Reference</i>	<i>Data</i>	M_∞	α_1	α_2	Re_δ
Schmisser <i>et al</i> [200]	RANS	4.96	18°	18°	1.39×10^5
Panaras[227]	RANS	4.96	18°	18°	1.39×10^5
Schülein and Zheltovodov[195, 228, 207]	E	4.96	18°	18°	1.39×10^5

Table 19: Details of Computations

<i>Reference</i>	<i>Type</i>	<i>Grid</i>	SA	TA
Schmisser <i>et al</i> [200]	RANS	$153 \times 143 \times 103$	2nd	SS
Panaras[227]	RANS	$127 \times 101 \times 91$	2nd	SS

Table 20: Flow Conditions

<i>Reference</i>	<i>Data</i>	M_∞	α_1	α_2	Re_δ
Schmisseur <i>et al</i> [200]	RANS	4.96	23°	23°	1.39×10^5
Panaras[227]	RANS	4.96	23°	23°	1.39×10^5
Schülein and Zheltovodov[195, 228, 207]	E	4.96	23°	23°	1.39×10^5

Table 21: Details of Computations

<i>Reference</i>	<i>Type</i>	<i>Grid</i>	SA	TA
Schmisser <i>et al</i> [200]	RANS	$229 \times 179 \times 129$	2nd	SS
Panaras[227]	RANS	$117 \times 101 \times 91$	2nd	SS